



Studies of the Higgs Sector with the CMS experiment at the LHC and at Future Hadron Colliders

Doctoral dissertation presented by

Paola Mastrapasqua

in fulfillment of the requirements for the degree of Doctor in Sciences.

Thesis Jury

Prof. Giacomo Bruno	Supervisor	UCLouvain
Dr. Andrea Giammanco	President	UCLouvain
Prof. Fabio Maltoni	Secretary	UCLouvain
Prof. Steven Lowette		Vrije Universiteit Brussel
Prof. Loukas Gouskos		Brown University

September, 2025

Acknowledgements

“Sometimes I’ll start a sentence, and I don’t even know where it’s going. I just hope I find it along the way. ”

— Michael Scott

As I sailed back from a boat trip at the close of my final conference as a student, it struck me that this journey, just about to end, was the perfect metaphor for my PhD voyage over the past four years.

Before setting off, the whole group had been warned that, given the strong wind, the sea would be rough and that we’d be ‘dancing’ on the boat (which was really more of a motorized dinghy). So the question was: did we still feel like going? More or less convincingly, we all said yes –mainly because it was our last chance, as the following day we’d be heading back home.

Once we left the harbor, we quickly realized how badly we had underestimated just how frightening it could actually be. The waves were high, tossing the boat into the air before it slammed back down with a huge splash, leaving us completely soaked. It was a mix of fear and confusion that reminded me so much of my first days arriving in Belgium from Italy, when I thought it would be relatively quick to settle in, secure a grant, and figure out how a massive collaboration like CMS worked –only to crash into reality instead.

Despite this rough start, I slowly began to adapt to the new situation and even to enjoy the challenges in front of me, just as excitement eventually replaced fear on that boat, once I realized that the waves weren’t a nuisance to endure, but rather an extra feature kindly included in the ride.

As time went by, my confidence kept growing, and eventually the waves calmed down, making the whole journey far more enjoyable. Whenever we did hit a rough patch, I had already learned not to panic, knowing that one way or another we’d make it through. In fact, those moments turned out to be essential for growth and they made us appreciate the calmer stretches even more.

Of course, none of this would have been true had I not had companions on that boat—friends to celebrate the exciting moments with, to relax alongside in quieter times, and, why not, to share the insecurities and frustrations that inevitably come with the journey. And it would have been even less true without guides, the captains of the ship. This section of my thesis is therefore dedicated to all of them, whom I’ll now mention in no particular order (certainly not by importance), because each of them has been fundamental in their own way throughout these years.

I'll try not to get overly sentimental, but no promises –you know I can be very emotional sometimes.

I would like to begin by thanking my PhD committee, which was truly the best I could have hoped for. In all our conversations, you always treated me as an equal, and I deeply appreciated that. I admire your professionalism, and your evident passion for physics has inspired me to enjoy my work, to stay curious, and to never stop asking questions. A special thanks goes to Giacomo, who gave me the freedom to explore and choose my own path –to try, to make mistakes, and eventually to find the topic and group where I could truly thrive. The sense of independence I have today is also thanks to that.

Next in line is Angela and Stellina. You have been guides for me during the first years of the PhD, I don't know what I would have done without you. Thanks for the crash course on CMS and on your middle-school-vibe inside jokes, which left me equally confused at the very beginning. Our trip to Chicago for the CMS-DAS is one of the sweetest memory from these four years. I'll never forget that Mexican food at 2 am with the tablecloth featuring Jesus and the Virgin Mary (and also that you wanted to leave me sleeping in that Uber as a joke, cruel as usual).

A special thank you to everyone I met at CERN for making me love both our collaboration and the work we do together. Birgit, you've been a huge support ever since we first met in Hamburg and again during the thesis-writing process. To my fellow Tau people: working with you was a blast, and celebrating our milestones together –not to mention those memorable conferences (yes, Prague!)– made it even better. A particular thanks to Izaak and Andrea, always ready with heartfelt advices, whether professional or personal.

Thanks to all my CP3 family. It has been a real pleasure working with you and sharing our lunch breaks together. I truly enjoyed our outing days, which brought us closer not just as colleagues but as people. I want to thank in particular the CMS@CP3 group, with whom I shared ideas, CMS recommendations, and at times the frustrations that come with working in such a big collaboration. A special mention goes to Jindrich (probably one of the very (very) few who actually read this entire thesis –thanks, man!), Anna, and Agni, who were always there whenever I needed support. And, of course, I need to thank the ones I am happy to call friends, Ricardo, Jo, Cisco, Tommy, Stavros, Ze, Luca, Marco and Leo, who cured my homesickness and made me feel like I had a group I could rely on, my support network. Above all, thanks to my bro Simo, you have been the craziest and most supportive, caring friend here, you accompanied me in many adventures, that boat trip was just the latest; I know

we'll continue to vibe together wherever we'll be in the future, hopefully still as "grandi b—h della Fisica".

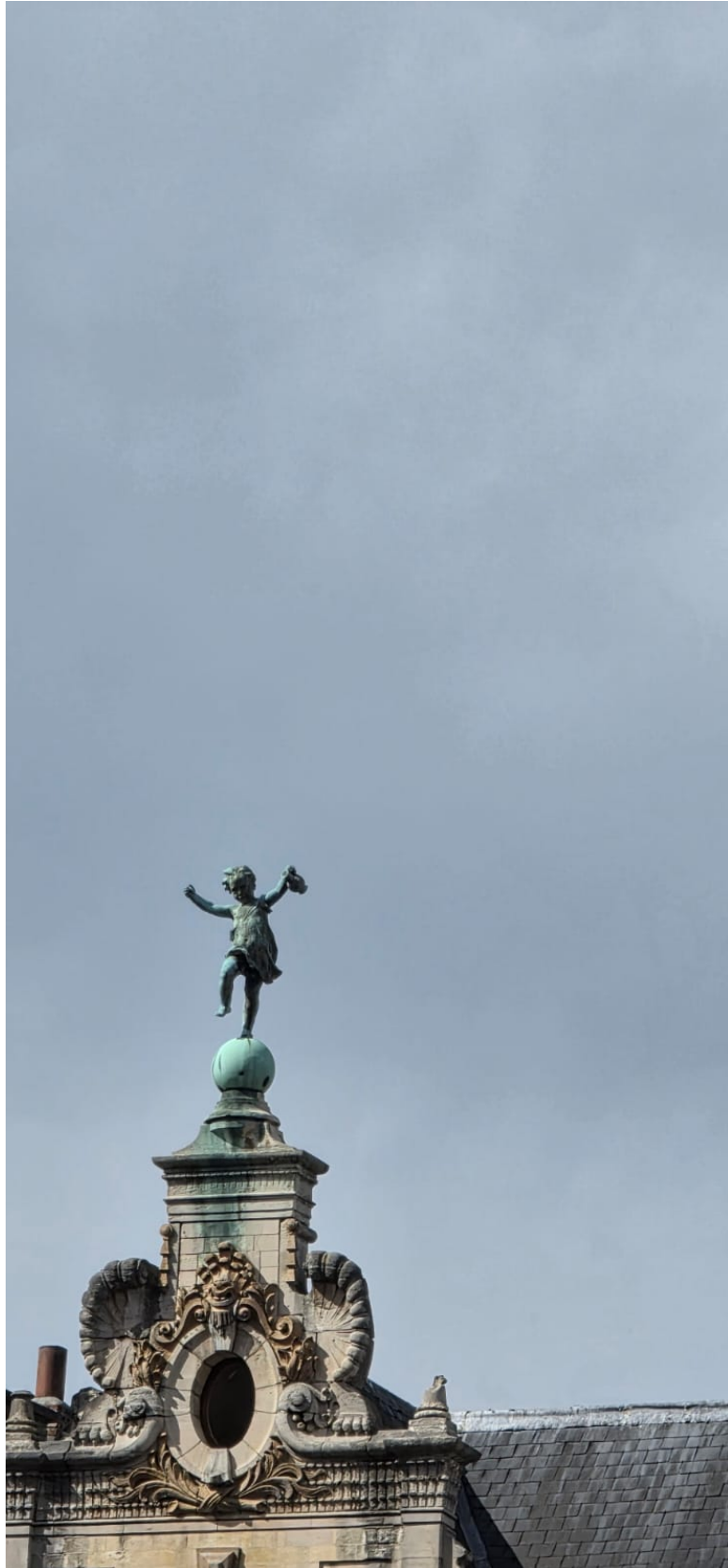
I'm also deeply grateful to the city that became my 2nd home over these years, a place I grew to love and will miss dearly as I move toward my next adventure. To Leuven and to the friends I've made here, I'll remember all the nights out in Oude Markt, or the *longest bar in Europe*, as they call it.

Finally, I want to thank all the people who supported me from Italy, with endless calls, messages, and hour-long voice notes. Even from afar, you made me feel close and connected. To my lifelong friend Paola, aka "la seconda figlia", thank you for always being there for me. To Ale, Mic, Viviana, and Irene: I can never wait to see you whenever I come back home. And to the "Amichetti" group, especially Angela, Davide, and Gabri, my brothers in spirit: thank you for the deep conversations about life and choices. I don't know where life will lead us, but I know we'll always share that bond and understand each other.

The biggest thank you to my Family, for teaching me everything that matters. The hardest thing about being part of such a loving, caring, understanding family is that leaving is so damn hard. Every time I come back I feel like I'm the happiest person, every time I leave that lump in my throat comes back again –and I suspect it always will. But that's okay. Despite the distance, we manage to stay present in each other's lives, to share and communicate, and to feel the love across the miles.

As a part of the Family that I choose for myself, the last thank you goes to Marco. I don't know what else is there to say that we haven't said to each other already in these (almost) 9 years. This all PhD experience in Belgium happened because of you, because we wanted to find a place where we could work and live together and we were lucky enough to find this beautiful one. These four years with you were just easy and natural and funny and emotionally warm and safe. I am not sure of where we will eventually settle in the world and doing what, but I am sure that as long as at the end of the day I come back to you, that day will be a good day and I'd be leaving the life that I want.

As this PhD journey comes to an end, the boat returns to the calm waters of the harbor just as the sunset paints the sky with its most beautiful colors. I find myself happy and grateful for all the things that I've learned, the experiences that I have lived, the people that I have met, and those who have always been there.



My favorite spot in Leuven. With that perfect Belgium-grey background.

Associated Publications

- CMS Collaboration. Identification of tau leptons using a convolutional neural network with domain adaptation in the CMS experiment. Technical report, CERN, Geneva, 2025. CMS-PAS-TAU-24-001. URL: <https://cds.cern.ch/record/2931189>
- P. Mastrapasqua. Hadronic tau lepton tagging with the CMS detector using domain adaptation to mitigate discrepancies between simulation and data. *PoS, ICHEP2024*:1039, 2025. doi:10.22323/1.476.1039
- A. Taliencio, P. Mastrapasqua and others. Higgs Self Couplings Measurements at Future proton-proton Colliders: a Snowmass White Paper. In *Snowmass 2021*, 3 2022. arXiv:2203.08042
- C. Caputo, P. Mastrapasqua and others. Higgs Self Couplings Measurements at Future proton-proton Colliders. *PoS, ICHEP2022*:1149, 2022. doi:10.22323/1.414.1149
- P. Mastrapasqua. Higgs Self-Coupling Measurements at Future Hadron Colliders: HL-LHC and FCC-hh. *Belgian Physical Society Magazine*, (1):20–27, 2024. Available online at BPS Magazine
- CMS Collaboration. Combination of searches for nonresonant Higgs boson pair production in proton-proton collisions at $\sqrt{s} = 13$ TeV. Technical report, CERN, Geneva, 2024. CMS-PAS-HIG-20-011. URL: <https://cds.cern.ch/record/2917252>
- E. Gallo, P. Mastrapasqua and others. Higgs self-coupling at the FCC-hh. In *Proceedings of the XXXI International Workshop on Deep Inelastic Scattering and Related Subjects (DIS2024)*, volume DIS2024, page 253, 2025. doi:10.22323/1.469.0253
- A. Taliencio, P. Mastrapasqua and others. Higgs self-coupling determination in the $b\bar{b}\gamma\gamma$ final state at the FCC-hh, 2025. Submitted to the 2025 Update of the European Strategy for Particle Physics. doi:10.17181/5mqfv-s _{β} xnd34
- M. Mangano, P. Mastrapasqua and others. Prospects for physics at FCC-hh, 2025. Submitted to the 2025 Update of the European Strategy for Particle Physics. doi:10.17181/bzhc2-s _{β} mem17

Contents

Introduction	1
1 The Standard Model of Particle Physics	3
1.1 The fundamental building blocks of Nature	3
1.2 Quantum Chromodynamics	4
1.3 Electroweak theory	9
1.4 Spontaneous Symmetry Breaking	11
1.5 Status of Higgs Boson Physics at LHC	16
1.5.1 Production mechanisms at LHC	17
1.5.2 Principal decay channels	18
1.5.3 Measurement of the Higgs boson mass	23
1.5.4 Higgs boson couplings	23
1.5.5 Higgs boson self-coupling	24
2 The Extended Higgs Sector	31
2.1 Limitations of the Standard Model	31
2.2 Two Higgs Doublet Models	35
2.2.1 Theory	35
2.2.2 Status of searches at LHC	40
2.3 Other BSM theories with an extended Higgs sector	46
2.4 How to find new Higgs bosons?	47
3 The LHC and the CMS experiment	51
3.1 The Large Hadron Collider	51
3.2 The Compact Muon Solenoid experiment	54
3.2.1 Coordinate system and kinematics of pp collisions . .	56
3.2.2 Magnet	58
3.2.3 Silicon Tracker	58
3.2.4 Calorimeter	61
3.2.5 Muon System	65
3.2.6 Gaseous Electron Multiplier (GEM)	71

3.2.7	The CMS Trigger System	74
3.3	Physics object reconstruction	76
3.3.1	Tracks and primary vertex	77
3.3.2	Particle Flow	79
3.3.3	Jets	81
3.3.4	Missing Transverse Energy	83
3.3.5	Tau leptons	84
3.4	CMS upgrade for the HL-LHC Era	90
3.4.1	Upgrade of the tracker system	90
3.4.2	The High-Granularity Calorimeter	92
3.4.3	The MIP Timing Detector	92
3.4.4	Upgrade of the Barrel Calorimeters and Muon Detectors	93
4	The FCC integrated program	95
4.1	FCC-ee: A Higgs factory, and much more	98
4.2	FCC-hh: The energy-frontier collider	100
4.2.1	Setting the energy and luminosity target	102
4.2.2	Detector considerations	107
4.2.3	Detector simulation	110
4.3	A physics case: Higgs boson characterization with the FCC program	115
5	Data Analysis Methods and Machine Learning Tools	119
5.1	From statistical models to likelihoods	119
5.2	The maximum likelihood estimation	120
5.3	Discovery as hypothesis test	124
5.3.1	Expected sensitivity and bands	128
5.3.2	Goodness of fit	128
5.4	Machine Learning Tools	132
5.4.1	Deep Neural Networks	133
5.4.2	Convolutional Neural Networks	138
5.4.3	Performance evaluation and reliability testing of ML models	140
6	The τ_h identification algorithm and its calibration	143
6.1	Misidentification of hadronically decaying tau leptons	143
6.2	The τ_h identification using a deep neural network with domain adaptation	145
6.2.1	Inputs	145

6.2.2	Classification architecture and loss function	148
6.2.3	Domain adaptation by backpropagation	150
6.2.4	Expected performance	156
6.3	Performance with $\sqrt{s} = 13$ and 13.6 TeV data	157
6.3.1	The τ_h energy scale correction and identification scale factors	161
6.3.2	The electron misidentification rate scale factors	165
6.4	Summary and outlook	173
7	Search for BSM scalar bosons via $H/A \rightarrow ZA/H \rightarrow \ell^+\ell^-\tau^+\tau^-$	181
7.1	Introduction	181
7.2	Samples	184
7.2.1	Data	184
7.2.2	Simulations	185
7.3	Object reconstruction	190
7.3.1	Muons	190
7.3.2	Electrons	191
7.3.3	Hadronic Taus	191
7.3.4	Jets	191
7.3.5	Missing transverse momentum	191
7.4	Corrections	192
7.4.1	τ_h energy scale	192
7.4.2	τ_h ID efficiency	193
7.4.3	$e \rightarrow \tau_h$ energy scale	193
7.4.4	$e \rightarrow \tau_h$ misidentification rate	193
7.4.5	$\mu \rightarrow \tau_h$ misidentification rate	194
7.4.6	Electron corrections	194
7.4.7	Muon corrections	194
7.4.8	Missing transverse momentum corrections	195
7.4.9	b-tagging efficiency	196
7.4.10	Pileup reweighting	197
7.4.11	$Z p_T$ reweighting	197
7.4.12	Pre-firing weight	197
7.5	Triggers	198
7.6	Analysis Strategy	198
7.7	Selection	200
7.7.1	$Z \rightarrow ee$ leg	202
7.7.2	$Z \rightarrow \mu\mu$ leg	202

7.7.3	$A \rightarrow \tau_e \tau_h$ leg	202
7.7.4	$A \rightarrow \tau_\mu \tau_h$ leg	203
7.7.5	$A \rightarrow \tau_h \tau_h$ leg	203
7.7.6	b-jet veto	203
7.7.7	Signal selection efficiency	203
7.8	Background estimation	205
7.8.1	Irreducible background estimation	205
7.8.2	Reducible background estimation	205
7.8.3	Control plots for the baseline selection	212
7.9	Parametric Deep Neural Network for enhanced sensitivity	220
7.10	Observables	221
7.11	Systematic uncertainties	234
7.11.1	Impacts	235
7.12	Results	236
7.13	Summary and Outlook	240
8	HH searches at Future Hadron Colliders	241
8.1	Projections of non-resonant HH searches to HL-LHC	241
8.1.1	Projections to HL-LHC with fast simulation	242
8.1.2	Projections of Run 2 results to HL-LHC with simple scaling	256
8.2	Projections of HH searches to FCC-hh with fast simulation	262
8.2.1	Non-resonant analysis	263
8.2.2	Resonant analysis	272
8.3	Summary and outlook	276
	Conclusion	279
	Bibliography	280
	Appendix	316
A	Study of (m_A, m_H) mass resolution	317
B	Signal sample full list	320
C	Z p_T correction weights	323
D	Distributions for $Z + 1L$ CR in 2016 and 2017	325
E	Closure Test	328
F	Choice of observables	330
G	Flavor-related uncertainty for the misidentification rate curves	333
H	Goodness of fit test	335

Introduction

In this thesis, I present the contribution—however small—that I have made to High Energy Physics at accelerators over the course of these four years of doctoral studies. My primary focus has been on Higgs Physics, exploring both what we can measure with precision within the framework of the Standard Model, and what we can search for in the vast landscape of possibilities Beyond the Standard Model.

As much as I would like to begin *in medias res* and dive straight into the action of my research, a proper introduction to the theoretical background, experimental context, and analysis tools is essential. For this reason, the first five chapters of this manuscript are devoted to a selection of topics that form the foundation and state-of-the-art context upon which this work is built.

They are organized as follows:

- **Chapter 1** offers a concise overview of the Standard Model, with an emphasis on Higgs boson physics. It concludes with a summary of the most recent and remarkable Higgs-related results from the Large Hadron Collider experiments.
- **Chapter 2** leaves the calm and familiar shores of the Standard Model to venture into the uncharted waters Beyond. It focuses on a specific extension of the Higgs sector known as the *Two Higgs Doublet Model*, and includes a review of the latest experimental findings in this area.
- **Chapter 3** outlines the key features of the Large Hadron Collider and the CMS experiment, with particular attention to detector technologies, the reconstruction of physics objects, and both planned and ongoing upgrades for the future.
- **Chapter 4** is a lucid dream about the future of High Energy Physics, delving into the Future Circular Collider program. It highlights the physics motivations and the unprecedented opportunities such a machine would offer for a deeper exploration of the Higgs sector.

- **Chapter 5** describes the methods exploited in this research, detailing the statistical and machine learning tools employed to obtain the results presented in the following chapters.

My research results are presented in the following three chapters:

- **Chapter 6** summarizes my work within the Tau Group in CMS, focused on the validation and calibration of a new and improved identification algorithm for hadronically decaying tau leptons. This tool is of key importance for analyses such as the one described in the next chapter.
- **Chapter 7** provides a detailed account of the search for additional Higgs bosons via the process $H/A \rightarrow ZA/H \rightarrow \ell^+ \ell^- \tau^+ \tau^-$ using data from the CMS experiment.
- **Chapter 8** presents projections I performed for di-Higgs searches at future colliders, in particular for the High-Luminosity phase of the Large Hadron Collider and the hadron Future Circular Collider.

The work spans a wide range: from the study of technical tools used by the entire collaboration, to physics analyses based on data from the ongoing experiment, to projections aimed at establishing the physics reach of future experiments, both near and far. I hope the reader will appreciate the variety of these interesting topics as much as I enjoyed working on them.

The Standard Model of Particle Physics

Over the last century, a combination of extraordinary experimental and theoretical efforts have lead to a deep understanding of the fundamental structure of the Universe. The result of this endeavor is the formulation of the so-called Standard Model of Particle Physics (SM), a theoretical framework that describes the fundamental constituents of Matter and the interactions among them. The success of the SM can be appreciated for both its remarkable ability to describe every observation to-date and for the historical role it had in predicting the existence of particles and interactions that were subsequently confirmed by experiments. One of the most crucial features of the SM is the existence of a scalar boson, the Higgs boson, which is necessary to give masses to the fundamental particles in a theoretically consistent way. The discovery of a Higgs-like boson at the Large Hadron Collider (LHC) in 2012 [10, 11] provided us with the last piece of the puzzle and paved the way for future discovery and precision programs at CERN and other facilities. In the following, I will briefly summarize the SM, focusing in particular on the Electroweak (EW) sector.

1.1 The fundamental building blocks of Nature

The SM is a Quantum Field Theory [12–14] describing three of the four fundamental interactions (electromagnetic, weak and strong force) and all the known elementary matter constituents.

In Fig. 1.1 the full list of the SM elementary particles is given. The summary table shows that the fundamental particles are classified in two categories according to their intrinsic angular momentum, the *spin*:

- **Bosons** are particles with integer spin values, that follow Bose-Einstein statistics. The carriers of the aforementioned fundamental forces belong to this category.
- **Fermions** are particles with semi-integer spin values, that obey Fermi-Dirac statistics. The particles that constitute the observable matter belong to this category.

The SM is based on the observation of the fundamental symmetries of nature:

- $SU(3)_C$ symmetry characterizes the Quantum Chromodynamics (QCD), the theory that describes strong interactions between the matter particles called *quarks* through the exchange of force-carriers called *gluons*.
- $SU(2)_L \times U(1)_Y$ symmetry characterizes the unified theory of electromagnetic and weak interaction. The electromagnetic interaction¹ is mediated by *photons* and affects all particles endowed with electric charge, i.e. quarks as well as the other type of matter particle existing in nature, the so-called *leptons* (neutrinos excluded because of the zero charge). The weak interaction, instead, affects all particles in nature and is mediated by the W^\pm and Z bosons.

The framework is completed by the *Electroweak Symmetry Breaking* (EWSB) mechanism that accounts for the particle masses, predicting the existence of the Higgs boson, a so far unique fundamental scalar particle.

1.2 Quantum Chromodynamics

Quantum Chromodynamics [16] is the gauge field theory that describes the strong interaction between quarks and gluons. The equivalent of the electric charge for strong interactions is the *color*. Quarks occur in three different colors (green, red or blue) and combine to form hadrons. There are two types of hadrons²: mesons, made of one quark and one anti-quark, and baryons, made of three quarks or anti-quarks.

Both mesons and baryons are colorless, or, equivalently, they are color singlet states. In mathematical language, this means that they are invariant under

¹The electromagnetic interaction alone is characterized by the $U(1)_{em}$ symmetry which is at the basis of the Quantum Electrodynamics (QED).

²Exotic hadron states have also been observed [17, 18].

Standard Model of Elementary Particles					
three generations of matter (fermions)			interactions / force carriers (bosons)		
	I	II	III		
mass	$\approx 2.2 \text{ MeV}/c^2$	$\approx 1.28 \text{ GeV}/c^2$	$\approx 173.1 \text{ GeV}/c^2$	0	$\approx 124.97 \text{ GeV}/c^2$
charge	$\frac{2}{3}$	$\frac{2}{3}$	$\frac{2}{3}$	0	0
spin	$\frac{1}{2}$	$\frac{1}{2}$	$\frac{1}{2}$	1	0
QUARKS	u up	c charm	t top	g gluon	H higgs
	$\approx 4.7 \text{ MeV}/c^2$	$\approx 96 \text{ MeV}/c^2$	$\approx 4.18 \text{ GeV}/c^2$	0	
	$-\frac{1}{3}$	$-\frac{1}{3}$	$-\frac{1}{3}$	0	
	$\frac{1}{2}$	$\frac{1}{2}$	$\frac{1}{2}$	1	
	d down	s strange	b bottom	γ photon	
LEPTONS	$\approx 0.511 \text{ MeV}/c^2$	$\approx 105.66 \text{ MeV}/c^2$	$\approx 1.7768 \text{ GeV}/c^2$	$\approx 91.19 \text{ GeV}/c^2$	
	-1	-1	-1	0	
	$\frac{1}{2}$	$\frac{1}{2}$	$\frac{1}{2}$	1	
	e electron	μ muon	τ tau	Z Z boson	
	$< 1.0 \text{ eV}/c^2$	$< 0.17 \text{ MeV}/c^2$	$< 18.2 \text{ MeV}/c^2$	$\approx 80.39 \text{ GeV}/c^2$	
	0	0	0	± 1	
	$\frac{1}{2}$	$\frac{1}{2}$	$\frac{1}{2}$	1	
	ν_e electron neutrino	ν_μ muon neutrino	ν_τ tau neutrino	W W boson	

Figure 1.1: A summary table [15] with all the SM particles: the fermions (on the left) are divided into quarks (in violet) and leptons (in green), while the bosons (on the right), are classified into gauge bosons, i.e. the carriers of the interactions (in red) and the scalar Higgs boson (in yellow). For each particle, the mass, electric charge and spin values are reported.

$SU(3)$ rotations in color space. As a consequence, the symmetry group of QCD is $SU(3)$, called color group.

In order to obtain the Lagrangian density for QCD, the Lagrangian density for free quarks is introduced:

$$L_{free} = \sum_{j=1}^f \bar{q}^j (i\gamma^\lambda \partial_\lambda - m_j) q^j, \quad (1.1)$$

where j is the flavor index, and $q^j = \begin{pmatrix} q_1^j \\ q_2^j \\ q_3^j \end{pmatrix}$ is the field describing a quark of flavor j and accounts for the three colors.

Given U , a transformation of $SU(3)$, it can be written as a function of the group generators T_k with $k = 1, \dots, 8$:

$$U = 1 + i \sum_{k=1}^8 \delta\varphi^k T_k, \quad (1.2)$$

where $\delta\varphi^k$ are infinitesimal parameters and T_k is defined as:

$$T_k = \frac{\lambda^k}{2} \quad (1.3)$$

In the previous equation, λ^k are the Gell-Mann matrices. In general, the number of generators of a symmetry group $SU(N)$ is $N^2 - 1$ and the group algebra is given by:

$$[T_a, T_b] = i f^{abc} T^c, \quad (1.4)$$

where f^{abc} are totally antisymmetric tensors, called *structure constants*. The Lagrangian density introduced for free quarks 1.1 results to be invariant under a global transformation (constant matrix) U of $SU(3)$:

$$q^j(x) \rightarrow U \cdot q^j(x) \quad (1.5)$$

By contrast, it is not invariant under a local transformation $U(x)$ of $SU(3)$:

$$q^j(x) \rightarrow U(x) \cdot q^j(x) \quad (1.6)$$

$$\begin{aligned} L_{free} &= \sum_{j=1}^f \bar{q}^j (i\gamma^\lambda \partial_\lambda - m_j) q^j \\ &\rightarrow \sum_{j=1}^f \bar{q}^j (i\gamma^\lambda \partial_\lambda - m_j + i\gamma^\lambda U^\dagger(x) \partial_\lambda U(x)) q^j \end{aligned} \quad (1.7)$$

Local invariance in color space, requires the introduction of 8 ($N^2 - 1$) vector fields $G_\lambda(x)$, called gluons:

$$\begin{aligned} G_\lambda(x) &= G_\lambda^a(x) \frac{\lambda_a}{2} = G_\lambda^\dagger(x), \quad a = 1, \dots, 8, \\ \text{Tr} G_\lambda(x) &= 0 \end{aligned} \quad (1.8)$$

The Lagrangian has to be modified to take into account the interaction between quarks and gluons. At this scope, on the basis of the "minimal coupling" in

electrodynamics, all ordinary derivatives ∂_μ are replaced by:

$$\partial_\mu \rightarrow D_\mu = \partial_\mu + ig_s G_\lambda(x) \quad (1.9)$$

where D_μ is called covariant derivative and g_s is a dimensionless coupling constant. Consequently, the Lagrangian density becomes:

$$L_q(x) = \sum_{j=1}^f \bar{q}^j(x) (i\gamma^\lambda D_\lambda - m_j) q^j(x) \quad (1.10)$$

This Lagrangian is invariant under local transformations. However, it is not complete, since it does not contain the gluon dynamics term. In order to construct this term, again on the basis of electrodynamics, a gluon field-strength tensor $G_{\lambda\rho}(x)$ is introduced:

$$G_{\lambda\rho}(x) = \partial_\lambda G_\rho(x) - \partial_\rho G_\lambda(x) + ig_s [G_\lambda(x), G_\rho(x)] \quad (1.11)$$

Its components $G_{\lambda\rho}^a$ are defined by:

$$G_{\lambda\rho}(x) = G_{\lambda\rho}^a \frac{\lambda_a}{2} \quad (1.12)$$

The quadratic term in Eq. 1.11 is typical of non-Abelian groups such as $SU(3)$.

At this point, the Lagrangian density for QCD can be written:

$$L_{QCD}(x) = -\frac{1}{4} G_{\lambda\rho}^a(x) G^{\lambda\rho a}(x) + \sum_{j=1}^f \bar{q}^j(x) (i\gamma^\lambda D_\lambda - m_j) q^j(x) \quad (1.13)$$

In conclusion, thanks to the application of the gauge principle, the QCD theory can be written as a function of a single parameter g_s or, more frequently, in terms of the *strong coupling constant* $\alpha_s = \frac{g_s^2}{4\pi}$, and predicts the existence of 8 gluons. Like photons, QCD gluons are vector fields with spin 1, but, differently from their QED counterpart, they carry color charges themselves, mediating color flips of quarks by absorption or emission. The main fundamental consequence of this property is that gluons can interact with each other, while photons cannot, at least not *directly* (meaning there is no photon-photon vertex in SM). Such a dissimilarity leads QCD to be profoundly different from QED.

Because of the gluon self coupling, QCD vacuum consists not only of virtual quark pairs ($q\bar{q}$) but it is also filled with virtual gluon pairs, as illustrated in Fig. 1.2. The polarizing effect due to quark pairs is similar to the QED

one³, while gluons have an opposite effect of antiscreening. Overall the effective color charge becomes larger with larger distance. Charge screening in QCD leads to the concept of *running coupling constants*. At short distance (large momentum transfer) the strong coupling decreases such that quarks can be considered approximately as free particles. This property is called *asymptotic freedom* and allows the usage of perturbation theory in calculations, in order to produce quantitative predictions for hard scattering cross sections in hadronic interactions. Conversely, at increasing distance the coupling becomes so strong that it is impossible to isolate a quark from a hadron. This mechanism is called *confinement* and explains why in Nature only colorless bound states of quarks are observed.

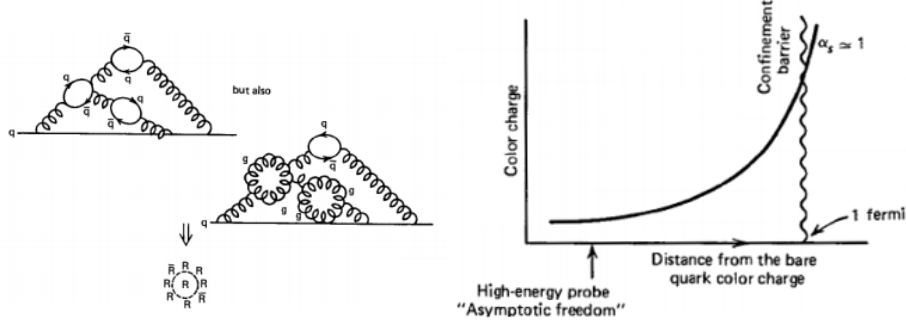


Figure 1.2: Illustration [19] of the antiscreen effect in QCD (left) and of an approximate behavior of the effective color charge versus the distance from the bare color charge (right). The distance r can be equivalently expressed in terms of the transferred four-momentum Q^2 between the charge and the probe, since $r \simeq 1/Q^2$.

The energy evolution of the strong coupling constant α_S can be approximately parametrized as:

$$\alpha_S(Q^2) \approx \frac{1}{\beta_0 \ln\left(\frac{Q^2}{\Lambda^2}\right)} \quad (1.14)$$

where β_0 is a constant first computed by Wilczek, Gross [20] and Politzer [21], and the quantity Λ is called *QCD scale* and is indicative of the energy range where non-perturbative dynamics dominates. Figure 1.3 [22] reports experimental results for α_S as a function of the momentum transfer, obtained with

³In QED the *vacuum polarization* leads to a screening effect of the charge, which appears smaller with increasing distance of the probe, i.e. with decreasing transferred four-momentum between the charge and the probe.

different techniques. The world average value of α_S at the energy scale of the Z boson is also quoted.

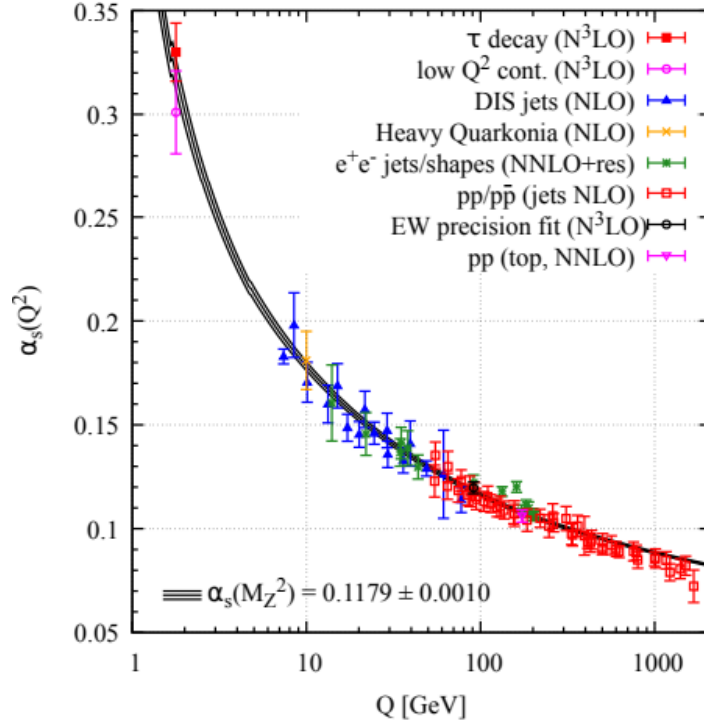


Figure 1.3: Summary of measurements of α_S as a function of the energy scale Q [19]. The respective degree of QCD perturbation theory used in the extraction of α_S is indicated in brackets (NLO: next-to-leading order; NNLO: next-to-next-to-leading order; NNLO+res.: NNLO matched to a resummed calculation; N3LO: next-to-NNLO).

1.3 Electroweak theory

The Electroweak theory [16] describes electromagnetic and weak interactions in a single unified model. The gauge group of the electroweak interaction is $SU(2)_L \times U(1)_Y$, where $SU(2)_L$ is the *weak isospin group* and $U(1)_Y$ is the *weak hypercharge group*.

The three generators of $SU(2)_L$ are:

$$T^a = \frac{\tau^a}{2}, \quad (1.15)$$

where τ^a , $a=1, \dots, 3$, are the Pauli matrices.

It is assumed, following experimental observations, that the left-handed components of a leptonic family form a doublet of $SU(2)_L$, while the right-handed component of the charged lepton behaves like a singlet of $SU(2)_L$, meaning that it is invariant under a $SU(2)_L$ transformation. For example, for the electronic family, we have: $\begin{pmatrix} \nu_e \\ e \end{pmatrix}_L$ and e_R .

They can be arranged into a unique spinor: $\psi = \begin{pmatrix} \nu_{eL} \\ e_L \\ e_R \end{pmatrix}$.

Under a local transformation of $U(1)_Y$ the spinor transforms as follows:

$$\psi \rightarrow e^{i\chi(x)Y} \psi \quad (1.16)$$

where Y is the matrix:

$$Y = \begin{pmatrix} y_L & 0 & 0 \\ 0 & y_L & 0 \\ 0 & 0 & y_R \end{pmatrix} \quad (1.17)$$

The parameter y_L is conventionally set to $-\frac{1}{2}$ and the value of y_R is set to -1 in order to have the correct form of the electromagnetic coupling.

As in the QCD case, the Lagrangian density is constructed in order to be invariant under local transformations of $SU(2)_L \times U(1)_Y$:

$$L = -\frac{1}{2}Tr(W_{\lambda\rho}(x)W^{\lambda\rho}(x)) - \frac{1}{4}B_{\lambda\rho}(x)B^{\lambda\rho}(x) + \bar{\psi}i\gamma^\lambda D_\lambda\psi(x) \quad (1.18)$$

D_λ is the covariant derivative, defined as:

$$D_\lambda\psi(x) = (\partial_\lambda + igW_\lambda^a(x)T_a + ig'B_\lambda(x)Y)\psi(x), \quad (1.19)$$

where g and g' are the gauge coupling constants, respectively for $SU(2)_L$ and $U(1)_Y$. $W_\lambda^a(x)$, with $a=1, \dots, 3$, are the vector fields corresponding to $SU(2)_L$ and B_λ is the vector field corresponding to $U(1)_Y$. The matrices T_a ($a=1, \dots, 3$) have the form

$$T_a = \begin{pmatrix} \frac{1}{2}\tau_a & 0 \\ 0 & 0 \end{pmatrix} \quad (1.20)$$

and they form, together with the hypercharge matrix Y , a representation of the generators of the group $SU(2)_L \times U(1)_Y$.

Finally, the strength tensors $W_{\lambda\rho}$ and $B_{\lambda\rho}$ are defined as follows:

$$W_{\lambda\rho}(x) = \partial_\lambda W_\rho(x) - \partial_\rho W_\lambda(x) + ig[W_\lambda(x), W_\rho(x)] \quad (1.21)$$

$$B_{\lambda\rho}(x) = \partial_\lambda B_\rho - \partial_\rho B_\lambda \quad (1.22)$$

The fields that describe the vector bosons W_λ^\pm and Z_λ , carriers of the weak interaction, and the photon A_λ , carrier of the electromagnetic interaction, can be derived from the vector fields W_λ^1 , W_λ^2 , W_λ^3 and B_λ , obtained from the application of the gauge principle to the electroweak interaction.

The charged boson fields are defined as:

$$W_\lambda^\pm = \frac{1}{\sqrt{2}}(W_\lambda^1 \mp iW_\lambda^2) \quad (1.23)$$

while, the neutral boson fields are given by:

$$\begin{aligned} Z_\lambda &= \cos\theta_W W_\lambda^3 - \sin\theta_W B_\lambda \\ A_\lambda &= \sin\theta_W W_\lambda^3 + \cos\theta_W B_\lambda \end{aligned} \quad (1.24)$$

where θ_W is the *weak mixing angle*, or *Weinberg angle* [23], function of the coupling constants g and g' :

$$\begin{aligned} \sin\theta_W &= \frac{g'}{\sqrt{g^2 + g'^2}} \\ \cos\theta_W &= \frac{g}{\sqrt{g^2 + g'^2}} \end{aligned} \quad (1.25)$$

1.4 Spontaneous Symmetry Breaking

The Lagrangian density presented in Eq. 1.18 lacks a term that accounts for the masses of the vector bosons—such a term would take the form, for example, of $m_W^2 W_\lambda^+ W^{\lambda-}$. However, the explicit inclusion of such a mass term is prohibited, as it would violate gauge invariance.

Nevertheless, experimental evidence confirms that the vector bosons W^\pm and Z , mediators of the weak interaction, possess non-zero masses.

Within the SM framework, the generation of mass for both the gauge bosons and the fermions is explained by the Brout-Englert-Higgs mechanism. This mechanism, independently proposed by Higgs [24, 25], and by Englert and Brout [26], incorporates the concept of *Spontaneous Symmetry Breaking* (SSB) in a gauge-invariant field theory.

In general, a SSB occurs when the Lagrangian of a system is symmetric under a certain transformation, while the ground state of the system is not. In order to make a simple example, let us consider a point particle moving along an axis ρ in a one-dimensional potential $V(\rho)$ given by:

$$V(\rho) = -\frac{1}{2}\mu^2\rho^2 + \frac{1}{4}\lambda\rho^4 \quad (1.26)$$

where $\mu^2 > 0$ and $\lambda > 0$ are fixed constants. This potential, represented in right Fig. 1.4, is symmetric under the transformation: $\rho \rightarrow -\rho$. The equilibrium positions of the system, obtained by requiring $\frac{\partial V}{\partial \rho} = 0$, correspond to $\rho_0 = \pm\sqrt{\frac{\mu^2}{\lambda}}$ and are not symmetric under the exchange of ρ and $-\rho$. As a consequence, the symmetry is spontaneously broken.

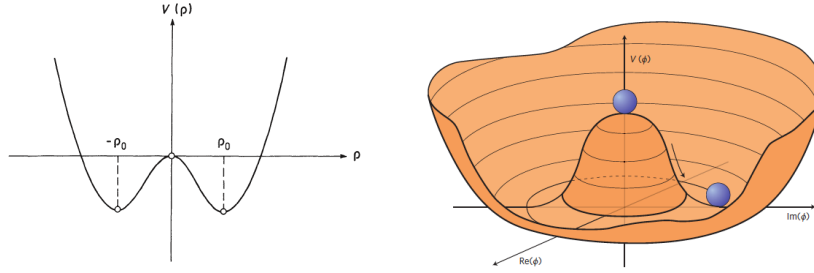


Figure 1.4: (Left) An example of one-dimensional potential $V(\rho)$ that shows spontaneous symmetry breaking. (Right) Representation of the Higgs potential as function of the real and imaginary parts of the field ϕ [27].

The theorized mechanism for EWSB requires additional scalar fields, called *Higgs fields*. Let us introduce two complex scalar fields ϕ_1 and ϕ_2 , which form a doublet of $SU(2)_L$:

$$\phi(x) = \begin{pmatrix} \phi_1(x) \\ \phi_2(x) \end{pmatrix} = \begin{pmatrix} \Re\phi_1(x) + i\Im\phi_1(x) \\ \Re\phi_2(x) + i\Im\phi_2(x) \end{pmatrix} \quad (1.27)$$

Under a transformation of $SU(2)_L$, $\phi(x)$ transforms as follows:

$$\phi(x) \rightarrow U(x)\phi(x), \quad (1.28)$$

while, under a transformation of $U(1)_Y$, it becomes:

$$\phi(x) \rightarrow e^{iy_H\chi(x)}\phi(x), \quad (1.29)$$

where y_H is the weak hypercharge of the doublet and is equal to $\frac{1}{2}$. Again, the Lagrangian is constructed in order to be invariant under gauge transformations:

$$L_H = (D_\lambda \phi)^\dagger (D^\lambda \phi) - V(\phi^\dagger \phi), \quad (1.30)$$

where D_λ is the covariant derivative, defined as:

$$D_\lambda = \partial_\lambda + igW_\lambda + ig'B_\lambda y_H \quad (1.31)$$

and $V(\phi^\dagger \phi)$ must be chosen in order to lead to a spontaneous symmetry breaking.

At this purpose, let us consider

$$V(\phi^\dagger \phi) = \frac{k}{2}\rho^2 + \frac{\lambda}{4}\rho^4 \quad (1.32)$$

with $k < 0$ and $\lambda > 0$. This potential, represented in left Fig. 1.4, has two stable equilibrium positions, corresponding to $\rho_0 = \pm\sqrt{\frac{-k}{\lambda}}$, and an unstable position: $\rho = 0$. The ground state is given by:

$$\phi = e^{i\alpha^a T^a} \begin{pmatrix} 0 \\ \frac{\rho_0}{\sqrt{2}} \end{pmatrix}, \quad a = 1, \dots, 3 \quad (1.33)$$

where T^a are the generators of $SU(2)_L$. Since the coefficients α_a vary with continuity, there is an infinite number of ground states. The gauge symmetry is broken when one of the infinite configurations of the ground state is chosen,

for example: $\phi_0 = \begin{pmatrix} 0 \\ \frac{\rho_0}{\sqrt{2}} \end{pmatrix}$.

If ϕ_0 is substituted to ϕ in the first term of Lagrangian equation 1.30, we obtain the term:

$$(D_\lambda \phi_0)(D^\lambda \phi_0) = \frac{g^2 \rho_0^2}{4} W_\lambda^- W^{\lambda+} + \frac{(g^2 + g'^2)}{4} \rho_0^2 \frac{Z_\lambda Z^\lambda}{2} \quad (1.34)$$

from which the vector boson masses can be derived:

$$m_W^2 = \frac{g^2 \rho_0^2}{4} = \frac{e^2 \rho_0^2}{4 \sin^2 \theta_W}, \quad m_Z^2 = \frac{(g^2 + g'^2) \rho_0^2}{4} = \frac{e^2 \rho_0^2}{4 \sin^2 \theta_W \cos^2 \theta_W} \quad (1.35)$$

The masses m_W and m_Z have been measured at LEP 2 [28], Tevatron [29] and by the ATLAS experiment at LHC [30] and the world average values are here reported [22]:

$$m_W = 80.3692 \pm 0.0133 \text{ GeV}, \quad m_Z = 91.1880 \pm 0.0020 \text{ GeV}, \quad (1.36)$$

The combination of the m_W measurements reported above does not include the Collider Detector at Fermilab (CDF) Collaboration result: $m_W = 80.433 \pm 0.0094$ GeV [31], which differs by 7σ from the SM prediction. Very recently, the CMS Collaboration published the result of the m_W measurement with data collected in 2016 [32]:

$$m_W = 80.3602 \pm 0.0099 \text{ GeV} \quad (1.37)$$

This result is particularly significant due to its extremely high precision, compared to other measurements used in the world average but excluding CDF, and its consistency with the SM prediction.

Let us consider a state $\phi'(x)$ that corresponds to a fluctuation around the the ground state:

$$\phi'(x) = \begin{pmatrix} 0 \\ \frac{\rho_0}{\sqrt{2}}(1 + \frac{\rho'(x)}{\rho_0}) \end{pmatrix} \quad (1.38)$$

By evaluating the Lagrangian density in this state, we obtain the term describing the interaction between the Higgs boson (H), carrier of the Higgs field $\rho'(x)$, and the weak vector bosons:

$$\begin{aligned} (D_\lambda \phi'(x))(D^\lambda \phi'(x)) = & m_W^2 \left(1 + 2\frac{\rho'(x)}{\rho_0} + \frac{\rho'(x)^2}{\rho_0^2}\right) W_\lambda^+ W^{\lambda-} \\ & + \frac{1}{2} m_Z^2 \left(1 + 2\frac{\rho'(x)}{\rho_0} + \frac{\rho'(x)^2}{\rho_0^2}\right) Z_\lambda Z^\lambda \end{aligned} \quad (1.39)$$

From equation 1.39, the Higgs boson couplings to W^+W^- and ZZ bosons result to be:

$$g_{HZZ} = \frac{2}{\rho_0} m_Z^2, \quad g_{HWW} = \frac{2}{\rho_0} m_W^2 \quad (1.40)$$

It can be seen that the Higgs boson couplings to the gauge bosons are proportional to the square of the boson masses. Moreover, by substituting $\phi'(x)$ in the expression for $V(\phi(x)^\dagger \phi(x))$, it results:

$$V(\phi'(x)^\dagger \phi'(x)) = \lambda \rho_0^2 \rho'^2 + \lambda \rho_0 \rho'^3 + \frac{1}{4} \lambda \rho'^4 \quad (1.41)$$

From the first term of this sum, the expression for the mass of the Higgs boson can be obtained:

$$m_H^2 = 2\lambda \rho_0^2 \quad (1.42)$$

λ corresponds to the Higgs self coupling constant and is a free parameter of the theory. Therefore, there is no a priori prediction for the Higgs mass. The second and the third terms of the sum provide the expressions respectively for the trilinear (λ_3) and quadrilinear (λ_4) self couplings. Within the SM, we have:

$$\lambda_3 = \lambda_4 = \frac{m_H^2}{2\rho_0^2} \quad (1.43)$$

The value of ρ_0 (called *vacuum expectation value*), is fixed by the Fermi coupling constant G_F :

$$\rho_0 = (\sqrt{2}G_F)^{-\frac{1}{2}} = 246 \text{ GeV} \quad (1.44)$$

So far, it has been shown as, through the EWSB mechanism, the weak bosons acquire mass, while the photon remains massless. Following a similar development, also the fermion mass terms can be introduced. For this aim, let us introduce the Yukawa Lagrangian that describes the interaction between the Higgs boson and fermions. In the case of the electron, it has the form:

$$L_{Yukawa} = -c_e \bar{e}_R \phi^\dagger \begin{pmatrix} \nu_{eL} \\ e_L \end{pmatrix} + h.c. \quad (1.45)$$

where c_e is a coupling constant (Yukawa coupling). The mass of the electron results to be:

$$m_e = -c_e \frac{\rho_0}{\sqrt{2}}, \quad (1.46)$$

while the neutrino is massless. For the other leptonic families, the Yukawa Lagrangian has an analogous expression. For what concerns the quarks, the weak isospin eigenstates (referred to with the corresponding primed letter) are different from the mass eigenstates, and the relations between them are defined by the *Cabibbo-Kobayashi-Maskawa matrix*, V_{CKM} :

$$\begin{pmatrix} d' \\ s' \\ b' \end{pmatrix} = V_{CKM} \begin{pmatrix} d \\ s \\ b \end{pmatrix} \quad (1.47)$$

In the case of the first quark generation, the Yukawa Lagrangian is defined as:

$$L_{Yukawa} = -c'_q \bar{u}_R \phi^T \epsilon \begin{pmatrix} u \\ d' \end{pmatrix}_L - c_q \bar{d}'_R \phi^\dagger \begin{pmatrix} u \\ d' \end{pmatrix}_L + h.c. \quad (1.48)$$

where $\epsilon = i\tau^2$. In a similar way, it can be derived for the other quark generations. From Eq. 1.45 and 1.48, it can be observed that the Higgs boson couplings to fundamental fermions are predicted to be linearly proportional to the fermion masses. Nonetheless, the EWSB mechanism does not explain the observed fermion mass hierarchy; in fact, the fermion masses, translated into Yukawa couplings (Eq. 1.46), constitute a substantial portion of the SM free parameters [22].

The field $\phi'(x)$ is constructed in order to be invariant under $SU(3)$ transformations. In fact, the Higgs boson does not interact with gluons, according to their massless nature.

The final expression of the SM Lagrangian reads as:

$$L_{SM} = -\frac{1}{4}G_{\lambda\rho}G^{\lambda\rho} - \frac{1}{4}W_{\lambda\rho}W^{\lambda\rho} - \frac{1}{4}B_{\lambda\rho}B^{\lambda\rho} + \bar{\psi}i\gamma_\lambda D^\lambda\psi + (D_\lambda\phi)^\dagger(D^\lambda\phi) - V(\phi) + L_{Yukawa} + h.c. \quad (1.49)$$

where the covariant derivative D_λ has the form:

$$D_\lambda = \partial_\lambda + ig_s G_\lambda + ig W_\lambda + ig' B_\lambda Y \quad (1.50)$$

1.5 Status of Higgs Boson Physics at LHC

In 2012, the ATLAS [10] and CMS [11] experiments at LHC discovered a new resonance with a mass of approximately 125 GeV. The subsequent studies of its properties proved the compatibility of the measured resonance with the SM Higgs boson [22], e.g. confirming its nature of CP-even scalar⁴ [35, 36].

In the following, the highlights of the Higgs boson physics at LHC are outlined. Many steps have been taken toward understanding the nature of this unique particle, yet several questions remain unanswered. In all observed production and decay modes measured so far, the rates and differential measurements are found to be consistent, within experimental and theoretical uncertainties, with the SM predictions. Nevertheless, several channels are still experimentally out of reach and the couplings of the Higgs boson to light fermions are yet to be proven, as well as the Higgs self-interaction. Moreover, within the current precision, a more complex sector with additional states is not ruled out, nor it has been established whether the Higgs boson is an el-

⁴While the hypothesis of a pure CP-odd scalar is rejected, the possibility of a mixed state of CP-even and -odd contributions is actually still possible. Analyses like in Refs. [33, 34] are searching for small CP-odd contribution that would represent an evidence of New Physics.

elementary particle or whether it has an internal structure like any other scalar particles observed before it.

Many unresolved problems within the SM are related to Higgs Boson physics. One of these is the naturalness or hierarchy problem: the Higgs boson mass is affected by the presence of heavy particles and receives quantum corrections which destabilize the weak scale barring a large fine tuning of unrelated parameters. Historically, this has been the prime argument for expecting new physics right at the TeV scale. New theoretical paradigms have been imagined, such as a new fermion-boson symmetry called supersymmetry (SUSY) [37] or the existence of strong interactions at a scale of the order of a TeV from which the Higgs boson would emerge as a composite state [38]. Beyond the naturalness problem, extensions of the SM Higgs sector with additional scalars have been proposed, for example, to provide explanations for the fermion mass hierarchies [39], to account for the Dark Matter abundance [40] or to modify the properties of the electroweak phase transition [41]. For these reasons and many others, the Higgs boson is considered a powerful tool to explore the manifestations of the SM and to probe the physics landscape beyond it.

1.5.1 Production mechanisms at LHC

The main production mechanisms for the Higgs Boson at the LHC are sketched in Fig. 1.5. In the picture, the Higgs interactions are labeled with the relevant *coupling modifier*, κ , defined as the ratio between the coupling and its SM expectation (see Sec. 1.5.4).

The main processes are summarized in the following:

- *Gluon fusion* (ggH), $gg \rightarrow H + X$ (see diagram (a) in Fig. 1.5). Since no direct gluon-Higgs coupling exists within the SM, the process is mediated by the exchange of a virtual, heavy top quark. Contributions from lighter quarks propagating in the loop are suppressed proportionally to m_q^2 . At high-energy hadron colliders, this mechanism has the largest cross section. At the Run 2 LHC center of mass energy (13 TeV), the cross section for this phenomenon is (at the next-to next-to next to leading order) $\sigma_{ggH}^{N^3LO} \approx 48.6 \text{ pb}$.
- *Vector-boson fusion* (VBF), $qq \rightarrow qqH$ (see diagram (b) in Fig. 1.5). It's the second largest cross section at LHC. It proceeds by the scattering of two quarks, mediated by the exchange of a W or Z boson, with the Higgs boson radiated off the weak-boson propagator. The scattered quarks give

rise to two energetic jets in the forward and backward regions of the detector. The cross section of this process, in pp collisions at 13 TeV, is $\sigma_{VBF} \approx 3.78 \text{ pb}$.

- *Higgs-strahlung (VH)*, $q\bar{q} \rightarrow VH$ (see diagram (c) in Fig. 1.5). It is a process of associated production with W or Z gauge bosons. In addition, for ZH production there is also a gluon-gluon induced contribution that involve top-quark loops, $gg \rightarrow VH$. The cross sections of this processes, in pp collisions at 13 TeV, are $\sigma_{WH} \approx 1.37 \text{ pb}$ and $\sigma_{ZH} \approx 0.88 \text{ pb}$.
- *Associated production with $t\bar{t}$ ($t\bar{t}H$)*, $gg \rightarrow Ht\bar{t}$ (see diagram (d) in Fig. 1.5). In this process, the Higgs boson radiates off top quarks, providing a direct probe of the top-Higgs Yukawa coupling. The cross section in pp collision at 13 TeV is $\sigma_{t\bar{t}H} \approx 0.50 \text{ pb}$. Similarly, the Higgs boson can be produced in association with a bottom quark, following the same diagram and with a comparable cross section.
- *Associated production with a single t (\bar{t}) quark (tH)* (see diagram (e,f) in Fig. 1.5). In this process another light quark is present in the final state. The cross section in pp collision at 13 TeV is $\sigma_{tH+\bar{t}H} \approx 0.07 \text{ pb}$.

Table 1.1 summarizes the theoretical cross sections of the dominant Higgs boson production processes in pp collisions as a function of the collision center of mass energy, \sqrt{s} , for $m_H = 125 \text{ GeV}$. The relative uncertainties, arising for instance from higher-order perturbative QCD corrections, theoretical uncertainties on Parton Distribution Functions (PDF) and α_S , EW corrections, are also reported. The trend is also visible in the left plot of Fig. 1.7. The experimental measurements for these cross sections are presented together with the decay rate ones in the next section, when the μ framework [22] for signal strengths is introduced.

1.5.2 Principal decay channels

The SM Higgs boson couples to vector bosons, with an amplitude proportional to the gauge boson mass squared m_V^2 , and to fermions with an amplitude proportional to the fermion mass m_f . Hence, for example, the coupling is stronger for the third generation of quarks and leptons than for those in the second generation. The observation of many Higgs boson decays to SM particles and

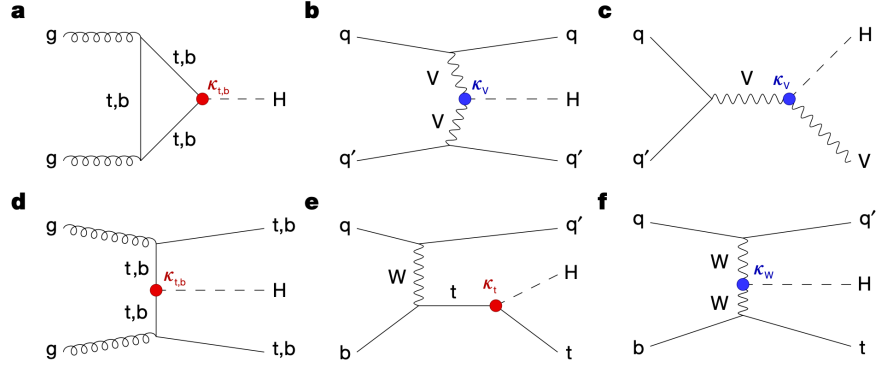


Figure 1.5: Main leading order Feynman diagrams contributing to the Higgs boson production in (a) gluon fusion, (b) Vector-boson fusion, (c) Higgs-strahlung (or associated production with a gauge boson at tree level from a quark-quark interaction), (d) associated production with a pair of top quarks, (e,f) associated production with a single top quark. The different Higgs boson interactions are labeled with the coupling modifiers κ , and highlighted in different colors for Higgs–fermion interactions (red) and Higgs–gauge-boson interactions (blue). The distinction between a particle and its antiparticle is dropped.

\sqrt{s} (TeV)	Production cross section (in pb) for $m_H = 125$ GeV					
	ggF	VBF	WH	ZH	$t\bar{t}H$	total
1.96	$0.95^{+17\%}_{-17\%}$	$0.065^{+8\%}_{-7\%}$	$0.13^{+8\%}_{-8\%}$	$0.079^{+8\%}_{-8\%}$	$0.004^{+10\%}_{-10\%}$	$1.23^{+15\%}_{-15\%}$
7	$16.9^{+5.5\%}_{-7.6\%}$	$1.24^{+2.2\%}_{-2.2\%}$	$0.58^{+2.2\%}_{-2.3\%}$	$0.34^{+3.1\%}_{-3.0\%}$	$0.09^{+5.6\%}_{-10.2\%}$	$19.1^{+5\%}_{-7\%}$
8	$21.4^{+5.4\%}_{-7.6\%}$	$1.60^{+2.1\%}_{-2.1\%}$	$0.70^{+2.1\%}_{-2.2\%}$	$0.42^{+3.4\%}_{-2.9\%}$	$0.13^{+5.9\%}_{-10.1\%}$	$24.2^{+5\%}_{-7\%}$
13	$48.6^{+5.6\%}_{-7.4\%}$	$3.78^{+2.1\%}_{-2.1\%}$	$1.37^{+2.0\%}_{-2.0\%}$	$0.88^{+4.1\%}_{-3.5\%}$	$0.50^{+6.8\%}_{-9.9\%}$	$55.1^{+5\%}_{-7\%}$
13.6	$52.2^{+5.6\%}_{-7.4\%}$	$4.1^{+2.1\%}_{-1.5\%}$	$1.46^{+1.8\%}_{-1.9\%}$	$0.95^{+4.0\%}_{-3.6\%}$	$0.57^{+6.9\%}_{-9.9\%}$	$59.2^{+5\%}_{-7\%}$
14	$54.7^{+5.6\%}_{-7.4\%}$	$4.28^{+2.1\%}_{-2.1\%}$	$1.51^{+1.8\%}_{-1.9\%}$	$0.99^{+4.1\%}_{-3.7\%}$	$0.61^{+6.9\%}_{-9.8\%}$	$62.1^{+5\%}_{-7\%}$

Table 1.1: The SM Higgs production cross sections for $m_H = 125$ GeV in pp collisions as function of \sqrt{s} [22]. The uncertainties are estimated assuming no correlation between α_S and PDF uncertainties.

the measurement of their branching fractions are a crucial test of the validity of the theory. Any sizeable deviation from the predictions could indicate the presence of New Physics.

The Higgs boson, once produced, rapidly decays into a pair of fermions or a pair of bosons. In the SM, its lifetime is $\tau_H \approx 1.6 \times 10^{-22}$ and its inverse, the natural width, is $\Gamma = \hbar/\tau_H = 4.14 \pm 0.02$ MeV, where \hbar is the reduced Planck's constant [42]. The natural width is the sum of all the partial widths, and the ratios of the partial widths to the total width are called branching fractions (BR) and represent the probabilities for that decay channel to occur. The main Higgs boson decays are sketched in Fig. 1.6. The Higgs boson does not couple directly to massless particles (for example, the gluon or the photon), but can do so through quantum loops (see for example c,d diagram in Fig. 1.6).

The main Higgs decay modes and their BRs are shown in Table 1.2. The dominant ones are $H \rightarrow b\bar{b}$ and $H \rightarrow WW^*$, followed by $H \rightarrow gg$, $H \rightarrow \tau^+\tau^-$, $H \rightarrow c\bar{c}$ and $H \rightarrow ZZ^*$. With much smaller rates the Higgs boson decays also into $H \rightarrow \gamma\gamma$, $H \rightarrow \gamma Z$ and $H \rightarrow \mu^+\mu^-$. Right Fig. 1.7 shows the BRs of the main decays as a function of the Higgs boson mass.

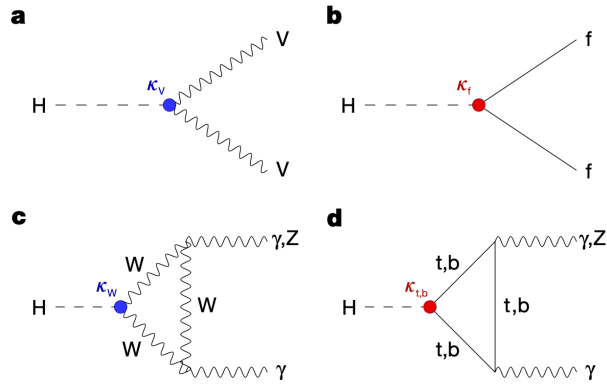


Figure 1.6: Higgs boson decays into heavy vector boson pairs (a), fermion–antifermion pairs (b) and photon pairs or $Z\gamma$ (c,d). The different Higgs boson interactions are labeled with the coupling modifiers κ , and highlighted in different colors for Higgs–fermion interactions (red) and Higgs–gauge–boson interactions (blue).

In order to describe the characterization of the Higgs boson properties, the concept of signal strength must be introduced.

The agreement between the observed signal yields and the SM expectations can be quantified by fitting the data with a model that introduces signal strength

Decay channel	Branching ratio	Rel. uncertainty
$H \rightarrow \gamma\gamma$	2.27×10^{-3}	2.1%
$H \rightarrow ZZ$	2.62×10^{-2}	$\pm 1.5\%$
$H \rightarrow W^+W^-$	2.14×10^{-1}	$\pm 1.5\%$
$H \rightarrow \tau^+\tau^-$	6.27×10^{-2}	$\pm 1.6\%$
$H \rightarrow b\bar{b}$	5.82×10^{-1}	+1.2% -1.3%
$H \rightarrow c\bar{c}$	2.89×10^{-2}	+5.5% -2.0%
$H \rightarrow Z\gamma$	1.53×10^{-3}	$\pm 5.8\%$
$H \rightarrow \mu^+\mu^-$	2.18×10^{-4}	$\pm 1.7\%$

Table 1.2: The BRs with relative uncertainties for a SM Higgs boson with $m_H = 125$ GeV [22].

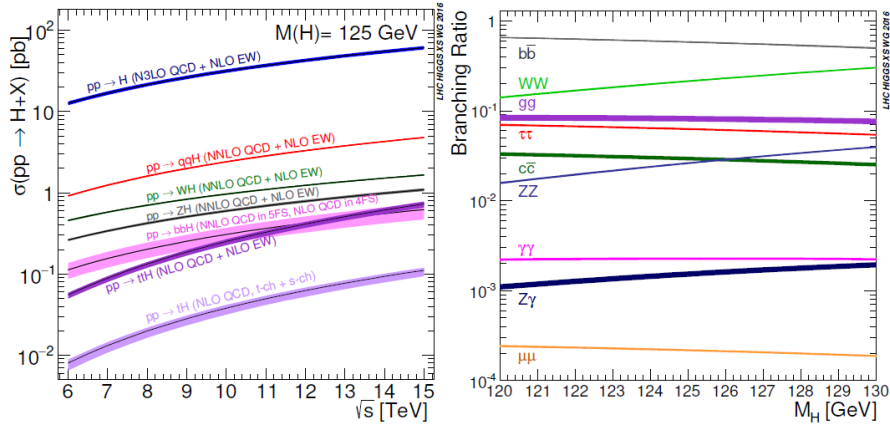


Figure 1.7: (Left) The SM Higgs boson production cross sections as a function of the center of mass energy for pp collisions. (Right) BRs for the main decays of the SM Higgs boson near $m_H = 125$ GeV. The VBF process is indicated here as $q\bar{q}H$. The theoretical uncertainties are indicated as bands [22].

parameters. These are generically labeled μ , and scale the observed yields with respect to those predicted by the SM, without altering the shape of the distributions. For a specific production and decay channel $i \rightarrow H \rightarrow f$, the signal strengths for the production μ_i and for the decay μ^f are defined as:

$$\mu_i = \frac{\sigma_i}{(\sigma_i)_{SM}}, \quad \mu^f = \frac{\mathcal{B}^f}{(\mathcal{B}^f)_{SM}} \quad (1.51)$$

where σ is the production cross section and \mathcal{B} is the branching fraction. Perfect agreement with SM expectations would yield all μ equal to one. A first test of compatibility is performed by fitting all data from production modes and decay channels with a common signal-strength parameter. At the time of discovery, the common μ was found to be 0.87 ± 0.23 by the CMS experiment. The new combination of all the Run 2 data yields $\mu = 1.002 \pm 0.057$, in excellent agreement with the SM expectation. The uncertainties in the new measurement correspond to an improvement by a factor of 4.5 in precision compared with what was achieved at the time of discovery. At present, the theoretical uncertainties in the signal prediction, and the experimental statistical and the systematic uncertainties separately contribute at a similar level, and they are 0.036, 0.029 and 0.033, respectively. Relaxing the assumption of a common signal-strength parameter, and introducing different μ_i and μ^f , CMS measurements are shown in Fig. 1.8 [43].

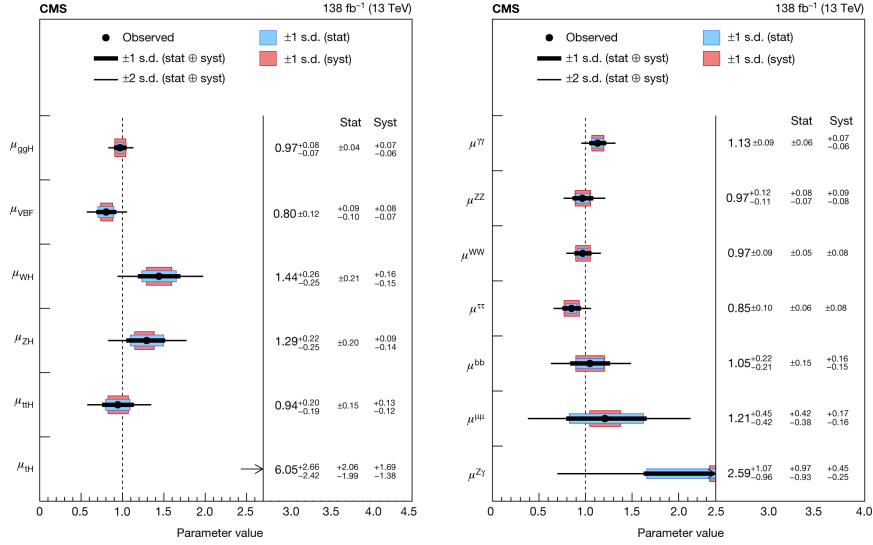


Figure 1.8: (Left) Signal-strength parameters μ_i extracted for various production modes, assuming $\mathcal{B}^f = (\mathcal{B}^f)_{SM}$. (Right) Signal-strength parameter μ_f for different decay channels, assuming $\sigma_i = (\sigma_i)_{SM}$. The thick and thin black lines indicate the 1σ and 2σ confidence intervals, respectively, with the systematic (syst) and statistical (stat) components of the 1σ interval indicated by the red and blue band, respectively. The vertical dashed line at unity represents the values of μ_i and μ_f in the SM [43].

1.5.3 Measurement of the Higgs boson mass

The decay channels that allow us to measure the Higgs boson mass with the highest resolution (typically 1-2%) are $H \rightarrow \gamma\gamma$ and $H \rightarrow ZZ^* \rightarrow 4l$, since all final state particles can be measured very precisely. Figure 1.9 shows, on the left side, the invariant mass distribution of di-photon candidates obtained by ATLAS and, on the right side, the CMS four lepton invariant mass distribution. The best mass resolution is achieved, by both the experiments, in the di-photon channel for central di-photon pairs.

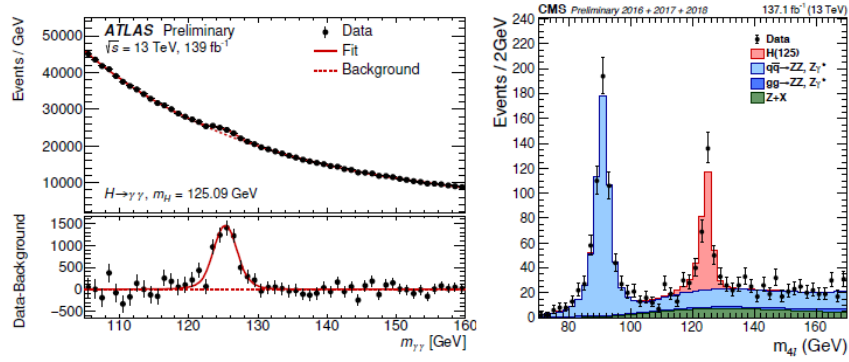


Figure 1.9: (Left) Invariant mass distribution of di-photon candidates observed by ATLAS in Run 2. The residuals of the data with respect to the fitted background are displayed in the lower panel. (Right) Four lepton invariant mass distribution observed by CMS in Run 2 data [22].

The most precise mass measurement has been obtained recently by the ATLAS collaboration, by combining the results in the di-photon and the four-lepton channels from Run 1 and Run 2 [44] [22]:

$$m_H = 125.11 \pm 0.09 \text{ (stat)} \pm 0.06 \text{ (syst)} \text{ GeV} \quad (1.52)$$

1.5.4 Higgs boson couplings

The first Higgs couplings to be measured at the LHC were those to bosons, as the particle was initially discovered through the analysis of bosonic final states. However, both the dominant Higgs production mechanism and its decay into photons only proceed through fermion loops, providing indirect evidence of the Higgs boson's coupling to fermions. A direct observation and measurement of these couplings—either through production or decay—is nevertheless essential to fully establish this interaction.

One of the highest priority goals of the LHC Run 2 physics program was the direct observation of the Yukawa coupling of the Higgs boson to fermions of the third generation (bottom and top quarks, and tau leptons). This objective was achieved independently by both ATLAS and CMS, even with only partial Run 2 datasets [22]. Furthermore, using the full Run 2 dataset, the CMS Collaboration reported [45] the first evidence for $H \rightarrow \mu\mu$ at 3σ level with a signal strength of $\mu = 1.19 \pm 0.40$ (stat.) ± 0.15 (syst.). This result constitutes the first direct evidence of the $H \rightarrow \mu\mu$ decay and therefore the first measurement of the Higgs Yukawa coupling to second generation leptons.

The current state of the art of the Higgs coupling measurements by ATLAS and CMS is summarized in Fig. 1.10. The fit has been performed by CMS (ATLAS) in the context of the so-called κ -framework, considering 6 (7) free coupling parameters: κ_W , κ_Z , κ_t , κ_τ , κ_b and κ_μ (and κ_c). The phenomenological parametrization relating the fermion and vector boson masses to the corresponding κ modifiers uses two parameters, denoted M and ϵ . The parametrization reads:

$$\begin{aligned}\kappa_F &= v \frac{m_F^\epsilon}{M^{1+\epsilon}} \quad \text{for fermions} \\ \kappa_V &= v \frac{m_V^{2\epsilon}}{M^{1+2\epsilon}} \quad \text{for vector bosons}\end{aligned}\tag{1.53}$$

where v is the SM Higgs boson vacuum expectation value. The SM is recovered when $(M, \epsilon) = (v, 0)$. In order to show both the Yukawa and vector boson couplings in the same plot in Fig. 1.10, a *reduced* vector boson coupling $\sqrt{\kappa} m_V / v$ is shown. The SM expectation is reported with a dashed blue (solid red) line for a comparison.

The remarkable agreement with the predictions of the EWSB mechanism over three orders of magnitude of mass is a powerful test of the validity of the underlying physics. Statistical and systematic uncertainties contribute at the same level to all measurements, except for κ_μ , which is still dominated by the statistical uncertainty.

1.5.5 Higgs boson self-coupling

As seen in Sec. 1.4, within the SM, the scalar potential of the Higgs field (h) has the following form:

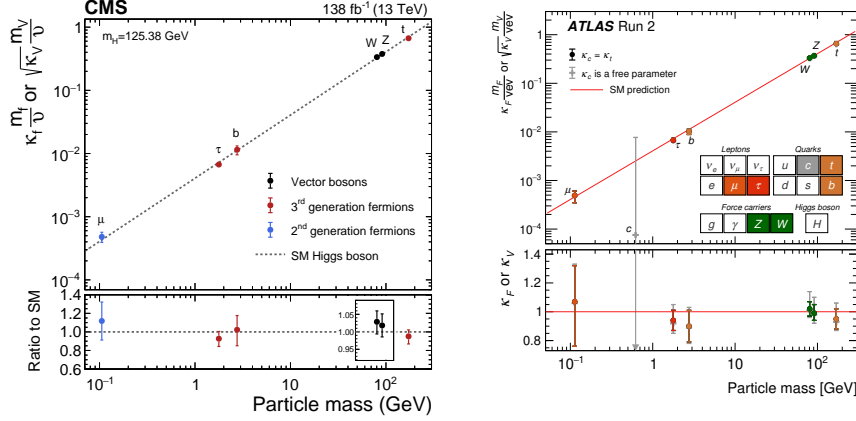


Figure 1.10: Measured coupling modifiers of the Higgs boson to fermions and heavy gauge bosons, as functions of fermion or gauge boson mass [43,46]. For gauge bosons, the square root of the coupling modifier is plotted, to keep a linear proportionality to the mass, as predicted in the SM. The coupling to charm quark has not been observed yet.

$$V(h) = \frac{m_H^2}{2} h^2 + \lambda_3 v h^3 + \frac{\lambda_4}{4} h^4 \quad (1.54)$$

which is a simple rewriting of Eq. 1.30, where now $v \approx 246$ GeV is the vacuum expectation value of h , λ_3 and λ_4 are respectively the Higgs trilinear and quartic self-coupling, and for Higgs mass $m_H = 125$ GeV, $\lambda_{SM} = \lambda_3 = \lambda_4 = m_H^2/2v^2 \approx 0.13$ [42].

Conveniently, most of the experimental results are usually reported in terms of the self-coupling modifier, κ_λ , defined as the ratio λ/λ_{SM} of the experimental measurement of the coupling to its SM predicted value, in order to parametrize any deviation from the theory.

Our current experimental knowledge on the Higgs boson self-interaction is extremely limited. Alternative potentials that differ substantially from the SM prediction in a region away from the minimum would be equally consistent with current data and therefore cannot be ruled out. Related to that is the question on the stability of the Higgs potential, namely the possibility for a lower energy vacuum to exist which would make our current vacuum state metastable (see Fig. 1.11). In this perspective, understanding the scalar potential would give information on how our universe formed and how it might end [27].

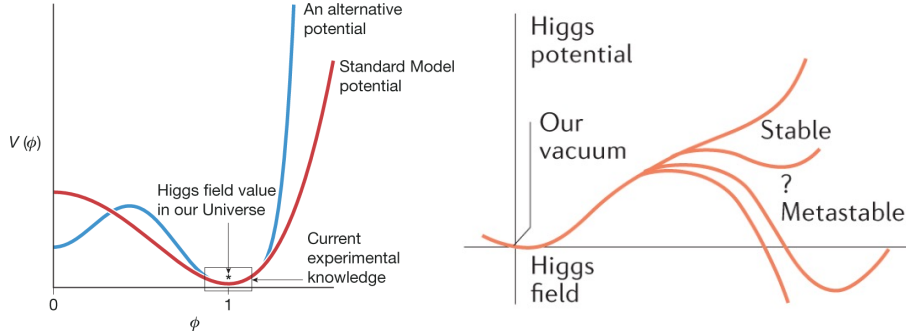


Figure 1.11: The potential energy density $V(\phi)$ associated with the field ϕ , as a function of the value of the field. (Left) The red curve shows the SM potential. The Higgs field has a value corresponding to a minimum of the potential and the region highlighted in black represents our current experimental knowledge of the potential. Alternative potentials that differ substantially from the Standard Model away from that minimum (for example, the blue curve) would be equally consistent with current data. (Right) The shape of the potential define the stability of the universe [47].

The most direct ways to probe the Higgs potential are searching for double (HH) and triple (HHH) Higgs production⁵: the former allows to measure λ_3 , the latter λ_4 . Due to the extremely small cross section of the triple Higgs production, the current studies at LHC are focused on Higgs boson pair final states. The HH production modes are shown in Fig 1.12. The leading production mechanism is the gluon fusion, that has two leading contributions: in the first one (Fig 1.12 a, the *triangle diagram*), two Higgs bosons emerge from a top or bottom quark loop; in the second (Fig 1.12 b, the *box diagram*), a single virtual Higgs boson, H^* , emerges from the top or bottom quark loop and then decays to two Higgs bosons. The explicit establishment of the latter contribution would represent a direct manifestation of the Higgs boson's self-interaction. The scattering amplitudes of the box and triangle diagrams are similar in magnitude but have opposite signs and interfere destructively (see Fig 1.13). This results in a small HH production rate, making its experimental observation challenging. In fact, the HH production cross section is calculated for $m_H = 125$ GeV to be ≈ 32 fb, three orders of magnitude smaller than the single Higgs boson cross section.

In order to access experimentally these rare events is, therefore, essential to find a trade-off between keeping the branching ratio high enough and enhanc-

⁵Single Higgs production is also sensitive to the self-coupling through NLO EW corrections.

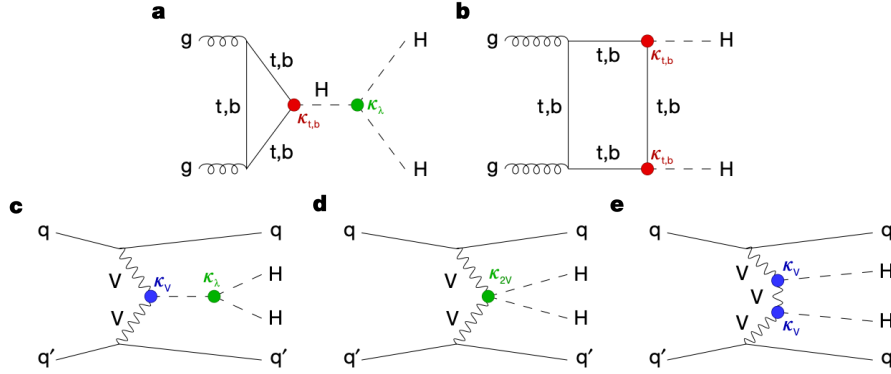


Figure 1.12: Higgs boson pair production through ggH (a,b) and VBF (c,d,e). The different Higgs boson interactions are labeled with the coupling modifiers κ , and highlighted in different colors for Higgs–fermion interactions (red), Higgs–gauge-boson interactions (blue) and multiple Higgs boson interactions (green).

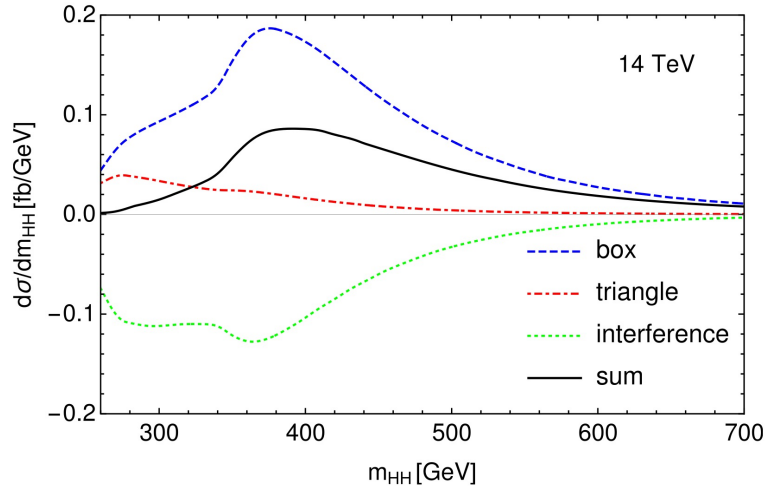


Figure 1.13: Higgs pair invariant mass distribution at leading order for the different contributions to the gluon fusion production mechanism and their interference [48].

ing the signal purity, by selecting and combining different Higgs boson decays. The branching ratios for the main combinations of Higgs decay channels are reported in Fig. 1.14.

Given its small cross section, the HH production has escaped detection at LHC so far. The results of the search are therefore expressed as an upper limit on the production cross section. Left Fig. 1.15 shows the expected and observed limits on the HH production by CMS, expressed as ratios with respect

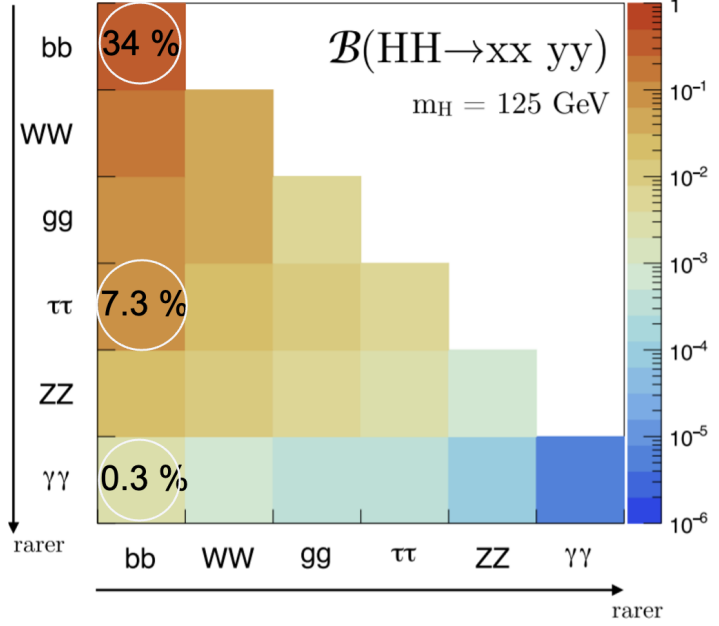


Figure 1.14: Branching ratios for the most important HH decay modes. The channel leading the sensitivity are the $bbbb$, $bb\gamma\gamma$ and $bb\tau\tau$.

to the SM expectation, in searches using the different final states and their combination. With the current dataset, and combining data from all currently studied modes and channels, the HH production cross section is found to be less than 3.4 times its SM expectation at 95% CL. Right Fig. 1.15 shows the evolution of the limits from the three most sensitive modes and the overall combination. The CMS projections for the High Luminosity LHC (HL-LHC) are also included and show how the expected sensitivity for this last foreseen stage of the LHC operation is sufficient to reach a combined limit below unity.

Figure 1.16 presents the expected and observed experimental limits on the HH production cross section by CMS as functions of the Higgs boson self-interaction coupling modifier κ_λ and the quartic $VVHH$ coupling modifier κ_{2V} (see Fig. 1.12). Cross section values above the solid black lines are experimentally excluded at 95% CL. The red lines show the predicted cross sections, which exhibit a characteristic dip in the vicinity of the SM values owing to the destructive interference of the contributing production amplitudes. The experimental limits on the HH production cross section also show a strong dependence on the assumed values of κ_λ or κ_{2V} . This is because the interference

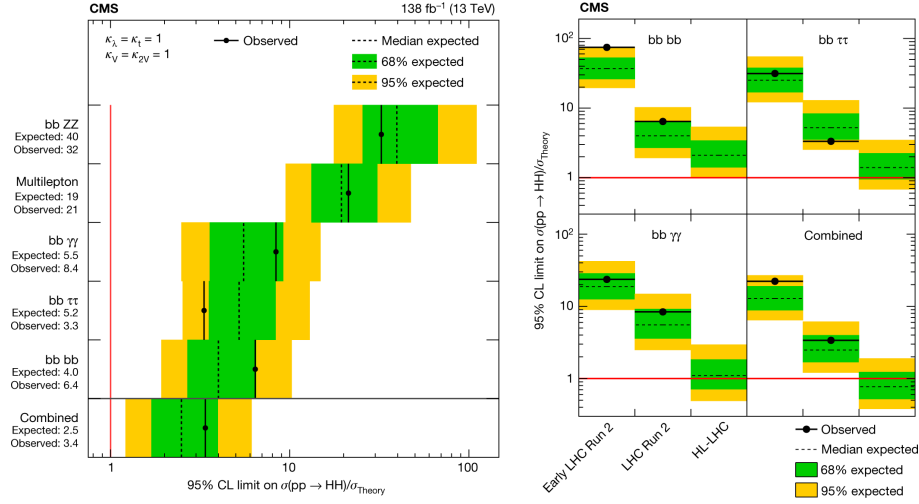


Figure 1.15: Limits on the HH production and their time evolution [43]. (Left) Expected and observed limits on the ratio of experimentally estimated production cross section and the SM expectation in searches using different final states and their combination. The search modes are ordered, from upper to lower, by their expected sensitivities from the least to the most sensitive. The overall combination of all searches is shown by the lowest entry. (Right) Expected and observed limits on HH production in different datasets: early LHC Run 2 data (35.9 fb⁻¹), present results using full LHC Run 2 data (138 fb⁻¹) and projections for the HL-LHC (3000 fb⁻¹).

between different subprocesses, besides changing the expected cross sections, also changes the differential kinematic properties of the two Higgs bosons, which in turn affects strongly the efficiency for detecting signal events. With the current dataset, CMS manages to constrain κ_λ in the range of 1.24 to 6.49 and κ_{2V} in the range of 0.67 to 1.38. The value $\kappa_{2V}=0$ is excluded, with a significance of 6.6σ , establishing the existence of the quartic coupling $VVHH$.

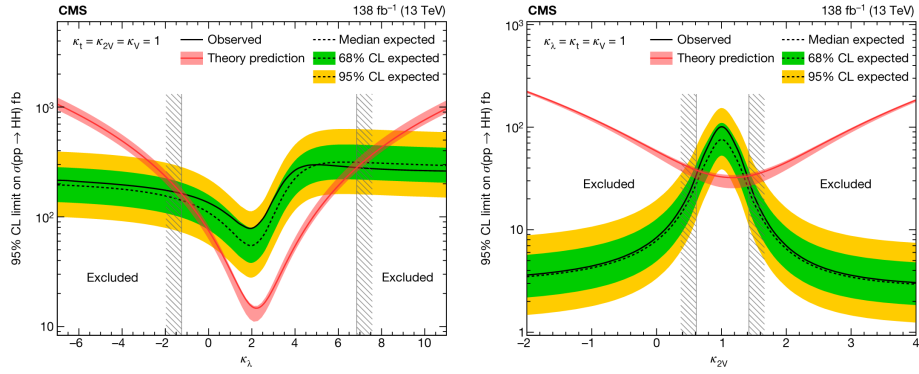


Figure 1.16: Combined expected and observed 95% CL upper limits [43] on the HH production cross section for different values of κ_λ (left) and κ_{2V} (right), assuming the SM values for the modifiers of Higgs boson couplings to top quarks and vector bosons. The green and yellow bands represent the 1 σ and 2 σ extensions beyond the expected limit, respectively; the red solid line (band) shows the theoretical prediction for the HH production cross section. The areas to the left and to the right of the hatched regions are excluded at the 95% CL.

The Extended Higgs Sector

In the previous chapter, Chapter 1, I outlined how the SM provides a remarkably accurate description of physical phenomena within its established domain. Nonetheless, there are several phenomena it fails to explain, as well as fundamental questions it leaves unanswered. Some of these open issues were already touched upon in Sec.1.5, where the pivotal role of the Higgs boson as a potential gateway to New Physics was emphasized.

In this chapter, I will summarize the key limitations of the SM that motivate the development of Beyond-the-SM (BSM) theories to expand its reach. The central idea is that the SM might represent just a low-energy approximation of a deeper, more comprehensive framework—much like Newtonian mechanics emerges as the low-velocity limit of relativistic mechanics. In the formulation of an extended theory that aims to address the shortcomings of the SM, it is often natural to extend the SM Higgs sector, leading to the prediction of additional Higgs bosons in such BSM theories. The CMS analysis presented in this thesis search simultaneously for two of such additional Higgs bosons, specifically in the mass region below 1 TeV. The search is designed to be as model-independent as possible, in principle looking only for a scalar resonance of a certain mass and width, but an interpretation of the results in terms of a specific two Higgs doublet model (2HDM) is also given. Hence, 2HDMs are covered in some detail in Chapter 2.2, while other BSM theories with an extended Higgs sector are introduced only briefly in Chapter 2.3.

2.1 Limitations of the Standard Model

The following provides an overview of several key open questions that lie beyond the SM reach. This list is not exhaustive and is presented without any particular order.

Gravity The SM successfully describes three of the four fundamental forces of nature—electromagnetism, the weak interaction, and the strong interaction—but it does not incorporate gravity. Unlike the other forces, gravity is currently described by Einstein’s General Relativity, a classical theory that does not fit within the quantum framework of the SM. Efforts to reconcile gravity with quantum mechanics have led to the development of quantum gravity theories [49], which propose that gravity, like the other fundamental interactions, is mediated by a force carrier: the hypothetical *graviton*. The graviton is predicted to be a massless, spin-2 boson, and its existence arises naturally in several theoretical frameworks, including string theory and extra-dimensional models such as the Randall–Sundrum scenario [50], where excitations of the graviton could potentially be detected at high-energy colliders. However, despite these theoretical motivations, no experimental evidence for the graviton has been found to date.

Dark matter and dark energy There is conclusive and abundant evidence from a wide range of astrophysical observations that the SM accounts for only about 5% of the total energy content of the universe. Approximately 95% of the universe consists of dark matter and dark energy [51].

Dark matter refers to a form of matter that does not interact with the electromagnetic force but does exert and respond to gravitational forces. Its exact nature remains unknown. Much of the evidence for dark matter comes from observing gravitational effects that cannot be explained by visible, baryonic matter alone. Notable examples include the anomalously flat rotation curves of galaxies, first measured by Rubin and Ford [52], and the gravitational lensing observed in the *Bullet Cluster* [53], which provides compelling evidence for the presence of collisionless dark matter. While SM neutrinos exhibit some of the necessary properties, they cannot account for the full observed dark matter distribution due to their low mass and relativistic nature in the early universe. In contrast, BSM theories such as SUSY predict more viable candidates, including Weakly Interacting Massive Particles (WIMPs), which remain among the most actively studied dark matter candidates. For a comprehensive overview of the observational evidence for dark matter, as well as the range of theoretical models proposed to explain it, see Ref. [51].

In addition to dark matter, dark energy constitutes an even larger fraction of the universe and is thought to be responsible for the observed accelerated expansion of the cosmos, as first inferred from Type Ia supernovae observations in the late 1990s [54]. Unlike dark matter, which clusters under gravity, dark

energy appears to act as a repulsive force on cosmological scales. Dark energy currently lies entirely outside the framework of the SM and its physical origin remains deeply mysterious, with possible explanations [55] ranging from a cosmological constant (Λ) in Einstein's field equations to dynamic fields such as quintessence.

Neutrino masses In the formalism of the SM, neutrinos are assumed to be massless. However, the discovery of neutrino flavor oscillations—the phenomenon in which neutrinos change flavor (electron, muon, tau) as they propagate—provides clear evidence that neutrinos possess non-zero masses [56,57]. This observation is incompatible with the minimal SM, which lacks the necessary terms to give neutrinos mass. Constraints on the neutrino masses can be derived from experiment - for example by studying the kinematics of weak decays involving neutrinos [58]. Although it is possible to extend the SM to include neutrino masses, the exact mechanism responsible for generating them remains an open question. Two primary approaches exist: either the neutrinos are *Dirac fermions*, hence their masses are produced by the same mechanism of other leptons in SM and right-handed neutrinos must be introduced in the theory, or they are *Majorana fermions*, which means another mechanism (e.g. the Seesaw one [59]) gives neutrinos masses implying neutrinos are their own antiparticle. The nature of neutrino mass—Dirac or Majorana—is still unknown and is the subject of active experimental efforts, such as searches for neutrinoless double beta decay, which would confirm a Majorana mass term if observed. A detailed review of the neutrino mass problem is given in Ref. [22].

Asymmetry of matter and antimatter The Big Bang should have created equal amounts of matter and antimatter in the early universe. But today, everything we see is made almost entirely of matter. In order to generate the observed matter–antimatter asymmetry from an initially symmetric universe, any successful theory must satisfy the three Sakharov conditions [60]: there must be processes that *violate baryon number* allowing the net production of baryons over antibaryons, *C and CP must be violated* to differentiate between matter and antimatter in physical processes (otherwise baryon-generating processes would produce equal amounts of matter and antimatter) and, finally, these baryon number- and CP-violating processes must occur *out of thermal equilibrium* (otherwise the CPT theorem would ensure that forward and reverse processes occur at equal rates, preventing the generation of any asymmetry). The SM does contain all three ingredients to some extent, e.g. the CP violation

in the CKM matrix. However, the strength and scale of these effects are far too small to account for the observed baryon-to-photon ratio of the universe, $\eta_B \approx 6 \times 10^{-10}$ as measured from the cosmic microwave background and Big Bang nucleosynthesis [61]. Although weak CP violation in the lepton sector and strong CP violation are, in principle, also predicted by the Standard Model and could potentially account for the remaining asymmetry, they have yet to be confirmed experimentally, and it remains unclear whether they provide a complete explanation.

The hierarchy problem From a more theoretical standpoint, the hierarchy problem highlights a structural issue within the SM [62]: while the electroweak scale is of order $\mathcal{O}(100)$ GeV, the Planck scale—where gravitational interactions become significant and the SM ceases to be valid—is vastly higher, around $\mathcal{O}(10^{19})$ GeV. The SM offers no mechanism to explain why such an enormous gap between these two fundamental scales exists, prompting the idea that a deeper, more fundamental theory might underlie the SM. This concern is closely tied to the principle of naturalness, which favors theories where dimensionless ratios between parameters are of order unity. In this context, the smallness of the Higgs boson mass presents a particular challenge. Within the SM, the physical Higgs mass arises from a combination of a bare mass term and quantum corrections, the latter of which grow quadratically with the energy cutoff scale. If the SM remains valid up to a very high scale, such as the Planck scale, the bare Higgs mass must be finely tuned to cancel these large corrections, resulting in the observed mass of 125 GeV. This extreme sensitivity to high-scale physics is considered unnatural and has driven theoretical exploration of extensions to the SM that could stabilize the Higgs mass without fine-tuning.

Despite its shortcomings, the SM remains an exceptionally successful framework, accurately describing all current experimental observations. However, it offers limited insight into the deeper reasons why the parameters and structures we observe take their specific forms. For instance, the SM does not explain the origin of the mass hierarchy among quarks and leptons, nor does it account for why there are exactly three generations of each. Likewise, electroweak symmetry breaking is implemented by postulating a particular form of the Higgs potential—an effective mechanism, but one that leaves open the question of why this potential should have its specific shape. Some of the BSM theories described in the following give more in-depth answers to these questions.

2.2 Two Higgs Doublet Models

In the SM, the Higgs sector is *minimal*, meaning that only one complex Higgs doublet is included in the theory. This is the simplest form to introduce electroweak symmetry breaking. However, the Higgs sector may also be more complicated, i.e. *extended* by including more additional fields than just the one Higgs doublet.

As the name suggests, the *Two Higgs Doublet Models* (2HDMs) are a class of models that include two Higgs doublets, hence theorize the existence of multiple physical Higgs bosons. The original motivation behind 2HDMs was to introduce additional sources of CP-violation, able to explain the observed matter-antimatter asymmetry [63]. Another motivation is that some broader BSM frameworks require at least two Higgs doublets. The best known example are SUSY theories, in which an even number of Higgs doublets are needed to generate masses for all fermions. SUSY theories are able to provide a solution for the naturalness problem and predict viable dark matter candidates. Moreover, some axion models that explain why CP-violation in the strong sector seems to be suppressed in nature also require two Higgs doublets [64, 65]. Thus, there is a clear incentive to explore the parameter space and rich phenomenology of 2HDMs. Detailed overviews of different types of 2HDMs and their implications can be found in [42, 66, 67].

2.2.1 Theory

The two Higgs doublets are constructed analogously to the doublet in the SM, each has four degrees of freedom, and both acquire vacuum expectation values which spontaneously breaks the electroweak symmetry and give mass to the fermions, and the vector bosons.

The predicted physical Higgs bosons are five in total:

- Two CP-even and neutral Higgs bosons, denoted as h and H .
- One CP-odd and neutral Higgs boson, usually referred to as A .
- Two charged Higgs bosons, denoted as H^\pm .

The masses of the Higgs bosons, m_h , m_H , m_A and m_{H^\pm} are free parameters of the model. In its most general form, the potential in terms of the two Higgs doublets Φ_1 and Φ_2 , can be written as

$$\begin{aligned}
V(\Phi_1, \Phi_2) = & m_{11}^2(\Phi_1^\dagger \Phi_1) + m_{22}^2(\Phi_2^\dagger \Phi_2) - \left[m_{12}^2(\Phi_1^\dagger \Phi_2) + \text{h.c.} \right] \\
& + \frac{\lambda_1}{2}(\Phi_1^\dagger \Phi_1)^2 + \frac{\lambda_2}{2}(\Phi_2^\dagger \Phi_2)^2 + \lambda_3(\Phi_1^\dagger \Phi_1)(\Phi_2^\dagger \Phi_2) \\
& + \lambda_4(\Phi_1^\dagger \Phi_2)(\Phi_2^\dagger \Phi_1) + \left[\frac{\lambda_5}{2}(\Phi_1^\dagger \Phi_2)^2 + \lambda_6(\Phi_1^\dagger \Phi_1)(\Phi_1^\dagger \Phi_2) \right. \\
& \left. + \lambda_7(\Phi_2^\dagger \Phi_2)(\Phi_1^\dagger \Phi_2) + \text{h.c.} \right]
\end{aligned} \tag{2.1}$$

and the Φ_1 and Φ_2 are complex Higgs doublets with hypercharge $Y = 1$:

$$\Phi_1 = \begin{pmatrix} \phi_1^+ \\ \frac{1}{\sqrt{2}}(v_1 + \phi_1 + ia_1) \end{pmatrix}, \quad \Phi_2 = \begin{pmatrix} \phi_2^+ \\ \frac{1}{\sqrt{2}}(v_2 + \phi_2 + ia_2) \end{pmatrix}. \tag{2.2}$$

Here we restrict to the CP-conserving models in which all λ_i and m_{12}^2 are real and the electroweak vacuum expectation values v_1 and v_2 are also real with $v^2 = v_1^2 + v_2^2 = (246 \text{ GeV})^2$.

In order to forbid tree-level Flavor Changing Neutral Current (FCNC), an additional Z_2 discrete symmetry is introduced under which the charge assignments of fields are shown in Table 2.1. Because of this Z_2 symmetry, the λ_6 and λ_7 terms in the general scalar potential in Eq. 2.1 are absent, while the soft breaking m_{12}^2 term is still allowed. The mass parameters m_{11}^2 and m_{22}^2 in the potential are determined by the potential minimization conditions at (v_1, v_2) :

$$\begin{aligned}
m_{11}^2 &= m_{12}^2 t_\beta - \frac{1}{2} v^2 (\lambda_1 c_\beta^2 + \lambda_{345} s_\beta^2), \\
m_{22}^2 &= m_{12}^2 / t_\beta - \frac{1}{2} v^2 (\lambda_2 s_\beta^2 + \lambda_{345} c_\beta^2),
\end{aligned} \tag{2.3}$$

where the shorthand notations $t_\beta \equiv \tan \beta = v_2/v_1$, $s_\beta \equiv \sin \beta$, $c_\beta \equiv \cos \beta$, and $\lambda_{345} = \lambda_3 + \lambda_4 + \lambda_5$ are employed.

Model	Φ_2	Φ_1	u_R^i	d_R^i	e_R^i
Type-I	+	−	+	+	+
Type-II	+	−	+	−	−
Lepton-specific	+	−	+	+	−
Flipped	+	−	+	−	+

Table 2.1: The Z_2 charge assignment in the four types of 2HDMs without FCNC. The other fields are even under Z_2 symmetry.

From the scalar potential in Eq. (2.1) with $\lambda_6 = \lambda_7 = 0$, we can obtain the mass matrices of the Higgs fields

$$\begin{pmatrix} \phi_1 & \phi_2 \end{pmatrix} \begin{pmatrix} m_{12}^2 t_\beta + \lambda_1 v^2 c_\beta^2 & -m_{12}^2 + \frac{\lambda_{345}}{2} v^2 s_{2\beta} \\ -m_{12}^2 + \frac{\lambda_{345}}{2} v^2 s_{2\beta} & m_{12}^2/t_\beta + \lambda_2 v^2 s_\beta^2 \end{pmatrix} \begin{pmatrix} \phi_1 \\ \phi_2 \end{pmatrix} \quad (2.4)$$

$$\begin{pmatrix} a_1 & a_2 \end{pmatrix} \left[m_{12}^2 - \frac{1}{2} \lambda_5 v^2 s_{2\beta} \right] \begin{pmatrix} t_\beta & -1 \\ -1 & 1/t_\beta \end{pmatrix} \begin{pmatrix} a_1 \\ a_2 \end{pmatrix} \quad (2.5)$$

$$\begin{pmatrix} \phi_1^+ & \phi_2^+ \end{pmatrix} \left[m_{12}^2 - \frac{1}{4} (\lambda_4 + \lambda_5) v^2 s_{2\beta} \right] \begin{pmatrix} t_\beta & -1 \\ -1 & 1/t_\beta \end{pmatrix} \begin{pmatrix} \phi_1^- \\ \phi_2^- \end{pmatrix} \quad (2.6)$$

The mass eigenstates are obtained from the original fields by the rotation matrices:

$$\begin{pmatrix} H \\ h \end{pmatrix} = \begin{pmatrix} \cos \alpha & \sin \alpha \\ -\sin \alpha & \cos \alpha \end{pmatrix} \begin{pmatrix} \phi_1 \\ \phi_2 \end{pmatrix}, \quad (2.7)$$

$$\begin{pmatrix} G^0 \\ A \end{pmatrix} = \begin{pmatrix} \cos \beta & \sin \beta \\ -\sin \beta & \cos \beta \end{pmatrix} \begin{pmatrix} a_1 \\ a_2 \end{pmatrix}, \quad (2.8)$$

$$\begin{pmatrix} G^\pm \\ H^\pm \end{pmatrix} = \begin{pmatrix} \cos \beta & \sin \beta \\ -\sin \beta & \cos \beta \end{pmatrix} \begin{pmatrix} \phi_1^\pm \\ \phi_2^\pm \end{pmatrix}, \quad (2.9)$$

where G^0 and G^\pm are Goldstone bosons which are absorbed as longitudinal components of the Z and W^\pm bosons. The remained physical states are the

five Higgs boson described above. Their masses are given by

$$m_{H,h}^2 = \frac{1}{2} \left[M_{P,11}^2 + M_{P,22}^2 \pm \sqrt{(M_{P,11}^2 - M_{P,22}^2)^2 + 4(M_{P,12}^2)^2} \right], \quad (2.10)$$

$$m_A^2 = \frac{m_{12}^2}{s_\beta c_\beta} - \lambda_5 v^2, \quad (2.11)$$

$$m_{H^\pm}^2 = \frac{m_{12}^2}{s_\beta c_\beta} - \frac{1}{2}(\lambda_4 + \lambda_5)v^2, \quad (2.12)$$

where M_P^2 is the mass matrix shown in Eq. 2.4.

The gauge-kinetic Lagrangian is given as

$$\mathcal{L}_g = (D^\mu \Phi_1)^\dagger (D_\mu \Phi_1) + (D^\mu \Phi_2)^\dagger (D_\mu \Phi_2). \quad (2.13)$$

We can obtain the neutral Higgs couplings to VV ($VV \equiv ZZ, W^+W^-$)

$$\begin{aligned} \mathcal{L}_g \supset & \frac{g^2 + g'^2}{8} v^2 ZZ \left(1 + 2\frac{h}{v} y_h^V + 2\frac{H}{v} y_H^V \right) \\ & + \frac{g^2}{4} v^2 W^+W^- \left(1 + 2\frac{h}{v} y_h^V + 2\frac{H}{v} y_H^V \right), \end{aligned} \quad (2.14)$$

where $y_h^V = \sin(\beta - \alpha)$ and $y_H^V = \cos(\beta - \alpha)$.

According to different charge assignments, there are four different models with Yukawa interactions:

$$-\mathcal{L} = Y_{u2} \bar{Q}_L \tilde{\Phi}_2 u_R + Y_{d2} \bar{Q}_L \Phi_2 d_R + Y_{\ell 2} \bar{L}_L \Phi_2 e_R + \text{h.c. (type I)}, \quad (2.15)$$

$$-\mathcal{L} = Y_{u2} \bar{Q}_L \tilde{\Phi}_2 u_R + Y_{d1} \bar{Q}_L \Phi_1 d_R + Y_{\ell 1} \bar{L}_L \Phi_1 e_R + \text{h.c. (type II)}, \quad (2.16)$$

$$-\mathcal{L} = Y_{u2} \bar{Q}_L \tilde{\Phi}_2 u_R + Y_{d1} \bar{Q}_L \Phi_2 d_R + Y_{\ell 1} \bar{L}_L \Phi_1 e_R + \text{h.c. (lep. spec.)}, \quad (2.17)$$

$$-\mathcal{L} = Y_{u2} \bar{Q}_L \tilde{\Phi}_2 u_R + Y_{d1} \bar{Q}_L \Phi_1 d_R + Y_{\ell 1} \bar{L}_L \Phi_2 e_R + \text{h.c. (flipped)}, \quad (2.18)$$

where $Q_L^T = (u_L, d_L)$, $L_L^T = (\nu_L, l_L)$, $\tilde{\Phi}_{1,2} = i\tau_2 \Phi_{1,2}^*$, and Y_{u2} , $Y_{d1,2}$ and $Y_{\ell 1,2}$ are 3×3 matrices in family space. These constitute the four 2HDM types:

Type-I In Type-I models, only one of the doublets - Φ_2 - couples to all fermions, i.e. to quarks and leptons. The other one only couples to gauge bosons. This type is also referred to as *fermiophobic*.

Type-II In Type-II models, Φ_1 couples to down-type quarks and leptons, whereas Φ_2 couples to up-type quarks. This type is also called MSSM-like, because it features in the *Minimal Supersymmetric Model*.

Lepton specific In lepton specific models, Φ_1 couples to leptons and Φ_2 to quarks.

Flipped Similar to Type-II, but flipped: In this type of models Φ_1 couples to down-type quarks, while Φ_2 couples to up-type quarks and leptons.

We can obtain the Yukawa couplings

$$\begin{aligned}
-\mathcal{L}_Y = & \frac{m_f}{v} y_h^f h \bar{f} f + \frac{m_f}{v} y_H^f H \bar{f} f \\
& -i \frac{m_u}{v} \kappa_u A \bar{u} \gamma_5 u + i \frac{m_d}{v} \kappa_d A \bar{d} \gamma_5 d + i \frac{m_\ell}{v} \kappa_\ell A \bar{\ell} \gamma_5 \ell \\
& + H^+ \bar{u} V_{\text{CKM}} \left(\frac{\sqrt{2} m_d}{v} \kappa_d P_R - \frac{\sqrt{2} m_u}{v} \kappa_u P_L \right) d + h.c. \\
& + \frac{\sqrt{2} m_\ell}{v} \kappa_\ell H^+ \bar{\nu} P_R e + h.c.
\end{aligned} \tag{2.19}$$

where $y_h^f = \sin(\beta - \alpha) + \cos(\beta - \alpha) \kappa_f$ and $y_H^f = \cos(\beta - \alpha) - \sin(\beta - \alpha) \kappa_f$. The values of κ_u , κ_d and κ_ℓ for the four models are shown in Table 2.2.

	Type-I	Type-II	lepton-specific	flipped
κ_u	$1/t_\beta$	$1/t_\beta$	$1/t_\beta$	$1/t_\beta$
κ_d	$1/t_\beta$	$-t_\beta$	$1/t_\beta$	$-t_\beta$
κ_ℓ	$1/t_\beta$	$-t_\beta$	$-t_\beta$	$1/t_\beta$

Table 2.2: The couplings κ_u , κ_d , and κ_ℓ for the four types of 2HDMs.

The 2HDM considered here has seven free parameters (versus fourteen of the most general case): m_h , m_H , m_A , m_{H^\pm} , α , $\tan \beta$ and the mixing parameter m_{12}^2 . The interpretation provided in the CMS analysis presented here is restricted to the so-called *alignment limit*, which occurs when $\cos(\beta - \alpha) \rightarrow 0$. In this case, one of the two CP even Higgs bosons (usually the one denoted with h) has couplings exactly like the SM-Higgs boson and is, therefore, identified with it. The interpretation offered is based on a Type-II 2HDM, while other models can be tested in the future.

2.2.2 Status of searches at LHC

There are usually two ways to probe the extended Higgs sectors: through their modifications to the SM-like Higgs couplings tested by Higgs coupling precision measurements, and direct searches for BSM Higgs bosons at high energy colliders. The current direct searches at the LHC include both conventional search channels of $H/H^\pm/A \rightarrow f\bar{f}, VV'$, as well as final states involving a SM-like Higgs $H \rightarrow Vh, hh$. Under the alignment limit of the 2HDM, both the decays $H \rightarrow VV$ and $H \rightarrow Vh, hh$ as well as the VH and VBF production modes vanish at tree level, making a discovery more challenging. However, if there is a mass hierarchy between the BSM Higgs bosons, additional exotic decay modes, such as $H/A \rightarrow ZA/H$, $H/A \rightarrow H^\pm W^\mp$, $H \rightarrow AA$, H^+H^- or $H^\pm \rightarrow H/AW$ open up and quickly dominate the decay branching fractions. Such exotic decay modes open a new window to search for new BSM scalar bosons.

This section summarizes the 2HDM-inspired searches of new neutral scalars carried out in ATLAS and CMS. The list and the categorization is taken from Ref. [68] and updated with the most recent publications.

A more comprehensive summary report of the searches for additional scalars at LHC with Run 2 data can be found in Ref. [69]¹.

Conventional channels Most of the existing direct searches for BSM Higgs bosons focus on their conventional decays into a pair of quarks, leptons or gauge bosons. The following table presents a summary of recent searches performed at the 13 TeV LHC.

channel	CMS	ATLAS
$A/H \rightarrow \mu^+\mu^-$	[70, 71]	[72]
$A/H \rightarrow b\bar{b}$	[73, 74]	[75]
$A/H \rightarrow \tau^+\tau^-$	[76–79]	[80]
$A/H \rightarrow \gamma\gamma$	[81–83]	[84–86]
$A/H \rightarrow t\bar{t}$	[87, 88]	[89]
$H \rightarrow ZZ$	[90, 91]	[92]
$H \rightarrow W^+W^-$	[91, 93]	[94]

¹This report has been compiled by the ATLAS collaboration. While all the reported searches exists also for CMS, a comprehensive reference encompassing all Run 2 analyses is not currently available.

Note that the $gg \rightarrow A/H \rightarrow t\bar{t}$ channel involves a non-trivial interference with the SM backgrounds that has been taken into account in the analysis.

Exotic Decays into the SM Higgs Away from the alignment limit, the heavy CP-odd Higgs can decay into the SM-like Higgs via $A \rightarrow hZ$. Additionally, the heavy CP-even Higgs can decay into a pair of SM-like Higgs bosons, $H \rightarrow hh$. The following table presents a summary of such searches performed at LHC.

channel	ATLAS		CMS	
	8 TeV	13 TeV	8 TeV	13 TeV
$A \rightarrow hZ \rightarrow b\bar{b}\ell^+\ell^-$	[95]	[96]	[97]	[98]
$A \rightarrow hZ \rightarrow \tau^+\tau^-\ell^+\ell^-$	[99]	[100]	[97]	[101]
$H \rightarrow hh$	[102]	[103]	[104]	[105]

A detailed summary by CMS of searches for SM Higgs production through decays of heavy resonances can be found in Ref. [106].

Exotic Decays of the SM Higgs If the BSM scalars are sufficiently light, $m_{A/H} < m_h/2$, exotic decays of the SM-like Higgs $h \rightarrow AA/HH$ open up. While the decay $h \rightarrow HH$ vanishes under the alignment limit, the decay $h \rightarrow AA$ is unsuppressed. The following table lists the current LHC searches that consider this channel.

channel	ATLAS	CMS
$h \rightarrow AA \rightarrow b\bar{b}b\bar{b}$	[107]	[108]
$h \rightarrow AA \rightarrow b\bar{b}\tau^+\tau^-$	[109]	[110, 111]
$h \rightarrow AA \rightarrow b\bar{b}\mu^+\mu^-$	[112]	[111, 113]
$h \rightarrow AA \rightarrow \tau^+\tau^-\tau^+\tau^-$	[114]	[115]
$h \rightarrow AA \rightarrow \tau^+\tau^-\mu^+\mu^-$	[116]	[117]
$h \rightarrow AA \rightarrow \mu^+\mu^-\mu^+\mu^-$	[118]	[119]
$h \rightarrow AA \rightarrow \gamma\gamma\gamma\gamma$	[120]	[121, 122]

Exotic Decays in BSM Sector If the two neutral BSM Higgs states A and H have a sufficient mass splitting, $|m_A - m_H| > m_Z$, the exotic decay channel $H/A \rightarrow ZA/H$ opens up. Both ATLAS and CMS have performed searches listed in the following table. The analysis presented in this thesis work targets the $H/A \rightarrow ZA/H \rightarrow \tau^+\tau^-\ell^+\ell^-$ channel, using Run 2 data collected at a

higher center-of-mass energy (13 TeV) and with a significantly larger integrated luminosity (138 fb^{-1}), compared to Run 1 (8 TeV, 20 fb^{-1}).

channel	ATLAS	CMS
$H/A \rightarrow ZA/H \rightarrow \ell^+ \ell^- b \bar{b}$	[123] (13 TeV)	[124] (13 TeV)
$H/A \rightarrow ZA/H \rightarrow \ell^+ \ell^- \tau^+ \tau^-$	—	[125] (8 TeV)
$H/A \rightarrow ZA/H \rightarrow \ell^+ \ell^- t \bar{t}$	[126] (13 TeV)	[127] (13 TeV)

In Ref. [68] these direct LHC searches are used to constraint the Type-I and Type-II 2HDM parameter space. Further constraints arise from flavor physics, electroweak precision observables, and global fits to Higgs coupling modifiers.

In the scenario where the heavy scalar masses are degenerate, i.e. $m_H = m_A = m_{H^\pm}$, decays such as $A \rightarrow HZ$ or $H \rightarrow AZ$ are kinematically forbidden². The phenomenology is therefore dominated by conventional decay channels into SM particles. Exclusion plots are reported in Fig 2.1 in the $(m_A, \tan \beta)$ plane for both Type-I and Type-II models. In the Type-I case, constraints are most effective at low $\tan \beta$ due to the enhancement of gluon fusion production. In the Type-II case, constraints extend to high $\tan \beta$ because of the enhanced bottom and lepton Yukawa couplings. Notably, the alignment limit ($\cos(\beta - \alpha) \rightarrow 0$) suppresses the couplings of the heavy CP-even scalar H to gauge bosons, reducing the sensitivity of $H \rightarrow VV$ and $H \rightarrow hh$ channels. Similarly, $A \rightarrow hZ$ is suppressed in this limit. The analysis shows the importance of combining different search strategies, including Higgs coupling fits, width constraints, and direct resonance searches.

For the scenario in which the heavy CP-even and CP-odd Higgs bosons are non-degenerate in mass, exotic decays of the form $A \rightarrow ZH$ and $H \rightarrow ZA$ (provided the mass splitting exceeds the Z boson mass) becomes of particular interest because they remain unsuppressed in the alignment limit, where many conventional decay channels lose sensitivity. Exclusion limits are shown in Fig. 2.2 in the (m_A, m_H) plane for several fixed values of $\tan \beta$ and under the alignment limit. When $m_A > m_H + m_Z$, the $A \rightarrow ZH$ channel becomes accessible and often dominant. Conversely, $H \rightarrow ZA$ is favored when $m_H > m_A + m_Z$. The branching ratios for these decays are typically large, and the resulting final states such as $A \rightarrow ZH \rightarrow \ell^+ \ell^- b \bar{b}$ or $A \rightarrow ZH \rightarrow \ell^+ \ell^- \tau^+ \tau^-$ provide clean experimental signatures.

²This is true also for the less extreme case in which the mass difference between the two neutral scalars is smaller than the Z boson mass.

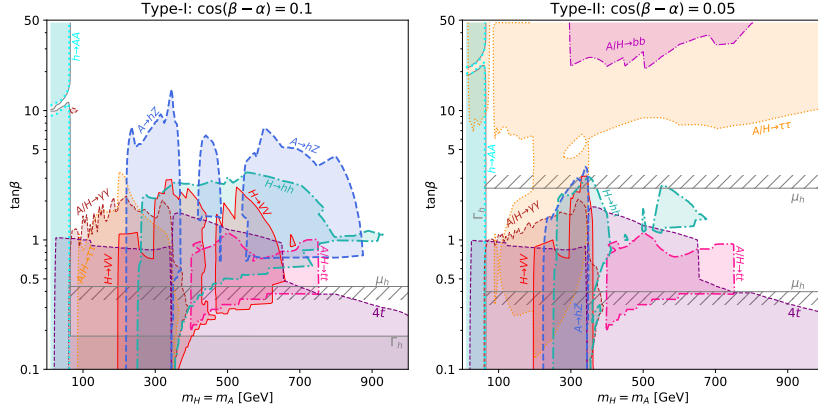


Figure 2.1: Constraints for degenerate heavy Higgs mass spectrum $m_A = m_H = m_{H^\pm}$. 95% C.L. exclusion region in the $m_{A/H}$ vs. t_β plane on the Type-I 2HDM with $c_{\beta-\alpha} = 0.1$ (left) and Type-II 2HDM with $c_{\beta-\alpha} = 0.05$ (right) originating from i) the measurement of the Higgs width Γ_h (grey), ii) the conventional search results on $H/A \rightarrow \tau^+\tau^-$ (dotted orange), $H/A \rightarrow b\bar{b}$ (dot-dashed pink), $H \rightarrow VV$ (red), $H/A \rightarrow \gamma\gamma$ (dashed brown), $H/A \rightarrow t\bar{t}$ (dot-dashed magenta) and $4t$ production (dashed purple), and iii) exotic decay channels $A \rightarrow hZ$ (dashed dark blue), $H \rightarrow hh$ (dot-dashed green) and $h \rightarrow AA$ (dotted cyan). Region enclosed by the grey hatched line are excluded at 95% CL by the current Higgs coupling measurements [68].

For both Type-I and Type-II 2HDMs, the combination of all channels cover the majority of the region in which one of the Higgs masses is below the di-top threshold, $m_A, m_H < 2m_t$. In addition to $A/H \rightarrow ZH/A$, these constraints come from direct searches for the lighter BSM Higgs state which decays into conventional final states $A/H \rightarrow \gamma\gamma$ and $\tau^+\tau^-$. In particular, the gap region for $A/H \rightarrow HZ/AZ$ is mostly covered by these searches. However, these channels become inefficient for Higgs mass above $2m_t$, where $A/H \rightarrow t\bar{t}$ opens up. This region can be probed by the measurements of $t\bar{t}Z$ rate, which effectively constraints the process $A/H \rightarrow ZH/A \rightarrow t\bar{t}Z$. The direct searches recently presented by ATLAS and CMS in the channel $A/H \rightarrow ZH/A \rightarrow \ell^+\ell^-t\bar{t}$ are expected to strongly improve these indirect constraints.

Constraints are analyzed in the $(\tan \beta, m_A)$ plane for fixed m_H (see Fig. 2.3). They come from direct search channels of the BSM Higgs bosons, the Higgs coupling μ_h and Higgs width Γ_h precision measurements, and the $4t$ cross section measurements. While for $m_A \lesssim 300$ GeV, the strongest conventional search constrains are related to the decay of the pseudoscalar A , at large $m_A \gtrsim 300$ GeV constraints mainly come from direct searches for H , whose

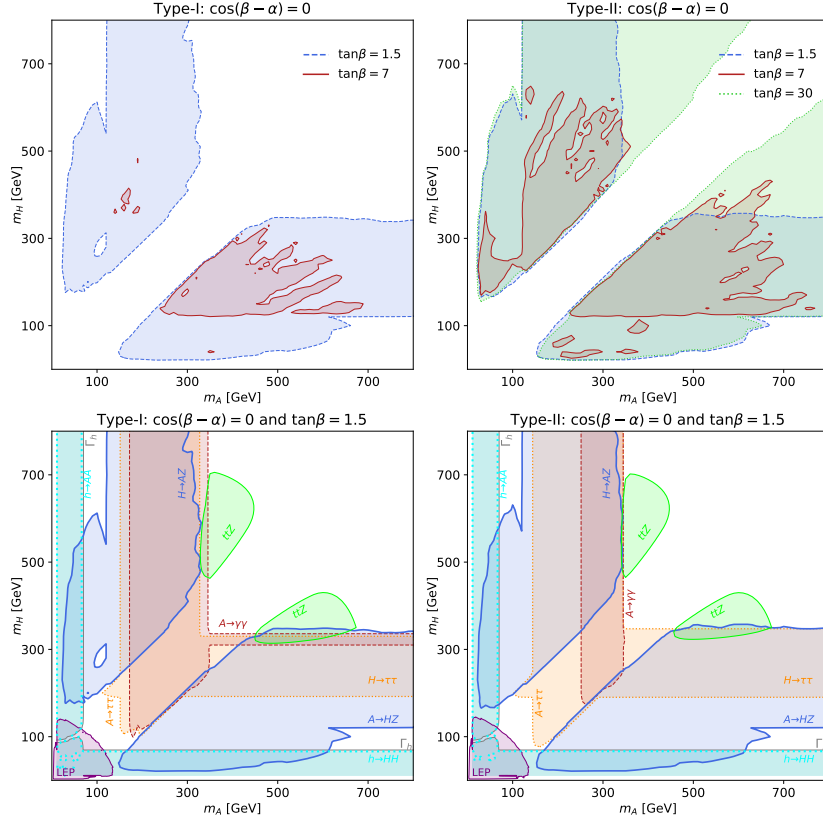


Figure 2.2: Constraints on the Type-I (left panel) and the Type-II (right panel) 2HDM in m_A vs. m_H plane. **Top:** Parameter space excluded at 95% C.L. by the $A/H \rightarrow HZ/AZ$ search in the alignment limit, $c_{\beta-\alpha} = 0$, for $t_\beta = 1.5$ (blue), 7 (red) and 30 (green). **Bottom:** Constraints at 95% C.L. for $c_{\beta-\alpha} = 0$ and $t_\beta = 1.5$ from LHC searches for $A/H \rightarrow H/AZ$ (blue), $A/H \rightarrow \tau^+\tau^-$ (dotted orange), $A/H \rightarrow \gamma\gamma$ (dashed brown), $h \rightarrow AA/HH$ (dotted cyan) and $t\bar{t}Z$ production (green) as well as LEP searches (purple) and the Higgs width measurement $\Gamma_h \in (0.08, 9.16)$ MeV (grey) [68].

mass is fixed to $m_H = 200$ GeV. Therefore, there is no dependence on m_A for the $\tau^+\tau^-$, $\gamma\gamma$ and $4t$ exclusion limits in the large m_A region.

For the Type-I 2HDM with $c_{\beta-\alpha} = 0.1$, the small $m_A < m_h/2$ and the small $t_\beta \lesssim 2 - 3$ are excluded combining all channels, with the $A \rightarrow HZ$ gap of $|m_A - m_H| < m_Z$ region completely covered by the $A/H \rightarrow \tau^+\tau^-$ and $\gamma\gamma$, the $4t$, and the $A \rightarrow hZ$ channels. For the Type-II 2HDM with $c_{\beta-\alpha} = 0.05$, the small $t_\beta \lesssim 1$ region is covered mostly by the $H/A \rightarrow \gamma\gamma$, the $4t$, and the

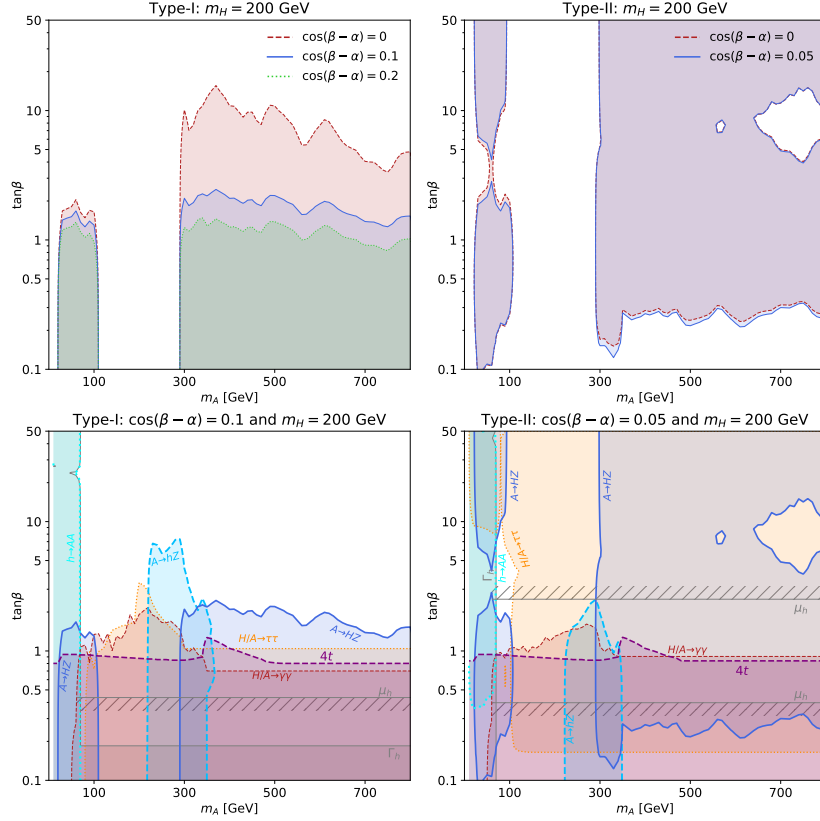


Figure 2.3: Constraints on the Type-I (left panel) and the Type-II (right panel) 2HDM in $m_A - t_\beta$ plane. **Top:** Parameter space excluded at 95% C.L. by the $A/H \rightarrow H/AZ$ search for $m_H = 200$ GeV and $c_{\beta-\alpha} = 0$ (red), 0.1 (blue) and 0.2 (green) in the left panel and $c_{\beta-\alpha} = 0$ (red) and 0.05 (blue) in the right panel. **Bottom:** Constraints at 95% C.L. for $m_H = 200$ GeV and $c_{\beta-\alpha} = 0.1$ from LHC searches for $A \rightarrow HZ$ (blue), $A \rightarrow hZ$ (dashed dark blue), $H \rightarrow AA$ (dashed cyan), $H/A \rightarrow \tau^+\tau^-$ (dotted orange), $H/A \rightarrow \gamma\gamma$ (dashed brown) and $4t$ production (dashed magenta) as well as the global fit of SM-like Higgs couplings strength μ_h (grey hatched region) and the Higgs width measurement $\Gamma_h \notin (0.08, 9.16)$ MeV (grey) [68].

$A \rightarrow HZ$ and hZ channels, while large t_β region is covered by $H/A \rightarrow \tau^+\tau^-$ and $A \rightarrow HZ$.

The study highlights the importance of combining conventional decay modes, exotic BSM-to-BSM decays, and precision Higgs observables. The exotic decay channels, in particular, prove crucial for probing the alignment limit and significantly enhance the overall exclusion reach for neutral scalars in the 2HDM.

2.3 Other BSM theories with an extended Higgs sector

Supersymmetry SUSY is probably the most well-known BSM theory. In supersymmetric models, a superpartner for each SM particle exists, with the spin modified by half a unit but otherwise the same quantum numbers. The superpartners of bosons are fermions and vice versa. The fact that such superpartners with the same mass as the SM particles have not been observed implies that SUSY is a broken symmetry. SUSY models provide explanations for several of the questions the SM is unable to answer. For example, loop corrections to the Higgs mass involving the superpartners cancel those of the SM particles, solving the hierarchy problem (see e.g. Refs. [128, 129]). Furthermore, if the superpartners carry a new quantum number that is conserved, the so-called *R-parity*, the lightest supersymmetric particle is stable, i.e. it cannot decay to any SM particle despite potentially being very massive, and thus poses a viable dark matter candidate (see e.g. Refs. [130, 131]). Finally, SUSY predicts a unification of the electromagnetic, weak and strong forces at high energies, and it is even possible to integrate gravity into some SUSY theories (see e.g. Ref. [132]). The downside of SUSY is that it contains many free parameters, leading to a wide range of models. This complexity makes it difficult to produce precise predictions that can be conclusively tested or excluded. Good overviews of the SUSY formalism in general are given in Refs. [133–135]. The simplest possible SUSY model consistent with the SM is the *Minimal Supersymmetric Standard Model* (MSSM) [136]. The Higgs sector of the MSSM is a Type-II 2HDM, as in SUSY a single Higgs doublet cannot couple to both up- and down-type quarks because the scalar fields are represented by chiral multiplets while their complex conjugates have opposite chirality.

Electroweak singlet A simpler extension of the SM are the *electroweak singlet models*, which include one additional (real or complex) scalar field that transforms as a singlet under the SM symmetry group. Such models present the simplest, minimal BSM solution to the question why there is a matter-antimatter asymmetry and what could be a viable DM candidate [42]. If a real field X is added, the modified, gauge-invariant Higgs potential reads

$$V(\Phi, X) = \mu_1^2 \Phi^\dagger \Phi - \mu_2^2 X^2 + \lambda_1 (\Phi^\dagger \Phi)^2 + \lambda_2 X^4 + \lambda_3 \Phi^\dagger \Phi X^2 \quad (2.20)$$

where the μ_i^2 as well as λ_1 and λ_2 need to be positive and λ_3 needs to satisfy $\lambda_3 > -2\sqrt{\lambda_1\lambda_2}$ for the potential to be bounded from below. The model then predicts two mass eigenstates with mixing angle α in the Higgs sector. If the mass eigenstates are non-degenerate, one could correspond to the SM Higgs and the other to a new neutral Higgs boson—e.g. one of the two targeted in this thesis. The coupling of this additional Higgs to vector bosons is modified by a factor $\sin \alpha$ with respect to the SM couplings in these models. A more in-depth overview of the electroweak singlet models can be found in Refs. [42, 67].

Composite Higgs Whereas in the SM the Higgs boson is an elementary particle, in composite Higgs models it is a bound state of a new strong interaction, i.e. the composite Higgs is not point-like but made of smaller components, held together by this new force. If f denotes the energy scale at which the components of the composite Higgs become relevant - just like e.g. quarks only become "visible" if protons are scattered at high energies - and v the vacuum expectation value of the Higgs field, in such a model the couplings of the Higgs boson to vector bosons are modified by a factor $\sqrt{1 - \frac{v^2}{f^2}}$ with respect to the SM [137]. Heavy Higgs bosons could then occur as higher energy excitations of the composite Higgs, similar to excited hadrons, where several states of different mass exist. The key motivation behind composite Higgs models is that they provide a solution for the hierarchy problem. Recent reviews of composite Higgs models and their compatibility with LHC data can be found in Refs. [137, 138].

2.4 How to find new Higgs bosons?

The BSM analysis presented in this thesis work is a search for two new neutral Higgs bosons, which in the 2HDM interpretation would be the CP-even H and the CP-odd A bosons, assuming that the other neutral CP-even Higgs boson, the h , is the already observed SM Higgs boson. Although generally this search strives to be as model independent as possible—i.e. it looks only for two scalar resonances of a certain mass—some assumptions on the production and decay modes, as well as the mass and width hypothesis, are needed to guide where it is worth to look exactly, and why³. These assumptions can be based on what

³An alternative approach to such theory motivated direct searches for specific signatures are model agnostic searches recently developed in CMS, as in Ref. [139], where anomaly detection machine learning methods can look for a generic deviation from the expected distributions.

we know about the SM Higgs boson or on certain BSM benchmark scenarios (see e.g. Ref. [42]), as outlined in the following.

Production mode The first thing to know when searching for neutral Higgs bosons in CMS data is how it would be likely produced in pp collisions. As seen in Sec. 1.5.1, the dominant production mechanism for the SM Higgs boson at LHC is gluon fusion. The direct search presented here assumes that also additional neutral Higgs bosons would be produced mainly via this mechanism.

Decay channels and width Since the Higgs boson is not a stable particle, it can only be reconstructed through its decay products, as discussed in Sec. 1.5.2. Therefore, identifying the most likely decay channels is essential for any analysis targeting additional Higgs bosons.

Given the structure of the modified Higgs potential (Eq. 2.1), the extended Higgs sector allows for interactions among the Higgs bosons themselves. If there is a significant mass splitting between the scalar states, heavier Higgs bosons can decay into lighter ones. In the search described here, the heavier of the two neutral scalars, A or H , decays into the lighter one accompanied by a Z boson. This decay mode dominates over a wide range of A/H masses in the alignment limit of the 2HDM⁴, as shown in the left panel of Fig. 2.4. Conveniently, the leptons from the Z boson decay provide a clean and efficient trigger for identifying such events.

Turning to the possible decay modes of the lighter neutral Higgs boson, the structure of the Yukawa couplings in the extended Higgs sector (Eq. 2.19) implies that decays to heavier fermions are preferred, similarly to the SM. In the alignment limit, this makes bottom quarks and tau leptons the most likely final states (see right panel of Fig. 2.4). Once the new Higgs mass is sufficiently large, decays into top quark pairs become kinematically allowed and quickly dominate.

This analysis specifically targets the final state involving tau leptons, which offers the dual advantage of a clear experimental signature and sensitivity to low Higgs masses, down to 20 GeV. Complementary analyses focus on final states with bottom or top quarks.

⁴Recall that in the alignment limit, the coupling of H to vector bosons is suppressed (see Eq. 2.13), and the pseudoscalar A does not couple to vector bosons at tree level in the CP-conserving 2HDM.

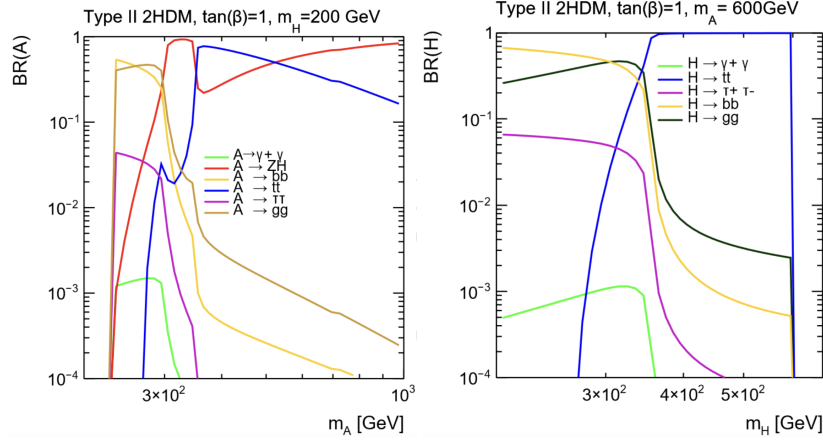


Figure 2.4: (Left) Branching ratio of the A boson as a function of its mass. (Right) Branching ratio of the H boson as a function of its mass. Both plots refer to a Type-II 2HDM where $\tan\beta = 1$ and $m_A > m_H$. Values are computed with 2HDMC-1.8.0 [140].

Another important aspect of Higgs phenomenology is the total decay width of the new Higgs bosons. In many BSM interpretations, the additional Higgs bosons are assumed to have a negligible width relative to their mass—just like the SM Higgs boson. For illustration, Fig. 2.5 presents the relative width of the H boson at three different mass values, within the parameter space of a Type-II 2HDM.

Especially for the lower mass scenario and in particular near the alignment limit of $\cos(\beta - \alpha) \approx 0$ the relative width of the heavy Higgs could be very small, of the order of 0.1% of its mass or even less. Thus, in a large fraction of 2HDM parameter space the narrow width approximation (NWA) can be used. The NWA is a central assumption in the 2HDM interpretation of the CMS search presented here, allowing interference effects to be neglected—as it is only justified within the NWA framework.

Mass range Finally, it should be emphasized that there are no theoretical predictions for the masses of the A and H bosons. The mass ranges explored in the search presented here are therefore determined by practical considerations. The lower bound for the lighter BSM Higgs boson mass is set by the minimum value at which it can be reliably detected through tau leptons in the CMS detector. The upper bound is chosen based on the decision to focus on resolved tau candidates (i.e. a non-boosted topology), and on the expectation that a suf-

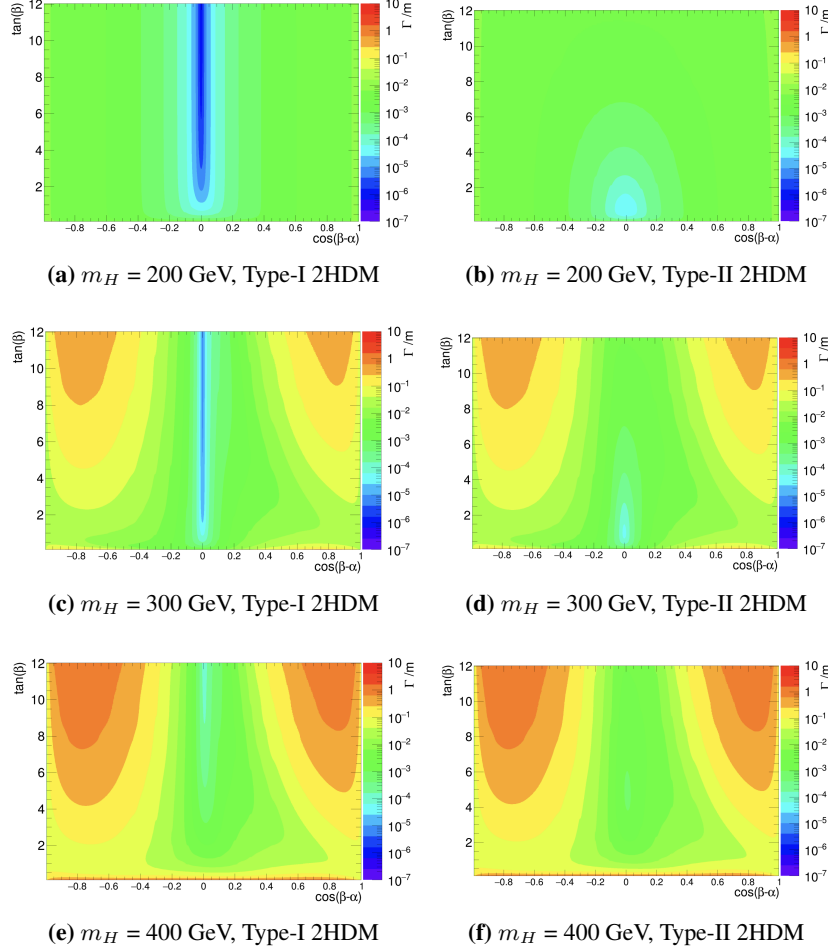


Figure 2.5: Contours of the relative width of the H boson with respect to its mass, Γ/m , as a function of the 2HDM parameters $\cos(\beta - \alpha)$ and $\tan \beta$ for Type-I and Type-II models and three different H boson masses [141].

ficient number of events will occur within this energy range at the LHC. The mass range for the heavier BSM Higgs boson is chosen accordingly, taking into account the requirement $m_{H/A} > m_{A/H} + m_Z$.

In principle, none of the aforementioned assumptions necessarily hold for BSM Higgs bosons, as the underlying new physics may follow a paradigm not yet envisioned by existing theories. Nonetheless, this thesis search aims to identify possible deviations from the SM expectations in the chosen final state, regardless of the specific nature of the new physics responsible for them.

Chapter 3

The LHC and the CMS experiment

3.1 The Large Hadron Collider

The LHC stands as the world's most powerful particle accelerator, engineered to collide protons or lead ions at unprecedented energies. It occupies a 27-kilometer circular tunnel, 100 meters underground, located at CERN in Geneva. This tunnel, initially built between 1983 and 1988 for the Large Electron-Positron Collider (LEP), was later repurposed for the LHC. Construction of the LHC spanned from 1998 to 2008, with the primary goal of verifying the SM by detecting the elusive Higgs boson. The collider also explores the TeV-energy range, searching for New Physics, e.g. in the form of SUSY particles, which were widely considered potential extensions of the SM at the time.

The accelerator is designed to collide proton beams at a center-of-mass energy of $\sqrt{s} = 14$ TeV, reaching an instantaneous luminosity of $1 \times 10^{34} \text{ cm}^{-2}\text{s}^{-1}$. Additionally, it can collide lead ions with an energy of 5.0 TeV per nucleon, reaching peak luminosities of $10^{27} \text{ cm}^{-2}\text{s}^{-1}$. Proton and heavy ion beams are accelerated in bunches, with 40 million bunch crossings occurring per second. These bunches are directed to collide at four key interaction points along the tunnel, where the detector systems of the LHC four major experiments are located, as illustrated in Fig. 3.1.

These experiments are: *ALICE* (A Large Ion Collider Experiment), *ATLAS* (A Toroidal LHC ApparatuS), *CMS* (Compact Muon Solenoid), and *LHCb* (Large Hadron Collider beauty). *ATLAS* and *CMS* are multipurpose detectors, designed to discover the Higgs boson and investigate possible BSM scenarios. *ALICE* focuses on studying quark-gluon plasma created in heavy ion

collisions, while LHCb examines particles produced in the forward region, particularly focused on the study of heavy-flavored mesons.

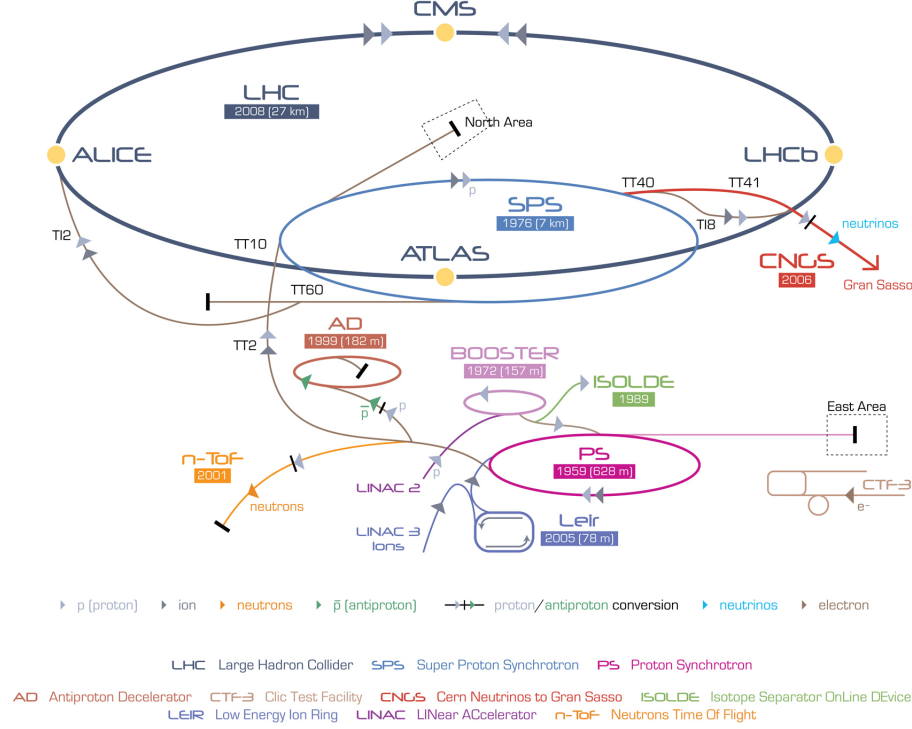


Figure 3.1: Illustration of the CERN accelerator complex (Image: CERN).

Proton beams are generated from hydrogen gas, undergoing several stages of acceleration and focusing. Initially, negative hydrogen ions are produced at 160 MeV by LINAC2 and then passed through the Proton Synchrotron Booster (PSB), where electrons are stripped, leaving only protons. These protons are further accelerated by the Proton Synchrotron (PS) and Super Proton Synchrotron (SPS) to an energy of 450 GeV before being injected into the LHC rings for final acceleration.

Within the LHC, superconducting dipole magnets, operating at an 8.3 T magnetic field, guide the proton beams along their circular path. These magnets are cooled to 1.9 K using superfluid helium. The beams are focused by quadrupole magnets, while eight radiofrequency cavities per beam accelerate them.

A critical parameter in collider experiments is luminosity, which measures the number of particle collisions per unit time relative to the interaction cross section:

$$\mathcal{L} = \frac{1}{\sigma} \frac{dN}{dt}$$

Luminosity depends on various machine parameters, including beam size, bunch content, and revolution frequency. In the LHC, each beam is made of about 2500 bunches, separated by 25 ns intervals, and each proton bunch typically contains around 10^{11} protons.

Left Fig. 3.2 illustrates the LHC's integrated luminosity achievements during Run 1 (2010-2012), Run 2 (2015-2018) and beginning of Run 3 (2022-2024). During Run 1, proton-proton (pp) collisions were first achieved at a center-of-mass energy of 7 TeV in 2011, later increased to 8 TeV in 2012. This period culminated in the discovery of the Higgs boson by the CMS and ATLAS collaborations. Following upgrades, the LHC resumed operations in 2015, reaching 13 TeV collisions until 2018. By the end of Run 2, the LHC exceeded its design luminosity by a factor of two. After further upgrades, pp collisions restarted in 2022 with Run 3, which is currently ongoing and expected to end in 2026.

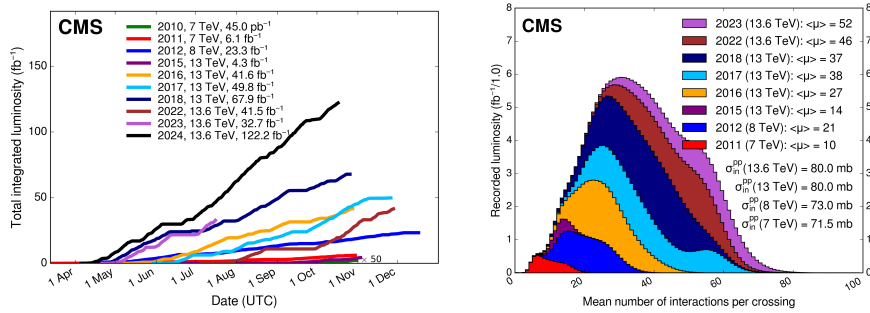


Figure 3.2: (Left) Luminosity delivered to the CMS experiment during stable beams for pp collisions at nominal center-of-mass energy, in 2010-2012 (Run 1), 2015-2018 (Run 2) and 2022-2024 (Run 3) data taking periods, separately for each year [142]. (Right) Distribution of the average number of interactions per crossing (PU) for pp collisions in Run 1, Run 2 and beginning of Run 3. The overall mean values and the minimum-bias¹cross sections are also shown [142].

Given the high beam intensities, multiple pp collisions occur with each bunch crossing, a phenomenon known as *pileup* (PU). In physics analyses, only the highest energy collision is typically considered, with the others classified as pileup events. The LHC was designed with an average PU of 25. Right Fig. 3.2 shows the PU distribution measured by CMS during Run 1, Run 2 and Run 3. It is evident that Run 3 pp collisions are characterized by significantly higher instantaneous luminosity, resulting in a much more intense pileup. Operating at this level of pileup represents an unprecedented challenge for both the detector apparatus, which was originally designed for lower radiation intensity, and the software reconstruction chain.

A significant upgrade, the HL-LHC [143], is planned after the end of Run 3. Figure 3.3 shows the expected plan for this phase, with the current operation of LHC terminating in 2026 and the Run 4 starting around 2030, after approximately 4 years of long shutdown. This upgrade will considerably boost the luminosity delivered to the experiments, increasing of a factor ≈ 3 the peak luminosity and collecting a data equivalent of 3000 fb^{-1} in 10 years of operation (see Fig. 3.4). The enhanced luminosity will increase sensitivity to rare decays, allowing us to probe with higher precision the SM and tackle the most elusive hints of New Physics.

3.2 The Compact Muon Solenoid experiment

The CMS experiment [147] is one of the four major experiments at the LHC. The detector has a cylindrical structure typical of collider experiments, with an approximate length of 30 m and a diameter of 15 m. As its name implies, a key component of the CMS apparatus is a superconducting solenoid with an internal diameter of 6 m, generating a magnetic field of 3.8 T.

Starting from the interaction point and moving outward, the detector consists of a silicon pixel and strip tracker, a lead tungstate crystal electromagnetic calorimeter (ECAL), and a brass and scintillator hadron calorimeter (HCAL), all housed within the solenoid. Having both the calorimeters within the magnetic field is a key feature of the CMS detector system, distinguishing it from

¹Type of data collection that aims to record a broad, unbiased sample of all inelastic collisions, without favoring any specific final state or process.

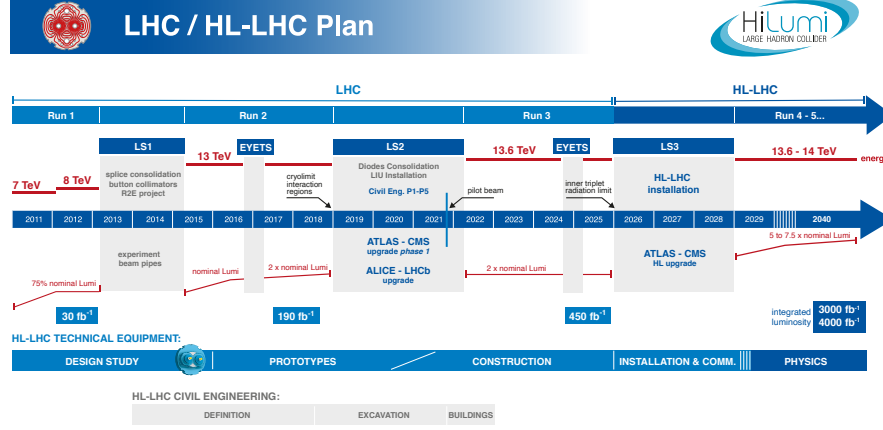


Figure 3.3: Timeline for the LHC and HL-LHC upgrades. The current expected timeline for the start of Run 4 is now 2030 (updated on September 2024 by CERN Council) [144].

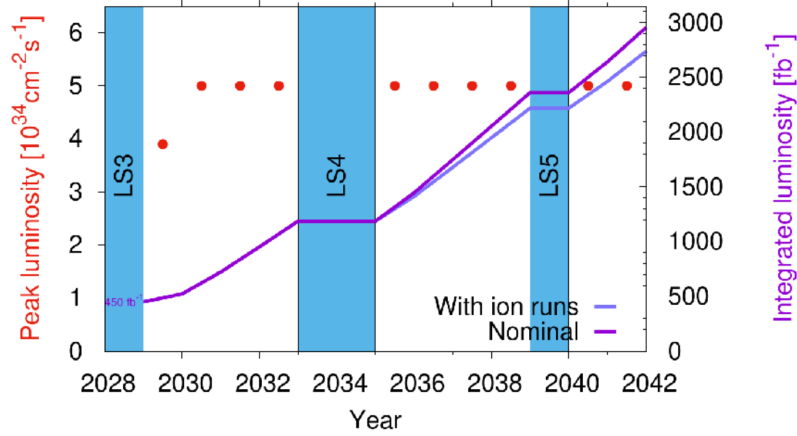


Figure 3.4: Expected peak and integrated luminosity during HL-LHC. The figure shows when the long operation shutdowns are expected [145].

the ATLAS system, which has the hadronic calorimeter outside the magnetic field.

Outside the solenoid, the muon reconstruction system is composed of gaseous detectors embedded in the steel flux-return yoke, which is essential for guiding the magnetic field lines. Figure 3.5 illustrates the structure of the CMS detector.

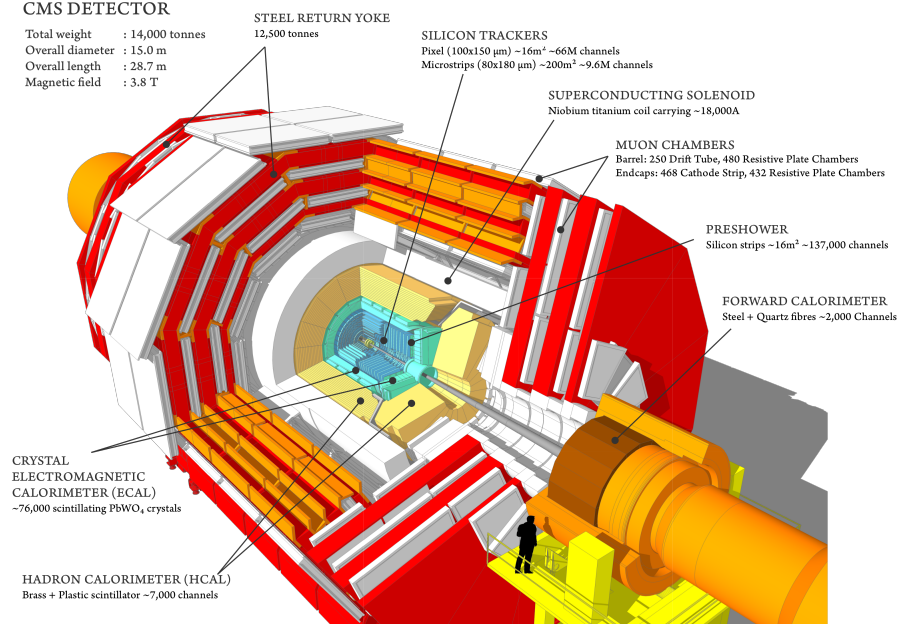


Figure 3.5: Layout of the CMS detector [146].

3.2.1 Coordinate system and kinematics of pp collisions

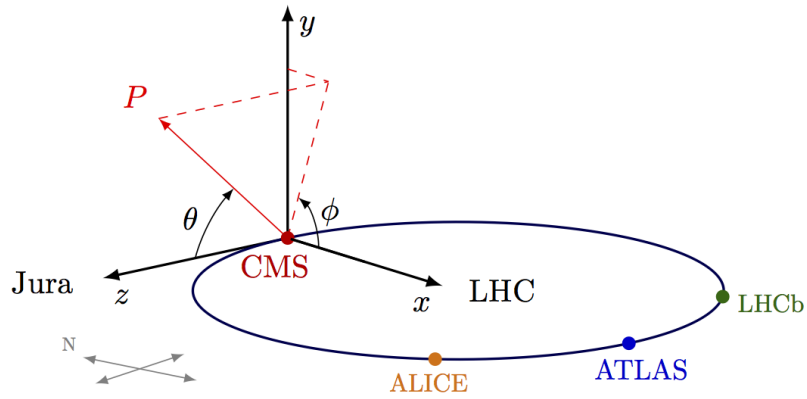


Figure 3.6: CMS coordinate system [148].

The CMS detector is symmetrically structured around the proton beam line, with the collision point at its center. Consequently, the coordinate system used is as depicted in Fig. 3.6, where the z -axis aligns with the beam line, and collisions occur at $z = 0$. In this system, the x - y plane is transverse to the

beam, with the y-axis pointing upwards towards the surface and the x-axis pointing towards the LHC ring's center (right-handed coordinate system).

Spherical coordinates provide a convenient solution for describing the positions of outgoing particles, given the symmetrical design of the apparatus. The radial coordinate r is the distance from the z-axis on the x-y plane, the azimuthal angle ϕ is measured in this plane starting from the x-axis, and the polar angle θ is measured relative to the z-axis.

The three-momenta of the particles are often described using two components, the longitudinal momentum p_z and the transverse momentum p_T , defined as:

$$|\vec{p}_T| = |p| \sin \theta = \sqrt{p_x^2 + p_y^2}. \quad (3.1)$$

Similarly, the transverse energy is defined as $|\vec{E}_T| = |\vec{E}| \sin \theta$. The transverse components of momentum and energy are convenient for describing the kinematics of pp collisions, as they are Lorentz-invariant quantities. Moreover, the transverse plane is where the missing energy (carried away, for example, by neutrinos) can be inferred, whereas in the longitudinal direction the initial energy of the colliding proton constituents is unknown.

A commonly used spatial coordinate to describe a particle's angle relative to the z-axis is the pseudorapidity η , defined as:

$$\eta \equiv -\ln \left[\tan \frac{\theta}{2} \right] = \operatorname{arctanh} \left(\frac{p_z}{|p|} \right) \quad (3.2)$$

where θ is the polar angle. As θ approaches zero, η tends towards infinity. Particles produced at high η are referred to as being produced in the *forward* direction. In the limit of relativistic particles, pseudorapidity converges to the definition of rapidity, y :

$$y \equiv \frac{1}{2} \ln \left(\frac{E + p_z}{E - p_z} \right) \quad (3.3)$$

and differences in pseudorapidity are Lorentz invariant under boosts along the z-axis. The angular separation between particles is often measured using:

$$\Delta R \equiv \sqrt{(\Delta \eta)^2 + (\Delta \phi)^2} \quad (3.4)$$

which is also Lorentz invariant under boosts along the z-axis in the relativistic limit.

3.2.2 Magnet

The superconducting solenoid of the CMS apparatus provides a uniform magnetic field in the axial direction which is essential to bend charged particles and thus determine the particles charge/mass ratio from the track curvature.

The magnet is made of refrigerated superconducting niobium-titanium coils, for a total length of 13 m and a diameter of 6 m. It was originally designed to generate a magnetic field of 4 T, but it was then operated at 3.8 T in order to ensure better longevity [149]. The tracker and the calorimeter detectors are housed within the solenoid, which is surrounded by the return yoke, a 12-sided iron structure that contains and guides the field lines. This return yoke extends up to 14 m of diameter and is composed of three layers. The muon detectors are embedded in the return yoke, interleaved with its layers.

Charged particle trajectories are bent by the magnetic field and the curvature is exploited to determine the electric charge sign and the transverse momentum. In particular, the best momentum resolution σ_{p_T}/p_T achievable for a solenoidal magnetic field, is given by:

$$\frac{\sigma_{p_T}}{p_T} = S \times \frac{8 p_T}{0.3 \cdot B \cdot R^2} \quad (3.5)$$

where B is the magnetic field intensity in Tesla, S is the sagitta of the particle trajectory and R is the solenoid radius, both measured in meters. In order to maximize the p_T resolution, it is necessary to have large magnetic field intensities along with large sized magnets.

In case of the CMS experiment, the presence of the return yokes allows to establish a strong magnetic field, provided by the large solenoid magnet, while keeping the overall size of the apparatus limited and compact, as the name indicates. Figure 3.7 shows the magnetic field distribution within the CMS apparatus: the nominal intensity of 3.8 T is established in the volume of the inner tracker and calorimeters, while it is reduced to 1.5 - 2 T in the volume defined by the return yoke.

3.2.3 Silicon Tracker

The tracker detector of the CMS experiment is optimized to reconstruct with great precision the trajectories of charged particle within the 3.8 T magnetic field provided by the solenoid. Being the innermost detector of the apparatus,

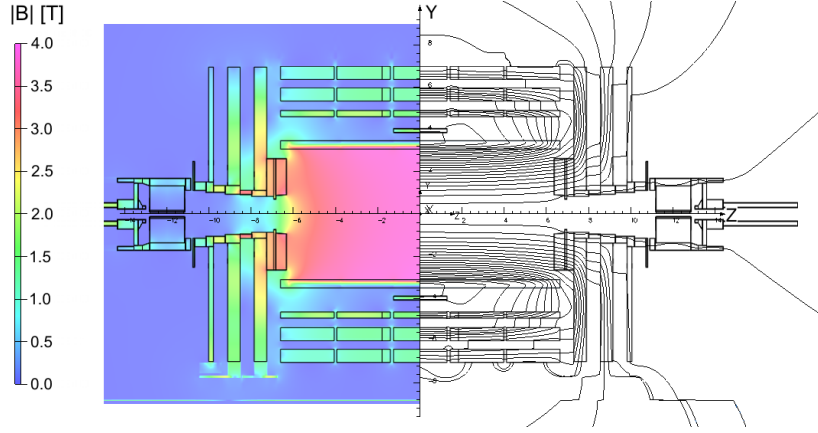


Figure 3.7: Illustration of the longitudinal section of the CMS detector displaying the distribution of the magnetic field intensity (left) and lines (right) [149].

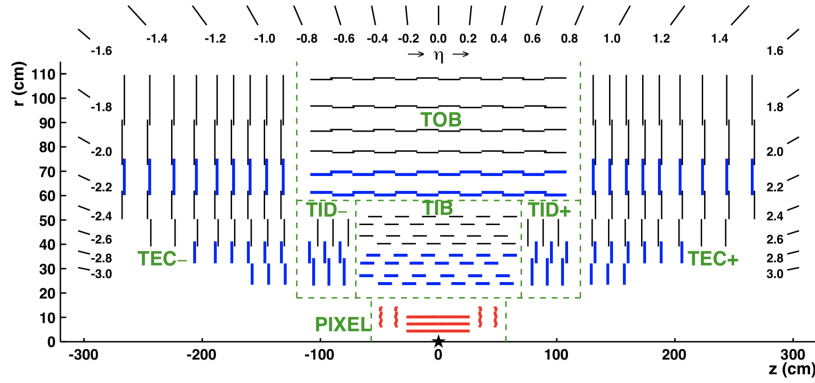


Figure 3.8: Schematic cross section of the CMS tracker in the r - z plane. Due to the tracker symmetry around $r = 0$, only the top half is displayed [150].

it is positioned closest to the interaction point. The tracker has a cylindrical structure, measuring 5.8 m in length and 2.5 m in diameter. It employs silicon detector technology, chosen for its high radiation hardness, fine granularity and large hit redundancy, which are crucial to perform a good pattern recognition. The CMS tracker structure is optimized to be as lightweight as possible, ensuring that it minimally alters the trajectory of the particles crossing it. A sketch of the tracker in the $r - z$ plane is displayed in Fig. 3.8.

The innermost part of the tracker consists of layers of silicon pixel detectors. In the original design, the pixel detectors covers the pseudorapidity range of $|\eta| < 2.5$. The cylindrical part, called Tracker Pixel Barrel (TPB). is composed of three layers, which have diameters ranging from 8.8 cm to 20.4 cm.

In addition, two disks, called Tracker Pixel Endcap (TPE), are located at each end of the TPB. The pixel detector provides a very good resolution on the impact parameter, which is crucial for the reconstruction of secondary vertices, such as those created by the decay of heavy-flavor hadrons.

Each pixel cells has a size of $100 \times 150 \mu\text{m}^2$, offering high granularity. This design provides spatial resolutions of $10 \mu\text{m}$ in the $r - \phi$ plane (perpendicular to the beam axis) and $20 \mu\text{m}$ along the z-axis (parallel to beamline).

The original CMS pixel tracker was upgraded for Run 2 in order to handle the increased luminosity and center-of-mass energy of the LHC, as well as the higher PU environment. During the extended year-end technical stop of the LHC in 2016/2017 the original CMS pixel detector has been therefore replaced with the CMS *Phase-I* pixel detector. As shown in Fig. 3.9, the Phase-I detector layout has several improvements over the original design.

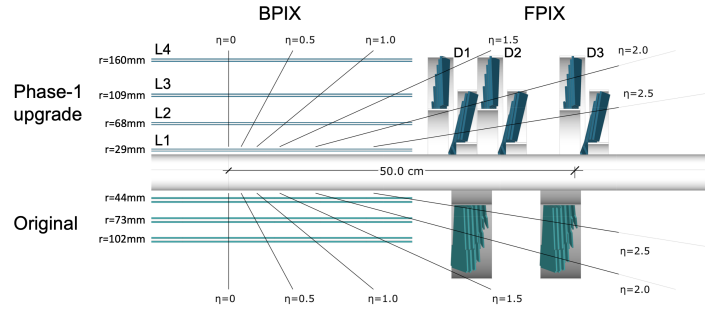


Figure 3.9: Layout of the CMS Phase-I pixel detector compared to the original detector layout, in longitudinal view [151].

The CMS Phase-I pixel detector consists of 4 barrel layers (instead of three from the original design) and 3 endcap disks on each side (instead of two). These additional layers and disks extend the hit coverage in regions of high pseudorapidity. The Phase-I pixel upgrade also introduced a digital readout chip capable of handling higher rates and a new cooling system, necessary to maintain the detector's performance at high luminosities.

The outermost part of the CMS silicon tracker is composed of silicon microstrip detectors, which are structured with different geometries, each optimized for a different region of the detector volume. The barrel is organized in two parts [150]:

- the Tracker Inner Barrel (TIB) consists of 4 layers and is characterized by a single-hit resolution of $13\text{--}38 \mu\text{m}$ in the $r - \phi$ direction.

- the Tracker Outer Barrel (TOB) consists of 6 layers and ensures a resolution of 18-47 μm in the $r - \phi$ direction and 47 μm in the longitudinal direction, similar to the TIB.

The endcap disks are equipped with concentric rings of silicon strip modules: the Tracker Inner Disks (TID) comprise three disks, while the Tracker Endcaps (TEC) comprise nine disks. The TID and TEC disks are characterized by the same spatial resolution as the TIB and TOB layers, respectively.

3.2.4 Calorimeter

The CMS calorimeter system is a hermetic detector with the goal of measuring the energy of outgoing particles in collision, crucial for reconstructing the total energy of an event and for estimating the missing energy associated with undetected particles like neutrinos.

The energy measurement is based on detecting the energy loss of particles passing through the calorimeter material, where they produce cascades of secondary particles referred to as showers. The showers initiated by particles that interact only electromagnetically, such as electrons and photons, are called *electromagnetic showers*; the ones produced by hadrons that interact via the strong force are called *hadronic showers*. The CMS calorimeter comprises two subsystems optimized to contain and detect the two types of showers: the electromagnetic (HCAL) and the hadronic (HCAL) calorimeters.

Electromagnetic Calorimeter

The CMS ECAL is designed to detect photons and electrons with good energy resolution. The barrel and the endcap are equipped with 75848 lead tungstate (PbWO_4) crystals and cover a large range of pseudorapidity up to $|\eta| < 3$ [152]. Figure 3.10 displays a layout of the ECAL barrel, endcap and preshower subsystems:

- The ECAL Barrel (EB) is made of 61200 crystals which are 23 cm long and have a frontal surface of $\sim 2.2 \times 2.2 \text{ cm}^2$. They are arranged in modules and provide a coverage of $\Delta\phi \times \Delta\eta = 0.0175 \times 0.0175$.
- The two ECAL Endcaps (EE) are composed by 7324 crystals each and cover the pseudorapidity range $1.48 < |\eta| < 3.0$. The single EE crystals are characterized by a $\Delta\phi \times \Delta\eta$ that ranges from 0.0175×0.0175 to 0.05×0.05 .

- Two pre-shower detector (ES), consisting of two lead radiators and two planes of silicon strip detectors, are positioned in front of the two EE subsystems, respectively. The ES covers the pseudorapidity range $1.65 < |\eta| < 2.6$. It is aimed to identify two close-by photons from neutral pion decay, allowing for $\pi^0 - \gamma$ separation, and to improve the estimation of the direction of photons.

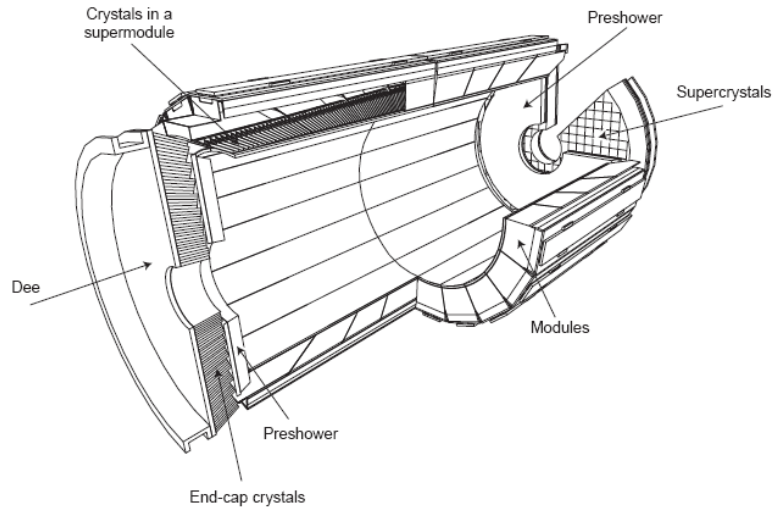


Figure 3.10: Layout of the the CMS ECAL, showing the crystal barrel and endcap detectors, as well as the silicon pre-shower detector [153].

When an electron enters the calorimeter material, it emits photons via the process of bremsstrahlung. These photons, if energetic enough, can in turn produce electron-positron pairs. The resulting secondary electrons and positrons then repeat the process. In this way, an electromagnetic shower develops and continues until the photon energies fall below the threshold for further pair production, which is roughly twice the electron rest mass. To effectively measure the energy of a primary electron or photon, the calorimeter must be large enough to contain most of the electromagnetic shower. The size of this shower depends on two parameters related to the calorimeter material: the radiation length X_0 and the *Molière radius*. The radiation length X_0 describes the longitudinal extension of the shower and is the mean distance over which a high-energy electron loses all but $1/e$ of its energy by bremsstrahlung. In practical terms, usually $25\text{--}30 X_0$ are needed to contain the shower. The radial spread of

the shower is instead described by the Molière radius, defined as the radius of an ideal cone that would contain the 90% of the energy released by the shower. The PbWO_4 crystals are characterized by a short radiation length (0.89 cm) and a small Molière radius (2.19 cm), ensuring a good shower containment within a limited volume.

The PbWO_4 crystals are scintillators, characterized by a scintillation decay time comparable with the 25 ns time interval between two consecutive bunch crossings and an emission peak at 425 nm. Each crystal is equipped with two avalanche photomultipliers (PMT) in the barrel and a single vacuum phototriode in the endcap, for scintillation light detection.

In general the energy resolution of an electromagnetic shower is parametrized as a function of the incident electron/photon energy, E , expressed in GeV:

$$\frac{\sigma_E}{E} = \frac{a}{\sqrt{E}} + \frac{b}{E} + c \quad (3.6)$$

where a , the stochastic term, depends on event to event fluctuations in lateral shower containment, photo-statistics and photodetector gain; b , the noise term, depends on the electronic noise and event pile-up; and c , the constant, depends on non-uniformity of the longitudinal light collection, leakage of energy from the rear face of the crystal and the accuracy of the detector inter-calibration constants. The ECAL barrel energy resolution was measured for electrons obtaining the following values: $a = 2.8\% \text{ GeV}^{1/2}$, $b = 12\% \text{ GeV}$ and $c = 0.3\%$ [153].

Hadron Calorimeter

The CMS HCAL [154] is a sampling calorimeter which utilizes alternating layers of brass (the absorber) and plastic scintillator (the active material). It is composed of a barrel (HB) and two endcap (HE) subsystems, as schematized in Fig. 3.11. As visible, a minor part of the HCAL, HCAL Outer (HO), is placed outside the magnet solenoid: in this way, the magnet itself and the return yoke serve as absorbers, enhancing the detection of high energy hadrons. A forward calorimeter (HF), instead, increases the geometrical acceptance in the range of pseudorapidity $2.9 < |\eta| < 5$.

Hadronic showers are in general much more complex than electromagnetic showers. When a hadron with an energy above around 5 GeV interacts with the calorimeter material, both inelastic and elastic scattering processes occur between the incoming particle and the nucleons in the atomic nuclei of the ma-

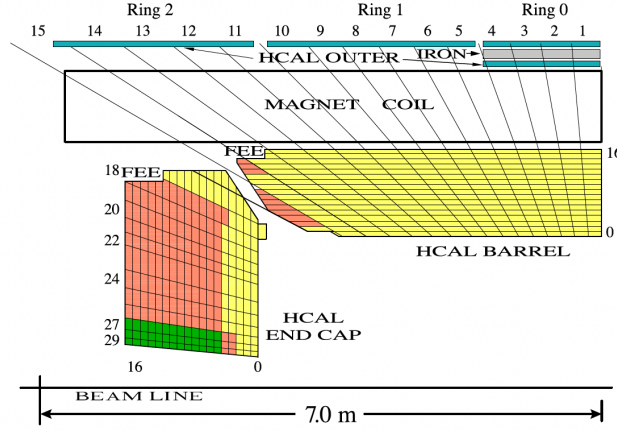


Figure 3.11: A quarter slice of the CMS HCAL detectors. The right end of the beam line is the interaction point. FEE denotes the location of the Front End Electronics for the barrel and the endcap [155].

terial. The high-momentum transfer in these interactions leads to the production of a large number of secondary hadrons, which in turn continue to interact, creating a cascade of further interactions and energy loss. The hadronic shower gradually ceases as the energy of the secondary hadrons decreases, eventually stopping through ionization energy loss or nuclear absorption. Neutral pions produced in the cascade, decay in two photons, which initiate electromagnetic showers. For this reason, a hadronic shower usually contains an electromagnetic component, which accounts for the 20-30% of its total energy.

In hadronic cascades, the lateral spread of the shower is primarily determined by large transverse momentum transfers in nuclear interactions, as opposed to the multiple scattering of charged particles that drives the lateral development of electromagnetic showers. This distinction leads to hadronic showers generally being broader and more complex in structure than electromagnetic ones.

The longitudinal extension of a hadronic shower can be described in terms of the *interaction length*, that is defined as the mean distance a hadron travels in a material before undergoing an inelastic interaction with a nucleus. The interaction length depends on the atomic number (A) of the detector material and is typically much larger than the electromagnetic interaction length. Because of that, hadronic showers penetrate much deeper into the calorimeter than electromagnetic showers. To effectively confine hadronic showers, dense, high- A materials are typically used in hadronic calorimeters. In the case of the CMS HCAL, brass is chosen as the absorber material, since it has a short

interaction length (~ 15 cm) and is non-magnetic. The energy is measured by plastic scintillators equipped with wavelength shifting fibres and photodiodes.

The HB is structured as 36 identical azimuthal wedges, each made up of brass absorber plates that are positioned parallel to the beam axis, interleaved with plastic scintillators segmented in both ϕ and η directions with a granularity of $\Delta\phi \times \Delta\eta = 0.087 \times 0.087$.

The HO complements the HB in the central region: their combination offers nearly 11 hadronic interaction lengths in total.

The HE, which covers the forward region, is similarly structured with 79-mm-thick brass plates. These plates are separated by 9-mm gaps that accommodate scintillators, and the HE granularity is $\Delta\phi \times \Delta\eta = 0.17 \times 0.17$.

Finally, the Hadronic Forward (HF) calorimeter extends the pseudorapidity coverage up to $|\eta| < 5$. It is constructed using steel and quartz fibers aligned parallel to the beam. Charged particles produce Cherenkov light in the quartz fibers, which is then collected by PMT tubes. The HF detector is housed within a radiation shielding which consists of layers of 40 cm thick steel, 40 cm of concrete, and 5 cm of polyethylene for neutron shielding.

The signals from photodiodes or PMTs are processed by being integrated and digitized through a custom-designed chip, which is located directly on the detector.

The hadronic energy resolution follows a similar parametrization to that used for the electromagnetic calorimeter:

$$\frac{\sigma_E}{E} = \frac{a}{\sqrt{E}} + c \quad (3.7)$$

where E is in GeV, a is a stochastic term and c is the constant term, which becomes dominant at high energies. For the barrel and the endcap region the resolution parameters are found to be $a = 90\% \text{ GeV}^{1/2}$ and $c = 4.5\%$, while for the HF $a = 172\% \text{ GeV}^{1/2}$ and $c = 9\%$ [155].

3.2.5 Muon System

Because muons can penetrate several metres of material losing little energy (mainly through ionization processes) unlike most particles, they are not stopped by any of the CMS calorimeters. Therefore, chambers to detect muons are placed in the outer part of the experiment where they are the only particles likely to produce a clear signal.

The muon system is housed within the three layers of the return yoke and relies on gaseous detectors of four different technology: Drift Tubes (DT),

Cathode Strip Chambers (CSC), Resistive Plate Chambers (RPC) and Gaseous Electron Multipliers (GEM). In the layout of Fig. 3.12, which displays the transverse section of a CMS quadrant, the configuration of the muon chambers is shown, with different colors for the different technologies employed.

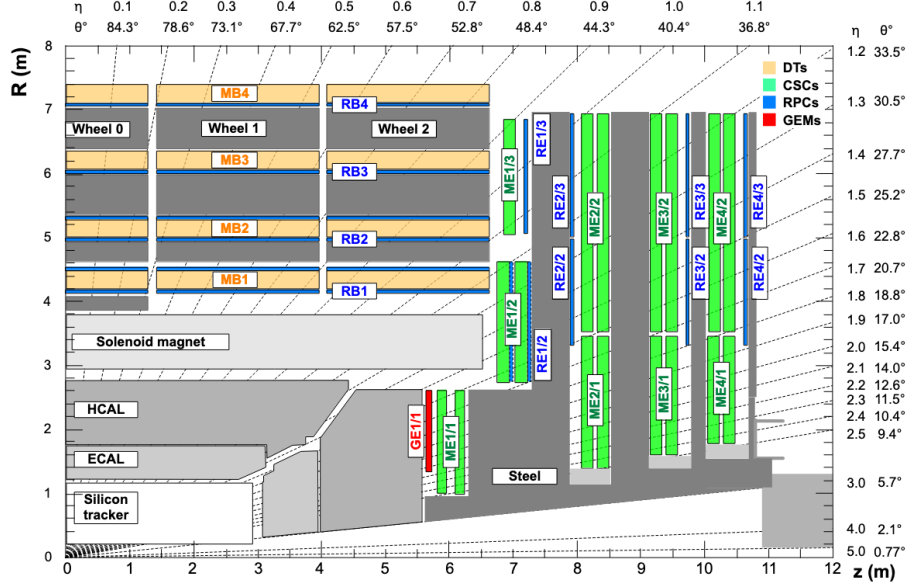


Figure 3.12: One quadrant of the CMS detector in its Run 3 configuration, with the Muon detectors in different colours [156].

The barrel system extends up to $|\eta| < 1.2$ and the endcap up to $|\eta| < 2.4$, which corresponds to the geometrical acceptance of the muon system.

In the muon chambers, each hit position is recorded, and the full muon track is reconstructed by combining hits from multiple detector layers. The return yokes provide a magnetic field of ~ 2 T, enabling precise momentum measurement in a compact setup. For this reason, the combined set of muon chambers is often referred to as the Muon Spectrometer.

However, in addition to muons, also other particles can reach the muon system, such as punch-through hadrons from the inner detectors and neutrons from particle showers or gaps in the HCAL's forward shielding. Neutron exposure, in particular, can be a risk to the gaseous detector's durability. Moreover, low energy neutrons can activate surrounding materials, leading to radiative de-excitations of the nuclei and photon emissions that generate background signals.

Drift Tubes

[illegible]

The 250 DT chambers are arranged across five wheels, covering a pseudorapidity range of up to $|\eta| < 2.1$. Figure 3.13 illustrates the configuration of one of these barrel wheels. The fundamental element of the DT system

is depicted in left Fig. 3.14. It is essentially a rectangular drift cell bounded by cathode aluminum strips on the sides and aluminum plates on the top and bottom, with an anode wire centered along the cell's symmetry axis. The cell is filled with an $\text{Ar-CO}_2(85\% - 15\%)$ gas mixture, which ionizes as charged particles pass through, generating electron-ion pairs that then drift toward the electrodes. The cathode electrodes are designed to shape the electric field within the cell, ensuring a uniform drift velocity across its width. This enables accurate conversion of drift time into distance. The maximum drift distance is ~ 21 mm, which translates in a maximum drift time of about 380 ns in $\text{Ar-CO}_2(85\% - 15\%)$ gas mixture, resulting in a single-wire resolution of approximately $200 \mu\text{m}$.

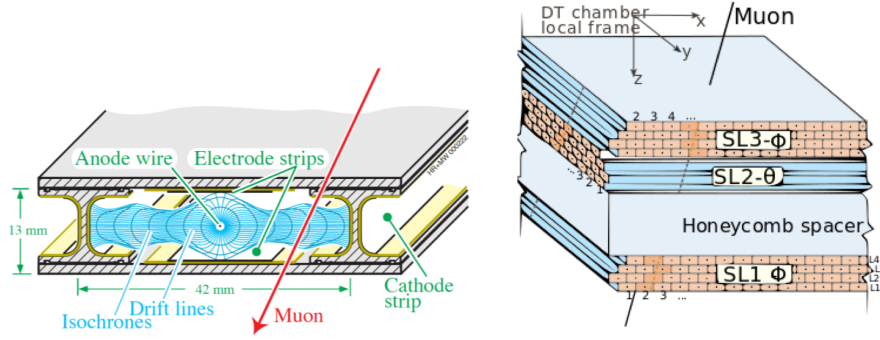


Figure 3.14: (Left) Section of a drift cell of a Drift Tube detector, showing the anode wire and the cathode strips, as well as the drift lines and the isochrones. (Right) Structure of a DT Chamber with three *superlayers* composed of 4 layers each [157].

Each DT chamber is composed of 2 or 3 superlayers, with each superlayer consisting of 4 layers of DT cells that are staggered by half a cell width, as illustrated in right Fig. 3.14. The superlayers are configured with wires oriented either parallel or transverse to the beam line, allowing for precise measurements of the muon position in both the $r - \phi$ plane and along the z -axis. The spatial resolution achieved in each DT chamber, by combining all layer measurements, is approximately $80\text{-}120 \mu\text{m}$ in the $r - \phi$ plane and $130\text{-}390 \mu\text{m}$ along the $r - z$ plane [157]. The design specifications for the DT subdetector set a time resolution requirement of 5 ns. However, tests have shown that the chambers and their associated electronics surpass this target, achieving a time resolution of under 3 ns for high- p_T muons [157].

Cathode Strip Chambers

The Cathode Strip Chambers (CSC) are installed on four disks (stations) within each endcap section, between the iron disks of the return yoke, which also function as shielding. The choice of CSC technology for the endcap, as opposed to DTs, is driven by the higher muon rates and the intense and inhomogeneous magnetic field in that region. The muon chambers in the endcap feature a trapezoidal design and are arranged to ensure complete coverage in the $r - \phi$ plane. The CSC is a type of multi-wire proportional chamber where the cathode plane is divided into strips that run perpendicular to the direction of the wires. When an ionizing particle crosses the gas volume, it generated electron-ion pairs. The electrons then drift toward the anode wires and, thanks to the strong electric field established within the chamber, they further ionize the gas, leading to an avalanche effect. This avalanche induces a distributed charge on the cathode plane, which is segmented into strips. By using the charge barycenter, the position of the particle track along the wire can be accurately reconstructed, as illustrated in Fig. 3.15.

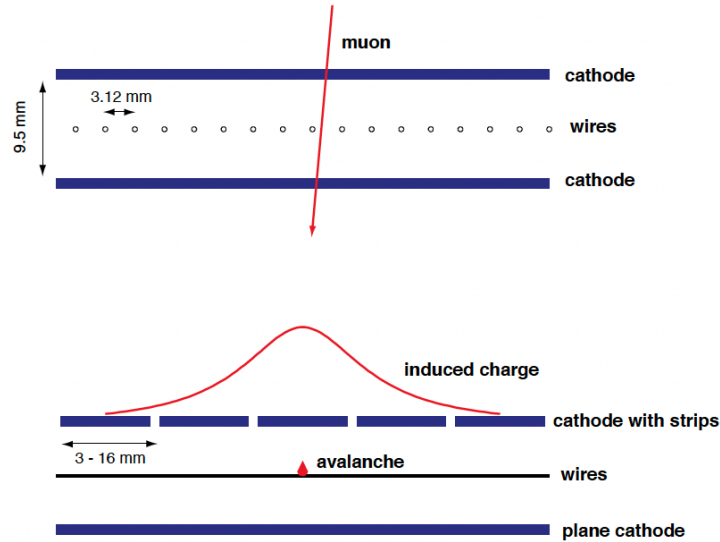


Figure 3.15: Principle of coordinate measurement with a cathode strip chamber. Top: cross section across wires. Bottom: across cathode strips. Close wire spacing allows for fast chamber response, while a track coordinate along the wires can be measured by interpolating the signals induced on the strips [158].

Each CSC trapezoidal chamber is constructed from six wire planes, with the cathode strips arranged radially to facilitate the measurement of the $r - \phi$ coordinates. Each plane consists of 80 cathode strips, with a pitch that varies between 2.2 and 4.7 mrad in the ϕ direction. The orthogonal anode wires are spaced from 2.5 to 3.16 mm apart. These chambers are filled with a gas mixture of CO₂, Argon and CF₄ in the proportion of 40%-50%-10%.

In each endcap muon station (ME1-ME4 in Fig. 3.12), two rings of chambers are installed, with the first station (ME1) containing three rings. Each ring is composed of either 18 or 36 trapezoidal chambers.

The spatial resolution achieved by the CSC subsystem varies from approximately 70 μm in the ME1/1 chamber to about 210 μm in the ME4/1 chamber, while the time resolution is around 3 ns [157].

Resistive Plate Chambers (RPC)

The RPCs are installed in both the barrel and endcap CMS sections, and they complement the DTs and CSCs with a very fast response time, crucial for trigger purposes. The RPC is a type of gaseous detector with planar geometry, composed of two bakelite planes coated with a thin film of graphite, a positively-charged anode and a negatively-charged cathode, separated by a 2 mm wide gas gap (a mixture of freon, isobutane, sulphur hexafluoride and water vapor). Each CMS RPC chamber is composed of two such gas gaps facing a shared layer of readout strips, as illustrated in Fig. 3.16. A high voltage of approximately 9.6 kV is applied on the outer graphite coated surfaces of the bakelite plates. When a charged particle crosses the gas volume, it initiates an ionization cascade, resulting in an avalanche that induces a signal on the readout strips.

In the barrel, RPCs chambers follow the same segmentation as the DT superlayers, as shown in Figs. 3.12, 3.13. Six layers of them are embedded within the barrel iron yoke: four of these layers situated in the inner and outer sides of the first two stations of the DT chambers, while the other two are located on the inner side of the third and fourth stations of the DTs. Each barrel RPC chamber is equipped with 96 readout strips running parallel to the beam line, with pitch ranging from 2.1 cm (in RB1) to 4.1 cm (in RB4).

In the endcap, the RPCs are organized across four stations, similarly to the CSCs. The chambers have a trapezoidal shape and are equipped with readout strips arranged radially characterized by a length spanning from 25 cm in the most forward RE1 chamber to 80 cm in the RE4 chamber and a strip pitch

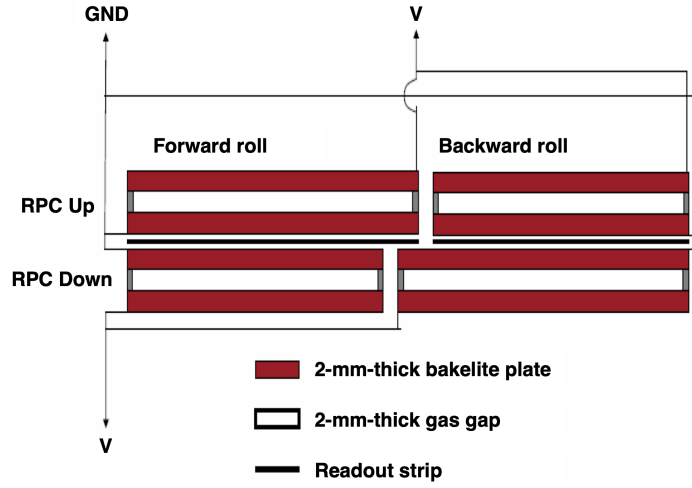


Figure 3.16: Schematic view of a RPC [157].

ranging The strip pitch also ranges from 0.7 up to 3 cm. The RPC performance benefits from a spatial resolution of approximately 1 cm and a time resolution around 2 ns.

3.2.6 Gaseous Electron Multiplier (GEM)

During the future high-luminosity phase of the LHC, the muon hit rate in the forward region is expected to reach a value of 5 kHz/cm² in the first muon layer. Such a high rate necessitates, in the forward region, of a detector resistant to radiation, with high rate capability and capable of minimize the number of misidentified tracks in order to keep the trigger rate under control [159].

Therefore, in order to enhance track reconstruction and trigger capabilities of the endcap muon system, large-area triple layer GEM detectors were installed in the CMS endcap before the start of Run 3. This single station, called GE1/1, covers a pseudorapidity range $1.55 < |\eta| < 2.18$ and is the first of three endcap rings that are foreseen for the HL-LHC upgrade. A sketch of the GE1/1 station is displayed in Fig. 3.17.

Each GE1/1 endcap ring contains two layers of 36 triple GEM chambers positioned just in front of the first CSC station, ME1/1, with each chamber spanning a 10 sector in azimuth. The chambers are manufactured in two different sizes: the odd-numbered chambers in GE1/1 are slightly longer to optimize pseudorapidity coverage while fitting within the spatial limitations set by

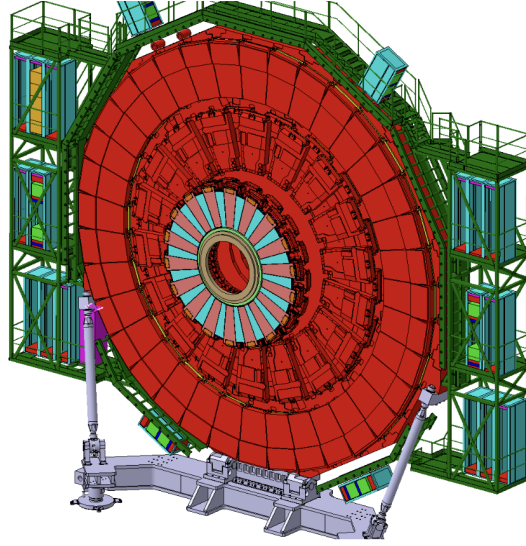


Figure 3.17: Sketch of GE1/1 system of one endcap [159].

the support structure, as illustrated in 3.18. The GE1/1 subsystem is located between 566 and 574 cm in z and spans a radial range of 145 to 230 cm.

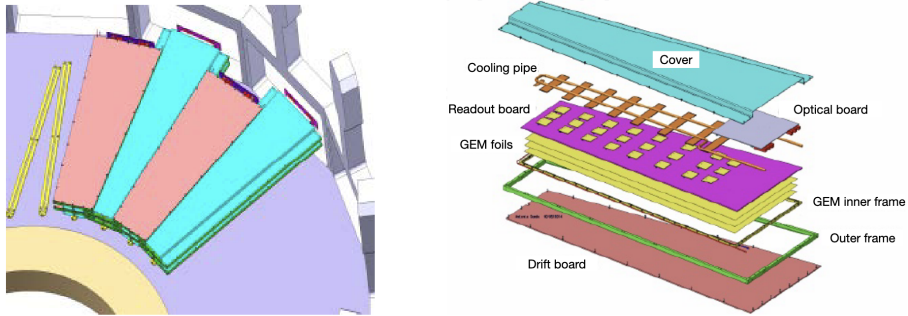


Figure 3.18: (Left) Layout of the GE1/1 chambers along the endcap ring, indicating how the short and long chambers fit in the existing volume. (Right) Blowup of the trapezoidal detector, GEM foils, and readout planes, indicating the geometry and main elements of the GEM detectors [160] [159].

The CMS triple GEM detector, a micro-pattern gas detector, consists of four gas layers separated by three GEM foils. At the base of this GEM assembly is a printed circuit board that holds the drift electrode. The top layer, the readout board, has radially oriented strips along the chamber's long side, with strip

pitch ranging from 0.6 to 1.2 mm. The readout board is segmented into up to $8 \times 3 \eta - \phi$ partitions, each equipped with 128 strips.

The basic unit of a GEM detector is the GEM foil, a thin polyimide sheet coated on both sides with copper and etched with a uniform array of fine holes. The polyimide layer is typically $50 \mu\text{m}$ thick, with a $5 \mu\text{m}$ copper coating on each side. The hexagonal hole pattern has a pitch of about $140 \mu\text{m}$, with holes generally taking on a biconical shape—inner diameters around $50 \mu\text{m}$ and outer diameters about $70 \mu\text{m}$, though specific dimensions vary by etching method (see left Fig 3.19). When a voltage difference is applied across the GEM foil, charge multiplication takes place within the holes. In a single GEM detector, most electrons are driven toward the anode by the induction field, while some are collected at the bottom of the GEM, as shown in right Fig 3.19. By cascading multiple GEM foils, each operating at a lower gain, the avalanche spreads over multiple holes, thus limiting charge density and reducing discharge risks. In CMS, the triple GEM foils operate at stable gains between 10^4 and 10^5 . The GEM detectors in the GE1/1 station operate with an Ar/CO₂ gas mixture in a 70:30 ratio. In GE1/1, pair of chambers are matched to form a "super-chamber", providing two measurement planes and maximizing the detection efficiency for the station.

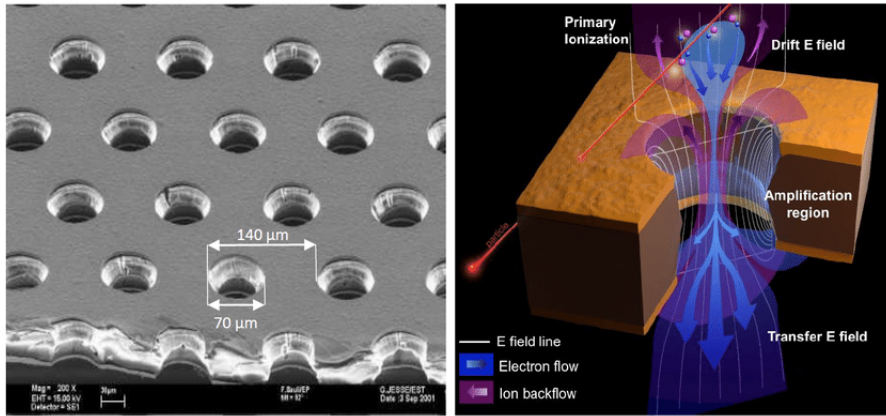


Figure 3.19: (Left) Scanning Electron Microscope picture of a GEM foil showing the hole pattern. (Right) Illustration of the avalanche formation inside a GEM hole [156].

GEM technology is well-suited for the high particle rates of the forward region, tolerating rates up to hundreds of kHz/cm^2 while providing precise spatial and timing resolution, approximately $250\text{--}500 \mu\text{m}$ and under 10 ns per

layer, respectively. When combined in the GE1/1 station, these layers achieve a spatial resolution of about $100\ \mu\text{m}$.

3.2.7 The CMS Trigger System

At the LHC proton bunches cross at a rate of 40 MHz and each bunch contains 10^{11} protons, resulting in a proton collision rate of 10^7 - 10^9 Hz. It is not possible to store the result of each collision to disk: considering a 2 MB size per event and a collision rate of 1 GHz, a storage capacity of approximately 1 PB/s would be required. With the current technologies, CERN is capable of storing a few tens of PB per year from the LHC.

For this reason, the CMS experiment is equipped with a two-level trigger system, responsible for selecting events that are interesting from the physics point of view, within a very broad research program. The first level trigger (L1T) is a hardware based system, designed to make very fast decisions ($4\ \mu\text{s}$ of latency) by exploiting only information reconstructed by the calorimeters and the muon detectors [161]. The L1T reduces the rate from 1 GHz to 110 kHz, which is further handled, in the next stage, by the high-level trigger (HLT), a software-based system which runs the full event reconstruction customized for fast processing. In Run 3, the HLT has reached a final output rate of 2.6 kHz. Additionally, the HLT stores extra samples, under the name of *parking* datasets, which are reconstructed with a certain delay and only when the resources are not needed for the main reconstruction, at a rate of 3 kHz. Another strategy in the trigger reconstruction, called *scouting*, allows us to store 30 kHz of HLT-reconstructed data and 40 MHz of L1T-reconstructed data, without undergoing offline reconstruction.

L1 Trigger

The L1 trigger selects events on the basis of information reconstructed by the calorimeters and the muon system, as schematized in Figure 3.20.

In particular, calorimeters and muon detectors reconstruct the so-called *Trigger Primitives* (TPs), which are basically energy and position measurements. The L1T calorimeter and muon systems then reconstruct jets, electrons, photons, hadronically decaying τ leptons, and muons, and the calorimeter trigger computes energy sums. Finally, the L1T *Global Trigger* (GT) makes the final decision, called *L1 Accept* (L1A), by applying selections on the multiplicity and kinematic quantities of these objects, as well as the proximity to each

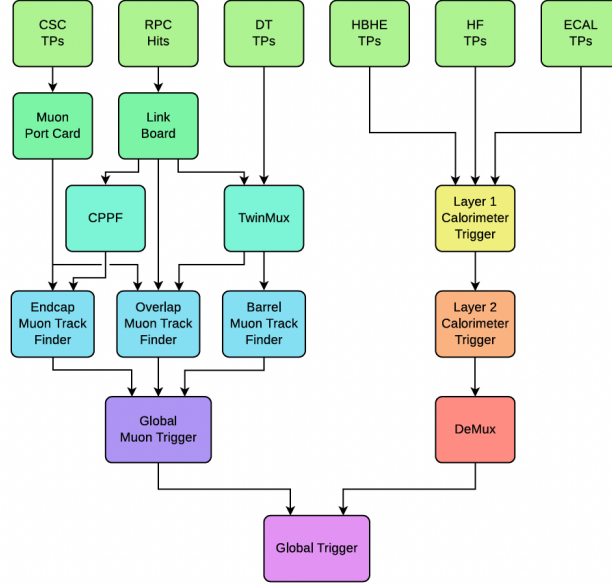


Figure 3.20: Overview of the CMS L1 trigger system. Trigger primitives (TP) from the forward (HF) and barrel (HCAL) hadronic calorimeters, and from the electromagnetic calorimeter (ECAL), are processed by the Calorimeter Trigger System and sent to a demultiplexing card (DeMux). Energy deposits (hits) from the resistive-plate chambers (RPC), cathode strip chambers (CSC), and drift tubes (DT) are processed either via a pattern comparator or via a system of segment- and track-finders and sent onwards to a global muon trigger (GMT). The information from the DeMux and GMT is combined in a global trigger (GT), which makes the final trigger decision. This decision is sent to the tracker, ECAL, HCAL or muon systems via the trigger, timing and control (TTC) system. The data acquisition system (DAQ) reads data from various subsystems for offline storage [161].

other, timing information and beam presence. A complete set of L1 selections dedicated to a specific region of the phase space is referred to as *L1 seed* and the so called *L1 menu* gathers together all the L1 seeds to be used during pp collisions.

The L1 latency, which is the time needed to perform this fast reconstruction and to decide whether to read out the full-event information, is $4\ \mu\text{s}$ for CMS and it includes the needed latency for taking the data out of the detector to the counting room and sending the L1A back to the on-detector electronics.

High Level Trigger

The L1T output rate is further reduced to 2.6 kHz by the HLT, a software-based trigger system which exploits the full event reconstruction to select events considered interesting for the wide CMS physics program. Since Run 3, the HLT has started to make use of graphical processing units (GPUs) in the farm. Many reconstruction algorithms were implemented to run on both central processing units (CPUs) and GPUs: they are executed on a GPU if available, otherwise on a CPU.

Both the L1 and the HLT output rates can be tuned by defining a prescale factor: in this case, not all the events passing the specific selection criteria are selected, but a random subset. A complete sequence of L1 and HLT selection criteria, including the prescale, is called *trigger path*.

The HLT selection consists of two sequential steps: first, the full information from calorimeters and muon detectors is exploited reducing the event rate by approximately one order of magnitude; then, also the information from the silicon tracker is reconstructed and further selections are applied.

HLT algorithms are very versatile, and therefore customized HLT paths dedicated to specific signals can be implemented. The event reconstruction performed at the HLT is mainly based on the same algorithms used for offline object reconstruction, but optimized for fast processing.

After the HLT makes the final decision, the data is initially stored locally on disk in raw data format and then transferred to the Tier-0 computing center, which perform offline reconstruction and store the data permanently.

Offline reconstruction consists of a large number of complex and sophisticated algorithms, described in Chapter 3.3, aimed at identifying the different particles created in the pp collisions.

For storage, different datasets are defined on the basis of different classes of trigger paths: for instance, the *Muon* and *Electron* datasets collect data selected by trigger paths applying primarily requirements on muons and electrons, respectively.

3.3 Physics object reconstruction

The raw detector information is combined and used to reconstruct physics objects, which are the input of all data analyses. A global event reconstruction is performed to identify few elementary objects: charged and neutral hadrons, electrons, photons, and muons. These are subsequently combined with sophis-

ticated algorithms to reconstruct more complex objects such as hadronically decaying τ leptons, jets, and missing transverse momentum.

3.3.1 Tracks and primary vertex

At the CMS experiment, track reconstruction relies primarily on the Combinatorial Kalman filter [162].

A track seed is initially built from either two hits and an estimated beam-spot or three hits, in order to reduce the number of possible hit combinations to be processed (*seed generation*). The track seeds allow to obtain a first estimate of the track parameters, essential for the track building process. Then, the Kalman filter extrapolates the seed trajectories along the expected flight path of a charged particle and assign additional hits to the track candidate (*track finding*) [163]. After the track finding step, the track parameters are fitted by taking into account all the hits associated to the track (*track fitting*). Tracks are then selected according to the normalized χ^2 value (*track selection*). This helps to discard tracks incorrectly reconstructed from hits of different particles.

This tracking sequence—seed generation, track finding, track fitting, and track selection—is repeated iteratively. Prompt tracks with high p_T , which are the easiest to find, are reconstructed at the first iterations, while later iterations target tracks more difficult to reconstruct. At the end of each iteration, hits already associated to a reconstructed track are removed to reduce the combinatorial complexity in the next iterations [164]. Additionally, the Cellular Automata (CA) track seeding algorithm developed for parallel architectures is employed to further enhance the efficiency of track reconstruction [164]. The CA algorithm creates hit doublets (cells) for each pair of layers and then compute the compatibility between adjacent cells as schematized in the sketch of Fig. 3.21.

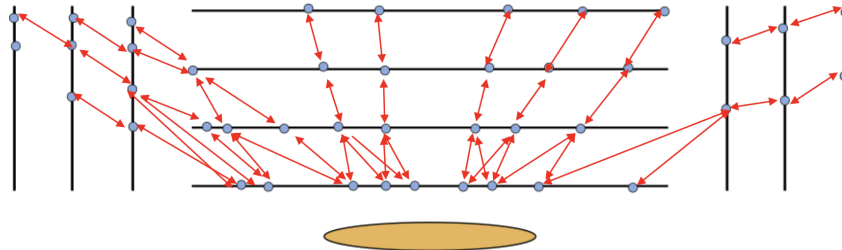


Figure 3.21: Sketch of the Cellular Automata track seeding [165].

This approach facilitates parallel processing of track candidates, thereby improving both the speed and robustness of pattern recognition. The integration of the Combinatorial Kalman filter and Cellular Automata provides a comprehensive framework for achieving high-quality track reconstruction in the CMS detector.

For each event, a large number of interaction vertices is originated, which includes the main hard scattering interaction, called *primary vertex* (PV), and the vertices from pileup collisions. The PV is reconstructed from the track collection following three main steps: selection of the tracks, clustering of the tracks compatible with the same interaction vertex and fitting for determining the vertex position. For each vertex reconstruction, a weight is assigned to the tracks used for that vertex, based on their compatibility with the vertex. At the end, the vertex with the highest summed track weights is selected as the PV. The resolutions in x and z are estimated to be, in minimum-bias events, less than 20 and 25 μm respectively, for primary vertices reconstructed with at least 50 tracks [163], as it can be observed in Figure 3.22 (red dots). Overall, a better resolution is observed in a jet-enriched sample (black dots), produced by requiring each event to have a reconstructed jet with transverse energy $E_T > 20$ GeV. Having significantly higher mean p_T , these tracks benefit from a better resolution.

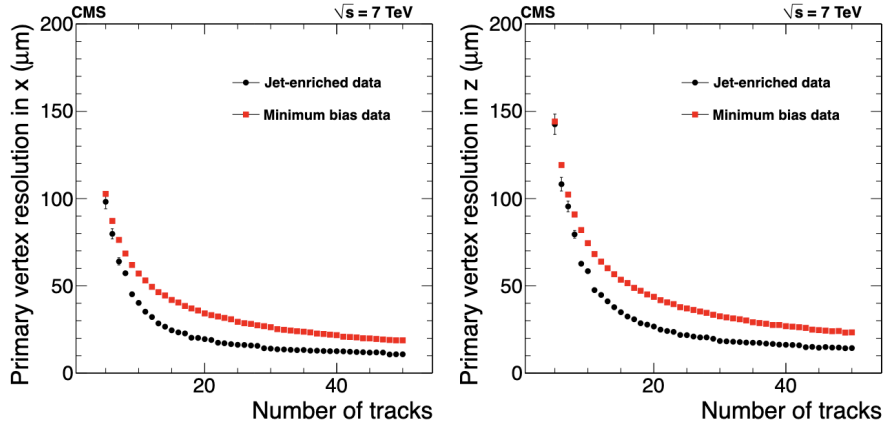


Figure 3.22: Primary-vertex resolution in x (left) and in z (right) as a function of the number of tracks at the fitted vertex, for two kinds of events with different average track p_T values [163].

Figure 3.23 shows the resolution, as a function of p_T , of d_0 and z_0 , defined as the coordinates of the impact point in the radial and z directions. These

results are evaluated on simulations of isolated muons with $p_T = 1, 10,$ and 100 GeV, in different η partitions.

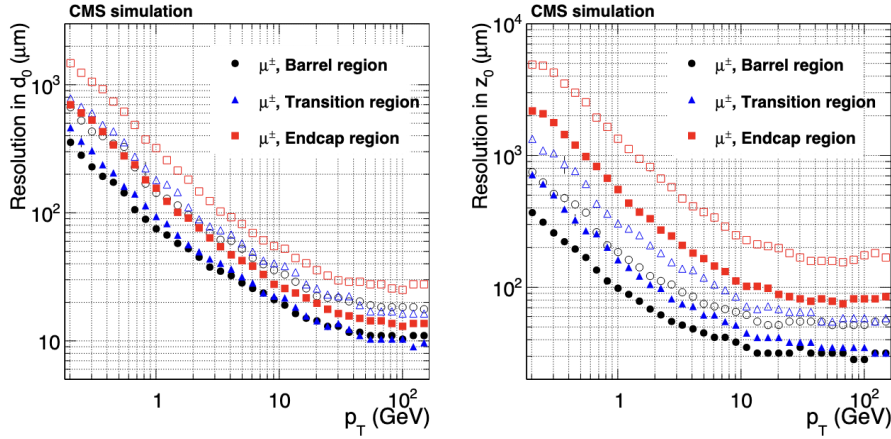


Figure 3.23: Resolution, as a function of p_T , of d_0 (left) and z_0 (right), for single isolated muons in the barrel, transition, and endcap regions, defined by η intervals of 0–0.9, 0.9–1.4 and 1.4–2.5, respectively. For each bin in p_T , the solid (open) symbols correspond to the half-width for 68% (90%) intervals centered on the mode of the distribution in residuals [163].

3.3.2 Particle Flow

Particle Flow (PF) reconstruction is a sophisticated technique used in the CMS experiment to achieve high-quality identification and reconstruction of particles produced in pp collisions. Figure 3.24 shows a sketch of different particle interactions with the subsystems of the CMS detector. In principle, before the introduction of the Particle Flow algorithm, jets can be reconstructed by exploiting only the information collected by the hadron calorimeter, while electrons and photons can be reconstructed primarily by the electromagnetic calorimeter, and muons can be reconstructed solely by the muon chambers. However, a significant improvement in event description can be achieved by correlating the basic elements from all the sub-detectors and combining all the information collected to identify each final-state particle and reconstruct their properties. This integrated approach, known as Particle Flow, leverages the strengths of each sub-detector to provide a more accurate and comprehensive picture of the collision events [165].

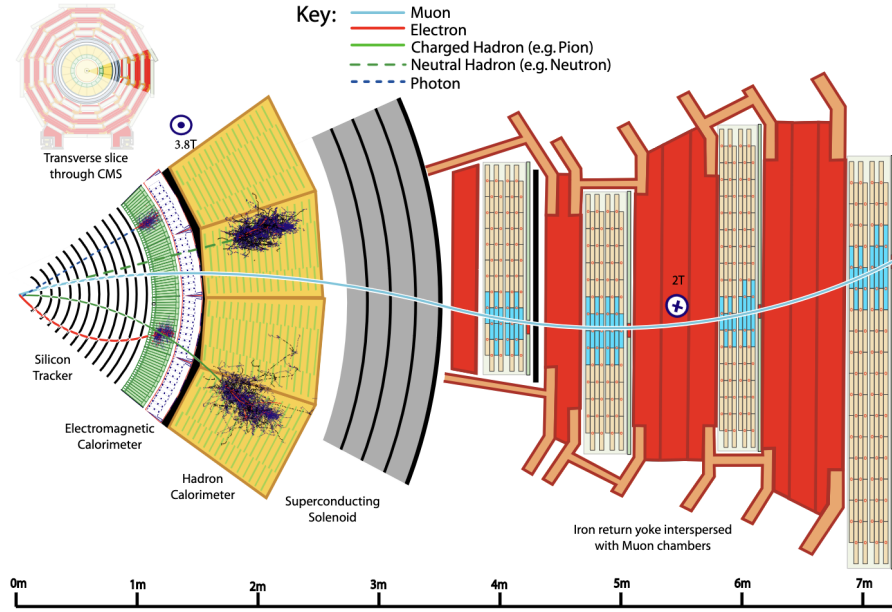


Figure 3.24: Sketch of the specific particle interactions in a transverse slice of the CMS detector, from the beam interaction region to the muon detector. The muon and the charged pion are positively charged, while the electron is negatively charged [165].

The PF approach consists of the following steps:

1. *Track reconstruction.* Tracks are reconstructed as described in 3.3.1. Originally, track reconstruction was aimed at measuring the momentum of energetic and isolated muons, at identifying energetic and isolated hadronic τ decays, and at tagging heavy flavor jets. It was then optimized for the PF algorithm with the iterative approach, which increases the tracking efficiency, while keeping the background rate under control.
2. *Calorimeter cluster finding.* The clustering algorithms in the calorimeters have the multiple purposes of detecting and measuring the energy and direction of stable neutral particles (photons and neutral hadrons), separating them from charged hadron energy deposits, reconstructing and identifying electrons and bremsstrahlung photons and retrieving energy measurements for charged hadrons with low quality or high- p_T tracks. The clustering is carried out independently in each subdetector. It starts from the identification of cluster seeds, i.e. cells that have an energy larger than the neighbouring ones besides overcoming a given threshold. Then, *topological clusters* are formed by taking into account the

neighbouring cells contributions under certain conditions. Final clusters are reconstructed from the topological clusters by using a dedicated algorithm and are accurately calibrated.

3. *PF element association.* While crossing the CMS subdetectors, each particle originates different PF elements that are connected together by a *link algorithm*. For instance, a track and a calorimeter cluster are linked if the extrapolated track position in the calorimeter is geometrically compatible with the cluster area. If more than one cluster is associated to the same track, the link which minimizes the spatial distance is kept.
4. *Particle identification.* Particles are identified in the following order: first, muons are reconstructed from silicon tracks linked with tracks in the muon system and their calorimeter deposits are subtracted from the Particle Flow hit collection. Then, it is the turn of electrons and isolated photons: electrons are reconstructed by combining tracks and ECAL clusters, while photons are reconstructed from ECAL clusters not connected to a track. Once muons, electrons, and isolated photons are identified and removed from the PF blocks, the remaining particles to be identified are hadrons from jet fragmentation and hadronization. These particles may be detected as charged hadrons (π^\pm , K^\pm , or protons), neutral hadrons (e.g. K_L^0 or neutrons), nonisolated photons (e.g. π^0 from decays), and more rarely additional muons (e.g. from early decays of charged hadrons). The ECAL and HCAL clusters not linked to any track give rise to photons and neutral hadrons, respectively. Finally, each of the remaining HCAL clusters of the PF block is linked to one or several tracks (not linked to any other HCAL cluster) and these tracks may in turn be linked to some of the remaining ECAL clusters (each linked to only one of the tracks), to reconstruct the charged hadrons.

3.3.3 Jets

Quarks and gluons produced in pp collisions generate a parton shower and hadronize, resulting in jets of collimated particles. At the CMS experiment, jets are reconstructed by clustering the PF objects with the anti- k_T algorithm [166] within the FastJet software package [167]. The algorithm follows an iterative procedure, which takes the various hadron candidates reconstructed by the PF algorithm and groups them into jets. For each object i of transverse momentum

$p_{T,i}$ a *distance* from the beam axis is defined as follows:

$$d_{iB} \equiv p_{T,i}^{-2}. \quad (3.8)$$

Another *distance* is associated to each possible pair in the following way:

$$d_{ij} \equiv \min(p_{T,i}^{-2}, p_{T,j}^{-2}) \frac{\Delta R_{ij}^2}{R^2}, \quad (3.9)$$

where $\Delta R_{ij}^2 \equiv (\varphi_i - \varphi_j)^2 + (\eta_i - \eta_j)^2$, and R is the size of the jet cone in the $\eta - \varphi$ plane. In the *non-boosted* cases, characterized by final-state-objects of relatively low transverse momentum, jets are normally clustered with a distance parameter ΔR of 0.4 (*AK4 jets*). Larger ΔR values (0.8 or 1.5) are, instead, used for the reconstruction of jets coming from Lorentz-boosted W , Z and Higgs bosons, from top quarks or from heavy new resonances. After ordering all the *distances* d_{iB} and d_{ij} in decreasing order the algorithm works as follows:

1. the smallest *distance* is examined:
 - a) if it is of type d_{iB} , then i is assigned to a jet;
 - b) if it is of type d_{ij} the momenta of the particles i and j are summed.
2. if the particle has been assigned to a jet it is removed from the list, then the algorithm investigates the new smallest *distance* available.

The procedure is started anew iteratively till each particle has been assigned to a jet. Jet energy and transverse momenta are measured in simulation using the properties of stable particles which have been clustered into a jet by the anti- k_t algorithm. Pile-up jets, electronic noise in the calorimeters, and other factors can cause a discrepancy between the jet modeling in simulation and the reconstructed jets. A calibration of the jet energy is performed in order to achieve a more accurate description of the jet properties at reconstruction level. The set of corrections applied to the jet energy and transverse momentum are globally referred to as *jet energy corrections* (JECs). Reconstructed jets are then usually identified as originating from heavy flavor quarks or light quarks, through a procedure called *heavy flavor tagging*, performed by several algorithms proposed in CMS [168–170]. The relevant one for the CMS analysis presented here is called *DeepJet* [168, 171] and is based on a convolutional recurrent neural network which receives, as input, low-level features from a large number of jet constituents. In the context of the analysis outlined here,

the jet tagging is solely used to identify jets initiated by bottom quarks and veto event with at least one of such jets.

3.3.4 Missing Transverse Energy

In pp collisions the hard scattering interaction can be assigned to two single partons belonging to the colliding protons, while the interaction between partons of the same proton can be neglected. Each parton has a momentum $\vec{p}_i = x_i \vec{P}$ equal to a fraction x_i of the proton momentum \vec{P} . The momentum fractions x_1 and x_2 carried by the colliding partons are not necessarily equal. The parton momenta \vec{p}_1 and \vec{p}_2 are therefore not required to be equal in module, but are both directed along the beam line. Therefore, the momentum associated to the partonic scattering center of mass, $\vec{p}_1 + \vec{p}_2$, has a projection in the transverse plane equal to 0. The physical variables chosen to describe a pp collision must be invariant under Lorentz boost along the z axis, e.g. the transverse momentum of a particle. In any collision the transverse momenta of the particles emitted must sum up to 0:

$$\sum_i \vec{p}_{T,i} = 0, \quad (3.10)$$

with $\vec{p}_{T,i}$ transverse momentum of the i -th particle, and the sum running on all particles produced in the hard scattering vertex. This is verified under the assumption that all particles are reconstructed and their energy is correctly measured. A more accurate depiction of what is observed experimentally is that some energy in the transverse plane is missing. This missing transverse energy (\vec{p}_T^{miss}) is defined as:

$$\vec{p}_T^{\text{miss}} = - \sum_i^{\text{reco.}} \vec{p}_{T,i}, \quad (3.11)$$

where the sum now runs over the reconstructed particles, and $\vec{p}_{T,i}$ is the reconstructed transverse momentum of each particle. The \vec{p}_T^{miss} itself combines detector inefficiencies effects with the presence of particles which escaped the detector without interacting, like neutrinos or neutral weakly interacting particles in BSM theories, collectively referred to as *invisible particles*. Tau leptons decay through weak charged current, and at least a neutrino is always present among the decay products. Hence, the CMS analysis presented in this thesis work strongly relies on the proper reconstruction of the \vec{p}_T^{miss} .

3.3.5 Tau leptons

Tau decays can either be fully leptonic, with the tau decaying into a muon or electron and two neutrinos, or involve hadrons (plus one tauon neutrino), with or without intermediate mesonic resonances (see the branching fractions reported in Fig. 3.25). In the following, fully leptonic decays will be referred to simply as *leptonic* (τ_l), while decays involving at least a charged hadron will be called *hadronic* (τ_h).

It is common to refer to the charged decay products of tau leptons as *prongs* and divide the decay channels according to the number of prongs. Leptonic decays are all *one prong* decays, thus they do not require other labeling aside from, where relevant, specifying whether the tau decayed into a muon (τ_μ) or an electron (τ_e). Hadronic decays instead are classified depending on the mesonic resonance involved, leading to the labels: τ_h with $h \in \{\pi, \rho, a_1^{1Pr}, a_1^{3Pr}\}$. The labels a_1^{1Pr} and a_1^{3Pr} are both associated to decays involving the a_1 meson as a resonance, and indicate respectively decays with one or three prongs.

When talking about reconstruction of tau leptons it is usual to refer implicitly to the identification of hadronic decays. This is because τ_l candidate is simply an isolated lepton reconstructed following the usual procedures for electrons and muons. The reason for not implementing more precise reconstruction techniques stems from the difficulty of separating τ_l candidates from prompt leptons. Leptonic decays involve always two neutrinos, making them 3-body decays, in which only one decay product is actually identified. This means that the fraction of energy of the decaying tau lepton carried by the prong falls within a continuous spectrum. Energy related quantities are therefore not different between τ_l and prompt leptons. Furthermore, tau leptons have decay lengths of the order of millimeters, making the distinction between leptons coming from the PV and the ones coming from vertices so close to the beamline extremely difficult.

Reconstruction of hadronically decaying tau leptons is operated in CMS with the hadron-plus-strip (HPS) algorithm [172, 173]. Candidate jets, photons and electrons reconstructed by the PF algorithm are tested for compatibility with hadronic decay channels of tau leptons. A typical τ_h candidate is an isolated collimated jet with low multiplicity. The HPS algorithm aims at identifying τ_h candidates with high efficiency while rejecting the main background: quark and gluon jets coming from the QCD multijet production.

The HPS algorithm is seeded by PF jet candidates identified by the anti- k_t algorithm with a cone size of $\Delta R < 0.4$. For each seeding jet, particles in an

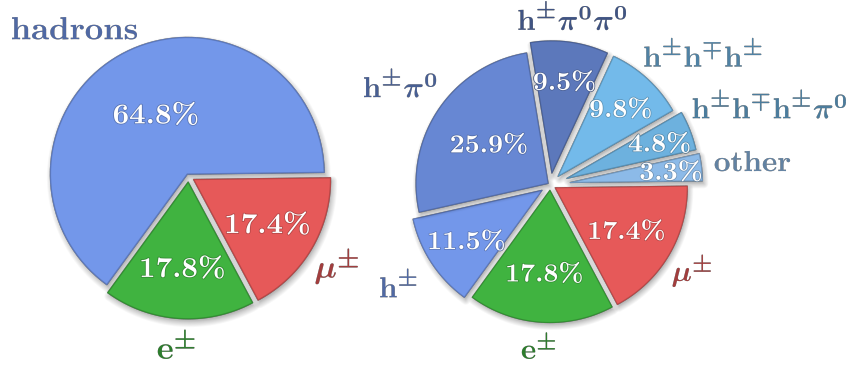


Figure 3.25: Pie charts representing the tau lepton decay channels with relative branching fractions. The right chart shows the detail of the different hadronic decay modes, separated in one prong ones and three prongs ones, thorough color code. The letter h is used to label charged hadrons.

η - ϕ cone of radius $\Delta R = 0.5$ around the jet axis are then tested as candidates for:

- **hadrons:** charged particles depositing their energy in both ECAL and HCAL;
- **strips:** a cluster of electrons and photons producing in ECAL signatures compatible with a π^0 decays.

Several tau hadronic decay channels include π^0 mesons, which decay into two photons almost 100% of the times. Photons have a chance of converting into an electron-positron pair, which then are separated along the φ direction due to the magnetic field. This results in an ECAL cluster narrow in η and extended in φ , referred to as *strip*. Photons and electrons in the jet cone are clustered to form a strip if they are found in a certain $\Delta\eta \times \Delta\varphi$ window. In Run 1 the window size was fixed and set to $\Delta\eta \times \Delta\varphi = 0.05 \times 0.20$ [172], while in Run 2 a *dynamic* strip reconstruction was introduced [173].

The algorithm proceeds iteratively:

1. a strip is seeded by the leading photon or electron (e/γ) found in the jet not yet assigned to a strip;
2. the position and transverse momentum of the leading e/γ are assigned to the strip as the position of its center (η^{strip} and φ^{strip}) and momentum (p_T^{strip});

3. the next highest p_T e/γ candidate is then assigned to the strip if the distance between its position ($\eta^{e/\gamma}$ and $\varphi^{e/\gamma}$) and the strip center satisfies the following relations:

$$\Delta\eta(e/\gamma - strip) < \max\left(f(p_T^{e/\gamma}) + f(p_T^{strip}), 0.15\right) \quad (3.12)$$

$$\Delta\varphi(e/\gamma - strip) < \max\left(g(p_T^{e/\gamma}) + g(p_T^{strip}), 0.30\right) \quad (3.13)$$

with

$$f(p_T) = 0.20 \cdot p_T^{-0.66} \quad (3.14)$$

$$g(p_T) = 0.35 \cdot p_T^{-0.71} \quad (3.15)$$

4. if the e/γ candidate is included in the strip then the properties of the strip are re-evaluated based on its constituents:

$$p_T^{strip} = \sum p_T^{e/\gamma} \quad (3.16)$$

$$\eta^{strip} = \frac{1}{p_T^{strip}} \sum p_T^{e/\gamma} \cdot \eta^{e/\gamma} \quad (3.17)$$

$$\varphi^{strip} = \frac{1}{p_T^{strip}} \sum p_T^{e/\gamma} \cdot \varphi^{e/\gamma} \quad (3.18)$$

5. the process continues till no other e/γ candidate is found within the strip window, and the clustering of a new strip is initiated using the unassigned e/γ candidates.

The algorithm improved strip reconstruction compared to the fixed-window one done in Run 1, as it allowed to tackle events with different topologies:

- high energy τ_h decay in highly collimated jets and the use of a smaller window size allows for better discrimination against quark and gluon jets;
- through multiple scattering in the tracker, electrons and positrons originated by the π^0 decay could fall outside the fixed window;

- charged pions could radiate low p_T particles by interacting with the tracker material reaching ECAL outside a fixed window.

The functions defined in Eq. 3.14 and 3.15 were chosen in order to include in a strip 95% of all electrons and photons coming from τ_h decay products. This was done by simulating single τ_h and reconstructing the distance in η and φ between the e/γ coming from τ_h decays and the τ_h direction of flight, used as a proxy for the strip center, and then fitting the contour representing the 95% quantile as shown in Fig. 3.26.

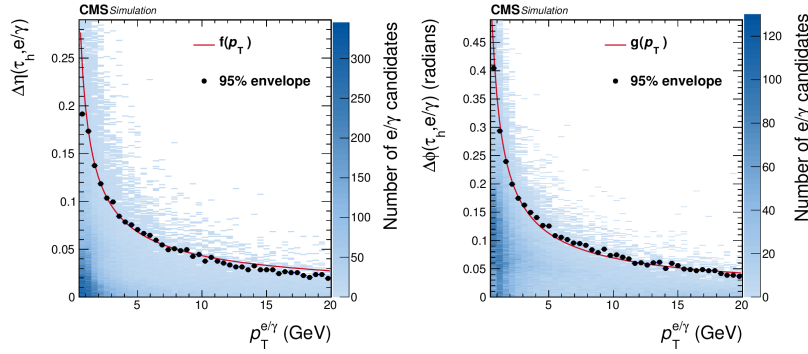


Figure 3.26: Distance in η (left) and in φ (right) between e/γ candidates and the τ_h direction of flight, as a function of $p_T^{e/\gamma}$. The dashed lines represent the functions $f(p_T)$ and $g(p_T)$ shown in Eq. 3.14 and 3.15 which are used to fit through the dotted points, which show 95% quantile for the given p_T bin [173].

The highest energy hadron and strip candidates selected (up to six each) are then combined as potential τ_h candidates and compared to the different hadronic decay modes of tau leptons. The assignment of a decay mode is based on the number of prongs and strips available and the invariant mass of the tau decay products.

For each τ_h^i candidate, corresponding to different combinations of hadrons and strips, the invariant tau lepton mass m_{τ_h} is reconstructed. It is defined as the module of the 4-momentum $p_{\tau_h} = (E_{\tau_h}, p_x^{\tau_h}, p_y^{\tau_h}, p_z^{\tau_h})$ obtained by adding the 4-momenta of the reconstructed visible decay products. It is useful to factorize the contribution on the tau invariant mass coming from the strips when defining the decay mode. This is done since the energy associated to a strip depends on its window size, as it affects how many electrons and photons are associated to the strip. An *ad hoc* estimation of this contribution is calculated

as [173]:

$$\Delta m_{\tau_h}^{strip} = \sqrt{\left(\frac{\partial m_{\tau_h}}{\partial \eta^{strip}} f(p_T^{strip})\right)^2 + \left(\frac{\partial m_{\tau_h}}{\partial \varphi^{strip}} g(p_T^{strip})\right)^2}, \quad (3.19)$$

where the two partial derivatives² in the equation represent the changes to the invariant mass brought by the distance of the strip from the τ_h direction of flight.

Based on the number of reconstructed hadrons and the values of m_{τ_h} and $\Delta m_{\tau_h}^{strip}$ of each τ_h candidate, the HPS assigns the decay mode as follows³:

- **one prong** (h^\pm): This DM corresponds to cases where only one charged hadron candidate was identified, not accompanied by good strip candidates, and $m_{\tau_h} < 1$. The choice of this mass window allows to target not only charged pions, but also the rarer decays to kaons. For this DM, m_{τ_h} is then assigned to be equal to the pion mass.
- **one prong plus one strip** ($h^\pm \pi^0$): A charged hadron is required to be identified together with a strip, and their visible invariant mass is required to be $0.3 - \Delta m_{\tau_h} < m_{\tau_h} < 1.3 \times \sqrt{p_T/100} + \Delta m_{\tau_h}$, with the upper limit constrained between 1.3 and 4.0.
- **one prong plus two strips** ($h^\pm \pi^0 \pi^0$): This DM requires one hadron to be reconstructed alongside two strips. Their visible mass should be $0.4 - \Delta m_{\tau_h} < m_{\tau_h} < 1.2 \times \sqrt{p_T/100} + \Delta m_{\tau_h}$, with the upper limit constrained between 1.2 and 4.0.
- **two prongs** ($h^\pm h^\pm (h^\mp)$): This DM is assigned to τ_h candidates where two charged hadrons are identified having invariant visible mass between $m_{\tau_h} < 1.2$. For this decay mode and the next one, the requirement on the τ_h candidate electric charge is relaxed to allow values differ-

²The two partial derivatives in Eq. 3.19 are analytically defined as:

$$\frac{\partial m_{\tau_h}}{\partial \eta^{strip}} = \frac{p_z^{strip} E_\pi - E^{strip} p_z^\pi}{m_{\tau_h}}, \quad (3.20)$$

$$\frac{\partial m_{\tau_h}}{\partial \varphi^{strip}} = \frac{p_y^{strip} p_x^\pi - p_x^{strip} p_y^\pi}{m_{\tau_h}}, \quad (3.21)$$

where $\mathbf{p}^\pi = (E_\pi, p_x^\pi, p_y^\pi, p_z^\pi)$ and $\mathbf{p}^{strip} = (E_{strip}, p_x^{strip}, p_y^{strip}, p_z^{strip})$ represent the 4-momenta associated respectively to the charged prong system (e.g. the pion in one prong decays) or the strip.

³The values for the tau lepton mass are all expressed in GeV.

ent from 1, the two charged hadron candidates can therefore have either equal or opposite charge.

- **two prongs plus one strip** ($h^\pm h^\pm (h^\mp) \pi^0$): Cases with two charged hadrons and a strip are assigned to this DM. The visible mass should fall within the range $m_{\tau_h} < 1.2 \times \sqrt{p_T/100} + \Delta m_{\tau_h}$, with the upper limit constrained between 1.2 and 4.0.
- **three prongs** ($h^\pm h^\pm h^\mp$): This DM is associated to three charged hadrons with no additional strip, their invariant visible mass is required to be $0.8 < m_{\tau_h} < 1.5$.
- **three prongs plus one strip** ($h^\pm h^\pm h^\mp \pi^0$): Three charged hadrons and a strip are required to be present, furthermore the mass of the tau candidate should be in the range $0.9 - \Delta m_{\tau_h} < m_{\tau_h} < 1.6 + \Delta m_{\tau_h}$.

At this stage the decay channels are selected with a rather loose selection, as can be noticed by the presence of the two prong channels which correspond to τ_h candidates with charge different from 1. Two prong decays can be originated by three prong decays where one of the charged hadrons was not reconstructed in cone around the jet axis. For most analyses such decays are excluded as they are not sufficiently well reconstructed. Only one and three prong decays are considered from this point onward.

It is common to label the hadronic decays with an integer index based on the number of prongs (n_{prongs}) and strips (n_{strip}):

$$DM = 5 \times (n_{prongs} - 1) + n_{strip} . \quad (3.22)$$

With this convention one prong decays are assigned the labels 0, 1 or 2, while three prong decay correspond to the indices 10 and 11. Another matter to consider is that DMs 1 and 2 are defined with a largely overlapping mass window. Furthermore, in the decay of sufficiently boosted a_1 meson, the two π^0 can be emitted quite close to each other. This leads to a large fraction of events in which one single strip can incorporate the decay products of both π^0 mesons. To account for that, all decays with DM 2 are merged into the DM 1 ensemble after the selection operated by the HPS algorithm. The DMs used in the CMS analysis presented in this thesis are 0,1,10,11. A schematic representation of these four DMs is shown in Fig. 3.27 to emphasize the expected signatures of each DM, those being the tracks and energy deposits in HCAL for the charged pions, and the electromagnetic clusters in ECAL originated by neutral pions.

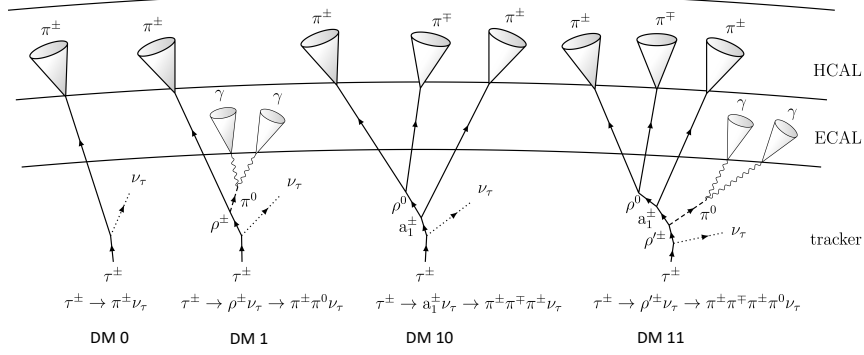


Figure 3.27: Schematic representation of the four HPS-DMs considered at analysis level. From left to right the DMs shown are: one prong, one prong plus π^0 s, three prong and three prong plus π^0 .

3.4 CMS upgrade for the HL-LHC Era

The HL-LHC era set to begin in 2030, will provide the CMS experiment with an instantaneous luminosity of up to $7.5 \times 10^{34} \text{cm}^{-2} \text{s}^{-1}$ from pp collisions at a center-of-mass energy of 14 TeV. To fully exploit this unprecedented data set, the experimental setups must be upgraded to withstand the challenging conditions of the HL-LHC⁴, including up to 200 simultaneous collisions per bunch crossing (PU events) and a substantial radiation dose delivered to the detectors. The increase in PU condition is expected to be mitigated with detectors that will have improved granularity and timing capabilities, while a new silicon tracker and endcap calorimeter will be installed to cope with the higher dose expected. Finally, a large fraction of the on-detector electronics, as well as the entire trigger and data acquisition system, will undergo a complete overhaul to address the larger event size and acquisition rate during the HL-LHC era. The full upgrade project is often called *Phase-II upgrade*.

3.4.1 Upgrade of the tracker system

The Phase-II Tracker System will again be divided into Inner Tracker and Outer Tracker systems, featuring a symmetrical barrel plus two endcaps geometry with acceptance extended up to $|\eta| < 4.0$ [174]. The Inner Tracker will be pixel-based, with a pixel size of $25 \times 100 \mu\text{m}^2$, organised in four barrel layers and eight small and four large discs per side, for a total of 2×10^9

⁴Furthermore, the radiation dose received so far makes the upgrade mandatory for the tracker and calorimeter endcaps, whose performance have shown degradation during Run 3.

channels. The Outer Tracker will feature 44 million strips and 174 million macropixels, organised in six barrel layers and five discs per side. The design of the Tracker addresses the need for radiation resistance and increased granularity, allowing for the reconstruction of approximately 1200 tracks per unit of η . It also has a much-reduced material budget in front of the calorimeters, preserving their resolution. Finally, in contrast to its Phase-I predecessor, the Phase-II tracker will contribute to the L1T decision through the Outer Tracker p_T modules, which are track stubs compatible with trajectories of particles with $p_T > 2$ GeV. Figure 3.28 shows the Tracker geometry and the logic for the reconstruction of the p_T modules.

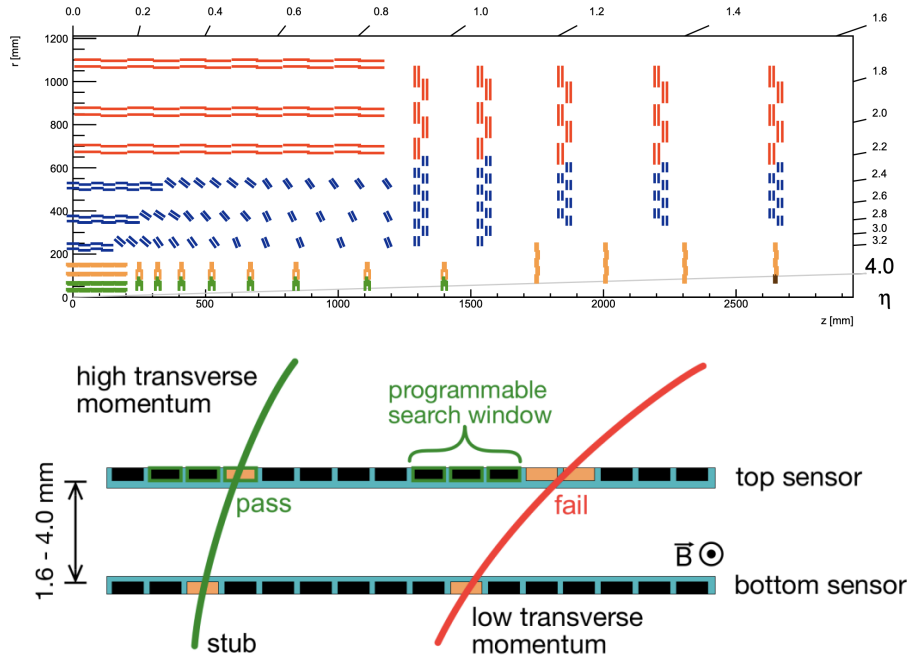


Figure 3.28: (Top) CMS Phase-II Tracker System geometry, divided into Inner Tracker (orange and green modules) and Outer Tracker (red and blue modules). (Bottom) Reconstruction of modules in the Outer Tracker, which are input to the L1T decision.

3.4.2 The High-Granularity Calorimeter

The upgraded endcap calorimetry system for the CMS Phase-II must meet several demanding criteria. It requires a high-density structure to ensure compact lateral development of particle showers, along with fine granularity in both lateral and longitudinal dimensions. Additionally, it must be capable of precise shower timing measurements. Crucially, the system must also contribute to the L1T decision. The High-Granularity Calorimeter (HGCAL) [175] is the proposed design to address those requirements. It is a 5D calorimeter (position, energy and time) with coverage in the region $1.5 < |\eta| < 3.0$, segmented into 47 layers, and divided into electromagnetic (CE-E) and hadronic (CE-H) sections, with both sections structured as sampling calorimeters. It uses two types of sensors: silicon cells in CE-E and the high-radiation part of CE-H, and scintillator cells elsewhere.

The CE-E section comprises 26 layers of silicon sensors interspersed with Cu, CuW and Pb absorbers, yielding a total of 27.7 and 1.5 radiation lengths. On the other hand, the CE-H section comprises 7 layers of Si sensors and 14 layers of mixed silicon–scintillator sensors, interspersed with stainless steel and Cu absorbers and corresponding to 8.5 interaction lengths.

3.4.3 The MIP Timing Detector

The MIP Timing Detector (MTD) [176] is a dedicated tracking layer designed to measure the production time of minimum ionising particles with high precision. A primary motivation for its implementation is the PU mitigation: due to the longitudinal spread of LHC proton bunches, pp interactions within a single bunch crossing are distributed both spatially and temporally, with a time spread characterized by a root mean square of approximately 200ps. This allows for pileup discrimination in both spatial and temporal dimensions, as illustrated in the left panel of Fig. 3.29. Beyond PU suppression, the MTD would also enhance sensitivity to a range of new physics scenarios, e.g. improving the identification of delayed particles and providing precise time-of-flight measurements of heavy charged long-lived particles.

The MTD is divided into two sections: the Barrel Timing Layer (BTL), a cylindrical detector located inside the Tracker support tube, covers $|\eta| < 1.5$; the Endcap Timing Layer (ETL), a pair of disks located in front of the HGCAL thermal screen, covers the region $1.6 < |\eta| < 3.0$. The BTL sensors are LYSO:Ce scintillating crystal bars, instrumented with 25 mm^2 cell-size silicon

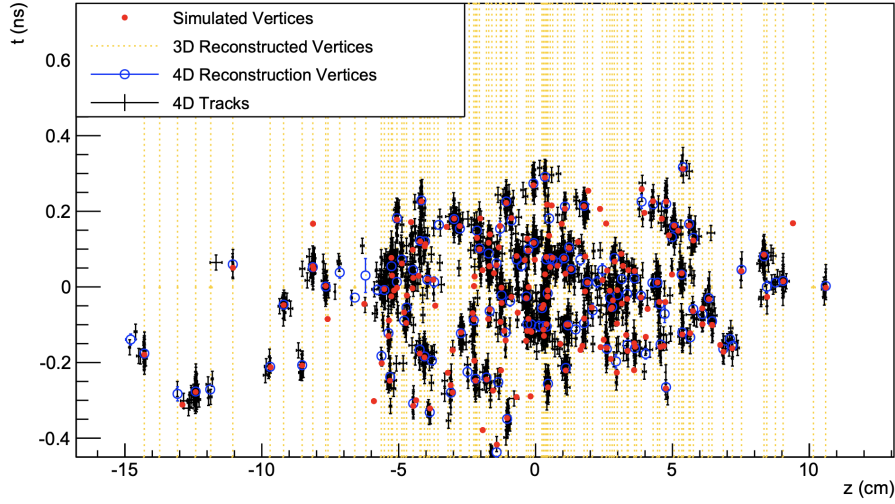


Figure 3.29: The pp interactions are spread both in the longitudinal coordinate and in time. Leveraging the separation in the two dimensions leads to a better identification of the PU vertices.

photomultipliers (SiPMs) on both ends of the crystal for readout. The ETL sensors are silicon low-gain avalanche diodes (LGADs), grouped in arrays and bump-bonded to a custom readout chip. The timing resolution for the MTD reaches 30–65 ps in the barrel region, and 35 ps per track in the endcap.

3.4.4 Upgrade of the Barrel Calorimeters and Muon Detectors

Besides the all-new endcap calorimeter and MIP timing detector, the other CMS subsystems will also undergo improvements for the CMS Phase-II. In order to address the extended latency and higher trigger rate requirements of the HL-LHC era, the CMS barrel calorimeters will undergo upgrades in their electronics systems [177].

The CMS muon system will also be upgraded to maintain high performance under increased radiation and event rate conditions [178]. New chambers will be added in the forward region: GEM detectors in the GE1/1 and GE2/1 stations, and improved RPCs (iRPCs) in the RE3/1 and RE4/1 stations (see Fig. 3.30). The new iRPC chambers will have lower electrode thickness, smaller gas gaps, lower charge thresholds and integrated readout strips, allowing better intrinsic timing resolution of 0.5 ns and better space resolution of

1.5 cm in η . These additions will extend muon acceptance up to $|\eta| = 2.8$ and improve redundancy, especially in the high- η region.

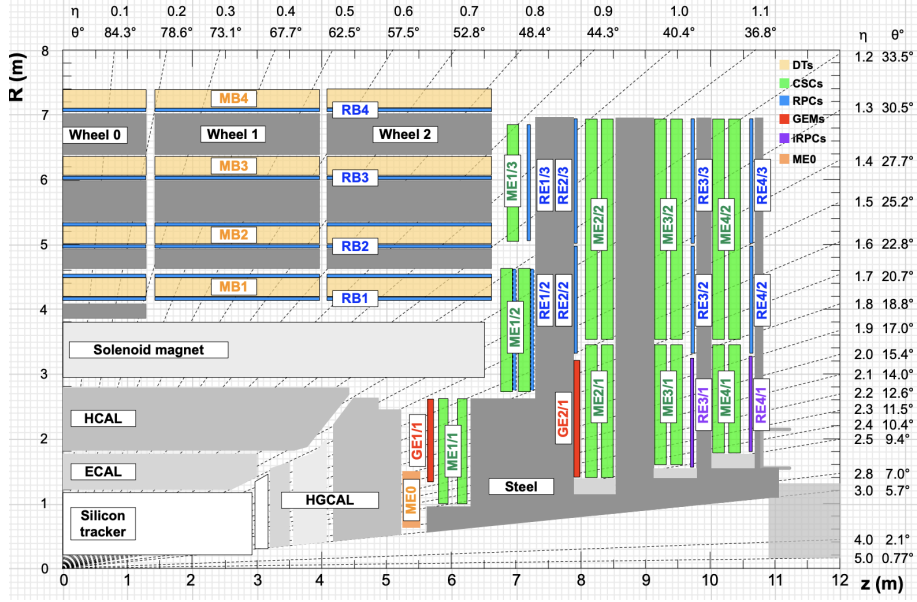


Figure 3.30: Overview of the CMS Phase-II muon systems, with the new GEM chambers (ME0, GE1/1 and GE2/1) and iRPCs (RE3/1 and RE4/1) [178]. The new stations will enhance CMS detection capabilities of forward muons.

All muon subsystems (DT, CSC, RPC, GEM) will also receive new electronics, with enhanced time resolution, radiation tolerance, and compatibility with the upgraded trigger and DAQ systems. The upgraded system will enable precise muon timing, improved spatial resolution, and robust triggering capability, even in the dense environment of the HL-LHC.

Chapter 4

The FCC integrated program

As noted in the 2020 update of the *European Strategy for Particle Physics*, “the successful completion of the high-luminosity upgrade of the (LHC) machine and detectors should remain the focal point of European particle physics, together with continued innovation in experimental techniques” — a goal motivated by the need to “exploit the full physics potential of the LHC and the HL-LHC.” At the same time, the Strategy identifies that for the future, “an electron-positron Higgs factory is the highest-priority next collider”, while “for the longer term, the European particle physics community has the ambition to operate a proton-proton collider at the highest achievable energy” [179].

The Future Circular Collider (FCC) integrated program [180–182] is the leading proposal to fulfill both of these strategic objectives within a unified long-term vision. It consists of a two-stage implementation hosted in a new 90-100 km tunnel near CERN (see Fig. 4.1). The first stage, *FCC-ee*, is a high-luminosity electron-positron collider operating at center-of-mass energies from 90 to 365 GeV. It is designed to deliver precision measurements of the Z, W, Higgs, and top quark — crucial for indirect searches for new physics. The second stage, *FCC-hh*, envisions a proton-proton collider operating at a center-of-mass energy of approximately 100 TeV, offering an unparalleled discovery reach for new particles and interactions. This staged approach would provide a coherent, long-term research infrastructure capable of addressing the most pressing open questions in particle physics, while serving the global scientific community for five decades or more.

While the LHC has successfully confirmed the SM predictions up to the TeV scale, its results also underscore the limitations of current approaches in addressing fundamental open questions in particle physics. Theories extending beyond the SM may reside at much higher energy scales, potentially requiring unnatural fine-tuning of the weak scale, or involving complex, as-yet-

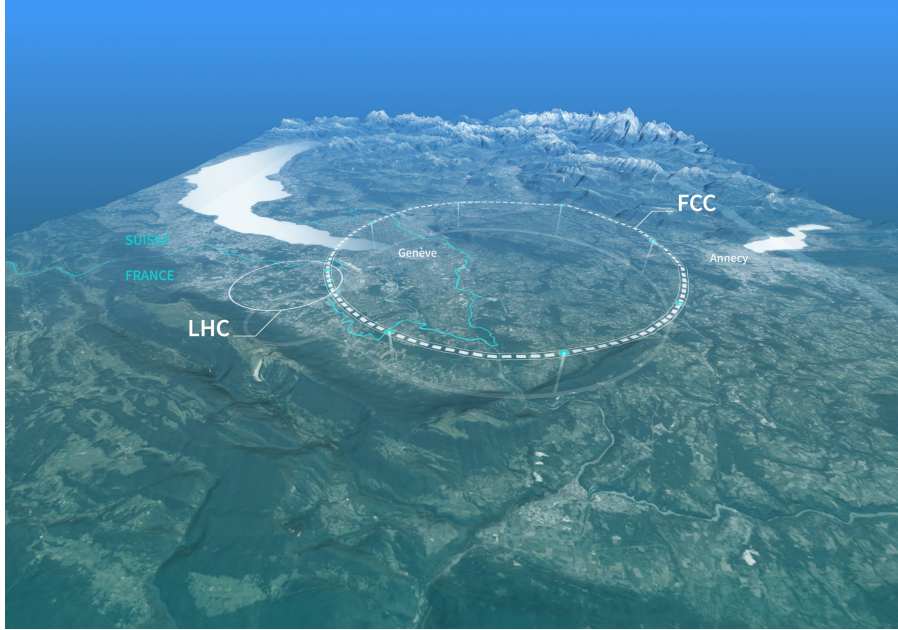


Figure 4.1: A schematic map showing a possible location for the Future Circular Collider (Image: CERN)

undetected structures. Alternatively, new physics might manifest through light, feebly interacting particles [183–185]. The possible mass range of such new phenomena spans an enormous spectrum, from meV to ZeV, and their couplings to SM particles could vary from order unity down to 10^{-12} or weaker. This vast parameter space calls for a new generation of experimental tools capable of exploring both the high-energy and high-intensity frontiers with unprecedented reach and sensitivity.

A next-generation collider program must then address several key objectives [186]:

- **Precision Higgs and electroweak studies:** Map the interactions of the Higgs boson and electroweak gauge bosons with an order-of-magnitude improvement in precision. Such studies could unveil traces of the dynamics responsible for electroweak symmetry breaking and the formation of the Higgs vacuum field, potentially probing timescales as early as 10^{-12} to 10^{-10} seconds after the Big Bang.
- **Comprehensive precision program:** Conduct a wide-ranging campaign of precision measurements in electroweak physics, QCD, flavor physics, Higgs properties, and top-quark interactions. These measurements would

aim to detect subtle deviations from SM predictions and thus access energy scales beyond the collider’s direct reach, leveraging high-statistics datasets and synergy across experimental and theoretical developments.

- **Search for light, weakly coupled new physics:** Greatly improve sensitivity to rare or elusive phenomena at low energies, including the discovery of light particles such as axion-like particles or sterile neutrinos. Particular emphasis is placed on dark matter searches that explore broad classes of dark-sector models and can either reveal or robustly exclude new candidate particles.
- **Enhanced discovery reach at the energy frontier:** Extend the direct discovery potential for new, heavy particles by at least an order of magnitude beyond current capabilities, opening the door to entirely new physics sectors.

The full FCC program is exceptionally well aligned with the outlined objectives. In particular, it offers unique sensitivity to new physics in the Higgs sector. The FCC-ee is expected to produce nearly three million Higgs bosons, enabling model-independent measurements of the Higgs boson’s mass, width, and couplings to the Z , W , τ , b , c particles. These measurements will achieve an order-of-magnitude improvement in precision over current capabilities, allowing for stringent tests of potential BSM origins of EWSB. Ultimately, the FCC-hh will generate approximately 20 billion Higgs bosons, and in synergy with FCC-ee, will deliver unparalleled measurements of the Higgs self-coupling, the top Yukawa coupling, and other rare or invisible decay modes—opening new avenues for probing the mechanisms that shaped today’s Higgs vacuum field.

The current FCC program schedule envisions 15 years of FCC-ee operation, followed by a 10-year transition period to dismantle the lepton collider and install the hadron one, and then 25 years of FCC-hh operation—resulting in a total duration of 50 years (see Fig. 4.2). This timeline is comparable to that of the combined LEP and LHC programs (1989–2041), which also can be considered as two sequential stages—a lepton collider followed by a hadron collider—of a unified physics program.

In the following, the FCC-ee and FCC-hh projects are presented in greater detail, highlighting both the operational aspects of the machines and their respective physics reach. This chapter places particular emphasis on the hadron collider, as it forms the context of Chapter 8. The discussion concludes with a

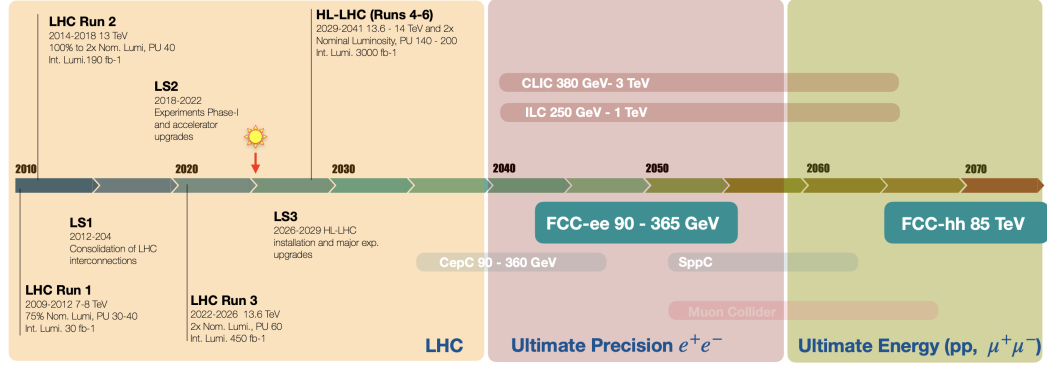


Figure 4.2: LHC schedule and long-term plan for future colliders, including alternative/parallel collider proposals to the FCC [187].

physics case study that illustrates the crucial interplay between the lepton and hadron stages in achieving the most comprehensive results.

4.1 FCC-ee: A Higgs factory, and much more

The FCC-ee collider is designed to operate with detectors at four interaction points, spanning a wide range of centre-of-mass energies. These include regions around the Z pole, the WW production threshold, the ZH production maximum, and up to and just beyond the top-quark pair production threshold. This operational scheme, forming the baseline plan, has been confirmed by the recommendations of the FCC feasibility study midterm review. The expected luminosities at these energy stages, along with the anticipated number of events, are summarized in Fig. 4.3.

The original motivation for constructing a circular e^+e^- collider was to create a high-luminosity Higgs Factory, operating at 240 GeV, within the existing LEP/LHC tunnel [188–190]. However, the decision to situate the FCC-ee in a new 90–100 km tunnel—destined ultimately to host a 100 TeV hadron collider—makes the project uniquely positioned within the global Higgs factory landscape. This expanded tunnel design brings major advantages that significantly extend the FCC-ee’s scientific reach beyond Higgs boson studies.

First, a tunnel of 90–100 km circumference is essential for a circular e^+e^- collider to reach the top-pair production threshold. This energy regime enables detailed and precise top quark measurements, which are crucial to the FCC’s broader electroweak and Higgs precision program. Access to the top quark

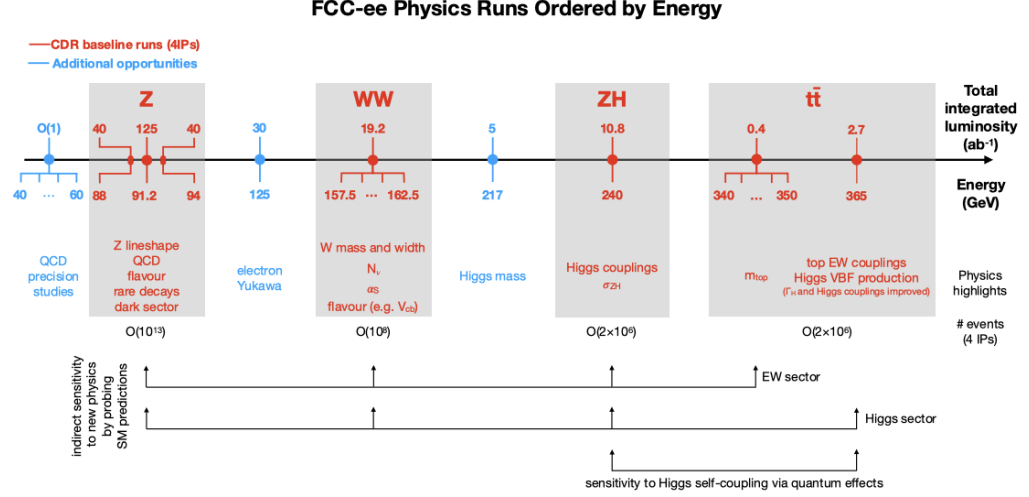


Figure 4.3: FCC-ee operational scheme, showing the designed center-of-mass energies and integrated luminosities of the different stages, including the expected number of events. The physics opportunities per each phase are highlighted [187].

threshold strengthens the collider’s role in probing the completeness and self-consistency of the SM.

Second, the luminosity of a circular collider at fixed power and centre-of-mass energy scales approximately with the ring’s circumference. This means that a 90–100 km design makes the FCC-ee the most luminous e^+e^- electroweak, Higgs, and top factory proposed to date, allowing extremely precise measurements with minimal statistical uncertainties.

Third, the same tunnel length enables unparalleled control of the centre-of-mass energy, both at the Z pole and the WW threshold, which is critical for the electroweak precision program and will serve as essential inputs to stringent tests of the SM.

FCC-ee also stands out among the Higgs factory projects for its unique opportunity to access the Higgs boson coupling to electrons [191–193], through the resonant production process $e^+e^- \rightarrow H$ at $\sqrt{s} = 125$ GeV [194]. This measurement depends on a combination of features exclusive to FCC-ee: high luminosity, operation with four detectors, continuous ppm-level centre-of-mass energy control, and the potential for centre-of-mass monochromatisation [195]. This represents both a unique opportunity and one of the most demanding challenges of the FCC-ee program. As a Higgs factory, FCC-ee benefits from all

the inherent advantages of an e^+e^- collider running near the ZH cross-section maximum. The cross section can be determined by counting events with an identified Z boson, where the mass recoiling against the Z peaks near the Higgs boson mass [196], independently of the specific Higgs decay modes. This approach allows a precise, model-independent measurement of κ_Z , the coupling of the Higgs to the Z boson. This absolute measurement can then serve as a reference standard for all other Higgs-related observables, including those measured at hadron or muon colliders. Furthermore, the position of the recoil mass peak yields an accurate Higgs boson mass, determined via the precise knowledge of the centre-of-mass energy. Combined with the measurement of the rate of ZH events where $H \rightarrow ZZ^*$ decays occur, which is proportional to κ_Z^4/Γ_H , this enables a model-independent determination of the total Higgs width Γ_H . Analysis of additional decay channels yields further model-independent partial width and coupling measurements.

The FCC-ee is expected to measure the Higgs couplings κ_Z and κ_W with precisions of 0.1% and 0.23%, respectively, after eight years of operation at $\sqrt{s} \geq 240$ GeV. Achieving comparable precision at linear e^+e^- colliders operating at 250 and 500 GeV or at 380 and 1500 GeV would require approximately 50 years [197, 198].

The many novel opportunities for physics measurements and searches at FCC-ee also bring a range of experimental and theoretical challenges. Reaching systematic uncertainties—both experimental and theoretical—that match the statistical precision made possible by FCC-ee’s luminosity and data volume demands in-depth studies of detector concepts, modes of operation, and theoretical modelling. A detailed review of these requirements can be found in Ref. [186]. Experimentation at FCC-ee is at once straightforward and highly sophisticated. The environment is clean, with negligible pile-up, precisely controlled center-of-mass energy, and minimal beamstrahlung and synchrotron radiation effects. Yet the richness of the program introduces complexity: matching experimental and theoretical accuracy to statistical capabilities, and tailoring detector configurations to the diversity of measurement channels, constitutes one of the central challenges for the FCC-ee research program.

4.2 FCC-hh: The energy-frontier collider

The comprehensive physics program of the FCC-hh is designed to build upon the insights gained from the FCC-ee and HL-LHC, both of which will signifi-

cantly elevate the expectations for future collider performance. Meeting these targets demands three major advancements:

- extending Higgs-boson studies to processes involving much smaller couplings—such as rare decays $H \rightarrow \gamma\gamma$, $H \rightarrow \mu^+\mu^-$, and $H \rightarrow Z\gamma$ —as well as to channels requiring higher center-of-mass energies, notably $t\bar{t}H$ and HH production;
- probing electroweak dynamics far beyond the electroweak symmetry-breaking scale;
- directly exploring the multi-TeV regime to identify the origins of possible deviations found in the FCC-ee precision measurements, and to extend the mass reach for diverse BSM scenarios—particularly those whose impact on low-energy EW observables is suppressed or those initiated by gluons.

The FCC-hh is uniquely positioned to address these challenges, offering an increase of approximately one order of magnitude in both centre-of-mass energy and peak luminosity compared with the HL-LHC, as shown in Fig. 4.4.

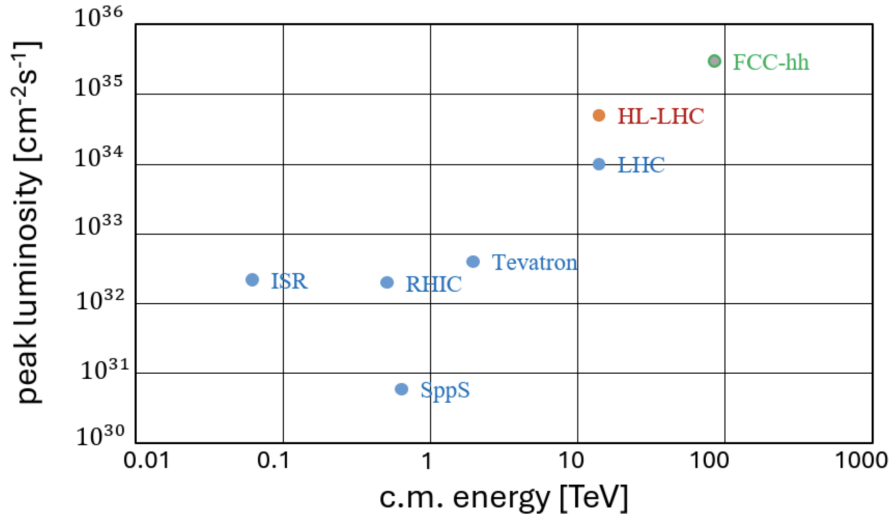


Figure 4.4: Peak luminosity versus center-of-mass energy for past and current hadron colliders (blue), the HL-LHC (red), and the proposed FCC-hh (green) [199].

On the Higgs front, the FCC-hh is expected to produce over 20 billion Higgs bosons, enabling sub-percent precision on key couplings such as κ_μ , κ_γ ,

κ_t and $\kappa_{Z\gamma}$. The large event yield at high transverse momentum allows measurements in kinematic regions with enhanced signal-to-background ratios and reduced systematic uncertainties. Moreover, by precisely measuring the ratio of these couplings to benchmark couplings determined with high accuracy at the FCC-ee (e.g. κ_Z), the FCC-hh enables sub-percent level determinations of these absolute Higgs couplings, achieving a precision beyond the reach of lepton colliders.

The prolific production of Higgs boson pairs at the FCC-hh enables a determination of the Higgs self-coupling with a precision better than 5%, even under conservative assumptions regarding systematic uncertainties. In addition, high- Q^2 Higgs production—via direct, associated, or vector boson fusion channels—offers unique sensitivity to higher-dimensional operators, probing new physics in a manner complementary to lepton colliders.

The discovery potential of the FCC-hh extends into the multi-TeV regime. It is capable of directly detecting new particles with masses up to ~ 40 TeV for s -channel produced electroweak or coloured resonances, and in the 10–20 TeV range for pair-produced strongly interacting particles such as squarks, stops, vector-like top partners, and gluinos. Weakly interacting particles can be probed in the 1.5–5 TeV range fully covering the theoretically motivated parameter space for WIMP dark matter candidates.

Equally crucial is the search for partners of the Higgs boson, which may lie in the multi-TeV domain. When combined with precise measurements of the Higgs self-coupling, these searches provide a powerful handle on theoretical models predicting a strong first-order electroweak phase transition, potentially offering insights into early-universe cosmology.

The precision program for the known elements of the Standard Model must be complemented by the direct exploration. The FCC-ee and the FCC-hh will complement each other on this tasks in a more comprehensive way than any other energy frontier project presently under consideration [186].

4.2.1 Setting the energy and luminosity target

Comprehensive studies on the feasibility of the FCC-hh project have been conducted over the past years, culminating in the publication of the FCC Conceptual Design Report (CDR) in 2018 [180–182]. This report established a baseline accelerator configuration targeting a center-of-mass energy of $\sqrt{s} = 100$ TeV and an integrated luminosity of 30 ab^{-1} . In the 2025 FCC Feasibility Study (FS) [186], an updated baseline configuration for the FCC-hh was pre-

sented, driven primarily by constraints on the ring geometry and the feasibility of the dipole magnet technology. The new baseline [200, 201] envisions the use of 14 T Nb_3Sn dipoles in a 90.7km tunnel, resulting in a reduced center-of-mass energy of $\sqrt{s} = 84\text{TeV}$, while maintaining a luminosity comparable to that in the CDR design¹. Table 4.1 reports the key machine parameters for the FCC-hh (both CDR and FS designs) and the HL-LHC, for comparison.

Parameter	FCC-hh FS	FCC-hh CDR	HL-LHC
collision energy [TeV]	84	100	14
dipole field [T]	14	16	8.33
circumference [km]	90.7	97.8	26.7
beam current [A]	0.5	0.5	1.1
synchr. rad. per ring [kW]	1200	2400	7.3
peak luminos. [$10^{34}\text{ cm}^{-2}\text{s}^{-1}$]	30	30	5 (lev.)
events/bunch crossing	1000	1000	132
stored energy/beam [GJ]	6.5	8.3	0.7
integr. luminosity / IP [fb^{-1}]	20000	20000	3000

Table 4.1: Comparison of accelerator parameters for FCC-hh (CDR and updated FS) and HL-LHC.

One may ask why a target of approximately 100 TeV in center-of-mass energy and 30 ab^{-1} in integrated luminosity is considered appropriate for the FCC-hh. Let us begin by discussing the motivation for the energy goal.

Although the LHC and other experiments have not provided concrete evidence pointing to a specific BSM scenario or mass scale, general theoretical and phenomenological arguments strongly support 100 TeV as a well-motivated benchmark for the FCC-hh. There is, in principle, no upper limit to the energy the high-energy physics community would like to achieve. If an energy of 120 TeV could be attained—without compromising luminosity—it would certainly be desirable. However, there is compelling evidence that 100 TeV is both necessary and sufficient to perform a range of critical measurements and provide definitive yes/no answers to key open questions that may remain unresolved after the HL-LHC, as well as to probe new scenarios that

¹The updated baseline assumes an integrated luminosity of 20 ab^{-1} per general-purpose detector. Physics projections are based on 30 ab^{-1} to account for a potential partial statistical combination of results from the two experiments.

might emerge following the FCC-ee phase. Several motivations are outlined below, with a more comprehensive discussion available in Ref. [180].

The Nature of the Higgs Potential Until new physics is discovered, a comprehensive understanding of the Higgs boson remains a central objective of high-energy physics. Two pivotal questions might remain unanswered even after the HL-LHC and FCC-ee: (i) How does the Higgs boson couple to itself? (ii) What was the nature of the electroweak phase transition (EWPT) that occurred approximately 10^{-10} s after the Big Bang, leading to the EWSB and the emergence of the Higgs vacuum expectation value? The second question has profound implications for understanding the observed matter-antimatter asymmetry of the Universe. If the EWPT were strongly first-order, it could have played a significant role in baryogenesis. Moreover, such a transition might have generated a stochastic background of gravitational waves—potentially detectable today—through the collisions of expanding bubbles of the new vacuum during the early Universe. These two questions are closely connected, as both hinge on the shape of the Higgs potential. While the potential is fixed in the SM, it can be modified in many BSM frameworks. In fact, such modifications are essential for realizing a strongly first-order EWPT. At 100 TeV, the FCC-hh aims to measure the Higgs trilinear self-coupling with a precision of about 5% in the SM—a target that could be further improved in BSM scenarios where the self-coupling is enhanced. In contrast, the HL-LHC is projected to reach a sensitivity of $\mathcal{O}(30\%)$ to deviations from the SM value [202]. Studies based on existing BSM models indicate that this 5% precision, together with the FCC-hh’s extended discovery reach for new particles relevant to EWSB dynamics, is both necessary and sufficient to determine whether the EWPT was strongly first-order.

Dark Matter A wide variety of scenarios have been proposed to explain the nature of dark matter, spanning an enormous range of mass scales—from ultra-light axions with sub-eV masses to primordial black holes. Among these, a particularly compelling and well-motivated class is that of thermal WIMPs. These are actively pursued in both direct and indirect detection experiments conducted in underground laboratories and space-based observatories. Should any of these searches yield a potential signal, it would be essential to confirm it through accelerator-based experiments. Moreover, collider experiments play a crucial role in probing regions of parameter space that may be inaccessible—or “blind spots”—to non-collider searches. The ability of accelerator experiments

to conclusively test the thermal WIMP paradigm is thus central to advancing our understanding of the DM puzzle. Thermal WIMPs cannot be arbitrarily heavy, as excessively massive candidates would lead to a cosmological relic abundance exceeding the observed DM density. Depending on the interaction mechanism the upper mass limit for thermal WIMPs lies in the range of approximately 1–3 TeV. Due to their weak interactions and correspondingly low production cross sections, only a portion of this mass window is within reach of the LHC. In contrast, the FCC-hh, with a center-of-mass energy of 100 TeV, is necessary and just sufficient to fully explore the remaining parameter space, thereby enabling a definitive test of the thermal WIMP hypothesis.

Probing the origin of new physics revealed by indirect evidence Historically, much of our knowledge of the electroweak gauge bosons, the Higgs boson, and the top quark was gained through their direct production at colliders, even though indirect evidence for their existence had been firmly established beforehand. The same paradigm is likely to apply in the future: any indirect signs of new heavy particles, emerging from precision measurements in flavor physics or electroweak and Higgs observables, will ultimately require direct production to determine their properties with certainty. This need will be even more pressing in the future than it was in the past, when the SM provided a clear and unified framework for interpreting indirect signals of e.g. the top quark and the Higgs. Precision measurements at FCC-ee will be sensitive to possible new phenomena at scales of tens of TeV. New physics at these scales can be revealed in the near future by flavor phenomena, as suggested by the studies of the current flavor anomalies in B decays, and might therefore call for direct searches of massive particles possibly well beyond the LHC reach. Achieving direct particle production at such energy scales is feasible only with a hadron collider operating at or near 100 TeV, making the FCC-hh an indispensable tool for the exploration of fundamental physics at the energy frontier.

The increase in center-of-mass energy from the LHC to the FCC-hh naturally leads to a significant extension of the discovery reach. Since the production cross section for a particle of mass M typically scales as $1/M^2$, achieving sensitivity to very heavy states also requires a substantial increase in integrated luminosity. As an illustrative example, Fig. 4.5 shows the integrated luminosity required for a 5σ discovery of a SM-coupled Z' gauge boson, as a function of its mass, for decay channels into leptons and top quarks. At the ultimate integrated luminosity goal of 30 ab^{-1} , the FCC-hh would be able to discover

a Z' boson with a mass up to 43 TeV. Even modest luminosities of a few tens of fb^{-1} , achievable within the first year of operation, would already extend the HL-LHC discovery reach by approximately a factor of two. The figure also illustrates the effect of increasing luminosity: while a tenfold increase in luminosity from 2.5 ab^{-1} to 30 ab^{-1} results in a more than 30% increase in mass reach, a further increase to 300 ab^{-1} yields less than a 20% additional gain, indicating a saturation of sensitivity at the highest mass scales.

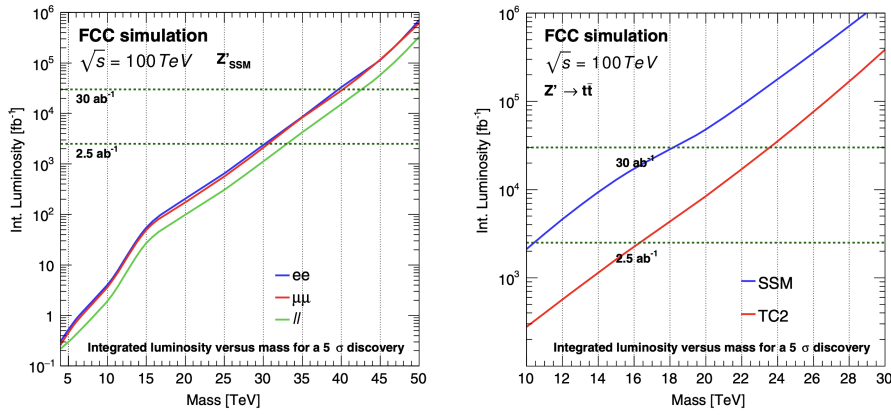


Figure 4.5: Integrated luminosity required for a 5σ discovery as a function of the Z' mass, for a SM-coupled Z' decaying into leptons (left) and top quarks (right) [182].

Beyond discovery, large statistics are essential for improving measurement precision and enhancing sensitivity to rare or elusive processes. The target of 30 ab^{-1} enables sub-percent level precision for several Higgs couplings that are inaccessible to the FCC-ee, including those to $t\bar{t}$, $\gamma\gamma$, $Z\gamma$, and $\mu\mu$. This luminosity also permits the aforementioned measurement of the Higgs trilinear self-coupling with a precision of around 5%. In general, the physics goals outlined in the preceding paragraphs can all be achieved with an integrated luminosity of 30 ab^{-1} . While certain specific measurements might benefit from even higher statistics and could justify more aggressive luminosity targets, no general arguments for a significantly higher baseline luminosity have been established at present. That said, future discoveries—whether from the HL-LHC, anomalies in FCC-ee precision observables, or new phenomena emerging at 100 TeV—may well motivate the need for greater integrated luminosity. Although additional data are always beneficial, there is currently no compelling case for exceeding the 30 ab^{-1} goal.

4.2.2 Detector considerations

FCC-hh is conceived as both a discovery and a precision measurement machine. As such, its detector(s) must be capable of measuring multi-TeV jets, leptons, and photons originating from heavy resonances with masses up to 50 TeV, while simultaneously enabling high-precision measurements of SM processes and being sensitive to a wide spectrum of BSM signatures at moderate transverse momentum.

Given the low mass of SM particles compared to the 100 TeV center-of-mass energy, many processes exhibit strong forward boosts, yet their transverse momentum spectra remain comparable to those at the LHC. A detector for FCC-hh must therefore extend precision tracking and calorimetry coverage to $|\eta| \approx 4$, while maintaining p_T thresholds for triggering and reconstruction similar to those of current LHC detectors.

The large expected PU poses a critical challenge. Whereas current LHC detectors operate with PU levels up to 60 and the HL-LHC will reach up to 200, FCC-hh anticipates up to 1000 PU events per bunch crossing. Addressing this challenge will require novel approaches and continued technological advancements, particularly in high-precision timing detectors.

Figures 4.6 and 4.7 depict the conceptual FCC-hh reference detector. This model is not a finalized technical design but serves as a basis for subsystem development and physics performance studies, helping to identify areas requiring focused R&D. The detector measures 50 m in length and 20 m in diameter—dimensions comparable to the ATLAS detector at the LHC.

The central region ($|\eta| < 2.5$) incorporates tracking, electromagnetic calorimetry, and hadronic calorimetry, all enclosed within a 4 T solenoid with a 10 m inner bore. To maintain performance in the forward region ($|\eta| > 2.5$), two forward solenoids, each with a 5 m bore and a 4 T field, are placed along the beam axis. Together, these provide a total solenoid volume of 32 m in length, supporting high precision momentum spectroscopy up to $|\eta| \approx 4$ and tracking up to $|\eta| \approx 6$.

The tracker aims for better than 20% momentum resolution at $p_T = 10$ TeV for high-mass resonances (e.g. Z') and better than 0.5% at the multiple scattering limit up to $|\eta| = 3$. The tracking cavity has a radius of 1.7 m, with the outermost layer positioned around 1.6 m from the beamline, enabling a full spectrometer arm to $|\eta| = 3$.

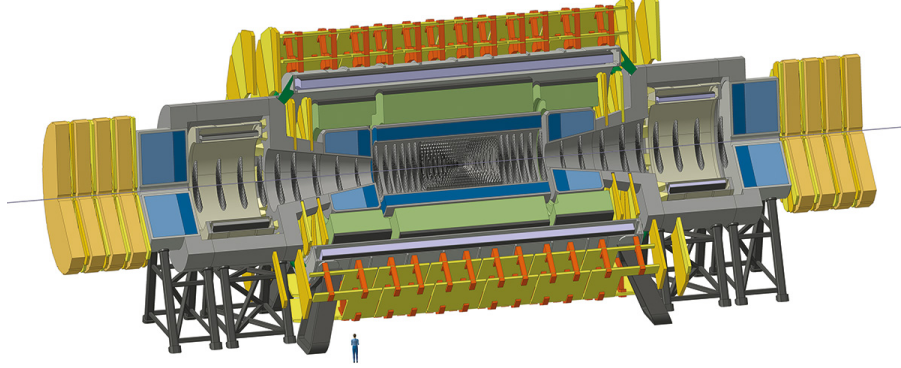


Figure 4.6: The FCC-hh reference detector with an overall length of 50 m and a diameter of 20 m. A central 10 m bore solenoid and two 5 m bore forward solenoids provide a 4 T magnetic field throughout the tracking volume [182].

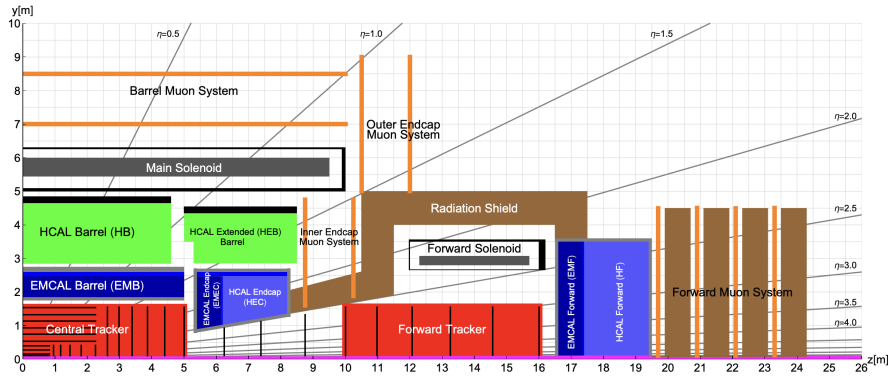


Figure 4.7: Longitudinal cross-section of the FCC-hh reference detector [182].

The ECAL, using approximately 30 radiation lengths, combined with the hadronic calorimeter HCAL, provides a total depth exceeding 10.5 nuclear interaction lengths. This ensures 98% containment of high-energy showers and limits punch-through to the muon system. The ECAL employs liquid argon (LAr) technology for its intrinsic radiation hardness. The barrel HCAL uses scintillating tiles with steel and lead absorbers, segmented into central and extended barrel sections. Endcap and forward HCAL regions also utilize LAr. Achieving calorimetric acceptance up to $|\eta| \approx 6$ requires an inner active radius of just 8 cm at a longitudinal distance of 16.6 m from the interaction point. The ECAL is specified to have an energy resolution of approximately $10\%/\sqrt{E}$, and the HCAL around $50\%/\sqrt{E}$.

Muon system design strongly influences the overall detector layout. In contrast to the LHC design era—when inner tracking capabilities were uncertain—future detectors will rely heavily on silicon-based tracking. Thus, muon systems will prioritize triggering and identification over standalone performance.

No magnetic shielding is assumed in the reference design. A massive iron yoke, as used in CMS, is deemed infeasible due to size and cost. Alternatives such as active shielding coils would demand access shafts exceeding 25 m in diameter. The unshielded coil, by contrast, can be lowered via a 15 m shaft and installed in a 37 m tall, 35 m wide cavern—dimensions similar to ATLAS. The stray magnetic field falls to 5 mT at 50 m radius, eliminating concerns for the adjacent service cavern, located 50 m away and separated by rock (Fig. 4.8).

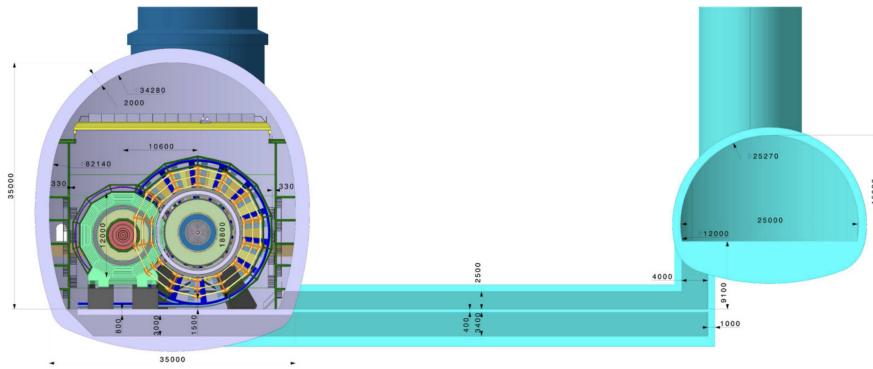


Figure 4.8: FCC-hh and FCC-ee detector caverns. A 50 m separation between the experiment and service caverns ensures minimal stray magnetic field and adequate radiation shielding [182].

Forward calorimetry generates a high flux of low-energy neutrons, some of which penetrate into the tracker volume. A heavy radiation shield surrounds the forward solenoids to prevent neutron ingress into the muon system and experimental cavern.

Radiation levels impose stringent requirements on detector technologies. At the innermost tracker radius ($r = 2.5$ cm), the charged particle rate reaches 10 GHz/cm², falling to 3 MHz/cm² at the outer radii. In the forward ECAL, rates can approach 100 GHz/cm². The 1 MeV neutron-equivalent fluence, critical for assessing long-term damage of silicon sensors and electronics in general, reaches 6×10^{17} /cm² at the first tracker layer, drops below 10^{16} /cm² beyond $r = 40$ cm, and falls to $\sim 5 \times 10^{15}$ /cm² at the outermost radii. Hence,

HL-LHC technologies are applicable beyond 40 cm, while new sensor and electronics solutions are needed for the inner tracker.

In the muon system, charged particle rates are dominated by electrons produced from high-energy photons, themselves resulting from neutron capture and thermalization in hadronic showers. In the barrel and outer endcap muon systems, rates remain below 500 Hz/cm^2 , increasing to 10 kHz/cm^2 in the inner endcap and up to 500 kHz/cm^2 in the forward region at 1 m from the beam. These rates are comparable to those encountered by current ATLAS and CMS muon systems, allowing continued use of gaseous detector technologies.

Future technological advancements may allow more compact detector configurations, e.g. a reduced magnet system without extended forward sections may become feasible. At the same time, future detector advancements might allow resolution and granularity improvements beyond current expectations. These considerations will evolve from future R&D and more detailed detector simulations studies.

4.2.3 Detector simulation

Given that there is no finalized technical design for the FCC-hh detector, a full event simulation is not yet available. Instead, a fast simulation using DELPHES [203] is typically employed. Rather than simulating the time-consuming interactions of stable particles with detector materials, DELPHES uses a parameterized detector response based on resolution and efficiency functions.

The DELPHES framework includes a track propagation system in a magnetic field, electromagnetic and hadronic calorimeters, and a muon identification system. Physics objects for data analysis are reconstructed from the simulated detector response. These include tracks, calorimeter deposits, and high-level objects such as isolated leptons, jets, taus, and missing transverse energy. DELPHES also implements a basic particle-flow reconstruction, which optimally combines tracking and calorimeter information to produce particle candidates. These candidates are then used as inputs for jet clustering, missing energy calculation, and isolation variables. Furthermore, DELPHES provides tools for heavy-flavor tagging and jet substructure analysis.

A comprehensive description of the DELPHES framework is available in Ref. [203]. The FCC-hh-specific DELPHES configuration files can be found in the official DELPHES release [204] and in the FCC-configuration software repository [205]. In the following, the key features are summarized [206].

Tracking Charged particles are propagated in a uniform axial magnetic field of 4 T within a cylindrical tracking volume defined by a radius $R_0 = 1.5$ m and a half-length $Z_0 = 5$ m. A Gaussian smearing is applied to the momentum and angular direction of the particles, with a fixed angular resolution of $\sigma_\theta = 10^{-3}$ rad. The tracking efficiency depends on the transverse momentum p_T and pseudorapidity $|\eta|$ of the particle (see Tables 4.2 and 4.3). If two tracks are within σ_θ , only the one with the highest p_T is kept, modeling reconstruction inefficiencies in dense environments.

p_T range	$ \eta < 2.5$	$2.5 < \eta < 4.0$	$4.0 < \eta < 6.0$	$ \eta > 6.0$
< 0.1 GeV	0%	0%	0%	0%
$0.1\text{--}0.2$ GeV	88%	84%	79%	0%
$0.2\text{--}0.3$ GeV	90%	86%	81%	0%
$0.3\text{--}0.5$ GeV	92%	87%	83%	0%
$0.5\text{--}1.0$ GeV	94%	89%	85%	0%
> 1.0 GeV	95%	90%	86%	0%

Table 4.2: Tracking efficiency for charged hadrons and electrons as a function of p_T and $|\eta|$.

p_T range	$ \eta < 2.5$	$2.5 < \eta < 4.0$	$4.0 < \eta < 6.0$	$ \eta > 6.0$
< 0.1 GeV	0%	0%	0%	0%
$0.1\text{--}0.2$ GeV	97%	95%	92%	0%
$0.2\text{--}0.3$ GeV	97%	95%	92%	0%
$0.3\text{--}0.5$ GeV	97%	95%	92%	0%
$0.5\text{--}1.0$ GeV	97%	95%	92%	0%
> 1.0 GeV	98%	96%	93%	0%

Table 4.3: Tracking efficiency for muons as a function of p_T and $|\eta|$.

Calorimetry Particles reaching the ECAL or HCAL calorimeters are assigned energy deposits based on parameterized resolution functions:

$$\left(\frac{\sigma_E}{E}\right)^2 = \left(\frac{S(\eta)}{\sqrt{E}}\right)^2 + \left(\frac{N(\eta)}{E}\right)^2 + C(\eta)^2,$$

where S , N and C are the stochastic, the noise and the constant terms, respectively. The ECAL is responsible exclusively for electrons, photons, and neutral pions, while the HCAL handles only long-lived hadrons. Muons do not leave deposits in either calorimeter. The values of S , N and C adopted for the FCC-hh calorimeters are summarized in Table 4.4.

Region	N_{ECAL}	S_{ECAL}	C_{ECAL}	N_{HCAL}	S_{HCAL}	C_{HCAL}
$ \eta < 4.0$	31%	8.2	0.15%	5%	48%	1%
$4.0 < \eta < 6.0$	31%	30	3.5%	5%	100%	1%

Table 4.4: ECAL and HCAL resolution parameters as a function of $|\eta|$.

Particle-Flow Reconstruction A simplified PF algorithm combines tracks and calorimeter deposits to optimize particle reconstruction. Charged particle momenta are taken from tracking when the resolution is better than calorimetry (typically up to several hundred GeV). Vice-versa at high energy, calorimeters provide a better momentum measurement. Neutral PF candidates are created when energy excesses are seen in calorimeter towers. PF objects, both charged and neutral, are used for jet clustering, lepton/photon isolation, and missing energy reconstruction. This hybrid approach improves energy resolution across a wide range of particle energies.

Object Identification Electrons, muons, and photons from PF candidates are assigned identification probabilities according to Tables 4.5, 4.6 and 4.7. For charged particles the identification efficiency is applied on top of the tracking efficiency. The isolation variable I is defined as:

$$I = \frac{\sum_{\Delta R < R, p_T(i) > p_T^{\min}} p_T(i)}{p_T(p)},$$

where the sum runs over the full list of PF candidates within a cone R excluding the particle under consideration.

p_T range	$ \eta < 2.5$	$2.5 < \eta < 4.0$	$4.0 < \eta < 6.0$	$ \eta > 6.0$
< 1.0 GeV	0%	0%	0%	0%
1–5 GeV	80%	80%	75%	0%
5–10 GeV	90%	85%	80%	0%
> 10 GeV	95%	90%	85%	0%

Table 4.5: Electron identification efficiency.

p_T range	$ \eta < 2.5$	$2.5 < \eta < 4.0$	$4.0 < \eta < 6.0$	$ \eta > 6.0$
< 1.0 GeV	0%	0%	0%	0%
1–5 GeV	95%	90%	85%	0%
5–10 GeV	97%	95%	90%	0%
> 10 GeV	99.9%	99%	95%	0%

Table 4.6: Muon identification efficiency.

p_T range	$ \eta < 2.5$	$2.5 < \eta < 4.0$	$4.0 < \eta < 6.0$	$ \eta > 6.0$
< 1.0 GeV	0%	0%	0%	0%
1–5 GeV	76%	76%	71%	0%
5–10 GeV	86%	81%	76%	0%
> 10 GeV	90%	86%	81%	0%

Table 4.7: Photon identification efficiency.

Jets and Missing Energy The missing transverse energy is computed as the magnitude of the total transverse momentum carried by the full list of reconstructed PF candidates. Jets are reconstructed using the anti- k_T algorithm with multiple radius parameters ($R = 0.2, 0.4, 0.8, 1.5$). Several jet collections are formed using different inputs (track-based, calorimeter-based, or PF-based). Jet substructure observables like N -subjettiness and soft-drop mass are computed and stored for each jet.

Heavy-Flavor Tagging The identification of jets that result from τ_h decays or the hadronization of heavy flavor quarks—typically b or c quarks—usually exploits tracking information, such as vertex displacement or low level detector input such as hit multiplicity. Such information is not available as a default in DELPHES. Therefore a purely parametric approach based on Monte-Carlo

generator information is used. The tagging efficiencies and misidentification rates depend on p_T and $|\eta|$, following Table 4.8 for b-tagging and Table 4.9 for τ_h tagging for the so-called *medium* working point.

p_T range	$ \eta < 4.0$	$ \eta > 4.0$
b-tagging efficiency		
< 20.0 GeV	0%	0%
20–50 GeV	75%	0%
50–100 GeV	84%	0%
100–200 GeV	85%	0%
200–500 GeV	83%	0%
500–1000 GeV	80%	0%
> 1000 GeV	80%	0%
c-mistag efficiency		
< 20.0 GeV	0%	0%
20–50 GeV	20%	0%
50–100 GeV	15%	0%
100–200 GeV	13%	0%
200–500 GeV	12%	0%
500–1000 GeV	11%	0%
> 1000 GeV	10%	0%
light mistag efficiency		
< 20.0 GeV	0%	0%
20–50 GeV	1.5%	0%
50–100 GeV	0.8%	0%
100–200 GeV	0.6%	0%
200–500 GeV	0.8%	0%
500–1000 GeV	1%	0%
> 1000 GeV	1.2%	0%

Table 4.8: B-tagging efficiencies and misidentification rates as a function of p_T and $|\eta|$.

This parameterized framework enables studies of realistic detector performance in FCC-hh, supporting physics projections and detector optimization for different operational scenarios.

p_T range	$ \eta < 4.0$	$ \eta > 4.0$
τ_h-tagging efficiency		
< 20.0 GeV	0%	0%
20–100 GeV	80%	0%
> 100 GeV	88%	0%
jet-mistag efficiency		
< 20.0 GeV	0%	0%
20–100 GeV	2%	0%
> 100 GeV	1%	0%

Table 4.9: τ_h -tagging efficiencies and $\text{jet} \rightarrow \tau_h$ misidentification rates as a function of p_T and $|\eta|$.

4.3 A physics case: Higgs boson characterization with the FCC program

The characterization of the Higgs boson is a central objective in current and future high-energy physics experiments. It provides a compelling physics case to illustrate the reach of the FCC program, particularly emphasizing the strong synergy between its lepton and hadron collider phases [186].

As shown in several studies [207–209], FCC-ee offers unparalleled opportunities for probing the Higgs boson beyond the capabilities of the HL-LHC or other proposed Higgs factories [210]. The expected improvements in the precision of Higgs boson coupling measurements are summarized in Table 4.10.

FCC-ee will quickly reach a regime of sub-percent precision in Higgs couplings, enabling not only the (indirect) detection of new physics but also the extraction of patterns indicative of specific BSM scenarios. These precision goals can be achieved in three years at $\sqrt{s} = 240$ GeV and in eight years at 365 GeV. By contrast, linear collider proposals at CERN would require several decades to match this level of sensitivity [212].

As Higgs measurements grow more precise, limitations from current electroweak inputs—such as those from LEP—will become significant. FCC-ee’s Z-pole run is essential to mitigate uncertainties in electroweak couplings, in particular the Zee vertex, which enters directly into the ZH production. The required precision on this vertex can be achieved using just a few 10^9 Z decays—less than a day of data taking. The Zee vertex components (left- and right-handed couplings) can be extracted from the partial width $\Gamma(Z \rightarrow e^+e^-)$

Coupling	HL-LHC	FCC-ee	FCC-ee + FCC-hh
κ_Z (%)	1.3*	0.10	0.10
κ_W (%)	1.5*	0.29	0.25
κ_b (%)	2.5*	0.38 / 0.49	0.33 / 0.45
κ_g (%)	2*	0.49 / 0.54	0.41 / 0.44
κ_τ (%)	1.6*	0.46	0.40
κ_c (%)	—	0.70 / 0.87	0.68 / 0.85
κ_γ (%)	1.6*	1.1	0.30
$\kappa_{Z\gamma}$ (%)	10*	4.3	0.67
κ_t (%)	3.2*	3.1	0.75
κ_μ (%)	4.4*	3.3	0.42
$ \kappa_s $ (%)	—	$^{+29}_{-67}$	$^{+29}_{-67}$
Γ_H (%)	—	0.78	0.69
$\mathcal{B}_{\text{inv}} (<, 95\% \text{ CL})$	$1.9 \times 10^{-2*}$	5×10^{-4}	2.3×10^{-4}
$\mathcal{B}_{\text{unt}} (<, 95\% \text{ CL})$	$4 \times 10^{-2*}$	6.8×10^{-3}	6.7×10^{-3}

Table 4.10: Expected 68% CL relative precision on Higgs couplings relative to the SM (κ parameters), total Higgs width Γ_H , and 95% CL upper limits on the invisible (\mathcal{B}_{inv}) and untagged (\mathcal{B}_{unt}) branching ratios. Results are shown for HL-LHC, FCC-ee, and the full FCC integrated program (FCC-ee + FCC-hh). HL-LHC numbers are derived under the constraint $|\kappa_V| \leq 1$ (denoted with *), since hadron colliders cannot access Γ_H directly. In some entries, SM parametric uncertainties (e.g. in m_b [211]) limit precision; values excluding these are also provided (after the slash). Taken from Ref. [186].

and from left-right asymmetry observables. These play a central role in disentangling new physics contributions in the SMEFT framework [208], and mitigate the EW contamination in the Higgs couplings determination.

As shown in Table 4.10, FCC measurements will reduce uncertainties in most Higgs couplings by an order of magnitude compared to the HL-LHC. Couplings such as κ_μ , κ_γ , κ_t and $\kappa_{Z\gamma}$ will initially remain dominated by the HL-LHC knowledge, but their model dependence will be lifted thanks to FCC-ee’s absolute κ_Z measurement. FCC-hh will further improve these precisions by using ratios of branching ratios, free of systematic uncertainties and normalized by the FCC-ee precise coupling determination. The successive improvements on the Higgs boson coupling precision when going from HL-LHC to FCC-hh, taking advantage on the way from the FCC-ee absolute and accurate coupling determination, are shown in Fig. 4.9.

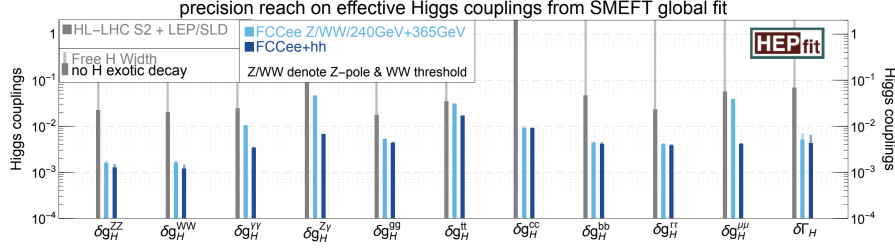


Figure 4.9: Projected Higgs coupling precision improvements from HL-LHC to FCC-hh using global SMEFT fits and FCC-ee input [186].

FCC-ee also enables a model-independent determination of the top Yukawa coupling by normalizing HL-LHC data with the absolute measurement of κ_Z . In addition, $e^+e^- \rightarrow t\bar{t}$ at 365 GeV allows extraction of Ztt couplings, which are critical for normalizing $t\bar{t}H$ production at FCC-hh. This calibration reduces top Yukawa coupling uncertainties to the percent level. The impact of FCC-ee on both κ_t and the Higgs self-coupling κ_λ is shown in Fig. 4.10.

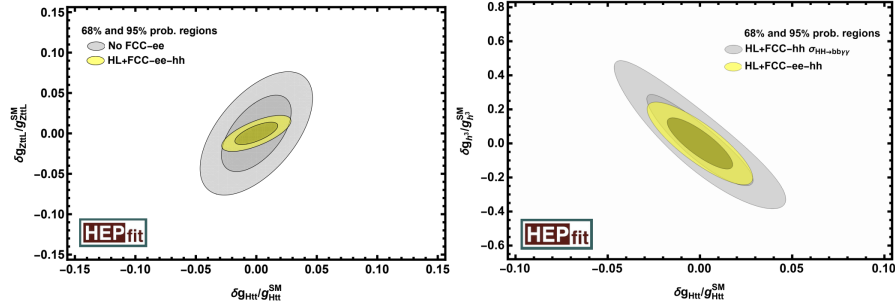


Figure 4.10: Effect of FCC-ee input on FCC-hh determination of the top Yukawa coupling (left) and Higgs self-coupling κ_λ (right), based on toy fits to simulated $HH \rightarrow b\bar{b}\gamma\gamma$ data [186].

The Higgs self-coupling κ_λ will be probed at HL-LHC with an uncertainty estimated at the time of the 2020 European Strategy to be about 50%, in a fit where only deformations of κ_λ are allowed. Since then, improved analysis techniques and the inclusion of additional decay channels have reduced this uncertainty to 26% [202]. At FCC-ee, loop corrections to Higgs production enable a stand-alone extraction of κ_λ at 28% precision, without assumptions on other couplings. Combining FCC-ee with HL-LHC further reduces the uncertainty to 18%.

The Higgs self-coupling will be uniquely and unambiguously probed at FCC-hh via Higgs boson pair production. Current estimates, combining the main decay channels, suggest that a precise determination, with an uncertainty as small as 3.4%, would be within the reach of a 100 TeV pp collider, and probably better by a factor of two as suggested by recent studies [7, 9], including the one presented in this thesis work in Chapter 8.

Figure 4.11 summarizes the expected precision at different FCC stages.

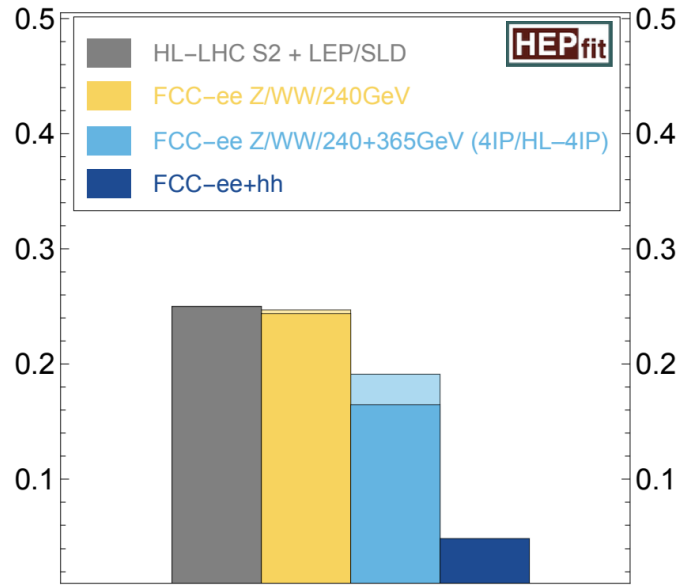


Figure 4.11: Progress in the precision on κ_λ , from FCC-ee to FCC-hh [186].

The FCC-hh projections for κ_λ assume that new physics affects only the Higgs self-coupling. In realistic scenarios, other effective operators could impact Higgs pair production. As illustrated in Fig. 4.10 (right), uncertainties in the top Yukawa coupling propagate into κ_λ extractions due to its presence in multiple diagrams contributing to $gg \rightarrow HH$. Precise control over κ_t —enabled by FCC-ee—therefore enhances the robustness of κ_λ measurements.

In conclusion, the FCC program’s unique combination of lepton and hadron collider stages offers a coherent and comprehensive approach to Higgs boson characterization. The synergetic use of FCC-ee and FCC-hh enables a level of precision that is not otherwise attainable, reinforcing the necessity of pursuing the full FCC vision as a long-term strategy for particle physics.

Chapter 5

Data Analysis Methods and Machine Learning Tools

Statistical analysis plays a crucial role in experimental physics, providing the tools needed to quantify the agreement between theoretical predictions and experimental data. The first part of this chapter introduces fundamental concepts such as statistical models, likelihoods, and related principles to ensure their meaning is clear when referenced in Chapters 6, 7 and 8. More details can be found in Refs. [213–215]. The second part of this chapter outlines the growing use of Machine Learning (ML) in High Energy Physics, with a focus on Deep Neural Networks (DNNs) and Convolutional Neural Networks (CNNs), whose concepts will be applied in Chapters 7–8 and Chapter 6, respectively.

5.1 From statistical models to likelihoods

Statistical models constitute the foundation of statistical inference and are therefore a prerequisite for any rigorous discussion of likelihood-based methods in High Energy Physics. Formally, a statistical model is a mathematical representation of a system that incorporates a set of assumptions about the underlying data-generating process and the theoretical framework under investigation. A classical example is linear regression, which models the relationship between a dependent variable and one or more independent variables under defined assumptions.

Statistical models provide a principled framework for interpreting experimental data. Let x denote a set of observed values, which may represent a single collision event, a group of events, or complex structures such as reconstructed particle tracks in the CMS detector. These observables may comprise both discrete and continuous components. Let α denote the set of model pa-

rameters, which could include detector response functions, calibration coefficients, or other quantities characterizing the system.

Due to intrinsic statistical fluctuations and experimental uncertainties, repeated measurements under fixed values of α will typically yield different outcomes. As a result, statistical models are generally expressed as probability density functions $p(x|\alpha)$, which describe the distribution of possible observations x conditional on a given parameter set α . These models are inherently probabilistic rather than deterministic, reflecting the stochastic nature of experimental measurements.

Central to the application of statistical models is the *likelihood function*, denoted $L(\alpha)$ or, more explicitly, $L(x|\alpha)$. Although often mistakenly equated with probability, the likelihood function is fundamentally different: it is a function of the parameters α , given fixed observed data x . It quantifies the degree of agreement between the observed data and the model specified by α . A well-formulated model will produce a likelihood function that assigns relatively high values to the observed data, indicating that the model parameters are consistent with the empirical evidence.

The likelihood function is instrumental in tasks such as parameter estimation, hypothesis testing, and model comparison, making it a central tool in modern data analysis.

5.2 The maximum likelihood estimation

In statistics, the *Maximum Likelihood Estimation* (MLE) is a method for estimating the parameters of a statistical model, given observed data. This is achieved by maximizing a likelihood function such that, under the assumed model, the observed data are the most probable. The value of the parameter that maximizes the likelihood function is referred to as the *maximum likelihood estimate*.

In many scenarios, the likelihood is a function of multiple parameters. However, in searches for new physics, the interest often focuses on estimating a single parameter, typically referred to as the *parameter of interest*. In this context, we denote it by μ , which commonly represents the *signal strength*. It is defined such that, $\mu = 0$ corresponds to the background-only hypothesis and $\mu = 1$ corresponds to the nominal signal+background hypothesis.

Consider a simplified case with a single analysis channel, consisting of one signal and one background component, and no systematic uncertainties. Let S and B denote the expected number of signal and background events, respec-

tively. The shapes of the signal and background distributions are denoted by $f_S(x)$ and $f_B(x)$, respectively, and are probability density functions normalized so that $\int dx f(x) = 1$. Given n observed events with observable values $\{x_1, \dots, x_n\}$, the likelihood function can be written as the product of a Poisson probability for observing n events when $\mu S + B$ are expected, and the probability density of obtaining x_e for event e based on the relative mixture $f_S(x)$ and $f_B(x)$ for a given value of μ :

$$P(\{x_1, \dots, x_n\} | n) = \text{Pois}(n | \mu S + B) \prod_{e=1}^n \frac{\mu S f_S(x_e) + B f_B(x_e)}{\mu S + B}. \quad (5.1)$$

If one imagines the data as being fixed, then this equation depends on μ and is called the likelihood function $L(\mu)$. Since the logarithm is a strictly increasing function, maximizing the likelihood is equivalent to maximizing the log-likelihood. This transformation is often preferred due to its favorable mathematical properties and improved numerical stability. Using $\text{Pois}(n | \nu) = \frac{\nu^n e^{-\nu}}{n!}$, the negative log-likelihood can be written as:

$$\begin{aligned} -\ln L(\mu) &= -n \ln(\mu S + B) + (\mu S + B) + \ln n! - \sum_{e=1}^n \ln \left[\frac{\mu S f_S(x_e) + B f_B(x_e)}{\mu S + B} \right] \\ &= (\mu S + B) + \ln n! - \sum_{e=1}^n \ln [\mu S f_S(x_e) + B f_B(x_e)], \end{aligned} \quad (5.2)$$

In practice, data are commonly binned into histograms. Let ν_b^{sig} and ν_b^{bkg} denote the expected number of signal and background events in bin b . The corresponding probability densities can then be written as:

$$f_S(x_e) = \frac{\nu_b^{\text{sig}}}{S \Delta_{b_e}}, \quad f_B(x_e) = \frac{\nu_b^{\text{bkg}}}{B \Delta_{b_e}}, \quad (5.3)$$

where b_e is the index of the bin containing x_e events and Δ_{b_e} is the width of that bin. Note that because the $f(x)$ are normalized to unity we have $S = \sum_b \nu_b^{\text{sig}}$ and $B = \sum_b \nu_b^{\text{bkg}}$. The binned likelihood becomes a product over Poisson probabilities for each bin:

$$\begin{aligned}
P(n_b|\mu) &= \text{Pois}(n_{\text{tot}}|\mu S + B) \prod_{b \in \text{bins}} \frac{\mu \nu_b^{\text{sig}} + \nu_b^{\text{bkg}}}{\mu S + B} \\
&= N_{\text{comb}} \prod_{b \in \text{bins}} \text{Pois}(n_b|\mu \nu_b^{\text{sig}} + \nu_b^{\text{bkg}}), \tag{5.4}
\end{aligned}$$

where n_b is the data histogram and N_{comb} is a combinatorial factor that can be neglected since it is constant.

In realistic analyses, the likelihood often depends on additional parameters not of direct interest—so-called *nuisance parameters*. These can represent modeling uncertainties, detector effects, or limited Monte Carlo statistics. Their presence complicates inference but is essential for accurately accounting for uncertainties.

In a generalization of the above model, the CMS experiment employs the COMBINE tool [216] to construct parameterized probability density functions (pdfs) using the ROOFIT [217] and ROOSTATS [218] frameworks. The tool is especially suited to binned template-based analyses, where the expected distributions of signal and background processes are provided as histograms. The full likelihood model used in inference is constructed incorporating:

- **Multiple channels:** Each corresponding to a distinct event category or selection region.
- **Multiple samples:** Including various signal and background processes.
- **Normalization factors:** Such as the signal strength parameter of interest μ , or additional unconstrained normalizations for background control.
- **Systematic uncertainties:** Implemented via nuisance parameters that modify yields and/or shapes, often correlated across processes and channels. The following notation is used in this thesis in order to discuss the systematic uncertainties:
 - **rate parameter:** it alters the normalization of a process. The corresponding nuisance parameter is assigned a pdf uniform within a defined range.
 - **lnN:** log-normal uncertainty, it alters the normalization of a process and the corresponding nuisance parameter is assigned a log-normal pdf.

- **lnU**: log-uniform uncertainty, it alters the normalization of a process and the corresponding nuisance parameter is assigned a log-uniform pdf within a given range.
- **shape**: dedicated templates are created representing the systematic variation with respect to the nominal distribution, it is used to treat uncertainties which do not simply alter the normalization of a template. The corresponding nuisance parameter is assigned a Gaussian pdf.
- **shapeU**: uniform shape uncertainty, it alters the shape of the distribution like the shape uncertainties. The associated nuisance parameter is instead assigned a uniform pdf within a given range.
- **Statistical uncertainties**: Bin-by-bin uncertainties due to finite Monte Carlo sample sizes, modeled using constrained nuisance parameters.

Each channel contains a set of binned templates for the processes under consideration. The templates are translated into pdfs that are parameterized by normalization coefficients and modified by shape morphing techniques to account for systematic effects.

The pdfs can be expressed with the following form, using the indices e for events, b for bins, c for channels, s for samples and p for parameters,

$$P(n_c, x_e, a_p | \phi_p, \alpha_p, \gamma_b) = \prod_{c \in \text{channels}} \left[\text{Pois}(n_c | \nu_c) \prod_{e=1}^{n_c} f_c(x_e | \alpha) \right] \times \prod_{p \in S + \Gamma} f_p(a_p | \alpha_p), \quad (5.5)$$

where:

- the following subsets of parameters are defined: $\{\phi_p\}$ are the unconstrained normalization factors (including μ for the signal), $S = \{\alpha_p\}$ are the parameters associated to systematics that have external constraints, $\Gamma = \{\gamma_{csb}\}$ are the bin-by-bin uncertainties associated to statistical errors,
- $f_p(a_p | \alpha_p)$ describes an auxiliary measurement a_p that constrains the nuisance parameter α_p .

The expected number of events in a given bin b of channel c is:

$$\nu_{cb}(\phi_p, \alpha_p, \gamma_b) = \gamma_{cb} \phi_{cs}(\alpha) \eta_{cs}(\alpha) \sigma_{csb}(\alpha), \quad (5.6)$$

where:

- γ_{cb} is the bin-by-bin scale factor used for statistical uncertainties,
- $\phi_{cs}(\alpha)$ is the product of unconstrained normalization factors for a given sample within a given channel (including μ),
- $\eta_{cs}(\alpha)$ is the parametrized normalization uncertainties for a given sample within a given channel,
- $\sigma_{csb}(\alpha)$ is the parametrized histogram for a given sample within a given channel (including shape variation due to systematic effect).

The mean number of events in each bin implies the following event-level probability density

$$f_c(x_e | \phi_p, \alpha_p, \gamma_b) = \frac{\nu_{cbe}}{\nu_c}, \quad \text{with} \quad \nu_c = \sum_{b \in \text{bins of } c} \nu_{cb}. \quad (5.7)$$

It is perhaps more convenient to think of the likelihood as a product over bins:

$$P(n_{cb}, a_p | \phi_p, \alpha_p, \gamma_b) = \prod_{c \in \text{channels}} \prod_{b \in \text{bins}} \text{Pois}(n_{cb} | \nu_{cb}) \prod_{p \in S + \Gamma} f_p(a_p | \alpha_p). \quad (5.8)$$

This likelihood is maximized to find the maximum likelihood estimates for the model parameters. The most used tool in CMS to perform this operation is MINUIT [219], which equivalently minimizes the negative log-likelihood function.

5.3 Discovery as hypothesis test

In particle physics, we frequently quantify the significance of an observed signal by quoting the p-value of the background-only hypothesis. One method for defining the p-value for a hypothesized value of μ is to construct a test statistic based on the profile likelihood ratio. The parameter of interest is the overall signal strength factor μ , which acts as a scaling to the total rate of signal events.

It is convenient to separate the full list of parameters α into the parameter of interest μ and the nuisance parameters θ : $\alpha = (\mu, \theta)$.

For a given data set and values for the observable, there is an associated likelihood function $L(\mu, \theta)$. Let's assume $\hat{\mu}$ and $\hat{\theta}$ are the values of the parameters that maximize the likelihood function $L(\mu, \theta)$ or equivalently minimize $-\ln L(\mu, \theta)$ and $\hat{\hat{\theta}}(\mu)$ is a conditional maximum likelihood estimate of θ that maximizes the likelihood function with μ fixed; this procedure for choosing specific values of the nuisance parameters for a given value of μ is often referred to as “profiling”. Similarly $\hat{\hat{\theta}}(\mu)$ is often referred to as “the profiled value of θ ”. Given these definitions, we can construct the profile likelihood ratio

$$\lambda(\mu) = \frac{L(\mu, \hat{\hat{\theta}}(\mu))}{L(\hat{\mu}, \hat{\theta})}, \quad (5.9)$$

which depends explicitly on the parameter of interest μ , implicitly on the data set and observables, and is independent of the nuisance parameters θ (which have been eliminated via profiling). Despite the fact that the rate of signal events is non-negative, thus $\mu \geq 0$, it is often convenient to allow $\mu < 0$ (which indicates a deficit of events signal-like with respect to the background only) as long as the pdf, $f_c(x_c|\mu, \theta) \geq 0$ everywhere. We define the test statistic \tilde{q}_μ to differentiate the hypothesis of a signal being produced at a rate μ from the alternative hypothesis of signal events being produced at a lower rate:

$$\tilde{q}_\mu = \begin{cases} -2\ln\tilde{\lambda}(\mu) & \hat{\mu} \leq \mu \\ 0 & \hat{\mu} > \mu \end{cases} = \begin{cases} -2\ln\frac{L(\mu, \hat{\hat{\theta}}(\mu))}{L(0, \hat{\hat{\theta}}(0))} & \hat{\mu} < 0 \\ -2\ln\frac{L(\mu, \hat{\hat{\theta}}(\mu))}{L(\hat{\mu}, \hat{\theta})} & 0 \leq \hat{\mu} \leq \mu \\ 0 & \hat{\mu} > \mu \end{cases} \quad (5.10)$$

Note that \tilde{q}_μ is a test statistic for a one-sided alternative (one-sided upper limit). The test statistic \tilde{t}_μ is used to differentiate signal being produced at a rate μ from the alternative hypothesis of signal events being produced at a lower or greater rate of μ (two-sided alternative),

$$\tilde{t}_\mu = -2\ln\tilde{\lambda}(\mu) \quad (5.11)$$

If we consider the parameter of interest $\mu \geq 0$ and we test at $\mu = 0$ then there is no “other side” and we have $\tilde{t}_{\mu=0} = \tilde{q}_0$. Finally, if one relaxes the constraint $\mu \geq 0$ then the two-sided test statistic is written t_μ or, simply, $-2\ln\lambda(\mu)$.

The test statistic should be interpreted as a single real-valued number that represents the outcome of the experiment. More formally, it is a mapping of the data to a single real-valued number. For the observed data the test statistic has a given value, $\tilde{q}_{\mu,\text{obs}}$. If one were to repeat the experiment many times the test statistic would take on different values, thus, conceptually, the test statistic has a distribution. Similarly, we can use our model to generate pseudo-experiments using Monte Carlo techniques or more abstractly consider the distribution. Since the number of expected events $\nu(\mu, \theta)$ and the distributions of the observable $f_c(x_c|\mu, \theta)$ explicitly depend on θ the distribution of the test statistic will also depend on θ . Let us denote this distribution

$$f(\tilde{q}_\mu|\mu, \vec{\theta}) . \quad (5.12)$$

The p -value for a given observation under a particular hypothesis (μ, θ) is the probability for an equally or more ‘extreme’ outcome than observed assuming that hypothesis

$$p_{\mu, \vec{\theta}} = \int_{\tilde{q}_{\mu, \text{obs}}}^{\infty} f(\tilde{q}_\mu|\mu, \theta) d\tilde{q}_\mu . \quad (5.13)$$

With this definition, small p -values are evidence against the corresponding hypothesis. The immediate difficulty is that we are interested in μ but the p -values depend on both μ and θ . In the frequentist approach the hypothesis $\mu = \mu_0$ would not be rejected unless the p -value is sufficiently small *for all* values of θ . Equivalently, one can use the supremum p -value for over all θ to base the decision to accept or reject the hypothesis at $\mu = \mu_0$.

$$p_\mu^{\text{sup}} = \sup_{\theta} p_{\mu, \theta} \quad (5.14)$$

The key conceptual reason for choosing the test statistics based on the profile likelihood ratio is that, according to Wilks’s theorem [220], asymptotically (i.e. when there are many events) the distribution of the profile likelihood ratio $\lambda(\mu = \mu_{\text{true}})$ is independent of the values of the nuisance parameters. In that limit $p_\mu^{\text{sup}} = p_{\mu, \theta}$ for all θ .

Since there may still be some residual dependence of the p -values on the choice of θ we would like to know the specific value of θ^{sup} that produces the supremum p -value over θ . Since larger p -values indicate better agreement of

the data with the model, it is not surprising that choosing $\theta^{\text{sup}} = \hat{\hat{\theta}}(\mu)$ is a good estimate.

Based on the discussion above, the following p -value is used to quantify consistency with the hypothesis of a signal strength of μ :

$$p_\mu = \int_{\tilde{q}_{\mu, \text{obs}}}^{\infty} f(\tilde{q}_\mu | \mu, \hat{\hat{\theta}}(\mu, \text{obs})) d\tilde{q}_\mu . \quad (5.15)$$

The 95% confidence-level upper limit in the so-called *modified frequentist approach*, CL_s , is calculated defining p'_μ as a ratio of p -values,

$$p'_\mu = \frac{p_\mu}{1 - p_b} , \quad (5.16)$$

where p_b is the p -value derived from the same test statistic under the background-only hypothesis

$$p_b = 1 - \int_{\tilde{q}_{\mu, \text{obs}}}^{\infty} f(\tilde{q}_\mu | 0, \hat{\hat{\theta}}(\mu = 0, \text{obs})) d\tilde{q}_\mu . \quad (5.17)$$

The CL_s upper-limit on μ is denoted μ_{up} and obtained by solving for $p'_{\mu_{up}} = 5\%$.

For discovery purposes, one is interested in compatibility of the data with the background-only hypothesis. Statistically, a discovery corresponds to rejecting the background-only hypothesis. This compatibility is based on the following p -value

$$p_0 = \int_{\tilde{q}_{0, \text{obs}}}^{\infty} f(\tilde{q}_0 | 0, \hat{\hat{\theta}}(\mu = 0, \text{obs})) d\tilde{q}_0 . \quad (5.18)$$

This p -value is also based on the background-only hypothesis, but the test statistic \tilde{q}_0 is suited for testing the background-only while the test statistic \tilde{q}_μ in Eq. 5.17 is suited for testing a hypothesis with signal.

It is customary to convert the background-only p -value into the quantile (or “sigma”) of a unit Gaussian. This conversion is purely conventional and makes no assumption that the test statistic q_0 is Gaussian distributed. The conversion is defined as:

$$Z = \Phi^{-1}(1 - p_0); \quad (5.19)$$

where Φ^{-1} is the inverse of the cumulative distribution for a unit Gaussian. One says the significance of the result is $Z\sigma$ and the standard discovery convention is 5σ , corresponding to $p_0 = 2.87 \cdot 10^{-7}$.

5.3.1 Expected sensitivity and bands

The expected sensitivity for limits and discovery are useful quantities, though subject to some degree of ambiguity. Intuitively, the expected upper limit is the upper limit one would expect to obtain if the background-only hypothesis is true. Similarly, the expected significance is the significance of the observation assuming some model signal rate. To find the expected limit one needs a distribution $f(\mu_{up}|\mu = 0, \theta)$. To find the expected significance one needs the distribution $f(Z|\mu = 1, \theta)$ or, equivalently, $f(p_0|\mu = 1, \theta)$. We use the median instead of the mean, as it is invariant to the choice of Z or p_0 . The expected limit and significance depend on the value of the nuisance parameters θ , for which we do not know the true values. The convention is then to use the profiled values of the nuisance parameters based on the observed data. Thus, for the expected limit we consider $f(\mu_{up}|0, \hat{\hat{\theta}}(\mu = 0, \text{obs}))$ and for the expected significance we use $f(p_0|\mu = 1, \hat{\hat{\theta}}(\mu = 1, \text{obs}))$. A consequence of this choice is that the expected limit and significance depend on the observed data through the conventional choice for θ . With these distributions we can also define bands around the median upper limit. CMS standard limit plot shows a dark green band corresponding to $\mu \pm 1$ defined by

$$\int_0^{\mu \pm 1} f(\mu_{up}|0, \hat{\hat{\theta}}(\mu = 0, \text{obs})) d\mu_{up} = \Phi^{-1}(\pm 1). \quad (5.20)$$

and a light yellow band corresponding to $\mu \pm 2$ defined by

$$\int_0^{\mu \pm 2} f(\mu_{up}|0, \hat{\hat{\theta}}(\mu = 0, \text{obs})) d\mu_{up} = \Phi^{-1}(\pm 2). \quad (5.21)$$

An example of such a plot is shown in Fig. 5.1.

5.3.2 Goodness of fit

A goodness-of-fit (GOF) test is a test of the null hypothesis when the alternative hypothesis is not specified. Since Neyman and Pearson taught us that (even for simple hypotheses) the best test of the null hypothesis depends on the alternative [222], there is no universally best GOF test. Nonetheless, the ubiquity of the χ^2 GOF test attests to its utility, at least for picking up cer-

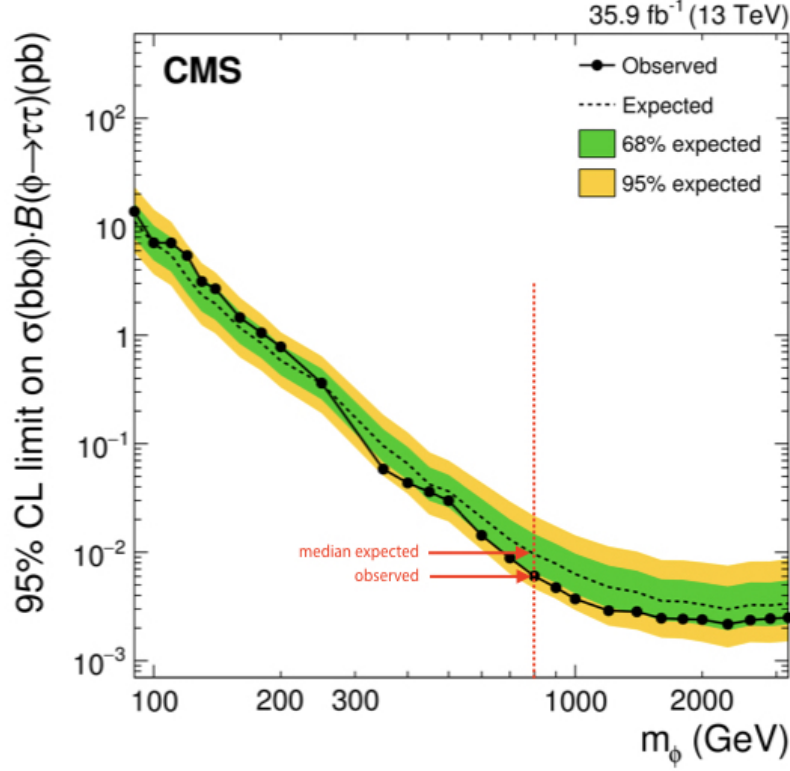


Figure 5.1: Expected and observed 95% CL upper limits on the product of the cross sections and branching fraction for the decay into τ leptons for the $bb\phi$ production. The expected median of the exclusion limit in the absence of signal is shown by the dashed line. The dark green and bright yellow bands indicate the central 68% and 95% intervals for the expected exclusion limit. The black dots correspond to the observed limits [221].

tain departures from the null hypothesis. In its usual form for uncorrelated Gaussian distributed data, one has

$$\chi^2 = \sum_i (d_i - f_i)^2 / \sigma_i^2, \quad (5.22)$$

where $d_i \pm \sigma_i$ is the i th measured data point with rms deviation σ_i (each assumed to be a known constant), and f_i is the model prediction, perhaps with parameters. Considered as a random variable (since a function of the random data), in many applications this test statistic, χ^2 , has a probability density

which is also frequently called the χ^2 function. For the same data and model as above, the likelihood is:

$$L = \prod_i \frac{1}{\sqrt{2\pi\sigma_i^2}} \exp\left(-\frac{(d_i - f_i)^2}{2\sigma_i^2}\right) \quad (5.23)$$

leading to the common statement that $-2\ln L$ is equal to χ^2 ; this is of course not correct since the former quantity has extra constants. According to Wilks's theorem, likelihood ratios obeying important regularity conditions have asymptotic probability densities which also follow the χ^2 probability density. Likelihoods have the appealing property of being independent of the metric in which parameters are described. Likelihood ratios inherit this property and furthermore are invariant under change of metrics in which the data are described. As seen previously, likelihood ratios, λ , are generally useful for comparing two hypotheses. Now they can be used as a basis for a generalization of Eq. 5.22 that is the one used for GOF test in the CMS COMBINE tool [216].

Given only a null hypothesis and the data, one can invent an alternative hypothesis for which f_i is equal to the data d_i at every measured value. Such a model, which typically needs as many parameters as there are data points, is called a *saturated model* [223]. In some circumstances, saturated models can be useful for comparisons with the null hypothesis, and in particular for providing a denominator in the likelihood ratio. For the Gaussian data above, the saturated model sets $f_i = d_i$, so that the likelihood of the data in the saturated model is

$$L_{\text{saturated}} = \prod_i \frac{1}{\sqrt{2\pi\sigma_i^2}} \quad (5.24)$$

The ratio of the two likelihoods above is then

$$\lambda = \prod_i \exp\left(-\frac{(d_i - f_i)^2}{2\sigma_i^2}\right) \quad (5.25)$$

and thus, importantly

$$\chi^2 = -2 \ln \lambda \quad (5.26)$$

From this point of view, the constants in $-2 \ln L$ were not just ignored; they were canceled when a ratio was formed. Since the saturated model does not depend on the parameters of the original model, the maximum of λ is of course at those parameters that maximize the original L .

The GOF method in CMS COMBINE evaluates a test statistic for the observed data and generates the expected distribution of the test statistic under the null distribution using pseudo-data. These can be used to determine a p-value under the null hypothesis. Figure 5.2 shows the distribution of the saturated test statistic in pseudo-data using an example statistical model as reported in Ref. [216].

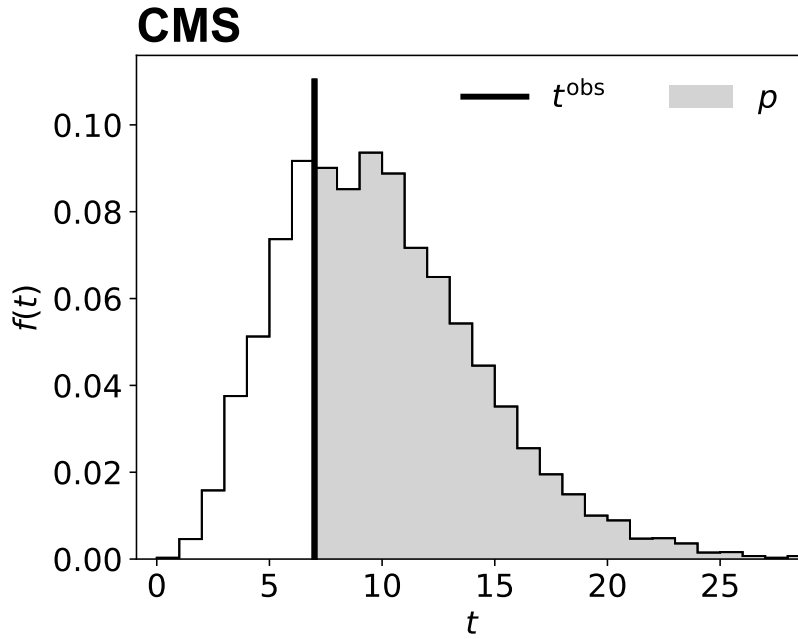


Figure 5.2: Distribution of the saturated test statistic (here called t) in 10,000 pseudo-data sets. The observed value of the test statistic is indicated by the black vertical line and the region used to determine p is indicated by the light gray shaded region.

5.4 Machine Learning Tools

Machine Learning techniques have become integral to modern particle physics analyses, driven by challenges in complex pattern recognition, high-dimensional data, and the need for fast, accurate inference. ML methods enhance both physics object reconstruction and broader physics measurements, revolutionizing workflows in experiments such as CMS. The application in CMS now ranges from the machine operation and data acquisition to the data analysis strategy for BSM searches and precision measurements. In the following there is a (non exhaustive) list of application taken from Ref. [224]:

- **Producing the data**

ML can be used to tune devices, control beams and perform analysis on accelerator parameters. It has already deployed successfully on accelerator facilities and potentially can be implemented for detector control.

- **Compressing data**

Autoencoders reduce the dimensionality of detector output, preserving essential features while lowering data size.

- **Data quality monitoring**

Online ML systems detect deviations in detector behavior, enabling rapid alerts for data quality issues.

- **Managing data**

ML forecasts dataset usage trends, enabling efficient file staging and cache prioritization in distributed computing environments.

- **Triggers**

Lightweight ML models deployed in the HLT improve efficiency under tight latency and resource constraints.

- **Reconstructing data**

Event reconstruction (in particular tracking and vertexing) is a pattern recognition task well suited for advanced machine learning techniques, such as Graph Neural Networks (GNNs).

- **Simulating data**

Generative Adversarial Networks (GANs) accelerate detector simulation, alleviating resource bottlenecks in full simulation pipelines.

- **Calibrating data**

Neural Networks calibrate jet energy by regressing the four-momentum and compensating for non-linear detector effects.

- **Particle identification**

Neural Networks tag jets originating from heavy-flavor quarks (b-tagging), improving efficiency and reducing misidentification compared to traditional methods.

- **Analyzing data**

Signals of interest can be very rare and difficult to detect, hence machine learning algorithms are trained to recognize specific signatures of new physical events, allowing for more efficient signal detection and classification. They can help identify rare events and reduce background contamination, improving the sensitivity of the analysis.

In this thesis, ML techniques are employed for particle identification and data analysis tasks. Specifically, a CNN is used for the identification of τ_h objects, as described in Chapter 6, while DNNs are trained to enhance the sensitivity of the $H/A \rightarrow ZA/H \rightarrow \ell\ell\tau\tau$ and HH searches, as discussed in Chapter 7 and Chapter 8, respectively. These two techniques will be described in detail in the following sections.

Both methods fall under the category of *supervised learning*, a type of ML in which the algorithm is trained on a labeled dataset. In supervised learning, each training example consists of an input (e.g. detector signals or event-level features) paired with the correct output label (e.g. particle type or signal/background classification). The goal is for the model to learn a mapping from inputs to outputs, enabling it to make accurate predictions on new, unseen data.

5.4.1 Deep Neural Networks

DNNs are a class of machine learning models inspired by the structure and function of the human brain. They consist of multiple layers of interconnected neurons, and are particularly effective at capturing complex, non-linear relationships in high-dimensional data. In recent years, DNNs have found widespread application across many domains, including image recognition, natural language processing, and High Energy Physics.

A neural network is composed of an input layer, one or more hidden layers, and an output layer (see Fig 5.3). Each layer consists of a number of artificial

neurons, also called nodes or units. Each neuron receives inputs, applies a linear transformation (typically a weighted sum plus a bias), and passes the result through a non-linear activation function.

Mathematically, the output of a neuron can be expressed as:

$$y = f \left(\sum_{i=1}^n w_i x_i + b \right), \quad (5.27)$$

where x_i are the input features, w_i are the weights, b is the bias term, and $f(\cdot)$ is the activation function.

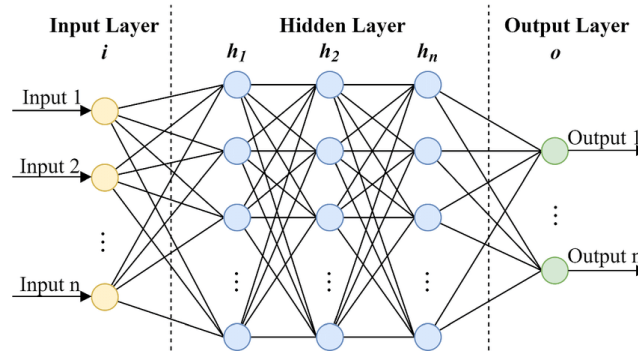


Figure 5.3: General Neural Network Architecture. The output of a unit (i) in a layer (l) is related to the output (o) of the earlier layer with outputs through a set of weights, a bias, and a non-linear activation function [225].

The fundamental components of a deep neural network are discussed in greater detail in the following.

Neurons Neural network nodes receive inputs, compute a weighted sum, add a bias, and apply an activation function to produce an output. Neurons are typically organized into layers: the input layer, one or more hidden layers, and the output layer.

Synapses Synapses represent the connections between neurons and are conceptually analogous to biological neural connections. In artificial neural networks, they are modeled as weighted links that transmit signals from one neuron to another.

Weights Weights are trainable parameters associated with the synapses. They determine the strength or influence of the connection between neurons. During training, the weights are adjusted to minimize the loss function and improve the model's performance.

Biases A bias is an additional trainable parameter added to the weighted input of each neuron. It allows the activation function to be shifted left or right, helping the network model data more flexibly, especially when the input is zero or in regions where activations need to shift.

Activation Functions Activation functions are mathematical transformations applied to the output of each neuron after computing the weighted sum and bias. They introduce non-linearity into the network, enabling it to approximate complex functions and model intricate relationships in the data. The choice of activation function impacts the network's learning dynamics, convergence behavior, and capacity to represent various data types. The most commonly used activation functions are:

- **Sigmoid:** Defined as $f(x) = \frac{1}{1+e^{-x}}$, this function maps input values into the (0, 1) range. It is traditionally used in binary classification problems but is less common in deep networks due to issues like vanishing gradients and saturation.
- **Tanh (Hyperbolic Tangent):** Defined as $f(x) = \frac{e^x - e^{-x}}{e^x + e^{-x}}$, the tanh function outputs values in the range (-1, 1). It provides stronger non-linearity than sigmoid but also suffers from the vanishing gradient problem in deep networks.
- **ReLU (Rectified Linear Unit):** Defined as $f(x) = \max(0, x)$, the ReLU function outputs zero for negative inputs and passes through positive inputs unchanged. ReLU is widely used due to its computational efficiency and ability to reduce vanishing gradients, although it can suffer from the "dying ReLU" problem, where neurons become permanently inactive by outputting only zeros after receiving large negative inputs.
- **Leaky ReLU:** An improvement over ReLU, it allows a small, non-zero gradient for negative input values. This helps prevent neurons from be-

coming inactive during training. It is defined as:

$$f(x) = \begin{cases} x & \text{if } x > 0 \\ \alpha x & \text{if } x \leq 0 \end{cases}$$

where α is a small constant (e.g. 0.01).

- **Softmax:** Used in the output layer for multi-class classification, the softmax function transforms a vector of real-valued scores z_i into probabilities:

$$\text{softmax}(z_i) = \frac{e^{z_i}}{\sum_{j=1}^K e^{z_j}}$$

where K is the number of output classes. The outputs are positive and sum to 1, forming a valid probability distribution.

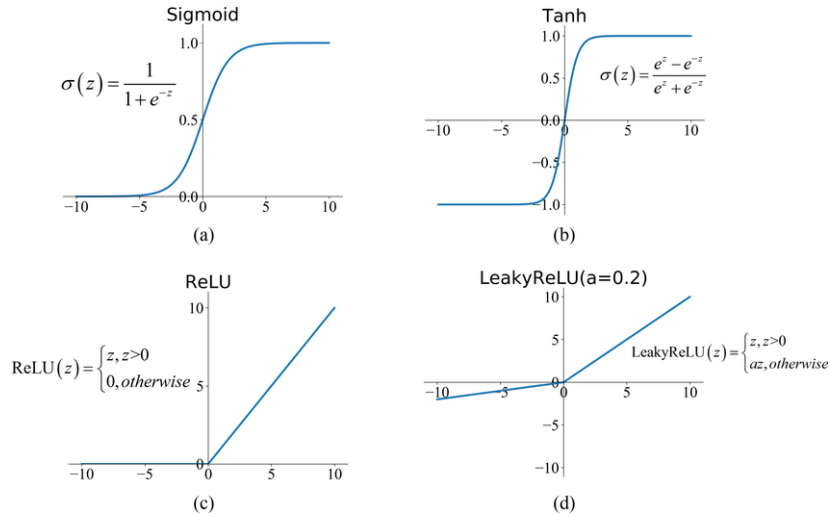


Figure 5.4: Commonly used activation functions [226]: (a) Sigmoid, (b) Tanh, (c) ReLU, and (d) LReLU.

As already mentioned, DNNs are trained using supervised learning. A labeled dataset is used to optimize the network parameters (weights and biases) by minimizing a loss function that quantifies the difference between the predicted and true outputs. The most commonly used optimization algorithm is stochastic gradient descent or one of its variants (e.g. Adam [227]).

The training process consists of:

- **Forward pass:** Input data is propagated through the network to compute the output.
- **Loss computation:** The output is compared with the true label using a loss function. For the classification task, a commonly used loss function is cross-entropy, especially when the output is a probability distribution over classes (e.g. in binary or multi-class classification). It quantifies the difference between the predicted probability distribution and the true labels. For a binary classification problem, where the true label $y \in \{0, 1\}$ and the predicted probability of the positive class is \hat{y} , the cross-entropy loss is defined as:

$$\mathcal{L}_{\text{CE}}(y, \hat{y}) = -[y \log(\hat{y}) + (1 - y) \log(1 - \hat{y})]. \quad (5.28)$$

Here, \hat{y} is the model's predicted probability that the instance belongs to class 1. The loss increases as the predicted probability diverges from the actual label. For multi-class classification with C classes and one-hot encoded true labels $y = (y_1, \dots, y_C)$ and predicted probabilities $\hat{y} = (\hat{y}_1, \dots, \hat{y}_C)$, the cross-entropy loss is given by:

$$\mathcal{L}_{\text{CE}}(y, \hat{y}) = - \sum_{i=1}^C y_i \log(\hat{y}_i). \quad (5.29)$$

In this case, $y_i = 1$ only for the correct class, so the loss reduces to the negative log-probability assigned to the correct class by the model. Minimizing this loss encourages the model to assign high probabilities to the correct class labels.

- **Backward pass:** The error is backpropagated to update the weights using gradient descent.

The performance and stability of DNNs heavily depend on the choice of training hyperparameters and configuration settings. Several important concepts that govern the training process are outlined below.

Batch Size The *batch size* determines the number of training examples used to compute the gradient and update the model's parameters in each iteration. Choosing the appropriate batch size involves trade-offs between computation time, memory usage, and convergence behavior.

Learning Rate The *learning rate* controls the step size during gradient descent updates. It is one of the most critical hyperparameters, since a too high rate can cause the model to overshoot minima or diverge, while a too low rate results in slow convergence or getting stuck in suboptimal minima. Learning rate schedules (e.g. exponential decay, cosine annealing) and adaptive optimizers like Adam can dynamically adjust the effective learning rate during training.

Epochs An *epoch* refers to one full pass through the entire training dataset. Typically, multiple epochs are needed for the model to converge. However, too many epochs can lead to overfitting, especially if regularization is not applied.

To avoid overfitting and improve the model's ability to generalize to unseen data, several regularization techniques are used:

- **Dropout** [228]: Randomly deactivating a subset of neurons during training.
- **L2 Regularization**: Adding a penalty term proportional to the square of the weights to the loss function.
- **Early stopping**: Halting training when performance on a validation set stops improving.

5.4.2 Convolutional Neural Networks

CNNs are a specialized class of deep neural networks designed to process data with a grid-like topology, such as images. Their architecture is particularly well-suited for extracting spatial hierarchies of features, making them highly effective for image classification, object detection, and other vision-related tasks. In High Energy Physics, CNNs are increasingly applied to calorimeter images, detector readouts, and other structured event data (like jets and τ_h objects).

A typical CNN consists of several layers that transform raw input data into increasingly abstract feature representations. These layers include convolutional layers, activation functions, pooling layers, fully connected layers, and an output layer. The structure and data flow in a standard CNN are illustrated in Figure 5.5, and each key component is explained below.

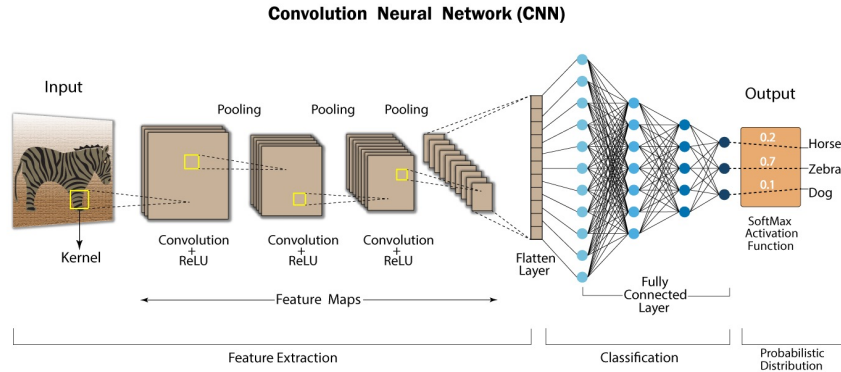


Figure 5.5: Example of a typical CNN architecture for image classification. The input image is processed through a series of convolutional, activation, and pooling layers, followed by fully connected layers and a softmax output.

Convolutional Layers The core operation of CNNs is the convolution. Each convolutional layer applies a set of filters (kernels) to the input image or feature map. These filters slide across the input, computing dot products at each position, resulting in a new feature map. This allows the network to detect local patterns such as edges or textures. Formally, a 2D convolution between input X and kernel K is defined in most deep learning frameworks as:

$$(X * K)(i, j) = \sum_m \sum_n X(i + m, j + n) \cdot K(m, n)$$

Activation Functions After convolution, each element of the feature map is passed through a non-linear activation function. The most common choice is the aforementioned ReLU.

Pooling Layers Pooling layers reduce the spatial dimensions of the feature maps, typically using operations like max pooling. For example, a 2×2 max pooling layer retains the maximum value from each 2×2 region, reducing data size while preserving important information. This helps control overfitting and adds some translation invariance.

Fully Connected Layers Once the spatial features have been extracted, the resulting feature maps are flattened into a vector and passed through one or more fully connected (dense) layers. Each neuron in these layers is connected

to all outputs from the previous layer. These layers combine high-level features and perform the final classification decision.

Output Layer For classification tasks, the output layer typically uses the softmax function to convert the final outputs into class probabilities.

5.4.3 Performance evaluation and reliability testing of ML models

Deep neural networks undergo rigorous validation and testing procedures to assess their performance and reliability. We can evaluate the performance of a neural network using various metrics and techniques; confusion matrix, ROC and AUC, cross-validation, loss function, precision, recall, and F1 score, etc. are such examples. The Receiver Operating Characteristic (ROC) curve and the Area Under the Curve (AUC) (see Fig. 5.6) are the most commonly used techniques to get insight into the true positive rate against the false positive rate at different classification thresholds. It provides a comprehensive view of the trade-off between sensitivity and specificity. The AUC is often used as a single metric to quantify the overall performance of a classifier.

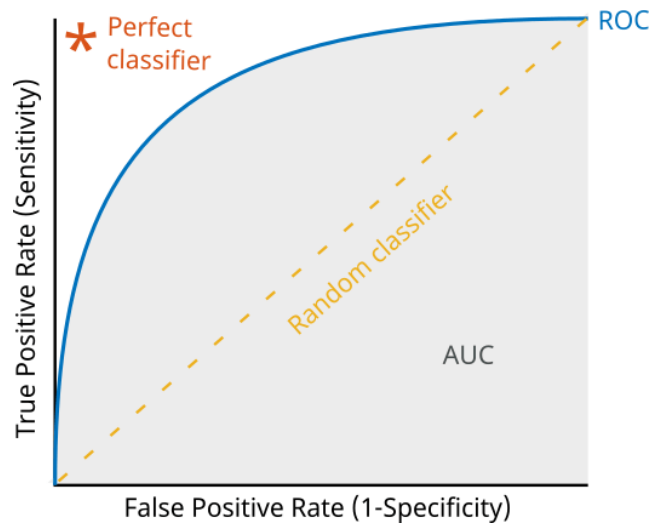


Figure 5.6: Example of ROC curve. The AUC reflects the performance of the classifier: a classifier with optimal performance has an area under the curve close to 1.) [229].

The confusion matrix in Fig. 5.7 also provides the counts of true positives, true negatives, false positives, and false negatives. From the confusion matrix, several metrics can be derived, including precision, recall, and F1 score. The *precision* measures the proportion of correctly predicted positive instances out of the total predicted positives. The *recall*, also known as *sensitivity*, calculates the proportion of correctly predicted positive instances out of the total actual positives. The *F1 score* is the harmonic mean of precision and recall, providing a balanced measure of a classifier's performance.

		Predicted Class		
		Positive	Negative	
Actual Class	Positive	True Positive (TP)	False Negative (FN) Type II Error	Sensitivity $\frac{TP}{(TP + FN)}$
	Negative	False Positive (FP) Type I Error	True Negative (TN)	Specificity $\frac{TN}{(TN + FP)}$
		Precision $\frac{TP}{(TP + FP)}$	Negative Predictive Value $\frac{TN}{(TN + FN)}$	Accuracy $\frac{TP + TN}{(TP + TN + FP + FN)}$

Figure 5.7: Confusion matrix and performance equations [230].

Cross-validation is a widely used technique to assess a model's generalization performance by splitting the dataset into multiple subsets, or *folds*. The neural network is trained and evaluated on different combinations of these folds, resulting in a more robust and unbiased estimate of its performance.

During training, the loss function provides valuable insight into the optimization and learning process. Monitoring both the training and validation loss can help determine how well the model is learning and whether it is overfitting or underfitting the data.

While any one of these evaluation techniques can offer useful information about model performance, it is often beneficial to consider multiple approaches together. This comprehensive assessment helps build a more reliable understanding of the network's behavior. Ultimately, the choice of evaluation methods depends on the nature of the problem, the characteristics of the dataset, and the specific objectives of the neural network application.

The τ_h identification algorithm and its calibration

The accurate reconstruction and identification of τ_h candidates is a key component of the CMS BSM analysis presented in Chapter 7. For this reason, I have dedicated significant effort over the past years to the CMS Tau Physics Object Group (TauPOG), with a primary focus on the validation and calibration of the latest τ_h identification algorithm, DEEPTAU v2.5. I currently serve as a Level-3 convener for the Tau Calibration–Quality–Modeling group, where I have been responsible for coordinating past and current Run 3 calibration campaigns. Additionally, I am the Contact Person for the DEEPTAU v2.5 paper, available in Ref. [1].

This chapter introduces DEEPTAU v2.5 and outlines its key features, highlighting the improvements made over the previous version, DEEPTAU v2.1. I will then discuss its calibration in detail, presenting the measurement of τ_h identification correction factors. Special emphasis will be given to the determination of the $e \rightarrow \tau_h$ misidentification rate correction factors, which I personally measured for the early Run 3 data.

6.1 Misidentification of hadronically decaying tau leptons

In Sec. 3.3.5 the HPS algorithm for the reconstruction of τ_h candidates have been presented. This algorithm is designed to be extremely efficient, indeed approximately 90% of genuine τ_h candidates are reconstructed by HPS, but it suffers from high levels of contamination. Several objects can be misidentified as hadronically decaying tau leptons by the HPS algorithm:

- **jets:** a highly collimated quark or gluon jet can be mistaken for any tau decay (see for example Fig. 6.1);
- **muons:** can produce a signature similar to a one prong tau decay;
- **electrons:** can emit photons via bremsstrahlung radiation and mimic the ρ meson decay and be reconstructed as one prong plus π^0 's decays.

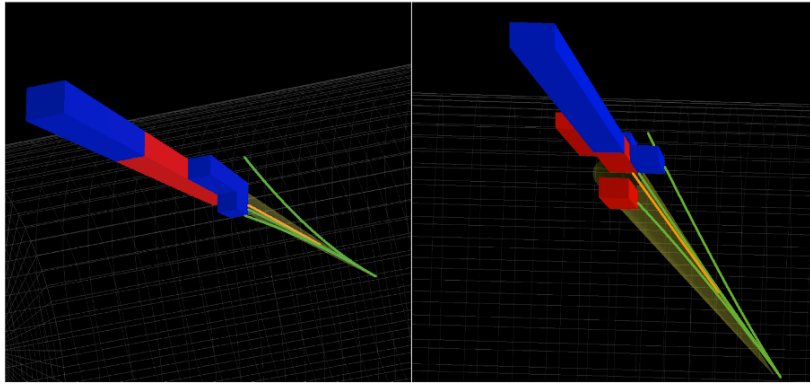


Figure 6.1: Simulation of a τ_h decay into $h^\pm h^\mp h^\pm \pi^0$ (left) and of a collimated jet resembling a τ_h (right) in the CMS detector.

As previously mentioned, a τ_h candidate is seeded by a PF jet in the HPS algorithm, making quark and gluon jets the highest source of contamination for the τ_h identification. Light leptons can also be misidentified as τ_h , electrons in particular can occasionally produce electromagnetic showers that reach the HCAL, mimicking the signature of a charged pion, and emit bremsstrahlung photons which could be reconstructed as a strip by the HPS algorithm. A schematic representation of these signatures is shown in Fig. 6.2.

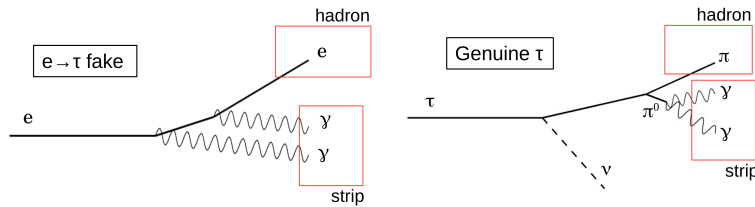


Figure 6.2: Schematic representation of the signatures identified by the HPS algorithm for an electron faking a τ_h (left) and a genuine τ_h (right).

To reduce the misidentification rate, and thus select a more pure sample of hadronically decaying tau leptons, several methods have been implemented in CMS throughout the years. First a cut-based isolation sum discriminator was implemented, later a Boosted Decision Tree discriminator [231] and, finally, for the end of Run 2, the DEEPTAU neural network-based identification was deployed. Its version v2.1 [232] has been used in the analysis presented in this thesis while its latest iteration, v2.5 [1], is described in the following since it is the one I have been working on for the current Run 3.

6.2 The τ_h identification using a deep neural network with domain adaptation

The DEEPTAU algorithm is a deep convolutional neural network that simultaneously discriminates τ_h candidates against quark and gluon jets, electrons and muons. The algorithm uses a combination of high-level input variables and information from particles in the vicinity of the candidate. The neural network outputs an estimation of the probabilities that a candidate is a genuine τ_h , or a quark and gluon jet, electron, or muon.

The latest iteration of DEEPTAU, v2.5, incorporates domain adaptation by backpropagation into the training workflow, to reduce performance discrepancies when the algorithm is applied to collision data. The algorithm was trained on a balanced mix of simulated events, and on pp collision data collected by the CMS detector in 2018 at $\sqrt{s} = 13$ TeV.

In addition to achieving better data-to-simulation agreement, DEEPTAU v2.5 also demonstrates improved classification performance compared to its predecessor, v2.1, with a larger and more balanced training dataset, optimized hyperparameters, and corrections of inconsistencies in the particle-level input grids.

6.2.1 Inputs

Particle-level inputs are stored in two overlapping grids in pseudorapidity-azimuth (η - ϕ) space, centred on the τ_h candidate axis, as shown in Fig. 6.3. The inner grid, encapsulating the signal cone, which contains the h^\pm and π^0 candidates, comprises 11×11 cells of size 0.02×0.02 . The outer grid of 21×21 cells of size 0.05×0.05 , contains the isolation cone.

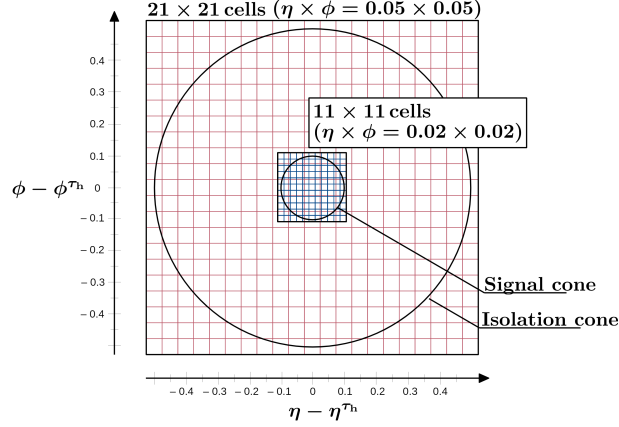


Figure 6.3: Inner and outer grid layout in η - ϕ space [232]. The inner grid encapsulates the signal cone of maximal radius 0.1, which contains the h^\pm and π^0 candidates, and consists of 11×11 cells with a size of 0.02×0.02 each. The outer grid contains the isolation cone of radius 0.5, and consists of 21×21 cells with a size of 0.05×0.05 each.

Properties of seven different types of reconstructed particles can be stored in each cell: those reconstructed by the PF algorithm (electrons, muons, photons, charged hadrons, and neutral hadrons), as well as electrons and muons reconstructed using dedicated standalone algorithms [233, 234].

The particle-level inputs are identical to those used in Ref. [232]. They include basic kinematic properties of each object: p_T , distance from the τ_h candidate axis in η - ϕ space ($\Delta\eta$ and $\Delta\phi$), and reconstructed charge. Track quality information, and compatibility with the PV, or possibly a secondary vertex (SV), is included, as well as characteristics of energy deposits in the detector (ECAL, HCAL, muon station hits). The estimated probability that the particle comes from another pileup interaction, is computed using the pileup-per-particle identification (PUPPI) algorithm [235].

There are 43 high-level input variables, which correspond to those used in Ref. [232], except for two that were removed in this work: the azimuthal angle ϕ of the τ_h candidate, to reduce dependence on detector conditions, and the absolute coordinates of the point of closest approach of the leading charged track because of mismodelling. The high-level variables used are mostly those which were found useful in previous multivariate analysis classifiers [236].

The high-level variables include τ_h candidate kinematic quantities (η , p_T , and energy) and charge, the number of charged and neutral hadrons associated with the τ_h candidate by the HPS decay mode reconstruction, and characteris-

tics of energy deposits from various particle types in the isolation cone. Information about the tracks is included: compatibility with the PV and properties of the SV, if reconstructed in a multiprong decay mode. Additionally, observables related to the η and ϕ distributions of the reconstructed energy in the π^0 strips, estimated pileup density, and calorimeter variables that provide good discrimination against electrons are used as input variables.

Integer inputs and variables with finite domain are transformed linearly to limit their values to the $[-1, 1]$ range. Other inputs are standardized using their mean values (μ_x) and standard deviation (σ_x),

$$x_{\text{std}} = \frac{x_{\text{orig}} - \mu_x}{\sigma_x}, \quad (6.1)$$

where x_{orig} is the original input, and x_{std} is the standardized input, which is then restricted to $[-5, 5]$ to remove outliers.

The reconstructed τ_h candidates are assigned a type: genuine τ_h , misidentified electron (e), and misidentified muon (μ), or misidentified quark or gluon jet (jet). Candidates matched to generated electrons and muons with $p_T > 8$ GeV, including those originating from leptonic tau decays, are assigned the e or μ classes, respectively. Leptons below these low p_T thresholds are not considered, as they are expected to be misidentified jet components (given that the HPS tau candidate must have $p_T > 20$ GeV). Those matched to a generated τ_h with visible $p_T > 15$ GeV are assigned genuine τ_h . In all of these cases the matching is performed with a cone $\Delta R = \sqrt{\Delta\eta^2 + \Delta\phi^2} < 0.2$. If a candidate is not matched to a generated lepton or genuine τ_h , it is assigned to the jet class. Only generated leptons and genuine τ_h originating from the PV are considered for τ_h candidate type assignment.

Approximately 100 million candidates, a balanced mix of the different types of τ_h candidates from various simulated events, are used to train the DEEPTAU algorithm in its default configuration. These events are simulated and reconstructed according to 2018 data-taking conditions. All types of reconstructed τ_h candidates are sourced from $Z/\gamma^* + \text{jets}$, $t\bar{t}$ (semileptonic and fully hadronic final states), and $W + \text{jets}$ events. Additional genuine τ_h candidates are obtained from $H \rightarrow \tau\tau$ and τ gun samples, and additional misidentified jets are obtained from simulated QCD multijet samples. Additional misidentified electrons are obtained from $Z' \rightarrow ee$ decays.

A loose selection is applied, with the candidate reconstructed by the HPS algorithm required to have a transverse momentum $20 < p_T < 1000$ GeV. Additionally, limits are imposed on the pseudorapidity $|\eta| < 2.5$ and longitu-

dinal impact parameter $|d_z| < 0.2$ cm (distance between the leading charged track and PV). Weights are applied in p_T and η bins to ensure a uniform distribution between the classes across the various training samples in all kinematic regions.

6.2.2 Classification architecture and loss function

The architecture used for τ_h type classification in this work is similar to the one described in Ref. [232]. The input variables (high-level features, and all the inner/outer grid cells) are initially processed separately using fully connected layers for feature extraction. Convolutional layers are then used to reduce the dimensionality of the grids to 1×1 . The processed features are then concatenated and passed through a final set of fully connected layers for τ_h type classification. A softmax activation function is then applied to yield probability estimates that the τ_h candidate is a genuine τ_h , jet, electron, or muon. The predicted output takes the form: $\mathbf{y}^{\text{pred}} = (y_e, y_\mu, y_\tau, y_{\text{jet}})$.

Batch normalization [237] and dropout regularization are applied after each fully connected and convolutional layer. Nonlinearities are introduced using the PReLU activation function [238].

The classification loss function used during the training of the neural network is a sum of a cross-entropy term [239] for the genuine τ_h target class, a focal loss component [240] for classification against all backgrounds combined, and three individual components for classification as electrons, muons, or jets when $y_\tau > 0.1$. The binary cross-entropy term assigns greater importance to very high genuine τ_h identification efficiency, which typically have higher misidentification rates. The addition of the focal loss terms improves the classification performance for genuine τ_h identification efficiencies in the 50–80% range, for which most physics analyses involving τ_h candidates show the highest sensitivity. Furthermore, in regions where the genuine τ_h identification efficiency is low, binary classification to separate signal from the combined backgrounds is more important than distinguishing between background types.

The loss function is defined as:

$$\begin{aligned}
L(\mathbf{y}^{\text{true}}, \mathbf{y}^{\text{pred}}) = & \underbrace{\kappa_\tau H_\tau(\mathbf{y}^{\text{true}}, \mathbf{y}^{\text{pred}}; \omega)}_{\text{Separation for all } \alpha} \\
& + \underbrace{(\kappa_e + \kappa_\mu + \kappa_j) \bar{F}_{\text{cmb}}(1 - y_\tau^{\text{true}}, 1 - y_\tau^{\text{pred}}; \gamma_{\text{cmb}})}_{\text{Focused separation of } e, \mu, \text{jet from } \tau_h} \quad (6.2) \\
& + \underbrace{\kappa_F \sum_{i \in \{e, \mu, j\}} \kappa_i \hat{\theta}(y_\tau - 0.1) \bar{F}_i(y_i^{\text{true}}, y_i^{\text{pred}}; \gamma_i)}_{\text{Focused separation of } \tau_h \text{ from } e, \mu, \text{jet for } y_\tau > 0.1}
\end{aligned}$$

where \mathbf{y}^{pred} and \mathbf{y}^{true} are the predictions and generator-level truth, respectively; H_τ is the categorical cross-entropy loss with ω a varying parameter for sample normalization; \bar{F}_x is the normalized focal loss; $\hat{\theta}$ is a smoothened step function that approaches 1 for $y_\tau > 0.1$ and 0 for $y_\tau < 0.1$. This step function disregards the discrimination between e , μ , and jets when the probability of a genuine τ_h is low. The default values of the κ and γ terms are given in Table 6.1.

The κ values affect the relative importance of predicting each class correctly. During the domain adaptation training, these constants were set to $\kappa_e = 2$, $\kappa_\mu = 5$, $\kappa_\tau = 6$, and $\kappa_j = 1$ in order to reduce the degraded performance of τ_h classification.

Parameter	Value	Emphasis on
κ_e	0.4	e separation
κ_μ	1.0	μ separation
κ_τ	2.0	τ_h separation
κ_j	0.6	Jet separation
κ_F	5.0	High τ_h identification efficiency
γ_e	2.0	e separation
γ_μ	2.0	μ separation
γ_j	2.0	Jet separation
γ_{cmb}	0.5	e, μ, jet separation combined

Table 6.1: Default values of the parameters used in the classification loss function for DEEPTAU training.

The loss function is minimized with the adaptive momentum estimation (*Adam*) algorithm [241] and the Nesterov-momentum accelerated variant (*NAdam*) [242].

The setup uses the TENSORFLOW v2.5.0 [243] Python library with KERAS v2.5.0 [244] as an interface. Training was performed using NVIDIA TESLA V100 and T4, as well as GEFORCE GTV 1080 Ti GPUs.

The discriminators against electrons, muons, and quark or gluon jets are defined as

$$D_\alpha(\mathbf{y}) = \frac{y_\tau}{y_\tau + y_\alpha}, \quad (6.3)$$

where y_α is the predicted probability that the τ_h candidate belongs to the target class $\alpha \in \{e, \mu, \text{jet}\}$. The discrimination of a genuine τ_h against a particular background improves as the corresponding discriminator score approaches 1.

6.2.3 Domain adaptation by backpropagation

DEEPTAU v2.1 was trained exclusively on simulated events. While these samples generally provide a good representation of the pp collision data, some of the features used as inputs are not perfectly modeled. As a consequence, the previous setup shows increasing discrepancies between observed data and expectations from simulations for high D_{jet} scores. This is particularly problematic since the affected region is the most important for analyses, as it has the highest genuine τ_h purity.

Previously, this mismodeling was only corrected using a set of dedicated calibration measurements, where simulations were fitted to the data, to determine identification efficiency scale factors. However, such corrections lead to larger uncertainties, and do not correct the shape of the discriminator output. The raw DEEPTAU v2.1 score could therefore not be reliably used as an input for analyses.

Simply removing any variables which are not perfectly described in simulation is not feasible, as they remain important for achieving good classification performance. Furthermore, studies have shown that the mismodeling is a highly multidimensional effect, making it very difficult to identify the affected set of inputs and correct them with traditional methods. A better approach is domain adaptation, which can discourage the algorithm from using combinations of features that are not well modeled in simulation by identifying differences between data and simulation in the hidden layers of the neural network during training.

The performance discrepancies between data and simulated samples are reduced at the training level by implementing domain adaptation by backpropagation in DEEPTAU v2.5. This involves simultaneously training two subnet-

works with competing goals. In this case, one is used for τ_h type classification, and the other for domain discrimination between data and simulated events. The goal is to maximize the classification performance while minimizing data-simulation discrimination. A mathematical description of the gradient reversal technique used to achieve this is available in Ref. [245]. This technique has previously been used for displaced jet tagging [246].

The advantages of this method are that the scale factors to correct residual differences can be brought closer to unity. Additionally, the network optimization algorithm would have the opportunity to find trainable parameter values that ensure good τ_h type discrimination while being less sensitive to mismodeling.

As the neural network training with domain adaptation requires collision data, the main challenge of this method is to define a set of collision events with sufficient genuine τ_h purity and control over background.

Event selection and mixing

Training the domain adaptation subnetwork requires a control region dataset containing a mixture of data and simulated events, along with a high purity of genuine τ_h candidates. The control region is a sample of $Z \rightarrow \tau\tau$ events in which one tau lepton decays to a muon, and the other to hadrons ($\mu\tau_h$). This decay channel is chosen as there is good control over genuine τ_h purity and background.

The selection requirements on the muon and τ_h candidates are summarized in Table 6.2. These are applied to data collected during 2018 by the CMS detector using a single-muon trigger with a nominal p_T threshold of 24 GeV, as well as $Z/\gamma^* + \text{jets}$, $t\bar{t}$, and $W + \text{jets}$ simulated events.

The transverse mass m_T of the muon plus the missing transverse momentum is defined as

$$m_T(\mu, p_T^{\text{miss}}) = \sqrt{2p_T^\mu p_T^{\text{miss}}(1 - \cos(\Delta\phi))}, \quad (6.4)$$

where $\Delta\phi$ is the azimuthal separation between the muon and \vec{p}_T^{miss} .

If there is more than one muon or τ_h candidate fulfilling the criteria in Table 6.2, the most isolated candidate is selected, unless they are equal, in which case the highest p_T candidate is chosen. A veto is imposed on events containing loosely identified additional electrons and muons.

Object	Selection requirement
Muon	$p_T^\mu > 25 \text{ GeV}$
	$ \eta^\mu < 2.1$
	$ d_z < 0.2 \text{ cm}, d_{xy} < 0.045 \text{ cm}$
	Relative isolation $I_{\text{rel}}^\mu < 0.15$
	Pass medium muon identification
	$m_T(\mu, p_T^{\text{miss}}) < 30 \text{ GeV}$
τ_h	$p_T^\tau > 20 \text{ GeV}$
	$ \eta^\tau < 2.3$
	$ d_z < 0.2 \text{ cm}$
	HPS decay mode with 1 or 3 prongs
	$D_{\text{jet}}^{\nu 2.1} > 0.9$
	$D_e^{\nu 2.1} > 0.168 \text{ (VVLoose)}$
	$D_\mu^{\nu 2.1} > 0.875 \text{ (Tight)}$
Pair	$\Delta R(\mu, \tau_h) > 0.5$
	Opposite electric charge

Table 6.2: Selection requirements for the domain adaptation dataset. The impact parameters for the muon (or τ_h candidate respectively), d_z and d_{xy} , are defined as the distances between the muon track (or leading charged-hadron track) and the PV. The medium muon identification is defined in Ref. [234]. The previous DEEPTAU discriminator scores described in Ref. [232] against quark and gluon jets, electrons, and muons, are denoted $D_{\text{jet}}^{\nu 2.1}$, $D_e^{\nu 2.1}$, and $D_\mu^{\nu 2.1}$. The transverse mass of the muon and the missing transverse momentum system is denoted as $m_T(\mu, p_T^{\text{miss}})$.

In order to improve the modeling of events involving a non-genuine τ_h , a looser selection is applied to increase the number of available events from simulated QCD multijet samples and misidentified muons originating from $Z/\gamma^* + \text{jets}$ processes. Only the τ_h candidate and pair selections in Table 6.2 are applied, and the p_T spectra are then reweighted to the expectation for the nominal selection yields.

The resulting purity in the domain adaptation dataset, defined as the fraction of events where the τ_h candidate originates from a tau lepton, is estimated from the proportions of different simulated processes to be 76%.

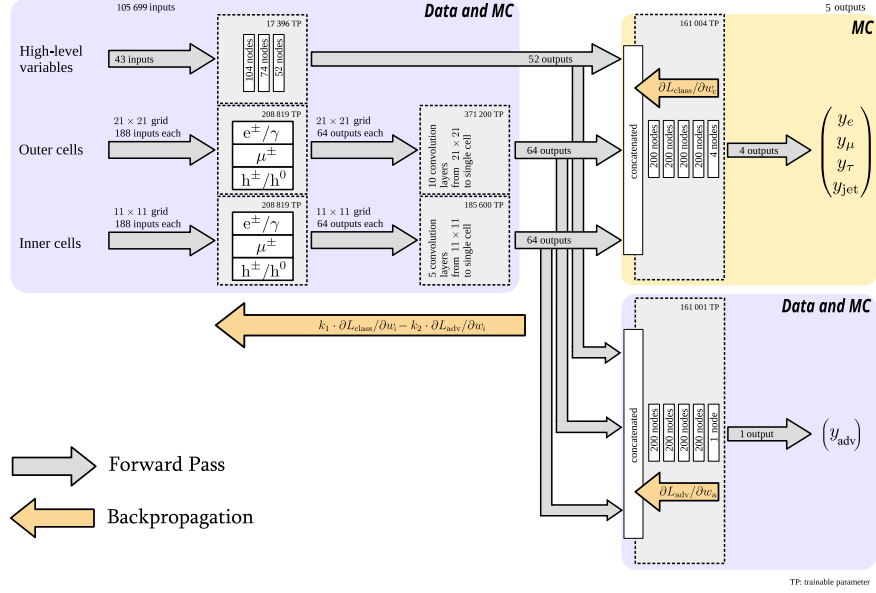


Figure 6.4: The DEEPTAU architecture with the domain adaptation configuration [247]. A set of final domain adaptation layers was introduced for data-simulation discrimination, consisting of several dense layers followed by a softmax layer that yields an output y_{adv} between zero and one. The backpropagation is modified to include the “adversarial loss”, as described in the text.

Domain adaptation subnetwork and backpropagation

A domain adaptation block was introduced to the network, which attempts to discriminate between data and simulated τ_h candidates. Similarly to the final classification layers described in Sec. 6.2.2, this takes the processed high-level and particle-level variables as inputs, before passing them through fully connected layers. A sigmoid activation layer is then used to cast the output to a value between 0 and 1, denoted as y_{adv} . The architecture of DEEPTAU in the domain adaptation configuration is shown in Fig. 6.4.

The domain adaptation loss function (“adversarial loss”) used to compare this prediction to the labels is defined as

$$L_{\text{adv}} = H_{\text{bin}}(y_{\text{adv}}^{\text{true}}, y_{\text{adv}}^{\text{pred}}), \quad (6.5)$$

where H_{bin} is a binary cross-entropy loss function [239]. A binary accuracy metric was introduced to evaluate the fraction of candidates for which the network successfully predicts the domain (data or simulation). The layers that

process the high-level variables, as well as the inner and outer grids, are referred to as common layers, since inputs for both the final domain adaptation and classification layers pass through these.

The model is first trained with only the classification architecture described in Sec. 6.2.2, in order to obtain a good τ_h candidate classification performance baseline before applying domain adaptation methods. The training is then continued with the domain adaptation control dataset and subnetwork introduced. For this step, the network backpropagation procedure is modified such that the gradients are passed to the optimization algorithm for the common layers.

The classification loss is denoted as L_{class} , and is computed on the output score of the τ_h classification, with only the τ_h candidates from the standard training dataset. The adversarial loss is computed on the domain adaptation output with only the τ_h candidates from the control region dataset. The gradients of L_{class} and L_{adv} are referred to as classification and adversarial gradients respectively.

In order to prevent data-simulation discrimination in the feature extraction layers, the signs of the adversarial gradients are reversed and combined linearly with the classification gradients. The combined gradient is expressed in the form

$$G = k_1 \frac{\partial L_{\text{class}}}{\partial w_i} - k_2 \frac{\partial L_{\text{adv}}}{\partial w_i}, \quad (6.6)$$

where w_i are the weights of the feature extraction layers and k_1 and k_2 are the domain adaptation hyperparameters that determine the relative importance of the τ_h candidate classification and prevent data-simulation discrimination. The sign reversal of the adversarial component of the gradients in the common layers means that the optimizer partially attempts to adjust the layer weights in the direction opposite to the one that improves data-simulation discrimination.

The gradients that are passed to the optimizer therefore encourage minimization with reduced sensitivity to mismodeling. Two Adam optimizers are used, each with a different learning rate. The principal optimizer targets the common layers and final classification layers, whereas the adversarial optimizer targets the final domain adaptation layers.

There is no gradient sign reversal in the final domain adaptation layers, as this provides a good measure of how much the network can actively discriminate data and simulated events with the information available at the output level of the common layers. An optimization of the domain adaptation hyperparameters was performed by comparing the distributions of y_{adv} for data and

simulated events using a χ^2 test, while monitoring the overall performance of the τ_h type classification. The optimal choice was $k_1 = 1$ and $k_2 = 10$.

The distributions of the DEEPTAU discriminator against quark and gluon jets for the model before and after the domain adaptation are shown in Fig. 6.5. The impact of the domain adaptation training on the DEEPTAU discriminator distribution against quark and gluon jets for the final model is visible on the right plot. The model was evaluated on events passing the control region selection, and the τ_h candidates were separated into their respective simulated event types and data. There is a significant improvement in data-simulation discrepancies in the highest discriminator score bins after domain adaptation training. The relative differences in the final bin are reduced from 17.4 to 0.9%. The genuine τ_h purity in this region is estimated from the proportions of different simulated samples in the final model distribution to be above 96%. Agreement in the control region overall is very good, with the data and simulated yields compatible within statistical uncertainties in the large majority of bins. The domain adaptation training therefore successfully reduced the effects of simulation mismodeling in the D_{jet} distribution for the data-taking conditions described in the domain adaptation dataset.

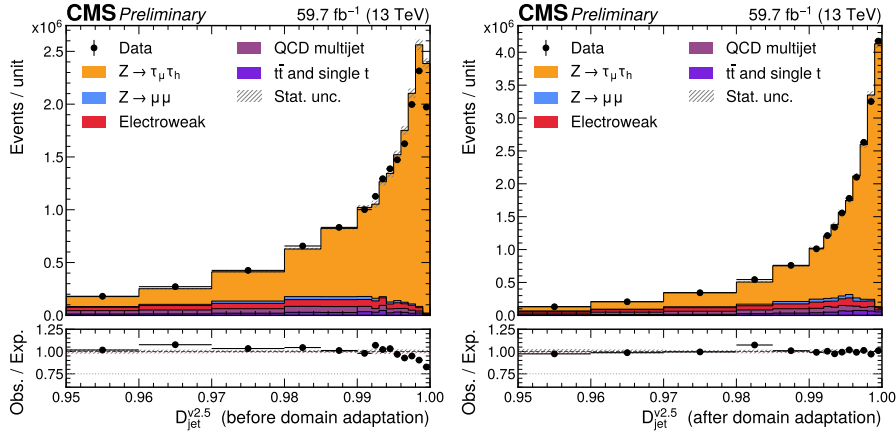


Figure 6.5: Distribution of the DEEPTAU discriminator against quark and gluon jets before (left) and after (right) domain adaptation, for the 2018 dataset used for domain adaptation training. There is significant improvement in data-simulation agreement in the control region, with the discrepancies in the final bin reduced to 0.9%.

The 2022 datasets with $\sqrt{s} = 13.6$ TeV are expected to showcase slightly weaker data-to-simulation agreement, as the data-taking conditions are not described in the domain adaptation dataset. Differences in the center-of-mass

energy, pileup, detector performance, and missing transverse momentum reconstruction with respect to 2018 are contributing factors. The distribution of the DEEPTAU discriminator against quark and gluon jets in the early 2022 data is shown for $D_{\text{jet}} > 0.95$ in Fig. 6.6 before and after the domain adaptation training. The inclusion of domain adaptation results in an appreciable improvement in the final bins, despite the training data not corresponding to equivalent detector conditions or collision energies. It is expected that if the domain adaptation algorithm were to be retrained with the inclusion of these new datasets, agreement would improve to a similar level as seen in the 2018 dataset.

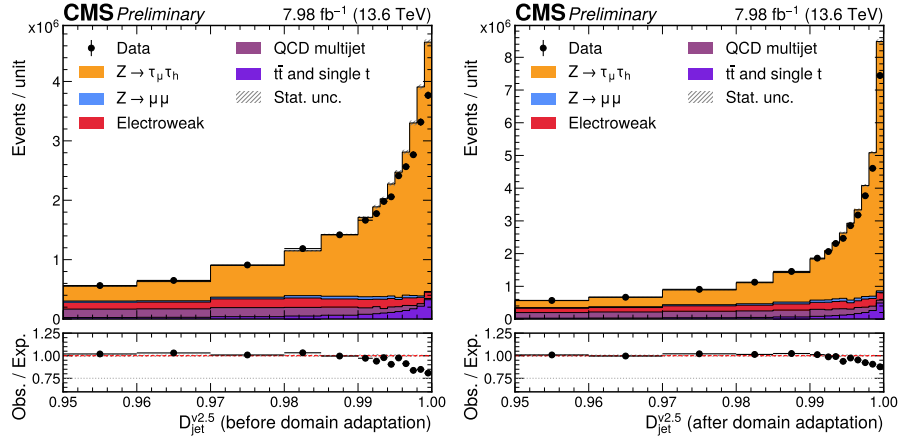


Figure 6.6: Distribution of the DEEPTAU discriminator against quark and gluon jets before (left) and after (right) domain adaptation, for the early 2022 dataset. An appreciable improvement in the final bins is visible with the inclusion of domain adaptation.

6.2.4 Expected performance

Working points are used to guide the usage of the DEEPTAU discriminators in physics analyses, with suitable corrections applied. The target genuine τ_h identification efficiencies, reported in Table 6.3, are defined as the efficiency for genuine τ_h in the $H \rightarrow \tau\tau$ event sample that are reconstructed as τ_h candidates with $30 < p_T < 70$ GeV to pass the given discriminator.

The resulting tagger demonstrates improved performance with respect to its predecessor, as is visible in Figs. 6.7–6.9, which show the misidentification probability as a function of the genuine τ_h identification efficiency. These are

	VVTight	VTight	Tight	Medium	Loose	VLoose	VVLoose	VVVLoose
D_e	60%	70%	80%	90%	95%	98%	99%	99.5%
D_μ			99.5%	99.8%	99.9%	99.95%		
D_{jet}	40%	50%	60%	70%	80%	90%	95%	98%

Table 6.3: Target genuine τ_h identification efficiencies for the different working points defined for the three discriminators. The target efficiencies are evaluated with the $H \rightarrow \tau\tau$ event sample for τ_h candidates with $p_T \in [30, 70]$ GeV.

inclusive plots that combine all commonly reconstructed decay modes. They are shown for the central pseudorapidity region ($|\eta| < 2.3$), and are separated into low- p_T (20–100 GeV) and high- p_T (100–1000 GeV) regions. The filled circles identify the discriminator working points, which do not match exactly the targeted efficiencies in Table 6.3 because of the different samples considered. It can be observed that the jet misidentification probability is reduced by $\sim 50\%$ across all defined working points. The improvement in electron rejection with respect to the previous version of the algorithm is particularly pronounced for the tightest working points, where the misidentification probability is reduced by almost a factor of two. The muon rejection performance is compatible between the two versions of the identification algorithm. The slightly worse performance of v2.5 in the high- p_T , low efficiency region for the D_e and D_μ discriminators is likely caused by domain adaptation, which can prevent the use of certain feature combinations that are useful for lepton discrimination but exhibit significant differences between data and simulation.

Figure 6.10 shows the distribution of the visible invariant mass m_{vis} of the reconstructed $\mu\tau_h$ system when applying DEEPTAU v2.5, compared to the application of the previous version. The working points chosen are Tight for D_μ , Medium for D_{jet} , and VVLoose for D_e . A reduction of the background from misidentified jets is estimated to be $\sim 30\%$, especially visible in the decrease of the $W + \text{jets}$ process.

6.3 Performance with $\sqrt{s} = 13$ and 13.6 TeV data

The calibration of the DEEPTAU v2.5 algorithm involves determining both identification (or misidentification rate) scale factors and energy scale correc-

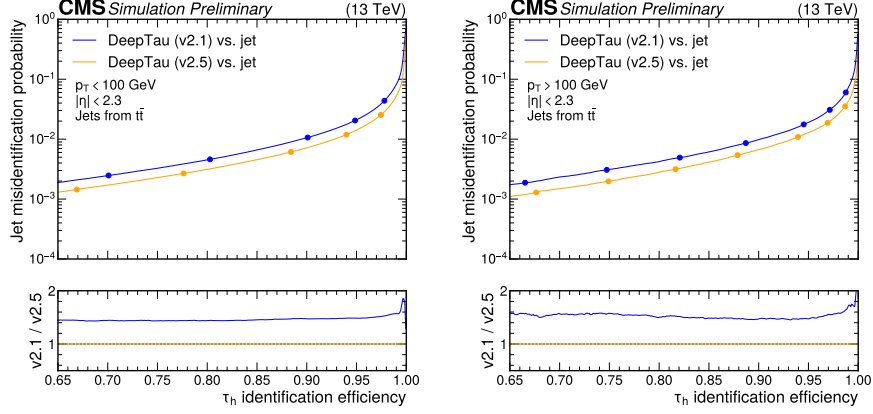


Figure 6.7: Jet misidentification probability versus genuine τ_h identification efficiency for low- p_T (left) and high- p_T (right) τ_h candidates, evaluated on 2018 simulated datasets. The genuine τ_h identification efficiency is estimated from $H \rightarrow \tau\tau$ simulations using reconstructed τ_h candidates that match generator-level τ_h objects. The jet misidentification probability is estimated from $t\bar{t}$ simulations using reconstructed τ_h candidates that do not match prompt electrons, muons, or products of τ_h decays at the generator level. The defined working points of the discriminator are indicated as filled circles.

tions. The scale factors are correction weights applied to simulated events to account for differences in the performance of the detector and of the reconstruction and identification algorithms between data and simulation. They are typically defined as the ratio of an efficiency (or misidentification rate) measured in real data to that measured in simulation, and are used to improve the agreement between predicted and observed data. The energy scale corrections are, instead, multiplicative correction factors to be applied to the four-momentum of the reconstructed objects. Their purpose is to adjust the simulated energy of a particle to better match the energy measured in data, thereby correcting for systematic differences in the energy response of the detector between simulation and observation. They are defined as the ratio of the energy measured in real data to that measured in simulation. The scale factors are generally measured as a function of the DEEPTAU D_{jet} , D_μ and D_e discriminator working points.

In this section I present a subset of the calibration measurements performed by TauPOG for the eras 2018 (Run 2) and 2022 (Run 3) and deployed centrally for analysts consumption. The complete set of measurements we perform for every data taking era comprises:

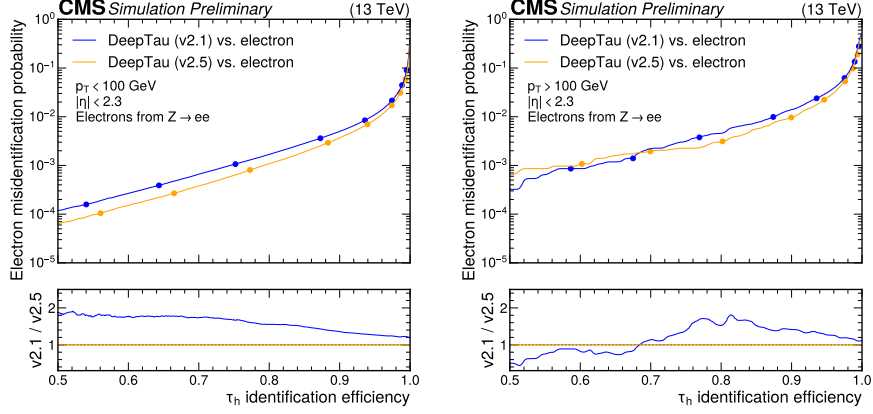


Figure 6.8: Electron misidentification probability versus genuine τ_h identification efficiency for low- p_T (left) and high- p_T (right) τ_h candidates, evaluated on 2018 simulated datasets. The genuine τ_h identification efficiency is estimated from $H \rightarrow \tau\tau$ simulations using reconstructed τ_h candidates that match generator-level τ_h objects. The electron misidentification probability is estimated from $Z/\gamma^* + \text{jets}$ simulation using reconstructed τ_h candidates that match electrons at the generator level. The defined working points of the discriminator are indicated as filled circles.

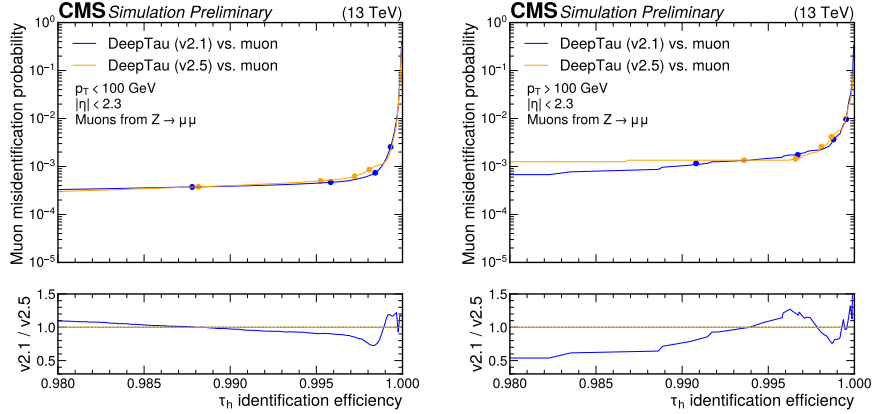


Figure 6.9: Muon misidentification probability versus τ_h identification efficiency for low- p_T (left) and high- p_T (right) τ_h candidates, evaluated on simulated 2018 datasets. The τ_h identification efficiency is estimated from $H \rightarrow \tau\tau$ simulations using reconstructed τ_h candidates that match generator-level τ_h objects. The muon misidentification probability is estimated from $Z/\gamma^* + \text{jets}$ simulation using reconstructed τ_h candidates that match muons at the generator level. The defined working points of the discriminator are indicated as filled circles.

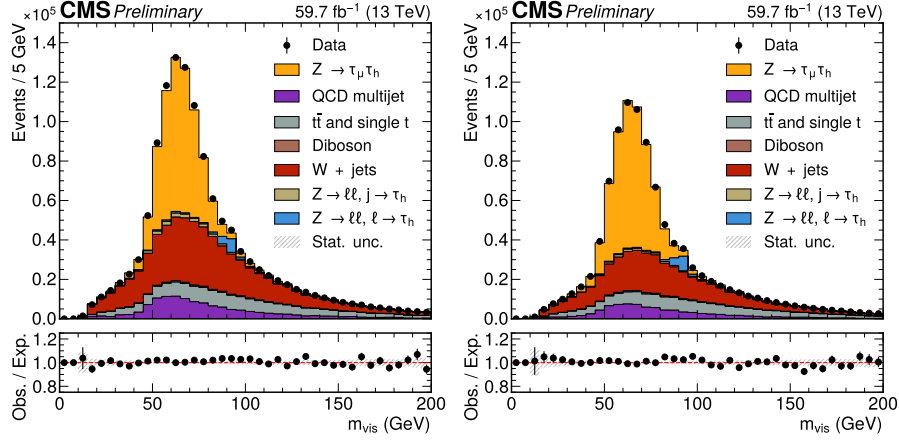


Figure 6.10: Distribution of the invariant mass of the reconstructed $\mu\tau_h$ system when using DEEPTAU v2.1 (left) and v2.5 (right) for discrimination in the 2018 dataset. The correction factors are applied in both cases.

- τ_h identification efficiency scale factors and energy scale corrections measured in $Z \rightarrow \tau\tau$ events in the $\mu\tau_h$ final state
- τ_h identification efficiency scale factors for high- p_T τ_h candidates measured in $W^* \rightarrow \tau\nu$ events
- muon misidentification rate scale factors in $Z \rightarrow \tau\tau$ events in the $\mu\tau_h$ final state in a region where most events come from the process $Z \rightarrow \mu\mu$
- electron misidentification rate scale factors and energy scale corrections in $Z \rightarrow \tau\tau$ events in the $e\tau_h$ final state in a region where most events come from the process $Z \rightarrow ee$

All of these measurements are performed using a tag-and-probe method [248] and represent essential ingredients for physics analyses involving τ_h objects in CMS. In the following, I will focus on the τ_h identification efficiency and electron misidentification rate scale factors and related energy scale corrections, as these represent the measurements to which I have contributed most significantly in the past years.

6.3.1 The τ_h energy scale correction and identification scale factors

Event selection

The events with a $\mu\tau_h$ final state are selected by requiring at least one well-identified and isolated muon, referred to as the “tag”, alongside one τ_h candidate that meets loose preselection criteria, termed the “probe”. The muon candidate must have $p_T > 25$ GeV, $|\eta| < 2.4$, and a relative isolation of $I_\mu < 0.15$. The τ_h candidate is required to have $p_T > 20$ GeV, $|\eta| < 2.3$, and must pass a specified threshold on the D_{jet} discriminator. Additionally, the τ_h candidate must satisfy the VVLoose working point of the D_e discriminator and the Tight working point of the D_μ discriminator to mitigate background from muons or electrons misidentified as τ_h candidates. Only decay modes h^\pm , $h^\pm\pi^0$, $h^\pm h^\mp h^\pm$, and $h^\pm h^\mp h^\pm\pi^0$ are considered. In cases where multiple lepton or τ_h candidates are identified, the one with the highest p_T is selected. The selected muon and τ_h candidates must be separated by $\Delta R > 0.5$ and opposite-sign (OS) charges. Additional leptons are vetoed. A cut on the transverse mass $m_T(\mu, p_T^{\text{miss}}) < 65$ GeV is included to improve signal-to-background ratio, reducing the $W + \text{jets}$ background.

In addition to the $\mu\tau_h$ event sample, a $\mu\mu$ event sample is defined to normalize the $Z \rightarrow \tau\tau$ event yields. This event sample adheres to the same trigger and muon selection criteria as the $\mu\tau_h$ event sample, ensuring that related uncertainties partially cancel in the normalization scale factor.

Background Estimation

The dominant backgrounds in this measurement are QCD multijet and $W + \text{jets}$ events. The QCD multijet background is estimated using a data-driven approach. The method used is commonly referred to as ABCD method: based on two uncorrelated variables the phase space is divided in four distinct region as shown in Fig. 6.11.

For illustration purposes let us define the regions in the following way:

- A) Signal Region (SR): which requires an isolated muon and a τ_h candidate having opposite electric charge;
- B) Same Sign (SS) isolated region: obtained by selecting an isolated muon and a τ_h candidate having the same electric charge;

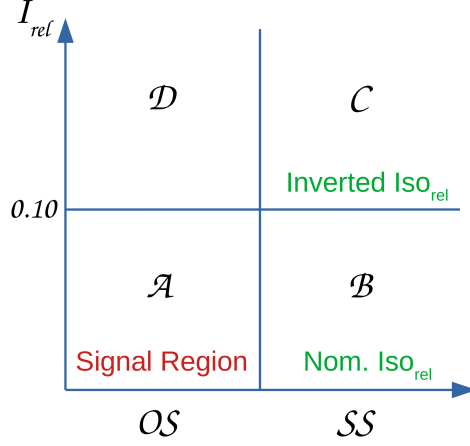


Figure 6.11: Schematic view of the ABCD method used for data-driven estimation of the QCD multijet production process.

- C) SS anti-isolated region: similar selection compared to region B, but with inverted cut on muon isolation;
- D) Opposite Sign (OS) anti-isolated region: same selection as for region A inverting the cut on muon isolation.

Since the variables are uncorrelated with each other, any selection performed on recorded or simulated events using one variable will select the same fraction of events regardless of what selection is applied on the other variable. By indicating with A, B, C, D the number of events in each region for a certain physical process, the following relation is derived:

$$\frac{A}{B} = \frac{D}{C} = SF_{SSOS} . \quad (6.7)$$

By measuring the value of $SF_{SSOS} = D/C$ in data, the QCD multijet production contribution in the SR can be estimated as:

$$QCD_{SR} = SF_{SSOS} \left(Data_B - \sum^{bkg.} MC_B \right) . \quad (6.8)$$

In practice, contributions from simulated MC samples (MC_B) are subtracted from the recorded data ($Data_B$) in region B. The obtained distribution is then scaled to estimate the QCD multijet production in the SR by multiplying it by the scale factor SF_{SSOS} .

The W +jets background is estimated from a high- m_T control region, while smaller backgrounds, such as the diboson, $Z/\gamma^* + \text{jets}$, and top quark processes, are estimated from simulation. For the background entirely estimated from simulation, the relevant simulation-to-data corrections have been applied, namely the muon scale factors, the pileup reweighting and the reweighting of the p_T distribution of the Z boson.

Systematic Uncertainty Model and Fit Results

The corrections are derived from a maximum likelihood fit to the m_{vis} distribution, i.e. the invariant mass of the visible decay products of the $\tau\tau$ pair. All known sources of systematic uncertainties are incorporated into the fit as nuisance parameters. Some of these uncertainties affect the yields of the involved processes, including integrated luminosity, muon identification, isolation, and trigger efficiencies, as well as uncertainties in the normalization of $t\bar{t}$, QCD multijet, and $Z/\gamma^* + \text{jets}$ backgrounds, and of quark and gluon jets misidentified as τ_h candidates. The remaining systematic uncertainties affect the shape of the m_{vis} distribution, including the energy scale for jets and leptons misidentified as τ_h candidates, the reweighting of the p_T distribution of the Z boson, and the uncertainties associated with the limited size of the simulated event samples. The rate of muons misidentified as τ_h candidates is treated as a yield parameter since these measurements are performed in parallel.

In the scale factor measurement for DEEPTAU v2.5, we explore how the τ_h identification efficiency scale factors are impacted by the choice of the nominal τ_h energy scale value and associated uncertainties. Studies such as the investigation detailed in our paper [1] have demonstrated that variations in τ_h energy scale values can significantly affect the efficiency scale factors. Moreover, the τ_h energy scale has been observed to depend on factors such as τ_h identification requirements, p_T , and decay modes, suggesting that the current uncertainty estimates may not fully capture all relevant variations. To address this, we developed an alternative method for handling τ_h energy scale uncertainties by externalizing them from the τ_h identification efficiency scale factor determination.

In this approach, the τ_h energy scale is fixed to the nominal value and a fit is performed to determine the τ_h identification efficiency scale factors without allowing the fit to over-constrain the τ_h energy scale uncertainties. The τ_h energy scale is then set as its post-fit value and is shifted by ± 1 standard deviations in

a second fit used to measure the corresponding variations in terms of efficiency scale factors and, hence, estimate the τ_h energy scale related uncertainty.

This method provides a more reliable treatment of τ_h energy scale uncertainties, ensuring that they are not overly reduced by the fit, and allowing for more consistent application across different analyses. This approach is particularly relevant for the $\tau_h\tau_h$ channel, where mismodeling effects are more pronounced and proper τ_h energy scale uncertainty treatment is critical for accurate results. An alternative approach to this problem is the combined (simultaneous) fit of energy scale corrections and scale factors, treating both as parameters of interest (POIs) within the fitting procedure. The strengths and limitations of this method are discussed in Ref. [1].

The scale factors are extracted in different τ_h p_T bins in order to take into account any p_T dependence. The lower bin edges 20, 25, 30, 35, 40, 50, 60, 80, and 100 GeV are used, where the last bin contains the scale factors for τ_h objects with $p_T > 100$ GeV. The scale factors are derived for each p_T bin of each decay mode of each data-taking period. A Laurent polynomial function is used to describe the trend in the scale factors, as it offers a better fit than a linear function. The Laurent polynomial is more flexible and reduces the χ^2 per degree of freedom compared to a linear fit. Unlike standard polynomials, Laurent polynomials can include terms with negative powers, making them more suitable in our case.

Figure 6.12 shows the τ_h identification efficiency scale factors for the 2018 and 2022 data-taking periods. The scale factors are derived for each p_T bin of each decay mode, but the summary plot in Fig. 6.12 combines the different decay modes according to their branching fractions and reconstruction efficiencies. The Medium D_{jet} , VVLoose D_e , and Tight D_μ working points are used.

The scale factors are generally a bit smaller than 1, typically within 20% of unity. Compared to the previous version of DEEPTAU, the scale factors measured for v2.5 are systematically closer to one in both 2018 and 2022, demonstrating that the domain adaptation approach leads to better agreement between data and simulation. The scale factors below 1 can be attributed to various factors, such as inaccuracies in the modelling of hadronization and imperfections in the simulation of the detector alignment and track hit reconstruction efficiencies.

To verify the performance of the derived scale factors a set of control plots are produced. Figures 6.13 and 6.14 show the 2022 m_{vis} distribution

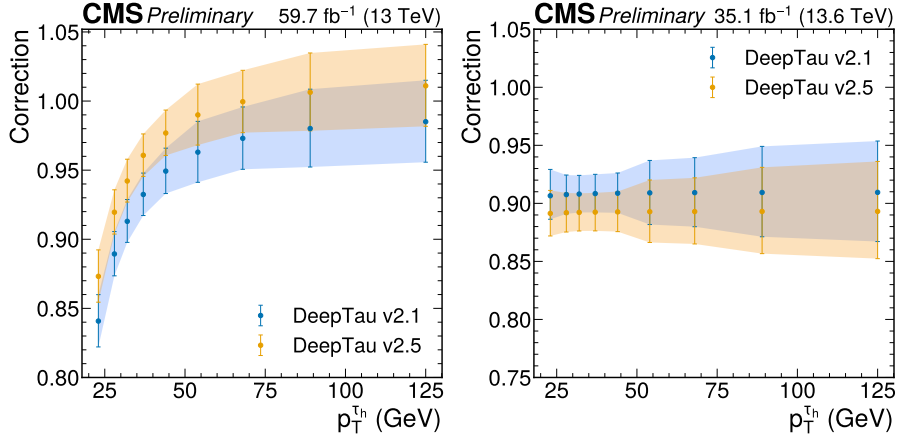


Figure 6.12: The data-to-simulation scale factors of the τ_h identification efficiency as functions of p_T in the 2018 (left) and 2022 (right) data-taking periods, including all τ_h decay modes, and requiring the D_{jet} Medium working point and $m_T(\mu, p_T^{\text{miss}}) < 65$ GeV. The vertical bars correspond to the combined statistical and systematic uncertainties in the individual scale factors. For a fair scale factor comparison in 2022, the tau energy scale have been fixed to the one measured for DEEPTAU v2.5 which showcases higher genuine purity.

in the $Z \rightarrow \tau_\mu \tau_h$ and $Z \rightarrow \tau_e \tau_h$ channels, respectively, before (left) and after (right) the application of the τ_h identification efficiency scale factors and the muon/electron misidentification rate scale factors. The data-to-simulation agreement is highly improved by the application of these scale factors.

6.3.2 The electron misidentification rate scale factors

The τ_h candidate found in simulated $Z \rightarrow ee$ events is an electron misidentified as an hadronically decaying tau lepton by the HPS algorithm. As such the $e \rightarrow \tau_h$ misidentification rate (FR) can be calculated as the fraction of simulated $Z \rightarrow ee$ events that pass the D_e discriminator for a certain WP:

$$FR = \frac{N_{Z \rightarrow ee}^{\text{pass}}}{N_{Z \rightarrow ee}^{\text{pass}} + N_{Z \rightarrow ee}^{\text{fail}}} . \quad (6.9)$$

The labels *pass* and *fail* are in this chapter assigned to events which possess a τ_h candidate that has been respectively identified as a genuine tau or an electron by the D_e discriminator.

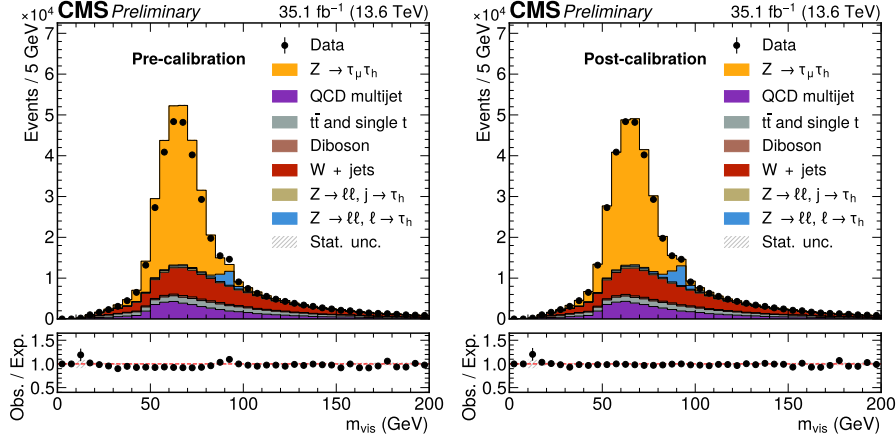


Figure 6.13: The m_{vis} distribution in the $Z \rightarrow \tau_\mu \tau_h$ channel for 2022 data before (left) and after (right) the full calibration. The DEEPTAU working points used are: Medium for D_{jet} , VVLoose for D_e and, Tight for D_μ . The application of correction factors improves the agreement between data and simulation.

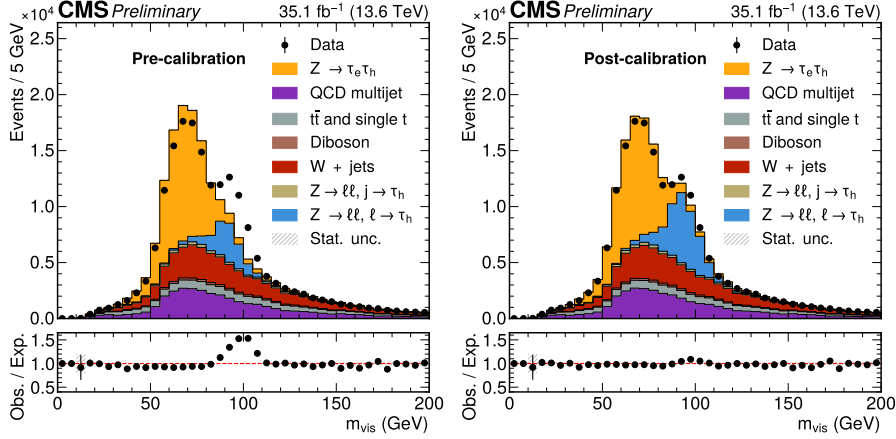


Figure 6.14: The m_{vis} distribution in the $Z \rightarrow \tau_e \tau_h$ channel for 2022 data before (left) and after (right) the full calibration. The DEEPTAU working points used are: Medium for D_{jet} , Tight for D_e and, Tight for D_μ . Specific 2022 detector conditions that affected electron reconstruction are not perfectly modelled in the simulation. As a result, the amount of electrons misidentified as τ_h is enhanced in data with respect to simulated events. The application of correction factors improves the agreement between data and simulation.

Measuring the same quantity in recorded data is inherently more complicated due to not being able to assert with certainty whether a τ_h candidate was indeed a genuine τ_h or not. A tag-and-probe method provides a good strategy

for such a measurement. It requires to select a reconstructed object as a *tag*, a well identified object whose nature is assumed to be known with certainty both in data and simulation. Another object, reconstructed in the same event, is then used to *probe* the efficiency of the classifier being studied. The strength of this method lies in selecting a tag and probe pair which can be easily assigned to a well identifiable physical process. The decay of a Z boson to leptons has a decay width of (83.984 ± 0.086) MeV [22] leading to a sharp resonance in the invariant mass distribution of the electron-positron pair. By measuring the $e \rightarrow \tau_h$ misidentification rate in a region enriched in $Z \rightarrow ee$ events it is possible to select a well reconstructed electron with a high degree of confidence that it was indeed an electron, and a loosely identified τ_h candidate which is in most instances a misidentified electron. These two objects serve as the tag and the probe for the measurement, and their selection is described in the following section.

Event selection

The $e\tau_h$ events for the measurement of scale factors of the electron misidentification rate are selected requiring a well-isolated electron triggering the event with p_T greater than 33 GeV and a OS τ_h candidate with a minimum p_T of 20 GeV passing the working points Medium for D_{jet} , Tight for D_μ and VVLoose or Tight for D_e . An additional cut $m_T(e, p_T^{\text{miss}}) < 60$ GeV is included to reduce W + jets background. The scale factors are derived separately in the ECAL barrel region ($|\eta| < 1.46$) and in the ECAL endcap region ($|\eta| > 1.56$) and in different τ_h decay modes, to account for the different levels of data–simulation disagreement observed across these categories. These differences are evident in the pre-fit control plots shown in Figs. 6.15 corresponding to the 2018 dataset. The discrepancy in the region around the 91 GeV peak can be cured with the combined action of electron misidentification rate scale factors and electron energy scale.

Background Estimation

Similarly to the τ_h identification scale factor measurements, also in this case the QCD multijet background is estimated with the ABCD method. All other background are completely estimated through Monte Carlo simulation.

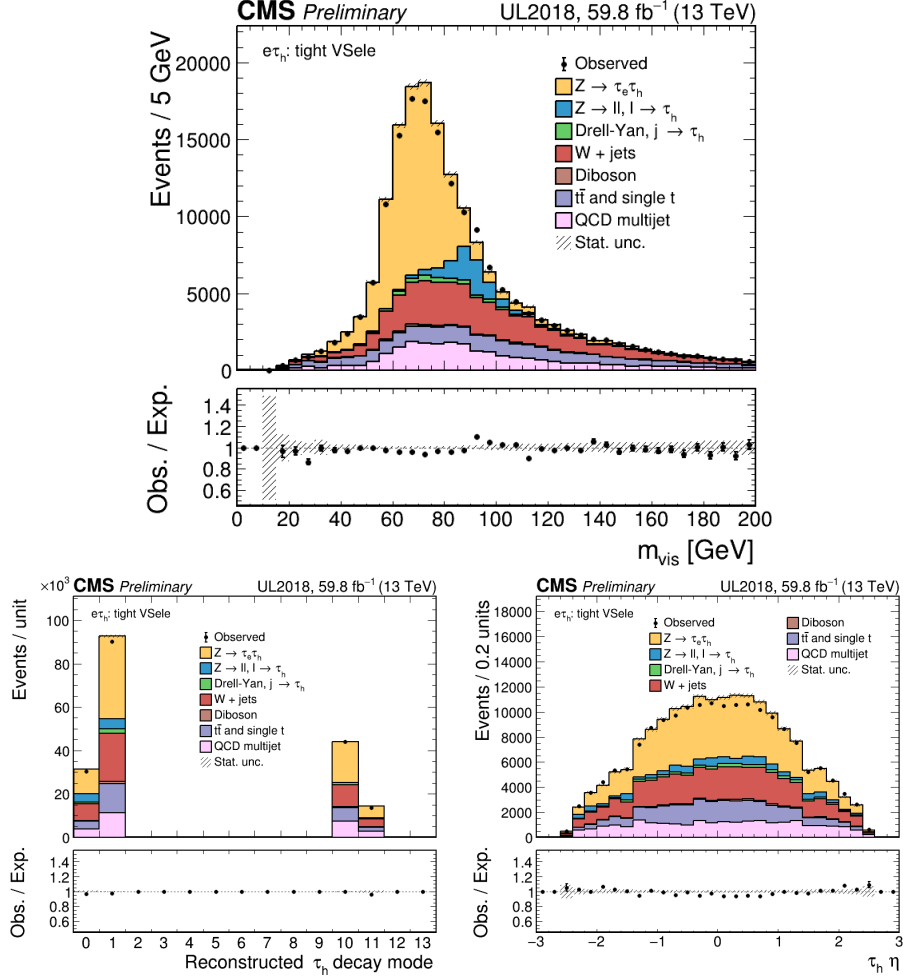


Figure 6.15: Control plots for the $e\tau_h$ channel in 2018 dataset. The Tight working point is used for the D_e discriminator.

Fit Model

Equation 6.9 provides an estimation of the $e \rightarrow \tau_h$ misidentification rate when performed on simulated $Z \rightarrow ee$ events. In order to measure the misidentification rate in real pp collision it is necessary to estimate the number of $Z \rightarrow ee$ events in data. This is done via a Maximum Likelihood fit of the modeled processes of interest to recorded data. The $Z \rightarrow ee$ process is treated as a signal in the fit, as it is the one used to estimate the $e \rightarrow \tau_h$ misidentification rate in data. The other processes are instead treated as a background for the measurement. The main POI for the fit is the scale factor needed to correct the mismodeling of the misidentification rate in simulation: ϵ_{FR} . It is defined as

the ratio between the misidentification rate estimated in data via the fit (FR'), and the one estimated in $Z \rightarrow ee$ simulation (FR):

$$\epsilon_{FR} = \frac{FR'}{FR} . \quad (6.10)$$

Both FR and FR' are evaluated based on the number of events that pass and fail the selection operated by a certain WP of the D_e classifier. Therefore the fit is performed simultaneously in two regions:

- PASS: the event has passed the D_e discriminator, the $Z \rightarrow ee$ events in this region correspond to instances when an electron is misidentified as a τ_h ;
- FAIL: the event was rejected by the D_e discriminator.

The misidentification rate is estimated as the fraction of $Z \rightarrow ee$ events which pass a certain WP of the D_e classifier. A correction applied to the misidentification rate does not affect the number of preselected events, i.e. the denominator of Eq. 6.9,

$$N^{tot} = N_{Z \rightarrow ee}^{pass} + N_{Z \rightarrow ee}^{fail} . \quad (6.11)$$

The total number of reconstructed events is kept constant by varying ϵ_{FR} . A correction applied to the misidentification rate is therefore interpreted as a migration of events between the two regions: an increase to the misidentification rate leads to a lower number of events being assigned to the FAIL region and more events be assigned to the PASS one. This means that the ϵ_{FR} parameter is anti-correlated between the two regions.

Taking into account that ϵ_{FR} does not affect the number of preselected events, Eq. 6.10 can be rewritten as

$$\epsilon_{FR} = \frac{FR'}{FR} = \frac{N_{Z \rightarrow ee}^{pass}}{N_{Z \rightarrow ee}^{pass}} , \quad (6.12)$$

with $N_{Z \rightarrow ee}^{pass}$ representing the number of $Z \rightarrow ee$ events estimated in data in the PASS region. In the fit the $Z \rightarrow ee$ normalization in the PASS region is therefore scaled by ϵ_{FR} in order to measure the misidentification rate.

In simulation, the number of $Z \rightarrow ee$ events in the FAIL region can be calculated by inverting Eq. 6.9, and is equal to

$$N_{Z \rightarrow ee}^{fail} = (1 - FR)N_{Z \rightarrow ee}^{tot} . \quad (6.13)$$

Varying ϵ_{FR} alters the $Z \rightarrow ee$ normalization in the FAIL region as

$$N'_{Z \rightarrow ee}{}^{fail} = \frac{1 - FR'}{1 - FR} N_{Z \rightarrow ee}^{fail} = \frac{1 - \epsilon_{FR} FR}{1 - FR} N_{Z \rightarrow ee}^{fail}, \quad (6.14)$$

with $N'_{Z \rightarrow ee}{}^{fail}$ representing the number of $Z \rightarrow ee$ events estimated in data in the FAIL region.

The total number of $Z \rightarrow ee$ events across the two regions is then assigned an uncertainty, estimated with a parameter which scales in a correlated way the $Z \rightarrow ee$ normalization in the PASS and FAIL regions. This and other systematic uncertainties for the measurement are detailed in the next section.

To accurately measure the correction to the misidentification rate, the uncertainty on the $Z \rightarrow ee$ normalization has to be constrained. This is done in the fit by using the number of events¹ in the FAIL region, which is dominated by $Z \rightarrow ee$ events. The m_{vis} distribution was instead chosen for the fit in the PASS region, see e.g. Fig. 6.19. The $Z \rightarrow ee$ template peaks around 91 GeV in this distribution, allowing higher sensitivity to the $Z \rightarrow ee$ process compared to the various backgrounds.

Systematic Uncertainty Model

As previously mentioned, the primary POI in the fit is ϵ_{FR} , which is anti-correlated between the PASS and FAIL regions. This parameter affects the normalization of the $Z \rightarrow ee$ template in both regions and is treated as a *rate parameter*, meaning it is allowed to float freely within a predefined range. The default range is $[0, 2]$, though it has occasionally been adjusted for specific WPs. In addition to ϵ_{FR} , the normalization of the $Z \rightarrow ee$ template is influenced by another parameter, ϵ_{vsJet} , which is correlated between the two regions. This parameter is also treated as a rate parameter, allowed to vary within the range $[0, 10]$. Its introduction is motivated by the observation that applying a cut on a given WP of a classifier can result in differing efficiencies between data and simulation not only for genuine τ_h candidates but also for misidentified objects. The ϵ_{vsJet} parameter is therefore introduced to account for potential mismodeling of the D_{jet} classifier efficiency in $Z \rightarrow ee$ events.

Another parameter which alters exclusively the $Z \rightarrow ee$ template is a shape uncertainty on the energy scale of the electrons misidentified as τ_h , often referred to as *Fake Energy Scale* (FES). In this case the FES has been treated

¹For practical reasons, the number of events in the failed region was obtained by filling a histogram of the m_{vis} distribution using only 1 bin.

as an additional POI in the fit in order to extract this correction together with the weight scale factor. Practically this means that the m_{vis} distribution for the $Z \rightarrow ee$ process is evaluated for different FES values and then a technique known as *horizontal morphing* [249] is used to interpolate between the templates. For the 2018 dataset we considered discrete FES variations of 0.5% between -5% and 5% with addition of $\pm 10\%$ while for 2022, because of the observed larger shift, discrete variations of 5% between -25% and 25% were considered. The other uncertainties included in the fit, both theoretical and experimental, are summarized in Table 6.4.

Name	Samples	Type	Value
Luminosity	All	lnN	5.0%
Electron efficiency	All	lnN	10 %
Jet $\rightarrow \tau_h$ FR	$Z \rightarrow jj, t\bar{t}$	lnN	20 %
Top cross-section	$t\bar{t}$	lnN	10 %
Diboson cross-section	Diboson	lnN	10 %
$Z/\gamma^* + \text{jets}$ norm.	$Z \rightarrow \tau\tau/ee/jj$	lnN	10 %
W + jets norm.	W + jets	lnN	20 %
QCD norm.	QCD multijet	lnN	20 %
τ_h energy scale	$Z \rightarrow \tau\tau$	shape	5 %
Electron energy scale	All	shape	4 %

Table 6.4: Systematic uncertainties and the processes they are applied to.

Results

The aim of the measurement is to calculate corrections for the $Z \rightarrow ee$ simulation to better describe the misidentification of electrons as τ_h observed in data. The scale factors adjust the normalization and correspond to the correction applied to the $Z \rightarrow ee$ normalization in the PASS region. As a function of the fit parameters, this is determined as:

$$SF = \varepsilon_{FR} \times \varepsilon_{vsJet} , \quad (6.15)$$

while the uncertainty on SF can be propagated by treating the two fit parameters as uncorrelated:

$$\left(\frac{\Delta SF}{SF} \right)^2 = \left(\frac{\Delta \varepsilon_{FR}}{\varepsilon_{FR}} \right)^2 + \left(\frac{\Delta \varepsilon_{vsJet}}{\varepsilon_{vsJet}} \right)^2 . \quad (6.16)$$

The FES corrections, instead, adjust the energy scale of the electrons misidentified as τ_h . This section presents the results for both the corrections, scale factors and FES, for each data taking period (2018, early 2022 and late 2022) and for each category, for the Tight D_e WP. The summary plots with the measurements can be found in Figs. 6.16, 6.17 and 6.18.

The FES measurements are always within 5% for 2018 and within 10% for 2022. While the majority of the misidentification rate scale factors are compatible with unity within their uncertainties, notable deviations are observed in the barrel region for decay mode $h^\pm\pi^0$ —and occasionally also for h^\pm —particularly in the 2022 dataset. These deviations are likely related to specific ECAL conditions in 2022 [250], which impacted the reconstruction of electrons and photons that are essential for *strip* formation in the HPS algorithm. Pre-fit and post-fit plots are reported in Figs. 6.19– 6.24 for the PASS region for DM h^\pm and $h^\pm\pi^0$, which are the most populated by misidentified electrons. The post-fit plots, in particular, serve as important sanity checks, demonstrating that the fit has converged and that the simulated templates have been appropriately adjusted to better describe the observed data.

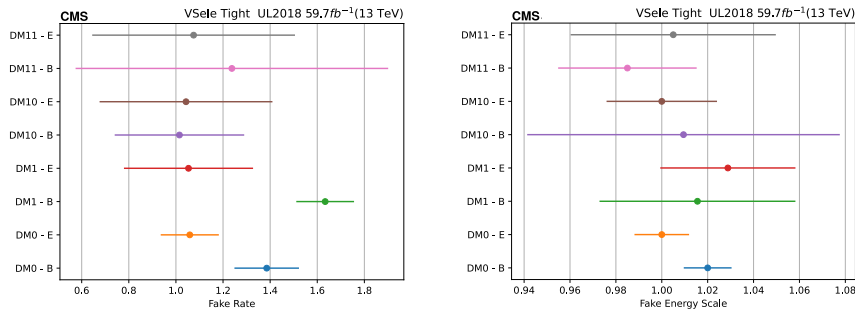


Figure 6.16: Summary plot of results for SFs (left) and FES correction (right) in 2018 dataset. Tight D_e working point. DM0 is the label for h^\pm , DM1 for $h^\pm\pi^0$, DM10 for $h^\pm h^\mp h^\pm$ and DM11 for $h^\pm h^\mp h^\pm\pi^0$. B stands for barrel and E for endcap.

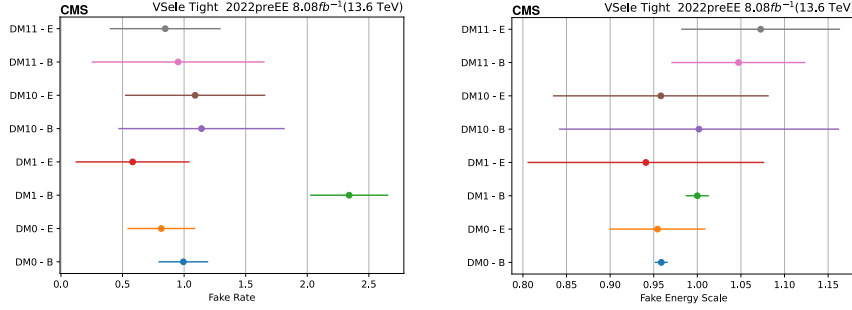


Figure 6.17: Summary plot of results for SFs (left) and FES correction (right) in early 2022 dataset. Tight D_e working point. DM0 is the label for h^\pm , DM1 for $h^\pm\pi^0$, DM10 for $h^\pm h^\mp h^\pm$ and DM11 for $h^\pm h^\mp h^\pm\pi^0$. B stands for barrel and E for endcap.

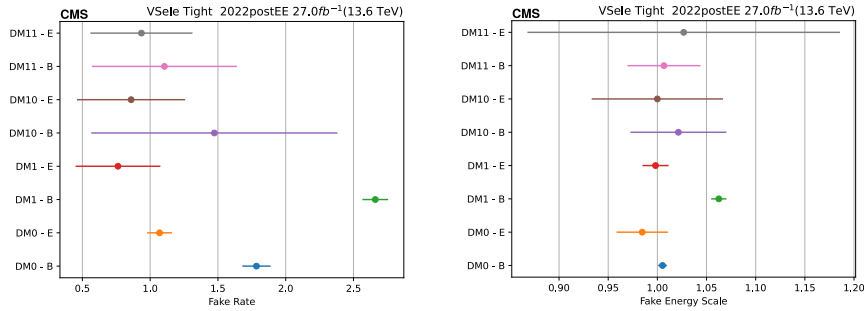


Figure 6.18: Summary plot of results for SFs (left) and FES correction (right) in late 2022 dataset. Tight D_e working point. DM0 is the label for h^\pm , DM1 for $h^\pm\pi^0$, DM10 for $h^\pm h^\mp h^\pm$ and DM11 for $h^\pm h^\mp h^\pm\pi^0$. B stands for barrel and E for endcap.

6.4 Summary and outlook

In this chapter, I presented the work I carried out within the TauPOG of the CMS Collaboration. The focus was primarily on the validation and calibration of the new version of the DEEPTAU algorithm, which is the recommended τ_h identification algorithm for Run 3. I demonstrated that DEEPTAU v2.5 not only achieves improved classification performance compared to v2.1, but also shows better agreement between data and simulation due to the implementation of domain adaptation techniques.

To quantify the improvement, we calibrated the algorithm using both 2018 data and early Run 3 data. In both cases, the resulting τ_h identification scale factors for v2.5 were found to be closer to unity, indicating better modeling in the simulation. As part of the calibration effort, I took particular respon-

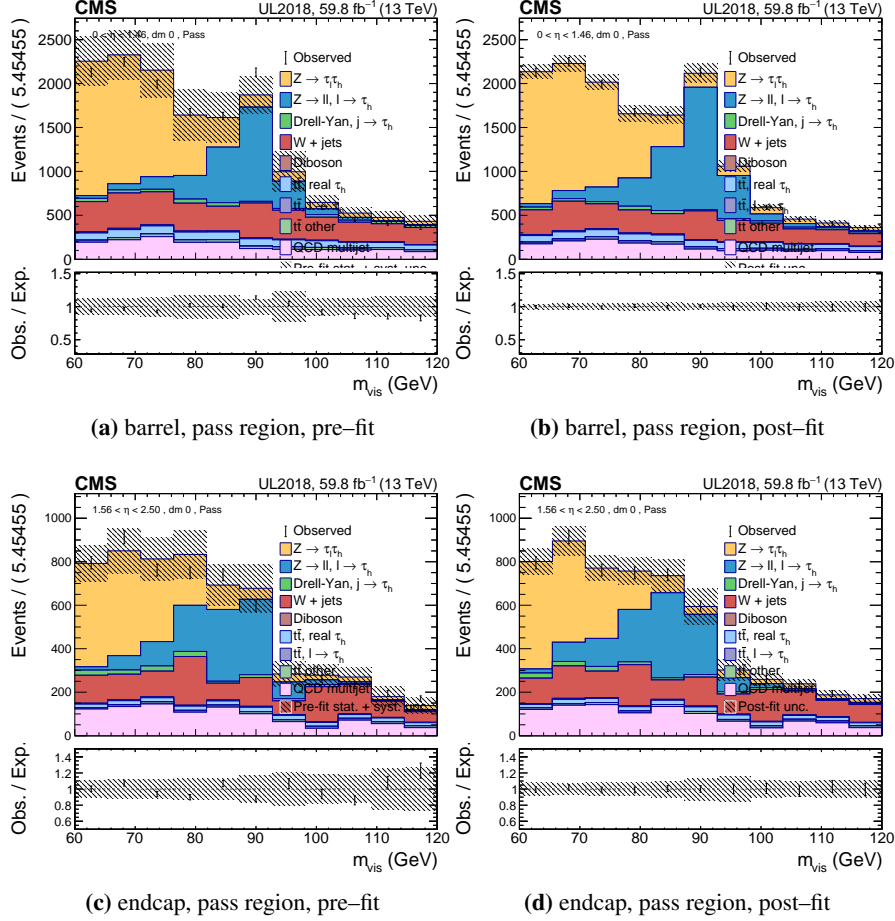


Figure 6.19: m_{vis} distributions for 2018 dataset, D_e Tight, h^\pm DM and divided in barrel (upper row) and endcap (lower row).

sibility for measuring the corrections associated with electrons misidentified as τ_h . This included deriving scale factors for the misidentification rate and corresponding energy scale corrections as functions of the D_e WP, the τ_h candidate's $|\eta|$, and DM.

These measurements have been repeated for the 2023 dataset, and we are currently working on the 2024 correction campaign. The 2024 data sample is significantly larger—more than three times the size of that from 2022—which allows for a reduction in statistical uncertainties and motivates the development of a more sophisticated model for systematic uncertainties.

In parallel, new τ_h identification algorithms have become available [170], based on the ParticleNet [251] and Particle Transformer [252] jet taggers, ex-

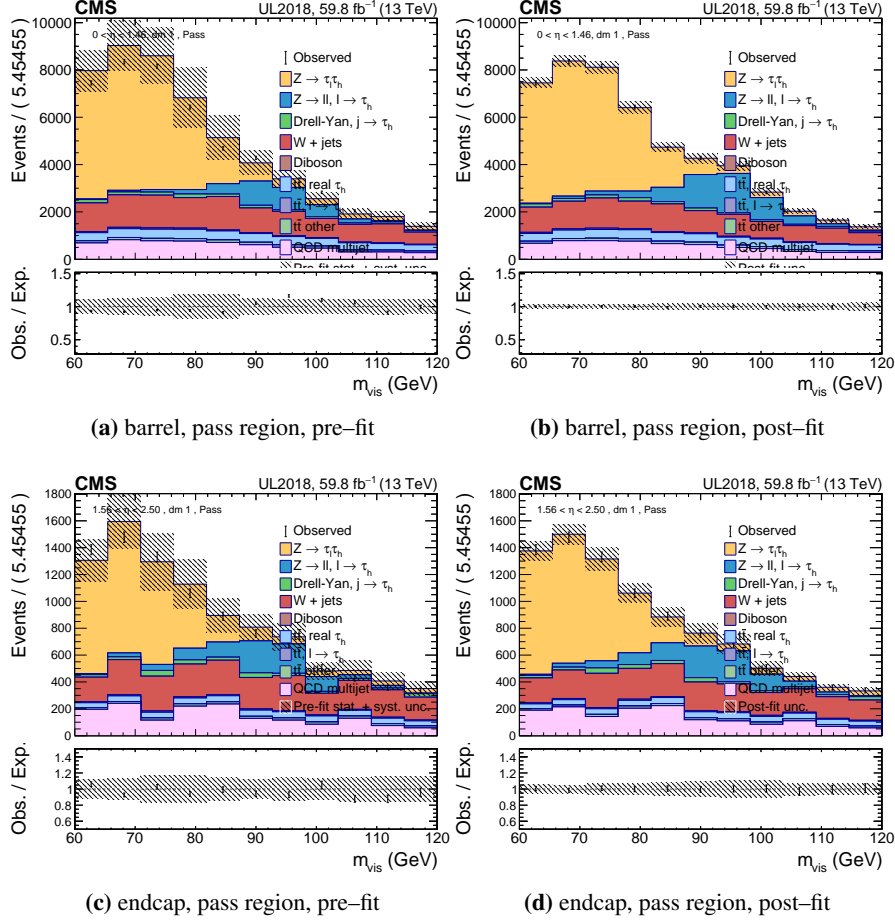


Figure 6.20: m_{vis} distributions for 2018 dataset, D_e Tight, $h^\pm\pi^0$ DM and divided in barrel (upper row) and endcap (lower row).

tended to include τ_h identification. These algorithms operate directly on jet objects and thus do not rely on the HPS algorithm. Nonetheless, they include machine learning-based decay mode and charge assignment procedures, which have shown competitive accuracy compared to HPS.

At present, I am coordinating the comparative studies of these three identification algorithms. While the analyses are ongoing, initial results indicate that the jet-based taggers offer improved rejection of jets but exhibit somewhat reduced discrimination power against electrons and muons. This may be due to the reduced use of lepton-specific features compared to DEEPTAU. Furthermore, DEEPTAU v2.5 continues to show superior agreement between data and simulation, reaffirming the effectiveness of the domain adaptation strategy.

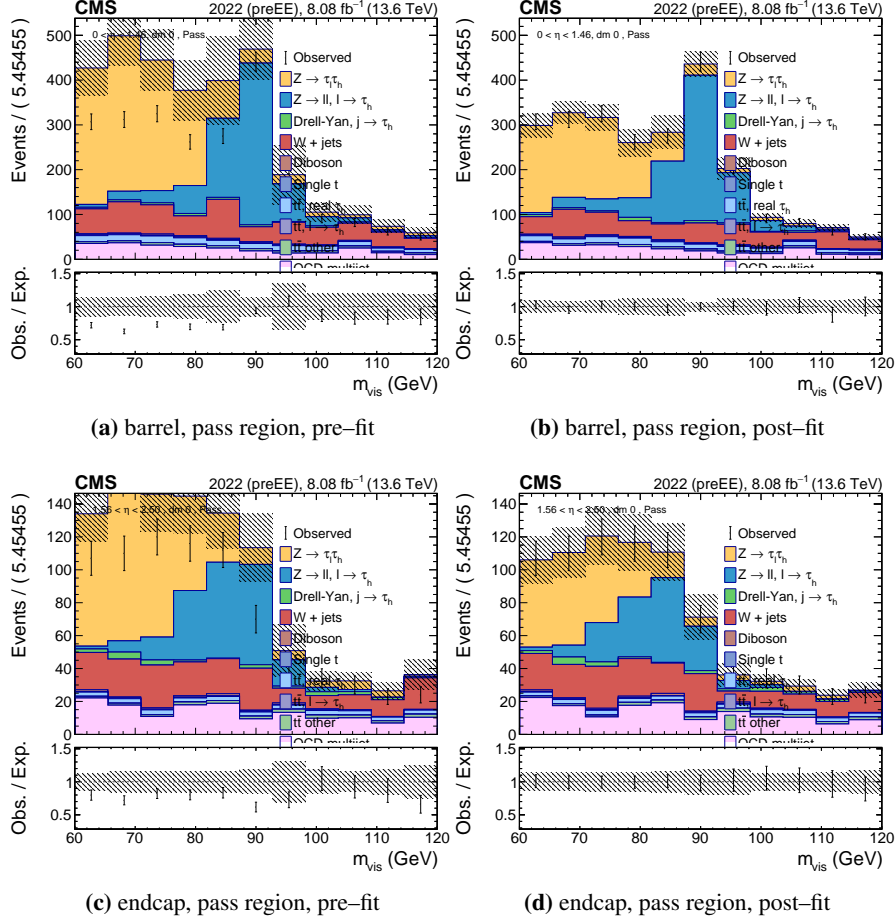


Figure 6.21: m_{vis} distributions for early 2022 dataset, D_e Tight, h^\pm DM and divided in barrel (upper row) and endcap (lower row).

Ultimately, the long-term objective is to develop a unified tagging algorithm capable of simultaneously identifying b, c, s, and light-flavor/gluon jets, τ_h , electrons, and muons. This would leverage the domain expertise embedded in current specialized taggers while consolidating their functionality into a single, albeit complex, machine learning model.

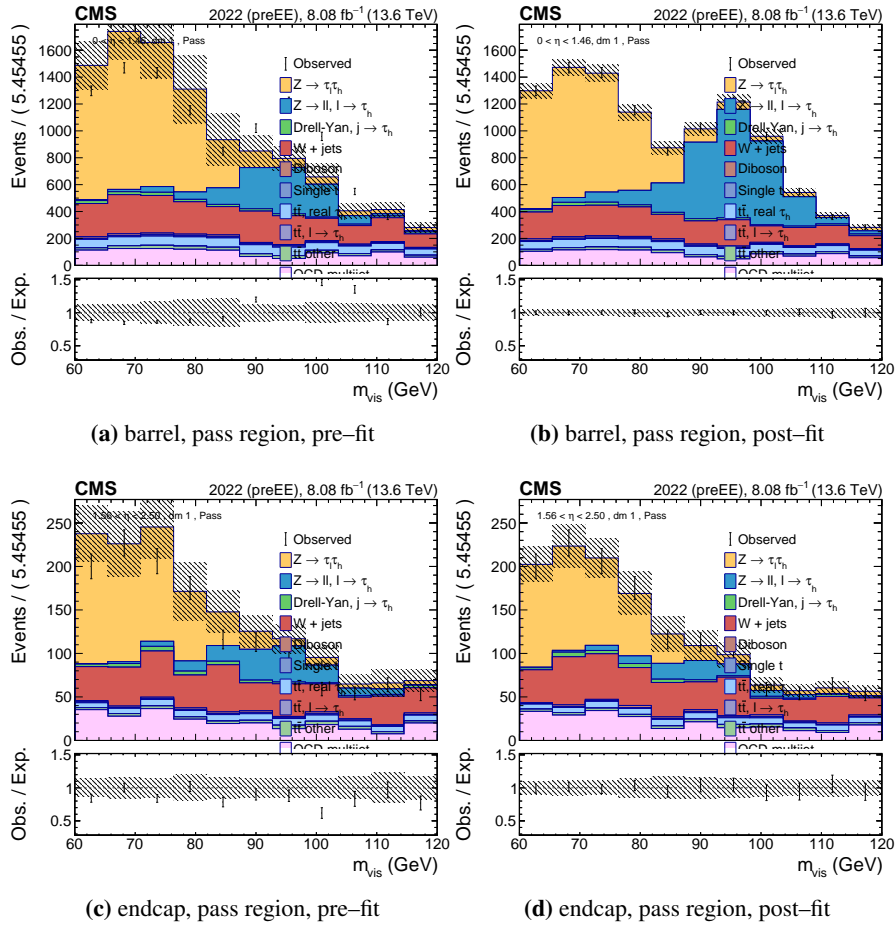


Figure 6.22: m_{vis} distributions for 2022 preEE dataset, D_e Tight, $h^\pm\pi^0$ DM and divided in barrel (upper row) and endcap (lower row).

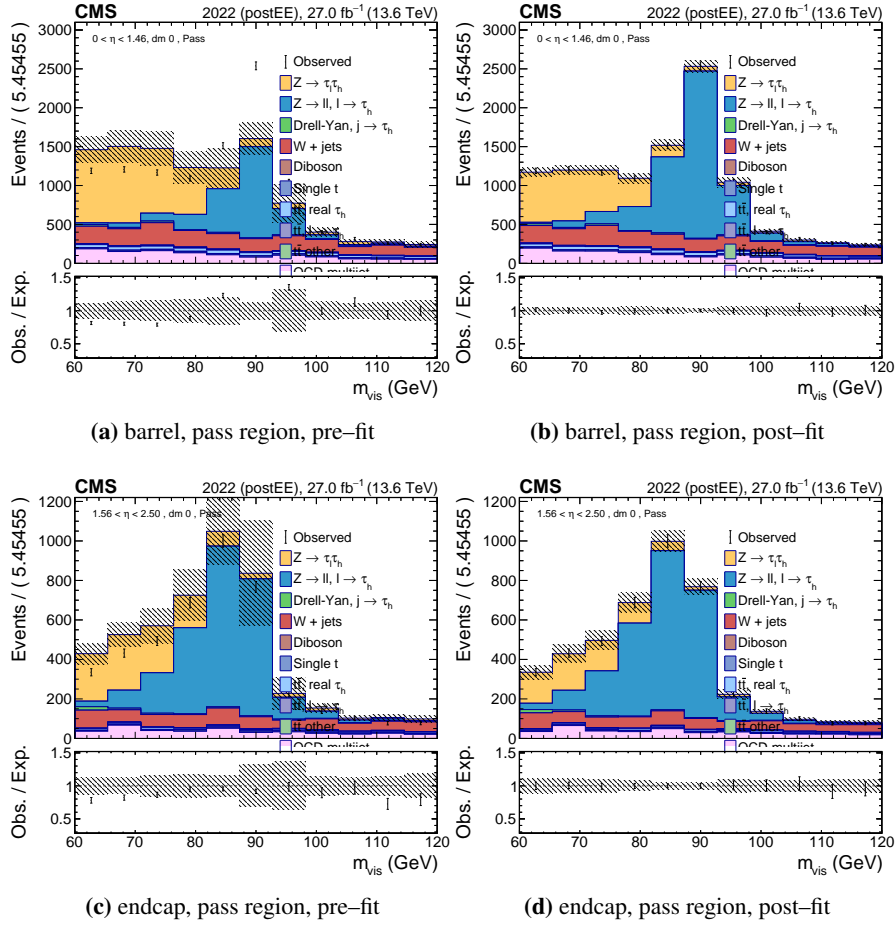


Figure 6.23: m_{vis} distributions for late 2022 dataset, D_e Tight, h^\pm DM and divided in barrel (upper row) and endcap (lower row).

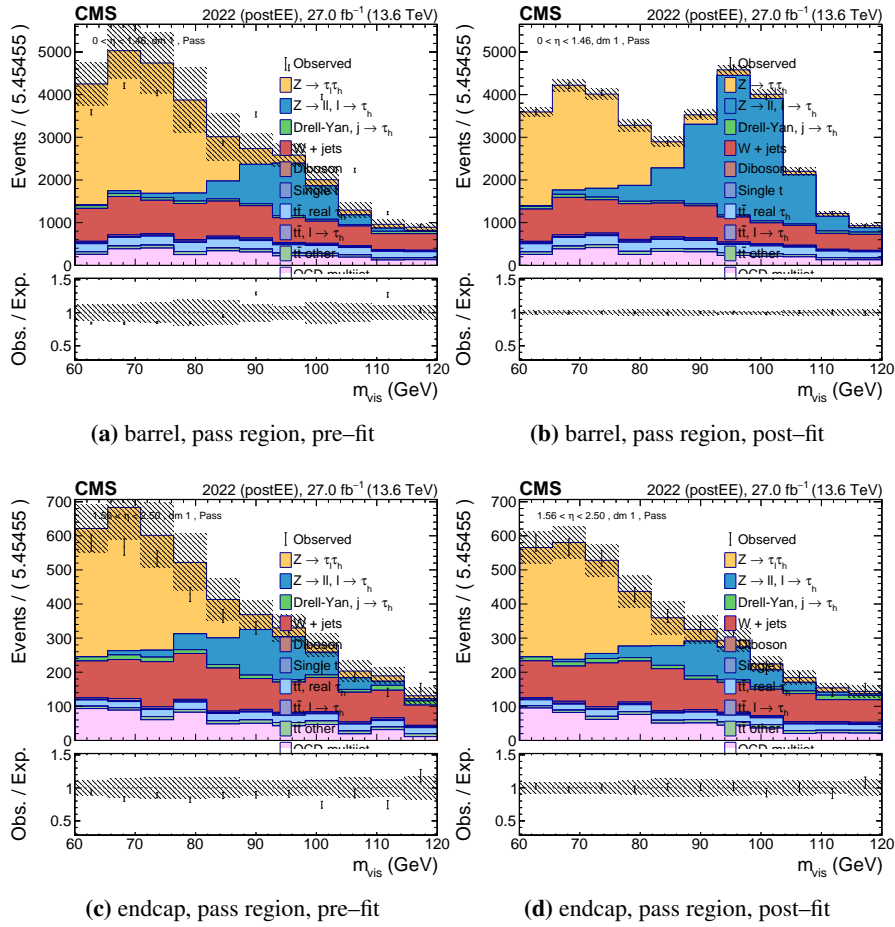


Figure 6.24: m_{vis} distributions for late 2022 dataset, D_e Tight, h^\pm DM and divided in barrel (upper row) and endcap (lower row).

Search for BSM scalar neutral bosons through the process $H/A \rightarrow ZA/H \rightarrow \ell^+ \ell^- \tau^+ \tau^-$ with CMS full Run 2 dataset

In this chapter, I present the search for BSM neutral scalar bosons through the process $H/A \rightarrow ZA/H \rightarrow \ell^+ \ell^- \tau^+ \tau^-$ ¹, using the full Run 2 dataset collected by the CMS experiment. I have been responsible for all aspects of this analysis and have been designated as the Contact Person for it.

The physics motivations and the 2HDM theoretical background for this search have been extensively discussed in Chapter 2, while the relevant details of detector object reconstruction in CMS—including a dedicated focus on τ_h identification—are provided in Chapters 3 and 6, respectively.

In the following, after a brief introduction on the previous results of this search, I will describe the adopted analysis strategy and present the expected results in a model independent fashion together with a 2HDM interpretation. At the time of writing, the analysis is undergoing internal CMS review and is currently in the so-called *unblinding* stage. Consequently, data in the signal region and observed results cannot yet be disclosed. Further internal documentation related to this analysis is available in Ref. [253].

7.1 Introduction

In Chapter 2, we discussed that, in its most general formulation, a 2HDM requires 14 parameters to describe the scalar sector. However, when a Z_2 symmetry is imposed to suppress flavor-changing neutral currents—consistent

¹Hereafter, the indication of the lepton charges will be omitted for notational convenience.

with experimental constraints—and the observed Higgs boson mass (125 GeV) and electroweak vacuum expectation value (246 GeV) are fixed, only seven free parameters remain.

Compatibility of a 125 GeV SM-like Higgs boson with 2HDMs is achieved in the *alignment limit*. In this regime, one of the CP-even scalars, either h or H , is identified with the observed Higgs boson, and the condition $\cos(\beta - \alpha) \approx 0$ holds.

In the alignment limit, theoretical studies [254] have shown that a large mass splitting (> 100 GeV) between the pseudoscalar A and the heavier CP-even scalar H can facilitate a strongly first-order electroweak phase transition. Such a transition is a necessary condition for electroweak baryogenesis, potentially explaining the matter–antimatter asymmetry observed in the Universe. In this scenario, the most probable decay of the pseudoscalar A is $A \rightarrow ZH$. Since the analysis strategy adopted here is largely model- and spin-independent, the results can also be interpreted in the reverse mass hierarchy scenario, where the pseudoscalar A is lighter than H and decays via $H \rightarrow ZA$.

The results presented in this thesis are based on pp collision data collected by the CMS experiment at $\sqrt{s} = 13$ TeV during Run 2 (2016–2018), corresponding to an integrated luminosity of 138 fb^{-1} . Three different τ -lepton pair final states are studied: $\tau_e \tau_h$, $\tau_\mu \tau_h$, and $\tau_h \tau_h$. Considering $Z \rightarrow \ell\ell$ decays ($\ell = e, \mu$), the analysis covers six final states in total.

The choice of these final states is motivated by the efficient triggering and reconstruction of a resonant dilepton system ($Z \rightarrow \ell\ell$), together with the $A/H \rightarrow \tau\tau$ decay, which has a high branching fraction across much of the 2HDM parameter space. Complementary channels involving $A/H \rightarrow b\bar{b}$ or $t\bar{t}$ decays, which also have significant branching fractions, are addressed in separate analyses, with a future combination foreseen.

A search targeting this process was already performed during Run 1, in combination with the $A/H \rightarrow b\bar{b}$ channel [255]. The final Run 1 results are included here for reference and for direct comparison with the results presented in this thesis. Figure 7.1 shows the model-independent 95% CL upper limits on the production cross section times branching ratio for the $\ell\ell\tau\tau$ and $\ell\ell b\bar{b}$ final states. Figure 7.2 presents the corresponding limits on a specific 2HDM benchmark scenario, demonstrating 95% CL exclusion in the regions $m_H = 200\text{--}700$ GeV and $m_A = 20\text{--}270$ GeV for $m_H > m_A$, or alternatively, $m_A = 200\text{--}700$ GeV and $m_H = 120\text{--}270$ GeV for $m_A > m_H$.

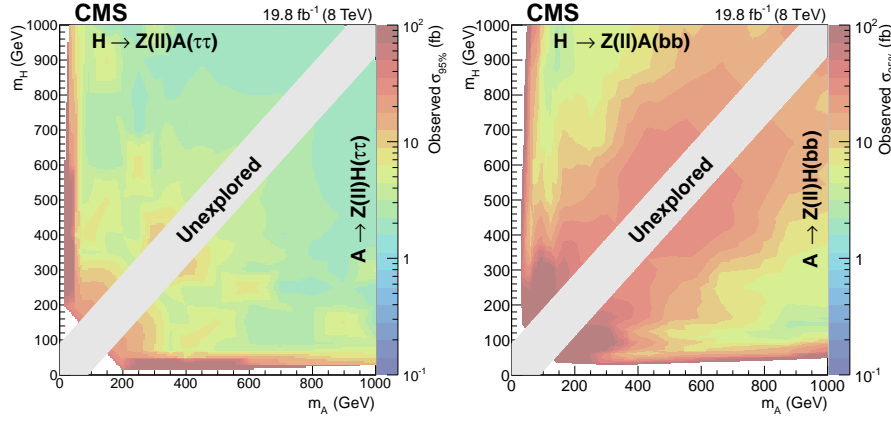


Figure 7.1: Observed 95% CL upper limits on $\sigma_{H/A \rightarrow Z(II)A(\tau\tau)}$ (left) and $\sigma_{H/A \rightarrow Z(II)A(bb)}$ (right) as a function of m_A and m_H [255].

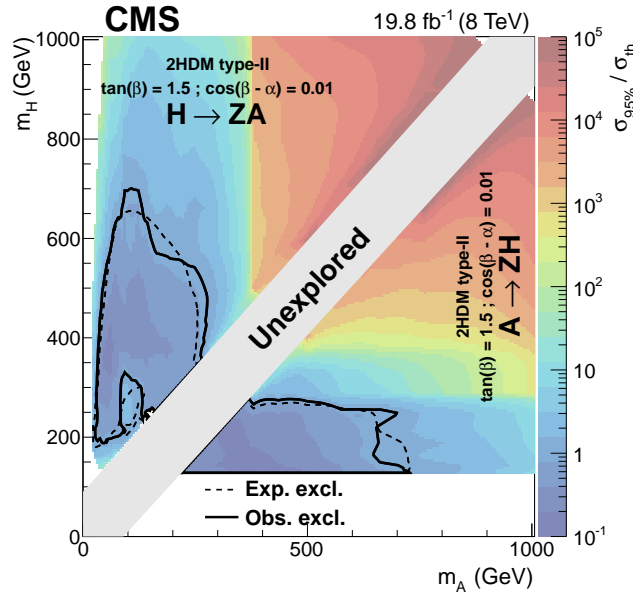
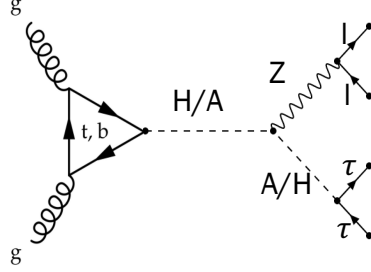


Figure 7.2: Observed limits on the signal strength $\mu = \sigma/\sigma_{th}$ for a 2HDM benchmark after combining results from $\ell\ell b\bar{b}$ and $\ell\ell\tau\tau$ final states [255]. Cross sections are normalized to the theoretical prediction for a 2HDM Type-II scenario with $\tan\beta = 1.5$ and $\cos(\beta - \alpha) = 0.01$. The dashed contour shows the expected exclusion region; the solid contour shows the observed exclusion.

The Feynman diagram corresponding to the signal process is shown in Fig. 7.3.

**Figure 7.3:** Feynman diagram of the signal process.

As detailed in Sec. 7.2.2, several signal samples were generated for different mass hypotheses. To maximize sensitivity and achieve the tightest possible exclusion limits, a parametric DNN was trained, as described in Sec. 7.9. A data-driven approach was used to estimate reducible backgrounds (Sec. 7.8). The evaluation of both experimental and theoretical systematic uncertainties relevant to this search is presented in Sec. 7.11. Final results, discussed in Sec. 7.12, are reported in terms of upper limits on the cross section times branching ratio ($\sigma \cdot \text{BR}$) and on the signal strength μ , providing both model-independent and model-dependent interpretations, in line with the Run 1 study.

7.2 Samples

7.2.1 Data

This analysis uses a data sample recorded by the CMS experiment during 2016, 2017 and 2018. The summary of the integrated luminosities for each year is provided in Table 7.1. The Table also shows the JSON files used to select only data collected and fully certified by the CMS collaboration. The analysis relies on two different primary datasets, *SingleElectron* and *SingleMuon*, and the overlap between the two is removed based on which triggers are fired in the event. The collision datasets used are listed in Table 7.2 for *SingleMuon* and in Table 7.3 for *SingleElectron*, and correspond to the *UltraLegacy* (UL) reprocessing campaign.

year	JSON	$L [\text{fb}^{-1}]$
UL2018	Cert_314472-325175_13TeV_Legacy2018_Collisions18_JSON.txt	59.83
UL2017	Cert_294927-306462_13TeV_UL2017_Collisions17_GoldenJSON.txt	41.48
UL2016	Cert_271036-284044_13TeV_Legacy2016_Collisions16_JSON.txt	36.31

Table 7.1: Recommended JSON files [256] with corresponding integrated luminosity.

Single Muon
UL2018
/SingleMuon/Run2018A-UL2018_MiniAODv2_NanoAODv9-v2/NANOAO
/SingleMuon/Run2018B-UL2018_MiniAODv2_NanoAODv9-v2/NANOAO
/SingleMuon/Run2018C-UL2018_MiniAODv2_NanoAODv9-v2/NANOAO
/SingleMuon/Run2018D-UL2018_MiniAODv2_NanoAODv9-v1/NANOAO
UL2017
/SingleMuon/Run2017B-UL2017_MiniAODv2_NanoAODv9-v1/NANOAO
/SingleMuon/Run2017C-UL2017_MiniAODv2_NanoAODv9-v1/NANOAO
/SingleMuon/Run2017D-UL2017_MiniAODv2_NanoAODv9-v1/NANOAO
/SingleMuon/Run2017E-UL2017_MiniAODv2_NanoAODv9-v1/NANOAO
/SingleMuon/Run2017F-UL2017_MiniAODv2_NanoAODv9-v1/NANOAO
UL2016-preVFP
/SingleMuon/Run2016B-ver2_HIPM_UL2016_MiniAODv2_NanoAODv9-v2/NANOAO
/SingleMuon/Run2016C-HIPM_UL2016_MiniAODv2_NanoAODv9-v2/NANOAO
/SingleMuon/Run2016D-HIPM_UL2016_MiniAODv2_NanoAODv9-v2/NANOAO
/SingleMuon/Run2016E-HIPM_UL2016_MiniAODv2_NanoAODv9-v2/NANOAO
/SingleMuon/Run2016F-HIPM_UL2016_MiniAODv2_NanoAODv9-v2/NANOAO
UL2016-postVFP
/SingleMuon/Run2016F-UL2016_MiniAODv2_NanoAODv9-v1/NANOAO
/SingleMuon/Run2016G-UL2016_MiniAODv2_NanoAODv9-v1/NANOAO
/SingleMuon/Run2016H-UL2016_MiniAODv2_NanoAODv9-v1/NANOAO

Table 7.2: Samples comprising the Run 2 Single Muon datasets.

7.2.2 Simulations

Backgrounds

The main sources of background in this analysis are the di-boson events, ZZ , with subsequent decay into leptons (irreducible background) and the misidentified leptons, often called in jargon *fakes*, from $Z/\gamma^* + \text{jets}$ (reducible background).

The MADGRAPH5_AMC@NLO [257, 258] generator is used for almost all the background samples except for the SM Higgs production ZH and the ZZ sample, where POWHEG 2.0 [259–261] is employed. The generators are interfaced with PYTHIA 8.2 [262] to model the parton showering and fragmentation, as well as the decay of the τ leptons. The PYTHIA parameters affecting the description of the underlying event are set to the CP5 tune [263]. Generated events are processed through a simulation of the CMS detector based on GEANT4 [264], and are reconstructed with the same algorithms used for data. The effect of pileup is taken into account by generating concurrent total inelastic collision events with PYTHIA. The simulated events

Single Electron
UL2018
/EGamma/Run2018A-UL2018_MiniAODv2_NanoAODv9-v1/NANOAO
/EGamma/Run2018B-UL2018_MiniAODv2_NanoAODv9-v1/NANOAO
/EGamma/Run2018C-UL2018_MiniAODv2_NanoAODv9-v1/NANOAO
/EGamma/Run2018D-UL2018_MiniAODv2_NanoAODv9-v3/NANOAO
UL2017
/SingleElectron/Run2017B-UL2017_MiniAODv2_NanoAODv9-v1/NANOAO
/SingleElectron/Run2017C-UL2017_MiniAODv2_NanoAODv9-v1/NANOAO
/SingleElectron/Run2017D-UL2017_MiniAODv2_NanoAODv9-v1/NANOAO
/SingleElectron/Run2017E-UL2017_MiniAODv2_NanoAODv9-v1/NANOAO
/SingleElectron/Run2017F-UL2017_MiniAODv2_NanoAODv9-v1/NANOAO
UL2016-preVFP
/SingleElectron/Run2016B-ver2_HIPM_UL2016_MiniAODv2_NanoAODv9-v2/NANOAO
/SingleElectron/Run2016C-HIPM_UL2016_MiniAODv2_NanoAODv9-v2/NANOAO
/SingleElectron/Run2016D-HIPM_UL2016_MiniAODv2_NanoAODv9-v2/NANOAO
/SingleElectron/Run2016E-HIPM_UL2016_MiniAODv2_NanoAODv9-v2/NANOAO
/SingleElectron/Run2016F-HIPM_UL2016_MiniAODv2_NanoAODv9-v2/NANOAO
UL2016-postVFP
/SingleElectron/Run2016F-UL2016_MiniAODv2_NanoAODv9-v1/NANOAO
/SingleElectron/Run2016G-UL2016_MiniAODv2_NanoAODv9-v1/NANOAO
/SingleElectron/Run2016H-UL2016_MiniAODv2_NanoAODv9-v1/NANOAO

Table 7.3: Samples comprising the Run 2 Single Electron datasets.

are weighted such that the distribution of the number of pileup interactions matches that in data.

The list of background simulations included in the analysis is available in Table 7.4.

Process	Dataset Name	$\sigma \times BR(\times \epsilon_{filter})$
$ZH, H \rightarrow \tau\tau$	/ZHToTauTau_M125_CP5_13TeV-powheg-pythia8	0.0554 pb
$Z \rightarrow \ell\ell$	/DYJetsToLL_M-50_TuneCP5_13TeV-madgraphMLM-pythia8	6077.22 pb
$t\bar{t}$	/TTJets_TuneCP5_13TeV-amcatnloFXFX-pythia8	831.76 pb
$t\bar{t}W(\rightarrow \ell\nu)$	/TTWJetsToLNu_TuneCP5_13TeV-amcatnloFXFX-madspin-pythia8	0.2043 pb
$t\bar{t}Z(\rightarrow \ell\ell)$	/TTZToLLNuNu_M-10_TuneCP5_13TeV-amcatnlo-pythia8	0.2439 pb
WW	/WW_4F_TuneCP5_13TeV-amcatnlo-pythia8	0.2086 pb
WWZ	/WWZ_TuneCP5_13TeV-amcatnlo-pythia8	0.1651 pb
WZZ	/WZZ_TuneCP5_13TeV-amcatnlo-pythia8	0.05565 pb
ZZZ	/ZZZ_TuneCP5_13TeV-amcatnlo-pythia8	0.01398 pb
$qq \rightarrow ZZ \rightarrow 4\ell$	/ZZTo4L_TuneCP5_13TeV-powheg-pythia8	1.256 pb
$qq \rightarrow ZZ \rightarrow 2q2\ell$	/ZZTo2Q2L_mllmin4p0_TuneCP5_13TeV-amcatnloFXFX-pythia8	3.676 pb
$qq \rightarrow ZZ \rightarrow 2\ell 2\nu$	/ZZTo2L2Nu_TuneCP5_13TeV-powheg-pythia8	0.9738 pb
$gg \rightarrow ZZ \rightarrow 2e2\mu$	/GluGluToContInToZZTo2e2mu_TuneCP5_13TeV-mcfm701-pythia8	0.00319 pb
$gg \rightarrow ZZ \rightarrow 2e2\tau$	/GluGluToContInToZZTo2e2tau_TuneCP5_13TeV-mcfm701-pythia8	0.00319 pb
$gg \rightarrow ZZ \rightarrow 2\mu 2\tau$	/GluGluToContInToZZTo2mu2tau_TuneCP5_13TeV-mcfm701-pythia8	0.00319 pb
$gg \rightarrow ZZ \rightarrow 4e$	/GluGluToContInToZZTo4e_TuneCP5_13TeV-mcfm701-pythia8	0.00159 pb
$gg \rightarrow ZZ \rightarrow 4\mu$	/GluGluToContInToZZTo4mu_TuneCP5_13TeV-mcfm701-pythia8	0.00159 pb
$gg \rightarrow ZZ \rightarrow 4\tau$	/GluGluToContInToZZTo4tau_TuneCP5_13TeV-mcfm701-pythia8	0.00159 pb
$WZ(3\ell\nu)$	/WZTo3LNu_TuneCP5_13TeV-amcatnloFXFX-pythia8	5.213 pb
$WZ(2q2\ell)$	/WZTo2Q2L_mllmin4p0_TuneCP5_13TeV-amcatnloFXFX-pythia8	6.419 pb
$V\gamma$	/ZGToLLG_01J_5f_TuneCP5_13TeV-amcatnloFXFX-pythia8	55.48 pb

Table 7.4: MC background samples included in the analysis. All samples are stored in nanoAOD format (NanoAODv9) and belong to the RunIISummer20UL campaign, with Global Tag 106X_upgrade2018_realistic_v16_L1v1 for UL2018, 106X_mc2017_realistic_v9 for UL2017, 106X_mcRun2_asymptotic_v17 for UL2016-postVFP and 106X_mcRun2_asymptotic_preVFP_v11 for UL2016-preVFP (2016APV). When available, all sample extensions are used.

Signal

In the context of the Type-II 2HDM, the benchmark scenario $H \rightarrow ZA$, with $Z \rightarrow \ell\ell$ and $A \rightarrow \tau\tau$, has been chosen. The reversed scenario in which $A \rightarrow ZH$ is also considered, and few benchmark points have been produced in this configuration to test if the analysis results are symmetrical by exchange of $A \leftrightarrow H$ (analysis non-sensitive to parity).

The MADGRAPH5_AMC@NLO generator, interfaced with PYTHIA 8.2, has been used to generate different signal processes according to different m_A and m_H combinations. The Universal FeynRules Output (UFO) model [265] used is 2HDMTII_NLO [266] [267]. The parton distribution function set is NNPDF31_NNLO_AS_0118_MC_HESSIAN_PDFAS [268], along with CP5 tune. The final signal samples have been obtained using the full simulation and reconstruction within the CMSSW official framework. The MadGraph datacards are stored in Ref. [269], while the request for central sample production can be found in Ref. [270].

In the minimal formulation of the 2HDM Lagrangian, the mass terms for the scalars are related to the parameter α and β . These two parameters determine the interactions of the various Higgs fields with the vector bosons and with the fermions. Considering the parameter space still favoured by direct searches, the chosen values for the couplings and their mixing are $\cos(\beta - \alpha) = 0.01$ (alignment limit) and $\tan \beta = 1.5$. Other relevant parameters are set to $m_{12}^2 = \sqrt{m_{H\pm}^2 \frac{\tan \beta}{1 + \tan^2 \beta}}$, and $\lambda_{6,7} = 0$ to ensure CP conservation at tree level.

The explored mass region corresponds to values of m_H and m_A varying in the ranges [170,1000] GeV and [20,800] GeV, respectively, with the constraint $m_H > m_A + m_Z$, as shown in Figure 7.4. The region where m_H and m_A are smaller than m_h for the processes $H \rightarrow ZA$ and $A \rightarrow ZH$ respectively, is forbidden by the model.

The mass points to simulate were derived to achieve a good coverage in the two-dimensional mass plane (m_A, m_H) in term of experimental mass resolution. A detailed explanation of the adopted strategy can be found in Appendix A. Few samples available privately were used to study the mass resolution in m_A and m_H , fit the 2D gaussian-like distributions and extract the 1- σ ellipses, shown in green in Figure 7.4. The reconstructed mass always appears shifted towards lower values with respect to the simulated one because of the missing energy carried away by neutrinos. As explained in Sec. 7.10, the energy of neutrinos from tau lepton decays is partially recovered by a dedicated algorithm that target SM Higgs Boson decay to tau pair. Starting from these

measured ellipses, the resolution for other mass points in the region of interest has been extrapolated (blue ellipses in the Figure). As visible, with this choice of points it is possible to cover the allowed region up to 1 TeV. Finally, the pink crosses mark the simulated benchmark points in the reversed scenario.

The production cross section used in the normalization of the signal samples is the one extracted from the SUSHI program [271] version 1.7.0, exploiting the NNLO predictions. Branching ratio calculation and check of the potential stability, perturbativity, unitarity are, instead, performed with 2HDMC [140] version 1.8.0. The cross section times branching ratio for the explored mass plane is shown in Fig. 7.5. The sudden drop after $m_A=300$ GeV is due to the possibility of the lighter boson to decay into top quarks, channel that soon becomes the dominant one, according to the model. The full list of centrally simulated samples can be found in Tables 24, 25 and 26 for $H \rightarrow ZA$ and in Table 27 for $A \rightarrow ZH$ in Appendix B, with related cross sections for the specific 2HDM benchmark model.

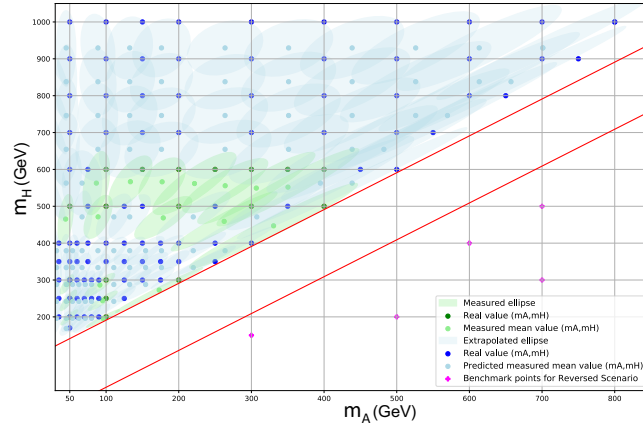


Figure 7.4: Dark dots (blue and green) show the simulated mass points for the process $H \rightarrow ZA \rightarrow \ell\ell\tau\tau$. The ellipses in light green show the measured 1σ contour of the reconstructed 2D m_A - m_H distribution. The ellipses in light blue are extrapolated starting from the green ones. The pink crosses mark the simulated benchmark points for the reversed process $A \rightarrow ZH \rightarrow \ell\ell\tau\tau$. For the full signal production (summarized in Tables 24, 25 and 26) mass points with $m_A=20$ GeV are added, while not appearing in this plot.

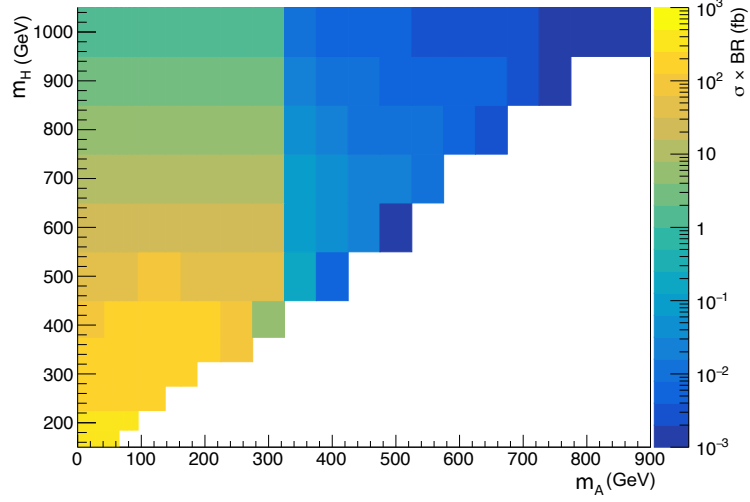


Figure 7.5: Cross section times branching ratio values for the process $H \rightarrow ZA \rightarrow \ell\ell\tau\tau$ (in fb), for the explored mass region.

7.3 Object reconstruction

A detailed description of the standard CMS object reconstruction based on the PF algorithm is provided in Sec. 3.3. For the reader's convenience, a brief summary is presented here, focusing on the reconstructed objects used in this analysis, along with the selection criteria applied.

7.3.1 Muons

Muons [272] are reconstructed from tracks found in the muon system, associated with tracks in the silicon tracking detectors. They are identified based on the quality of the track fit and the number of associated hits in the different tracking detectors. Muons are required to meet the medium criteria for identification as recommended by the MuonPOG. This requires meeting all criteria for the looser working point (identified as a PF muon, and is either a *Global* or *Tracker* Muon), as well as a high fraction of valid tracker hits, and either additional quality cuts on on global muons, or increased segment compatibility [273]. Muons are selected with $p_T > 10$ GeV, $|\eta| < 2.4$ and $|d_z| < 1.0$ cm and $|d_{xy}| < 0.5$ cm. Isolation conditions are applied on top the identification. The delta-beta corrected isolation with a cone size of 0.15 is used.

7.3.2 Electrons

Electrons [274] are reconstructed by linking the track and the cluster in the ECAL, without any signal left in the HCAL. Identification efficiency working points are then provided by a multivariate analysis (MVA) approach, where a Boosted Decision Tree (BDT) is trained on multiple electron variables, to distinguish between prompt and unmatched plus non-prompt electron processes. Cuts on the output discriminator values provide 80% and 90% electron identification efficiency working points [275]. Electrons identified in this analysis are required to match the 90% working point of the training that does include the isolation. No further isolation requirement is imposed, since it was already included in the identification task. In this analysis, electrons are selected with $p_T > 10$ GeV and $|\eta| < 2.5$, avoiding the transition region $1.44 < |\eta| < 1.57$. The requirement on the impact parameters is the same as muon's, i.e. $|d_z| < 1.0$ cm and $|d_{xy}| < 0.5$ cm.

7.3.3 Hadronic Taus

The reconstruction of τ leptons that decay into hadrons is performed with the HPS algorithm, while the DeepTau algorithm is used to reduce the incidence of jets, electrons and muons being misidentified as τ_h candidates by HPS. During Run 2, the v2.1 training of the DeepTau is recommended [276], with working point VVLoose for D_e (99% efficiency), Tight for D_μ (99.5% efficiency) and Medium for D_{jet} (70% efficiency). In this analysis the τ_h candidates are selected with $p_T > 20$ GeV, $|\eta| < 2.3$ and $|d_z| < 0.2$ cm. The τ_h candidates are also cleaned by the presence of muons and electrons in a ΔR cone of 0.4.

7.3.4 Jets

The jets used are $AK4$ PF jets. They are required to have a minimum p_T of 30 (20) and a maximum $|\eta|$ of 2.5 (2.4) for 2018/2017 (2016), and to pass the Tight identification working point [277]. They are cleaned by the presence of leptons by requesting a minimum ΔR of 0.4 with muons, electrons and τ_h candidates.

7.3.5 Missing transverse momentum

The missing transverse momentum, \vec{p}_T^{miss} , is reconstructed as the negative vectorial sum of the p_T of all PF objects. The raw \vec{p}_T^{miss} is systematically different

from true \vec{p}_T^{miss} , i.e. the transverse momentum carried by invisible particles, for several reasons including the non-compensating nature of the calorimeters and detector misalignment. To make experimental \vec{p}_T^{miss} a better estimate of true \vec{p}_T^{miss} , corrections are applied as described in Sec. 7.4.8 and recommended by the JMEPOG [278]. In this analysis the PF \vec{p}_T^{miss} is used [277]. A set of filters is applied to mitigate the impact of potential misreconstruction in the calculation of the \vec{p}_T^{miss} . Beam halo interactions (i.e., particles produced by interactions of the beam with non-collision material) can mimic genuine \vec{p}_T^{miss} signatures in the detector. Additionally, instrumental noise in the calorimeters, as well as poorly reconstructed PF muons, can result in spurious contributions to the \vec{p}_T^{miss} . Events are required to pass these \vec{p}_T^{miss} filters, both in simulation and data:

- *goodVertices*
- *globalSuperTightHalo2016Filter*
- *HBHENoiseFilter*
- *HBHENoiseIsoFilter*
- *eeBadScFilter*
- *EcalDeadCellTriggerPrimitiveFilter*
- *BadPFMuonFilter*
- *BadPFMuonDzFilter*
- *ecalBadCalibFilter* (only 2017 and 2018)

7.4 Corrections

A set of corrections has been applied in the analysis to improve the data-to-simulation agreement. All corrections are explained in detail in the following and the majority of them have been taken from Ref. [279] in the *correctionlib JSON* format [280].

7.4.1 τ_h energy scale

The energy scale of genuine τ_h candidates can be different between data and simulation. To correct for this, measurements are made in $Z \rightarrow \tau\tau$ events,

specifically in the $\mu\tau_h$ channel, using the visible mass of the $\mu\tau_h$ system as observable. The best τ_h energy scale correction is extracted by measuring the negative log-likelihood of the fit of the simulation to data for different values of the τ_h energy scale in simulation. The minimum of the negative log-likelihood gives the correction to be applied to all simulated genuine τ_h . The measured corrections are then applied as a direct scaling of the τ_h four-momentum. The τ_h energy scale corrections are propagated to all variables that are based on the τ_h four-momentum. The corrections as measured by the TauPOG for all years and are applied following the recommendations [276], selecting the ones suitable for the chosen tagger working points.

7.4.2 τ_h ID efficiency

Genuine τ_h identification efficiency can be different in data and simulation. To correct for this, measurements are made always in $Z \rightarrow \tau\tau$ events, specifically in the $\mu\tau_h$ channel, using the visible mass as observable, similarly to what described in Sec. 6.3.1 for DEEPTAU v2.5. The scale factors are provided by the TauPOG in bins of the tau decay mode and p_T . The p_T range is [20-140] GeV. For larger p_T values, as the analysis is sensitive to high- p_T τ_h , the scale factors measured with off-shell $W^* \rightarrow \tau\nu$ events are applied. The scale factors have been applied following the recommendations [276], selecting the ones suitable for the chosen tagger working points.

7.4.3 $e \rightarrow \tau_h$ energy scale

Much like the τ_h energy scale can be mismodeled in simulation, the energy scale of electrons faking τ_h candidates can be mismodeled as well. To correct for this, direct scalings of the four-momentum are applied to electrons faking τ_h candidates, i.e. reconstructed τ_h matched to an electron at generator level.

The corrections are based on the decay mode and η of the τ_h candidate and are working point dependent. They are measured by the TauPOG [276] in $Z \rightarrow \tau\tau$ events, specifically in the $e\tau_h$ channel, similarly to what described in Sec. 6.3.2 for DEEPTAU v2.5.

7.4.4 $e \rightarrow \tau_h$ misidentification rate

Scale factors are measured to adjust the electron misidentification rate in simulation to that of data. The corrections are binned in η and decay mode of the

τ_h matching with the electron at generator level, and are working point dependent. They are measured in the $e\tau_h$ channel by the TauPOG [276], similarly to what described in Sec. 6.3.2 for DEEPTAU v2.5.

7.4.5 $\mu \rightarrow \tau_h$ misidentification rate

Similarly to electrons, scale factors are measured to adjust the muon misidentification rate in simulation to that of data. The corrections are binned in η and decay mode of the τ_h matching with the muon at generator level, and are working point dependent. The measurement is performed centrally by the TauPOG in the $\mu\tau_h$ channel [276].

7.4.6 Electron corrections

The corrections applied for electrons are the following:

- Reconstruction scale factors (for p_T above and below 20 GeV)
- Identification scale factors for the chosen working point of the algorithm
- Energy scale and resolution based smearing (already applied at nanoAOD level)
- Trigger scale factors

These corrections are dependent on the p_T and η of the super-cluster and are provided directly by the EGAMMAPOG [281]. They are all available in the central repository, except for the trigger one taken from Ref. [282] searching for the condition most similar to the analysis (`singleElTrigEff*`).

7.4.7 Muon corrections

The corrections applied for muons are the following:

- Rochester correction (momentum scale correction)
- Identification scale factors for the chosen working point of the algorithm; the corrections are measured with the Z peak for medium- p_T muons ($p_T > 15$ GeV) and with the J/ψ resonance for low- p_T muons ($p_T < 15$ GeV)

- Isolation scale factor for the chosen strength of the isolation cut; the corrections are available only for medium- p_T muons (an additional uncertainty will be added in the fit to cover for the missing low- p_T isolation scale factors)
- Trigger scale factor for the chosen analysis trigger

These corrections are dependent on the p_T and η of the reconstructed muon and are provided directly by the MuonPOG [283]. They are all available in the central repository.

7.4.8 Missing transverse momentum corrections

Two kinds of corrections are applied to \vec{p}_T^{miss} , the type-I correction and the xy-shift correction [278]. The Type-I correction is the most popular \vec{p}_T^{miss} correction in CMS. This correction is a propagation of the jet energy corrections (JEC) to \vec{p}_T^{miss} . The Type-I correction replaces the vector sum of transverse momenta of particles which can be clustered as jets with the vector sum of the transverse momenta of the jets to which JEC is applied. In order to implement this kind of correction the CMSJMECALCULATORS package is exploited [284]. This requires to apply firstly JEC corrections to AK4 PF jets, even though jets are not explicitly used in this analysis. The specific JEC corrections used for data and simulation are listed in Table 7.5.

Year	Data	Simulation
2016-preVFP	Summer19UL16APV_RunBCDEF_V7_DATA	Summer19UL16APV_V7_MC
2016-postVFP	Summer19UL16_RunFGH_V7_DATA	Summer19UL16_V7_MC
2017	Summer19UL17_Run{B-C-D-E-F}_V5_DATA	Summer19UL17_V5_MC
2018	Summer19UL18_Run{A-B-C-D}_V5_DATA	Summer19UL18_V5_MC

Table 7.5: JEC for Run 2 data and simulation.

The xy-shift correction reduces the \vec{p}_T^{miss} phi modulation. The distribution of true \vec{p}_T^{miss} is independent of phi because of the rotational symmetry of the collisions around the beam axis. However, it is observed that the reconstructed \vec{p}_T^{miss} does depend on phi. The \vec{p}_T^{miss} phi distribution has roughly a sinusoidal curve with the period of 2π . The possible causes of the modulation include anisotropic detector responses, inactive calorimeter cells or tracking regions, the detector misalignment, the displacement of the beam spot. The amplitude of the modulation increases roughly linearly with the number of the pileup

interactions. The amplitude of the phi modulation is reduced by shifting the origin of the coordinate in the transverse momentum plane as a function of different particle species and in bins of eta. This correction is centrally provided by the JMEPOG.

7.4.9 b-tagging efficiency

The corrections related to b-tagging efficiency are introduced in the analysis following the BTV recommendations [285] for fixed working point scale factors. The b-tagging efficiency maps are computed in simulation using the main irreducible background ($ZZ \rightarrow 4L$) with a selection correspondent to the baseline selection of this analysis without the b-jet veto. The efficiency is computed as a function of jet p_T and truth-level flavor, with a unique bin in jet η because of lack of statistics. The efficiency maps are reported in Fig. 7.6.

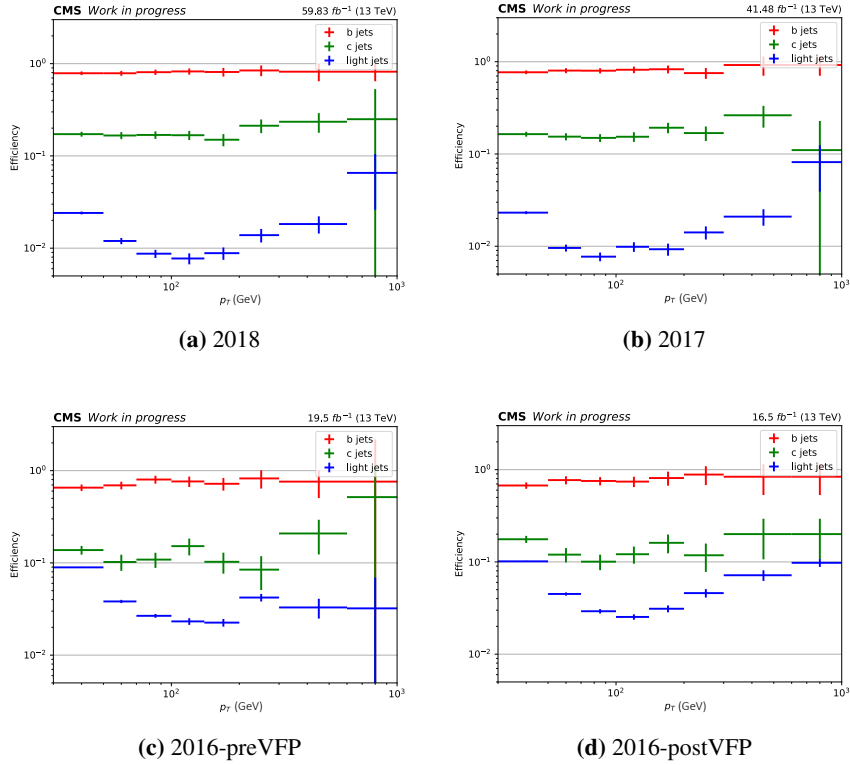


Figure 7.6: b-tagging efficiency in simulation as a function of jet p_T and flavor.

7.4.10 Pileup reweighting

In order to match the pileup conditions found in data, simulated samples are reweighted. The pileup weights are centrally computed by the LUMIPOG [256].

7.4.11 $Z p_T$ reweighting

A reweighting is applied to the $Z/\gamma^* + \text{jets}$ process to correct the generator-level $Z p_T$ distribution in LO MADGRAPH samples. A correction is produced in the $Z \rightarrow \mu\mu$ control region, as a function of the reconstructed $Z p_T$ and $m_{\mu\mu}$, to reduce the shape discrepancy between data and simulation. In this approach perfect muon resolution is assumed. Events in the di-muon region are selected by requiring two OS muons passing the medium identification working point and with a relative isolation smaller than 0.15. The leading muon is required to pass the lowest p_T cut corresponding to the fired trigger, while the sub-leading muon is required to have $p_T > 10$ GeV. The weights are computed as in the following:

$$weight = \frac{\text{observed } Z/\gamma^* + \text{jets}}{\text{simulated } Z/\gamma^* + \text{jets}} = \frac{\text{data} - (\text{non-}Z/\gamma^* + \text{jets bkg from sim.})}{\text{simulated } Z/\gamma^* + \text{jets}}$$

The weights are then applied to the $Z/\gamma^* + \text{jets}$ process, both to $Z \rightarrow \mu\mu$ and $Z \rightarrow ee$, as a function of the generator-level $Z p_T$ and $m_{\ell\ell}$. The generator level Z is found summing up the generator particles that are from the hard process final state and are either electrons or muons with PYTHIA status 1, or τ leptons with status 2. The $Z p_T$ and $m_{\ell\ell}$ distributions before and after the $Z p_T$ reweighting are shown in Fig. 7.7 for $Z \rightarrow \mu\mu$, for era 2018 as example. All weights applied are reported in Appendix C for the different eras.

7.4.12 Pre-firing weight

In 2016 and 2017, the data was affected by a problem related to the L1 ECAL and Muon pre-firing. This effect is not described by simulations, hence an event-dependent weight is applied to emulate it [286].

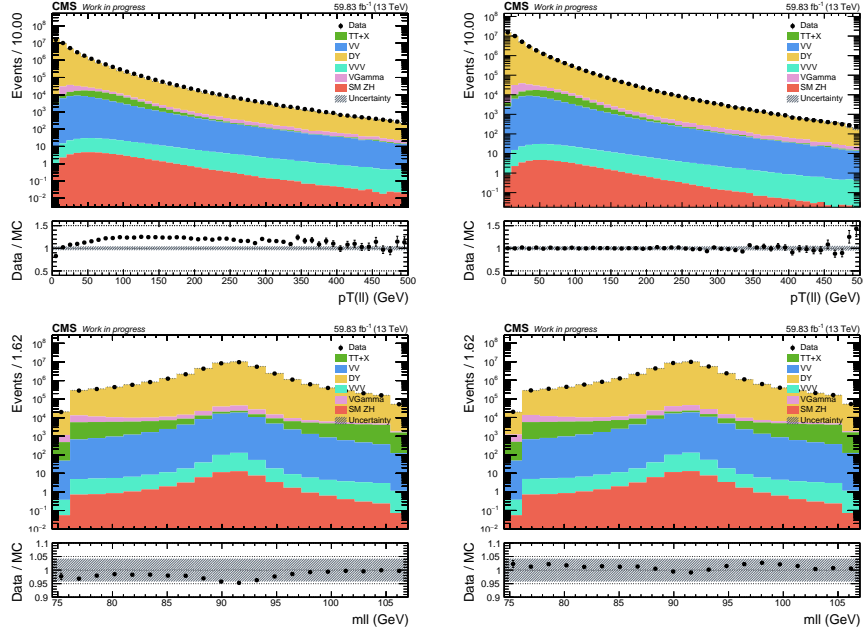


Figure 7.7: $Z p_T$ (Top Row) and $m_{\ell\ell}$ (Bottom Row) distributions before (left) and after (right) $Z p_T$ reweighting, in the $Z \rightarrow \mu\mu$ control region.

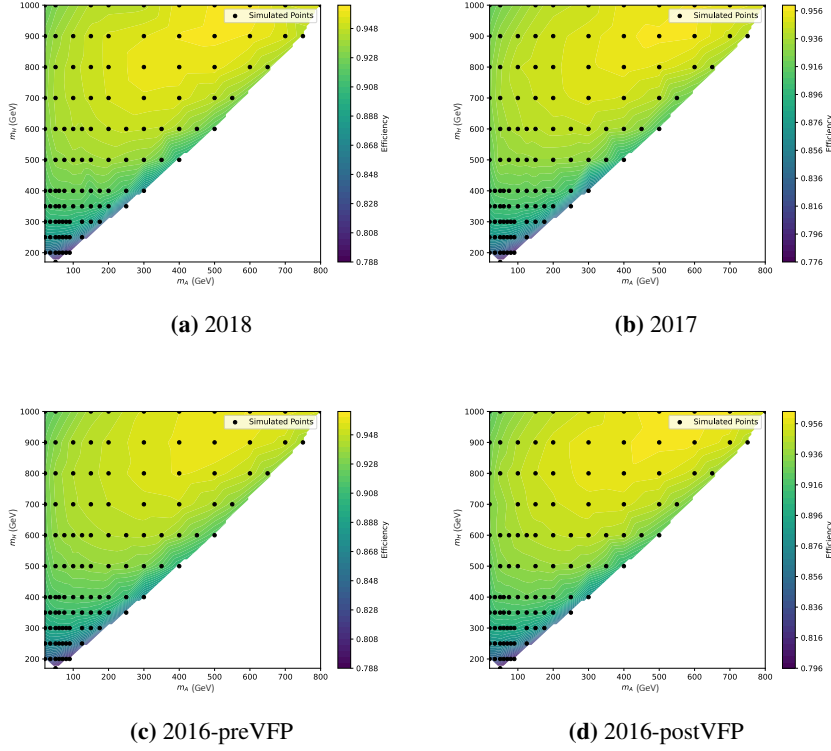
7.5 Triggers

The trigger paths used to select the events during the three data taking periods are listed in Table 7.6. Single muon triggers are used for the channels with $Z \rightarrow \mu\mu$ decays, and single electron triggers for the channels with $Z \rightarrow ee$ decays. For the scale factors refer to Sec. 7.4.7 and Sec. 7.4.6. In past similar searches [287], the addition of the double lepton triggers was proved to not increase significantly the analysis sensitivity, hence was not included in this analysis. The trigger efficiency for the signal events is reported in Fig. 7.8, divided by eras.

7.6 Analysis Strategy

The analysis strategy is sketched in Fig. 7.9. The first step is the selection of the Z and A legs that is described in Sec. 7.7. The baseline selection also includes lepton vetoes, to ensure orthogonality between the channels, and a

Year	Path
2016	HLT_IsoMu24
	HLT_IsoTkMu24
	HLT_Ele27_WPTight_Gsf
2017	HLT_IsoMu27
	HLT_Ele32_WPTight_Gsf_L1DoubleEG
2018	HLT_IsoMu24
	HLT_Ele32_WPTight_Gsf

Table 7.6: HLT trigger paths used in the analysis.**Figure 7.8:** Trigger efficiency (single muon + single electron triggers) for signal events.

b-jet veto, to remove the residual event overlap with similar analyses with jets in their final state (in preparation for an eventual combination).

The selection of a single Z boson plus one or two additional lepton(s) is used to define several control regions for the data driven background estimation, as explained in Sec. 7.8. The training of the Neural Network to increase purity is outlined in Sec. 7.9. Finally, the reconstructed invariant masses of the new scalars A and H are fitted, defining elliptical bins, to extract the final results (Sec. 7.10).

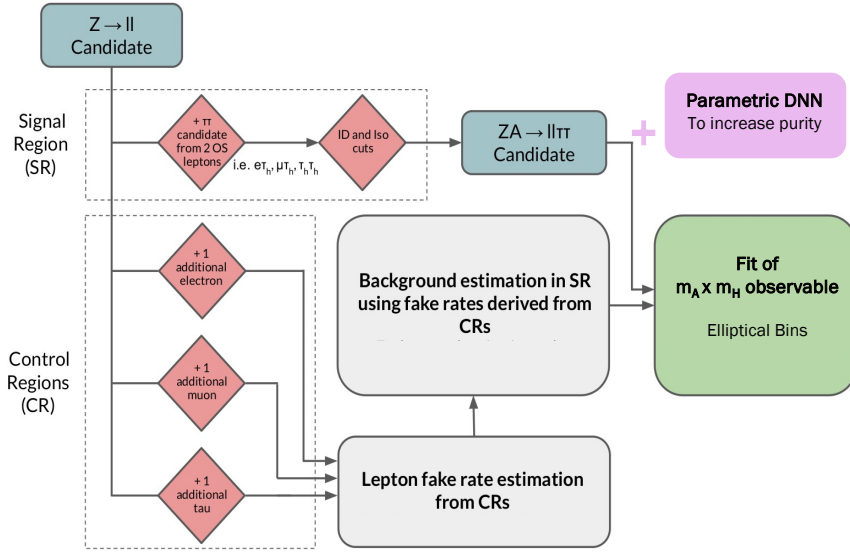


Figure 7.9: Sketch of the chosen analysis strategy.

7.7 Selection

The analysis is performed in 6 different final states corresponding to $Z \rightarrow ee$ or $Z \rightarrow \mu\mu$ with $A \rightarrow \tau_e\tau_h$, $A \rightarrow \tau_\mu\tau_h$, or $A \rightarrow \tau_h\tau_h$. The $Z \rightarrow \tau\tau$ are not studied, though the $Z \rightarrow ee$ and $Z \rightarrow \mu\mu$ channels catch a few $Z \rightarrow \tau\tau$ events because $\tau\tau \rightarrow ee/\mu\mu$ in 6% of the times. Given that the branching ratio of $Z \rightarrow \tau\tau$ is the same as $Z \rightarrow ee$ and $Z \rightarrow \mu\mu$, its addition can be considered in next iterations of this analysis to increase the event yields. $A \rightarrow \tau_e\tau_e$, $A \rightarrow \tau_\mu\tau_\mu$ and $A \rightarrow \tau_e\tau_\mu$ are not considered because they are characterized by a low branching ratio (12% in total, compared to 88% of decays with at least one τ_h) and are dominated by the large ZZ background, hence they would not add much more sensitivity to the analysis.

In the next sections, the selections for the Z and A legs are described separately. If there are more than two electrons or two muons in the event, the two OS leptons with invariant mass closest to the Z boson mass are paired together and treated as the Z boson decay products. The leptons not used to build the Z candidate are then paired to reconstruct the A boson. If more than a pair candidate is available, the one with the highest p_T is chosen.

The six different channels are designed to be mutually exclusive by vetoing additional leptons in the final state. The veto leptons are selected as the nominal leptons but loosening the identification requirements: loose identification + relative isolation < 0.5 for muons, loose working point of the MVA ID for electrons and VVVLoose working point for D_{jet} of DEEPTAU for τ_h . The selections applied on muons, electrons and τ_h candidates are summarized in Tables 7.7, 7.8 and 7.9, respectively.

Muons	
Nominal	Loose
$p_T > p_T^{\text{trig}} + 1 \text{ GeV (lead.)}$	-
$p_T > 10 \text{ GeV (sublead.)}$	same
$ \eta < 2.4$	same
$ d_{xy} < 0.5 \text{ cm}, d_z < 1 \text{ cm}$	same
medium ID	loose ID
iso < 0.15	iso < 0.5

Table 7.7: Summary of nominal and loose selection criteria for muons.

Electrons	
Nominal	Loose
$p_T > p_T^{\text{trig}} + 1 \text{ GeV (lead.)}$	-
$p_T > 10 \text{ GeV (sublead.)}$	same
$ \eta < 2.5$, no trans. reg.	same
$ d_{xy} < 0.5 \text{ cm}, d_z < 1 \text{ cm}$	same
WP90 (with iso) ID	WPL (with iso) ID

Table 7.8: Summary of nominal and loose selection criteria for electrons.

τ_h	
Nominal	Loose
$p_T > 20$ GeV	same
DM in [0,1,10,11]	same
$ \eta < 2.3$	same
$ d_z < 0.2$ cm	same
D_{jet} M	D_{jet} VVVL
D_e VVL, D_μ T	same

Table 7.9: Summary of nominal and loose selection criteria for τ_h .

7.7.1 $Z \rightarrow ee$ leg

These events are triggered with the single electron trigger, and are selected by requiring the presence of two nominal OS electrons. The leading electron has to be matched to the trigger object (with $\Delta R < 0.2$), and have p_T greater than 28 GeV in 2016 (33 GeV in 2017 and 2018), while the subleading must have p_T greater than 10 GeV. The electrons have to be separated from each other by $\Delta R > 0.3$ and have an invariant mass within 15 GeV of the Z boson mass.

7.7.2 $Z \rightarrow \mu\mu$ leg

These events are triggered with the muon trigger, and are selected by requiring the presence of two nominal OS muons. The leading muon has to be matched to the trigger object (with $\Delta R < 0.2$), and have p_T greater than 25 GeV in 2016 (28 GeV in 2017 and 25 GeV in 2018), while the subleading must have p_T greater than 10 GeV. The muons have to be separated from each other by $\Delta R > 0.3$, and have an invariant mass within 15 GeV of the Z boson mass.

7.7.3 $A \rightarrow \tau_e \tau_h$ leg

The $A \rightarrow \tau_e \tau_h$ leg is selected requiring one nominal electron and one nominal τ_h cleaned from the presence of muons and electrons in a ΔR cone of 0.4. The τ_h and the electron are separated from each other by $\Delta R > 0.3$ and must be OS.

7.7.4 $A \rightarrow \tau_\mu \tau_h$ leg

The $A \rightarrow \tau_\mu \tau_h$ leg is selected requiring one nominal muon and one nominal τ_h cleaned from the presence of muons and electrons in a ΔR cone of 0.4. The τ_h and the muon are separated from each other by $\Delta R > 0.3$ and must be OS.

7.7.5 $A \rightarrow \tau_h \tau_h$ leg

The $A \rightarrow \tau_h \tau_h$ leg is selected requiring two OS τ_h candidates cleaned from the presence of muons and electrons in a ΔR cone of 0.4. The two τ_h are separated from each other by $\Delta R > 0.3$.

7.7.6 b-jet veto

A b-jet veto is imposed to ensure orthogonality with other $H \rightarrow ZA$ analysis with jets in their final states. The jets are $AK4$ PF jets, selected to have minimum p_T of 30 (20) GeV and maximum η of 2.5 (2.4) for 2018/2017 (2016). They are required to pass the Tight JetID and the Medium b-tagging working point of the DeepJet tagger. The jets are cleaned by the presence of muons, electrons and τ_h by imposing a minimum ΔR separation of 0.4

Overall the veto does not affect significantly the yields of signal and main backgrounds (less than 5% decrease). The main effect of the veto is to reduce $t\bar{t}Z$ background, which was already a minor contributor to the final yields.

7.7.7 Signal selection efficiency

The baseline selection efficiency is evaluated for the different signal hypotheses under study. Figure 7.10 shows that the efficiency lies between 10% and 20% for most of the $m_H - m_A$ plane, while falls under 5% for the low mass values of m_A because of the p_T requirements.

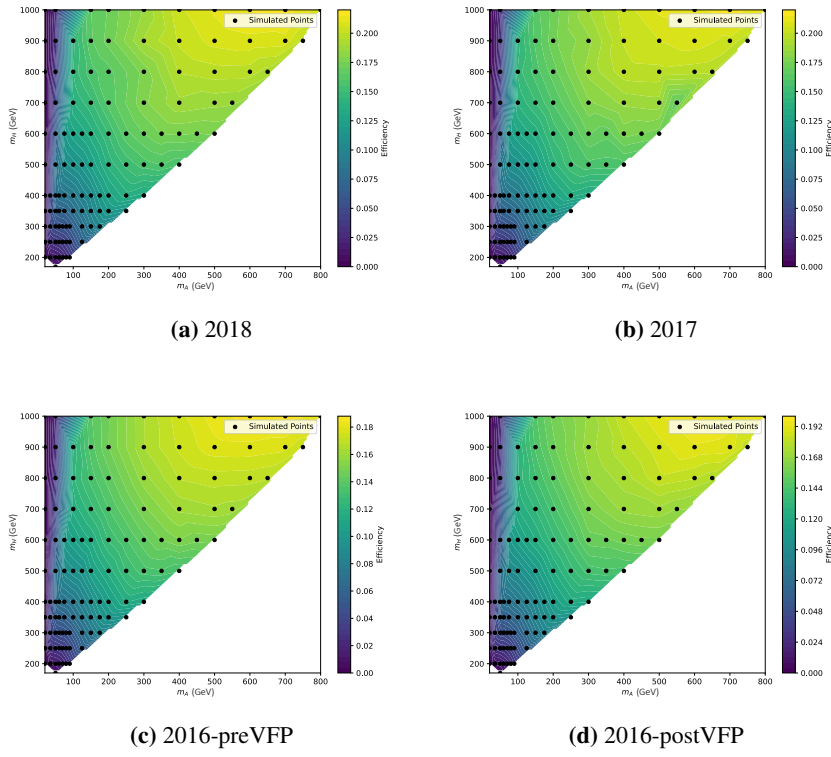


Figure 7.10: Signal selection efficiency as a function of m_H and m_A .

7.8 Background estimation

Methods based on data control samples and comparison with simulated events are used to estimate residual backgrounds after the selection described in Sec. 7.7.

7.8.1 Irreducible background estimation

In this analysis, the dominant irreducible background is $ZZ \rightarrow 4L$ (with L being either a light lepton or a tau lepton), with small irreducible contributions from WWZ , WZZ , ZZZ , and $t\bar{t}Z$. The SM $Zh \rightarrow \ell\ell\tau\tau$ is also considered an irreducible background. All these processes are estimated from simulation and scaled to their predicted cross section.

7.8.2 Reducible background estimation

$Z/\gamma^* + \text{jets}$ events (including both heavy- and light-flavor jets) and $WZ + \text{jets}$ processes constitute the main sources of background containing at least one misidentified lepton. In these cases, a genuine Z boson decaying into a pair of electrons or muons is reconstructed, while at least one jet or its constituents is misidentified as an isolated lepton.

Fake light leptons can originate from the semileptonic decays of heavy-flavor quarks, from misidentified hadrons, or, in the case of electrons, from photon conversions. Hadronic τ candidates can be mimicked by quark- or gluon-initiated jets.

Relying solely on simulation to estimate lepton misidentification rates is not advisable, as it often fails to fully model the complex instrumental effects responsible for such fakes and typically underestimates the associated uncertainties. Therefore, a data-driven method is employed to measure lepton misidentification probabilities directly in control regions enriched with fake leptons.

Given the final states considered in this analysis, where jets can be misreconstructed as electrons, muons, or τ_h candidates, the misidentification rates are evaluated separately but using a consistent methodology across all lepton flavors.

Misidentification probability measurements

The data-driven method used to estimate the reducible background relies on the *loose* and *nominal* selections applied to one and only one lepton candidate

(e , μ , or τ_h) found in addition to the Z candidate, which is selected as described in Sec. 7.7. This configuration defines the $Z + 1L$ control region (CR). The misidentification probability, $f(p_T)$, is derived by measuring the fraction of loosely selected leptons that also pass the nominal identification criteria, in bins of the lepton p_T . Statistical uncertainties on $f(p_T)$ are obtained by propagating the errors on the numerator and denominator of the ratio, using Poisson statistics (\sqrt{N}). The measurement is further separated into two pseudorapidity regions: the barrel region, defined by $|\eta| < 1.45$, and the endcap region, defined by $|\eta| > 1.45$.

The $\text{jet} \rightarrow \tau_h$ misidentification rate is then defined as follows:

$$f_r(p_T) = \frac{\text{Medium } D_{jet} \ \& \ \text{VVLoose } D_e \ \& \ \text{Tight } D_\mu}{\text{VVVLoose } D_{jet} \ \& \ \text{VVLoose } D_e \ \& \ \text{Tight } D_\mu} \quad (7.1)$$

where it is implicit that all other selections (p_T , η , etc...) follow the recipe described in Sec. 7.7. The looser selection for D_{jet} is chosen in order to have enough data in the $Z + 1L$ CR, but especially in the CRs that will be defined later.

The p_T distributions corresponding to the denominator and the numerator of the Eq. 7.1, are reported for 2018 as example in Fig. 7.11 (other years in Appendix D). All the recommended scale factors are applied here and, as they depend on the chosen tagger working point, they are different for the numerator and the denominator. Given that the contributions from genuine taus are not negligible, they have been subtracted both from the numerator and the denominator in the formula 7.1 (checking the generator truth). Figure 7.12 shows the tau misidentification probability in blue, separately for the barrel and endcap regions. The measurement is performed using data combined across all years (2016, 2017, and 2018), as consistent trends were observed across the datasets. The misidentification probability is found to be approximately flat as a function of p_T , with a slight increase observed above 100 GeV. For comparison and validation purposes, the red curve shows the same probability estimated using a mixture of $Z/\gamma^* + \text{jets}$ and $t\bar{t} + \text{jets}$ simulated samples, which reproduces the overall trend seen in data.

Recalling the definition of nominal and loose electron, the $\text{jet} \rightarrow e$ misidentification probability can be defined as follows:

$$f_r(p_T) = \frac{\text{mvaFall17V2Iso_WP90}}{\text{mvaFall17V2Iso_WPL}} \quad (7.2)$$

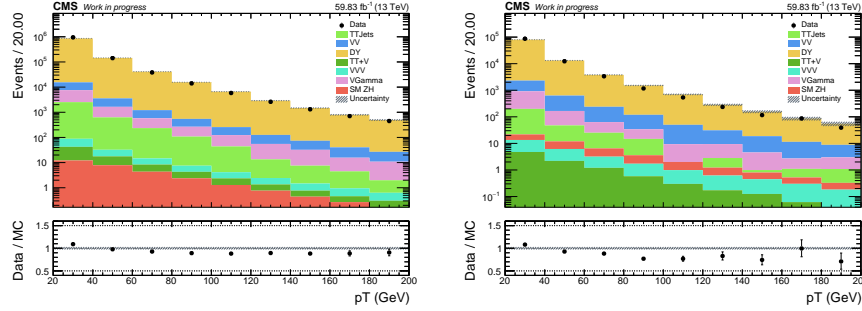


Figure 7.11: p_T distributions in the $Z + \tau_h$ CR for the τ_h candidate passing the loose (left) and nominal (right) identification criteria. Plots refer to 2018 data taking year.

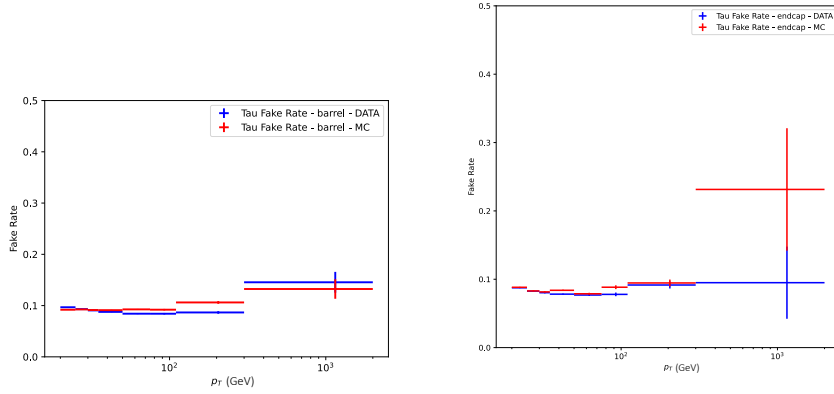


Figure 7.12: The jet $\rightarrow \tau_h$ misidentification probability computed with respect to the τ_h p_T is shown in the barrel (left) and endcap (right) region. The curves have been evaluated combining the Run 2 eras to reduce statistical fluctuations.

where it is implicit that all other selections (p_T , η , etc...) follow the recipe described in Sec. 7.7.

The p_T distributions in the $Z + 1L$ CR for the electron passing loose selection criteria and the nominal ones are reported in Fig. 7.13 for 2018 as example, the other years can be found in Appendix D. The same considerations on scale factors and real-third-lepton contribution subtraction as the τ_h case holds. The evaluated curves are reported in Fig. 7.14. The misidentification rate mainly decreases with p_T .

Recalling the definition of nominal and loose muon, the jet $\rightarrow \mu$ misidentification probability is defined as follows:

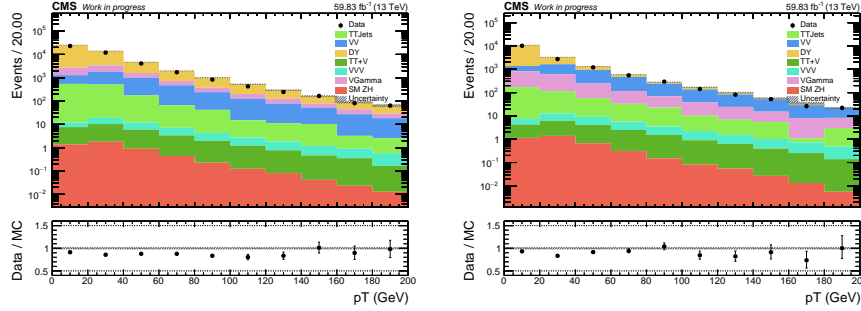


Figure 7.13: p_T distributions in the $Z + e$ CR for the electron candidate passing the loose (left) and nominal (right) identification criteria. Plots refer to 2018 data taking year.

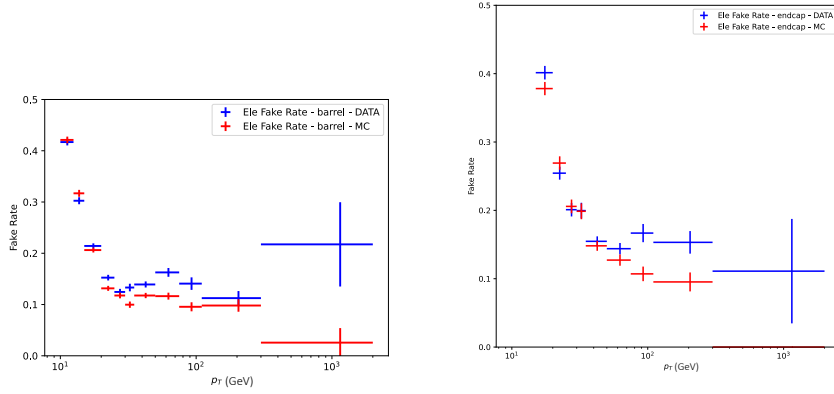


Figure 7.14: The $\text{jet} \rightarrow e$ misidentification probability computed with respect to the the electron p_T is shown in the barrel (left) and endcap (right) region. The curves have been evaluated combining the Run 2 eras to reduce statistical fluctuations.

$$f_r(p_T) = \frac{\text{mediumId} \& \text{pfRelIso04_all} < 0.15}{\text{looseId} \& \text{pfRelIso04_all} < 0.5} \quad (7.3)$$

where it is implicit that all other selections (p_T , η , etc...) follow the recipe described in Sec. 7.7. The p_T distributions for muon passing loose selection criteria and nominal ones are reported in Fig. 7.15 for 2018 as example, the other years can be found in Appendix D. The same considerations on scale factors and real-third-lepton contribution subtraction as the τ_h case holds. The evaluated curves are reported in Fig. 7.16. The misidentification rate decreases

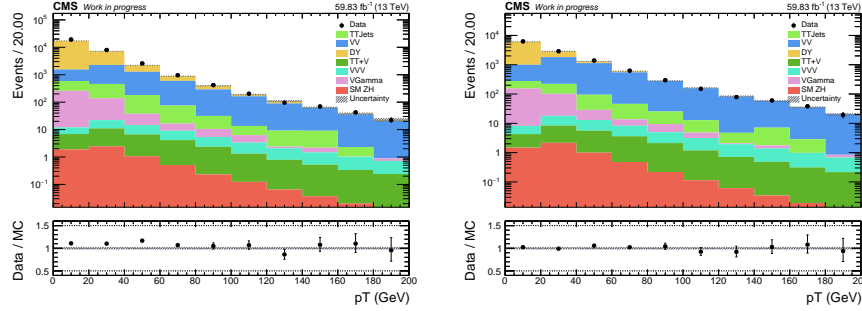


Figure 7.15: p_T distributions in the $Z + \mu$ CR for the muon candidate passing the loose (left) and nominal (right) identification criteria. Plots refer to 2018 data taking year.

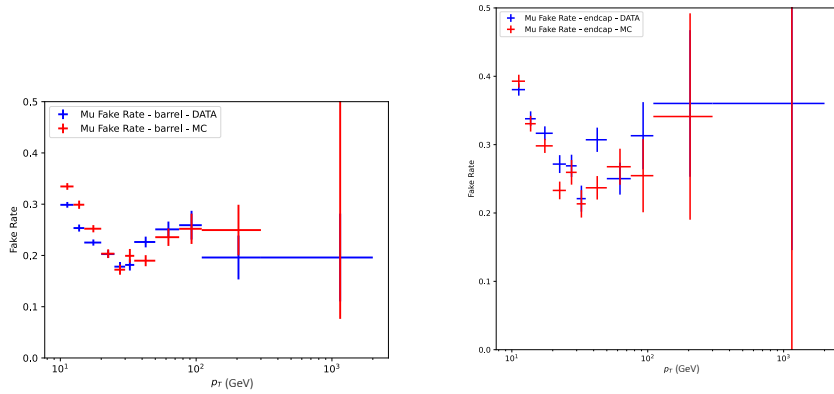


Figure 7.16: The $\text{jet} \rightarrow \mu$ misidentification probability computed with respect to the muon p_T is shown in the barrel (left) and endcap (right) region. The curves have been evaluated combining the Run 2 eras to reduce statistical fluctuations.

with p_T until ~ 30 GeV and then increases again reaching a plateau at higher momentum.

Background estimation using misidentification rates

Once the misidentification probabilities have been computed for each lepton flavor, three different control regions are defined where a Z candidate and two OS leptons are required. These control regions are defined as follows:

- **Control Region 00 (CR_{00}):** both leptons pass the loose identification criteria but not the nominal ones;

- **Control Region 10 (CR_{10}):** one lepton passes the nominal identification requirements, the other passes only the loose ones. In this control region the loose lepton is the sub-leading τ_h in the $\tau_h \tau_h$ and the light lepton in the $\ell \tau_h$;
- **Control Region 01 (CR_{01}):** as in the control region CR_{10} , but in this case the loose lepton is the leading τ_h in the $\tau_h \tau_h$, the tau in the $\ell \tau_h$ and the muon in the $e\mu$ final state.

Suppose that we have $N^{Z/\gamma^*+\text{jets}}$ of $Z/\gamma^* + \text{jets}$ events when selecting a Z candidate and two OS leptons. One can define four subsets of events in this sample:

$$\begin{aligned}
 N_{11}^{Z/\gamma^*+\text{jets}} &= N^{Z/\gamma^*+\text{jets}} f_1 f_2 \\
 N_{01}^{Z/\gamma^*+\text{jets}} &= N^{Z/\gamma^*+\text{jets}} (1 - f_1) f_2 \\
 N_{10}^{Z/\gamma^*+\text{jets}} &= N^{Z/\gamma^*+\text{jets}} f_1 (1 - f_2) \\
 N_{00}^{Z/\gamma^*+\text{jets}} &= N^{Z/\gamma^*+\text{jets}} (1 - f_1)(1 - f_2)
 \end{aligned} \tag{7.4}$$

where f_1 and f_2 represent the misidentification probabilities of the leading and the sub-leading lepton, respectively, depending on its transverse momentum. $N_{11}^{Z/\gamma^*+\text{jets}}$ is the yield of $Z/\gamma^* + \text{jets}$ in signal region. Given that we can safely assume that the CR_{00} is fully dominated by $Z/\gamma^* + \text{jets}$ ($N_{00} = N_{00}^{Z/\gamma^*+\text{jets}}$), one can take N_{00} from data in the CR_{00} and estimate the contribution of the $Z/\gamma^* + \text{jets}$ background to the signal region as:

$$N_{11}^{Z/\gamma^*+\text{jets}} = N_{00} \frac{f_1 f_2}{(1 - f_1)(1 - f_2)}. \tag{7.5}$$

Going further, one can use N_{00} to estimate the $Z/\gamma^* + \text{jets}$ contribution to the CR_{01} and CR_{10} as well, following the Eq. 7.4:

$$\begin{aligned}
 N_{01}^{Z/\gamma^*+\text{jets}} &= N_{00}^{Z/\gamma^*+\text{jets}} \frac{f_2}{(1 - f_2)} \\
 N_{10}^{Z/\gamma^*+\text{jets}} &= N_{00}^{Z/\gamma^*+\text{jets}} \frac{f_1}{(1 - f_1)}
 \end{aligned} \tag{7.6}$$

WZ+jets, instead, contributes only to the control regions CR_{01} and CR_{10} . However, given that these two control regions are a mixture of WZ + jets and $Z/\gamma^* + \text{jets}$ events ($N_{01} = N_{01}^{\text{WZ+jets}} + N_{01}^{Z/\gamma^*+\text{jets}}$, $N_{10} = N_{10}^{\text{WZ+jets}} + N_{10}^{Z/\gamma^*+\text{jets}}$), we can use the number of events N_{01} and N_{10} , for each control regions, estimated from data, and the already estimated $Z/\gamma^* + \text{jets}$ background to extract the contribution of WZ + jets in the signal region:

$$\begin{aligned} N_{11,01}^{\text{WZ+jets}} &= \left(N_{01} - N_{01}^{Z/\gamma^*+\text{jets}} \right) \frac{f_1}{1 - f_1} \\ &= \left(N_{01} - N_{00} \frac{f_2}{1 - f_2} \right) \frac{f_1}{1 - f_1} \\ &= N_{01} \frac{f_1}{1 - f_1} - N_{00} \frac{f_1 f_2}{(1 - f_1)(1 - f_2)} \end{aligned} \quad (7.7)$$

is the contribution to the signal region, coming from the CR_{01} , while

$$\begin{aligned} N_{11,10}^{\text{WZ+jets}} &= \left(N_{10} - N_{10}^{Z/\gamma^*+\text{jets}} \right) \frac{f_2}{1 - f_2} \\ &= \left(N_{10} - N_{00} \frac{f_1}{1 - f_1} \right) \frac{f_2}{1 - f_2} \\ &= N_{10} \frac{f_2}{1 - f_2} - N_{00} \frac{f_1 f_2}{(1 - f_1)(1 - f_2)} \end{aligned} \quad (7.8)$$

the one coming from the CR_{10} .

Therefore, the final contribution in the signal region will be:

$$\begin{aligned} N_{11} &= N_{11}^{Z/\gamma^*+\text{jets}} + N_{11}^{\text{WZ+jets}} \\ &= N_{11}^{Z/\gamma^*+\text{jets}} + N_{11,01}^{\text{WZ+jets}} + N_{11,10}^{\text{WZ+jets}} \end{aligned} \quad (7.9)$$

and making use of all the equations defined above (Eqs. 7.4, 7.5, 7.6, 7.7 and 7.8), the final formula we use to estimate the reducible background contribution in the signal region is:

$$N_{11} = N_{01} \frac{f_1}{1 - f_1} + N_{10} \frac{f_2}{1 - f_2} - N_{00} \frac{f_1 f_2}{(1 - f_1)(1 - f_2)}. \quad (7.10)$$

The final formula is telling us that, practically, one needs to count the number of events in each control region (CR_{01} , CR_{10} and CR_{00}) and “correct” this number with a proper weight coming from the misidentification probabilities described before in order to estimate the reducible background contribution to the signal region. Also in this case, the contributions of the SM ZH , WWZ , WZZ , ZZZ , $t\bar{t}Z$ and ZZ backgrounds are not negligible and need to be subtracted, properly propagating the statistical error to the final estimates.

The estimated yields for the reducible background are presented in Tables 7.10, 7.11, and 7.12 in Sec. 7.8.3, alongside the yields from simulated background processes and the expected signal yields for the benchmark mass hypothesis of $(m_H, m_A) = (600, 100)$ GeV. These results indicate that the reducible background constitutes one of the dominant background contributions in the analysis, comparable in magnitude to the irreducible $ZZ \rightarrow 4L$ background.

Control plots with the fake shapes are shown in Sec. 7.8.3 in Figures 7.17, 7.18 for the channel $Z + \mu\tau_h$, in Figures 7.19, 7.20 for the channel $Z + e\tau_h$ and in Figures 7.21, 7.22 for the channel $Z + \tau_h\tau_h$. Some of these variables have been used for the training of the parametric neural network as explained in Sec. 7.9.

Additionally, in order to further evaluate the validity of the method, we have performed a closure test using the simulated reducible background samples. The results are reported in Appendix E.

7.8.3 Control plots for the baseline selection

This section reports in Tables 7.10, 7.11 and 7.12 the simulated process yields together with the data driven background estimate after the baseline selection described in Sec. 7.7. Several control plots are here displayed to show agreement after the baseline selection.

Channel	$Z+\mu\tau_h$	$Z+e\tau_h$	$Z+\tau_h\tau_h$
HZA	1.981 ± 0.025	1.817 ± 0.024	2.462 ± 0.028
VV	23.80 ± 0.09	32.60 ± 0.11	23.40 ± 0.09
VVV	0.947 ± 0.024	0.854 ± 0.022	0.258 ± 0.010
TTV	0.472 ± 0.036	0.429 ± 0.036	0.061 ± 0.014
SM ZH	1.933 ± 0.029	1.880 ± 0.028	2.239 ± 0.031
Fakes	20.07 ± 5.91	31.75 ± 9.41	37.90 ± 11.13
Tot. MC	67.50 ± 9.41	47.23 ± 5.91	63.86 ± 11.13
Data	63.0 ± 7.94	44.0 ± 6.63	71.0 ± 8.43

Table 7.10: Yields for 2016 data taking year. The signal is simulated for the $(m_H, m_A) = (600, 100)$ GeV hypothesis.

Channel	$Z+\mu\tau_h$	$Z+e\tau_h$	$Z+\tau_h\tau_h$
HZA	2.557 ± 0.030	2.433 ± 0.029	3.308 ± 0.033
VV	30.110 ± 0.11	40.01 ± 0.13	30.49 ± 0.11
VVV	1.113 ± 0.026	1.084 ± 0.025	0.333 ± 0.011
TTV	0.747 ± 0.045	0.639 ± 0.042	0.098 ± 0.015
SM ZH	2.526 ± 0.024	2.336 ± 0.022	2.885 ± 0.024
Fakes	17.75 ± 6.19	43.94 ± 10.47	49.84 ± 12.83
Tot. MC	52.25 ± 6.19	88.012 ± 10.48	83.65 ± 12.83
Data	53.0 ± 7.28	76.0 ± 8.72	87.0 ± 9.33

Table 7.11: Yields for 2017 data taking year. The signal is simulated for the $(m_H, m_A) = (600, 100)$ GeV hypothesis.

Channel	$Z+\mu\tau_h$	$Z+e\tau_h$	$Z+\tau_h\tau_h$
HZA	3.713 ± 0.088	3.515 ± 0.085	4.689 ± 0.097
VV	43.03 ± 0.16	58.50 ± 0.18	44.31 ± 0.15
VVV	1.779 ± 0.039	1.699 ± 0.037	0.488 ± 0.016
TTV	1.081 ± 0.055	1.082 ± 0.054	0.151 ± 0.020
SM ZH	3.603 ± 0.034	3.380 ± 0.032	4.179 ± 0.035
Fakes	32.68 ± 8.04	51.81 ± 14.23	44.49 ± 14.93
Tot. MC	82.18 ± 8.04	116.47 ± 14.24	93.61 ± 14.93
Data	84.0 ± 9.16	91.0 ± 9.54	113.0 ± 10.63

Table 7.12: Yields for 2018 data taking year. The signal is simulated for the $(m_H, m_A) = (600, 100)$ GeV hypothesis.

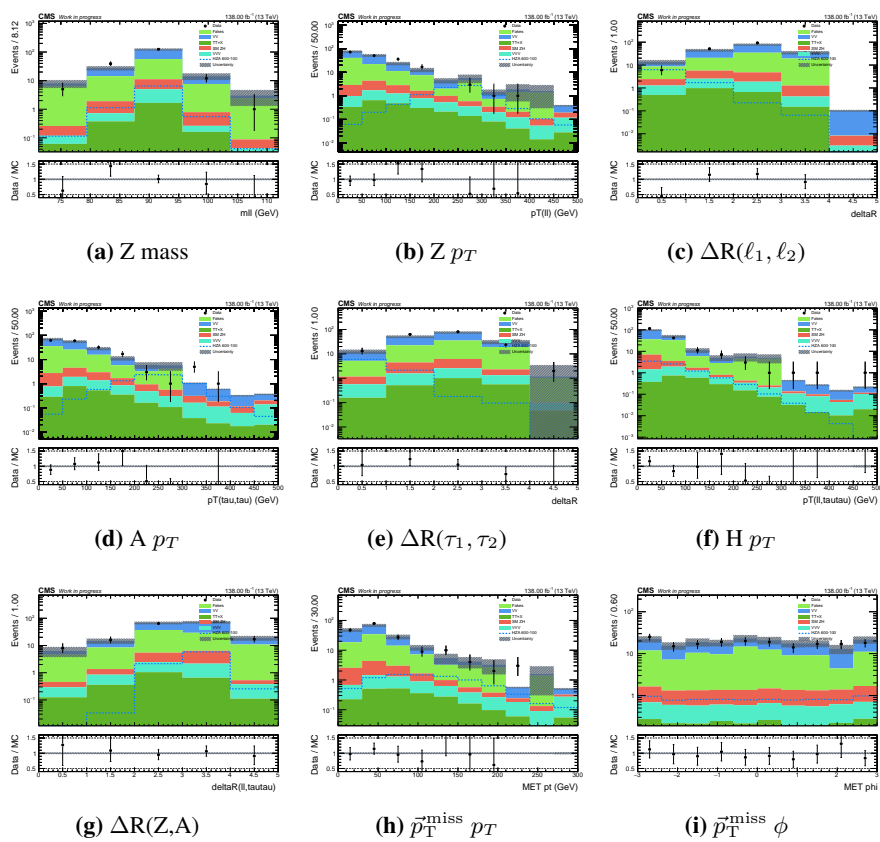
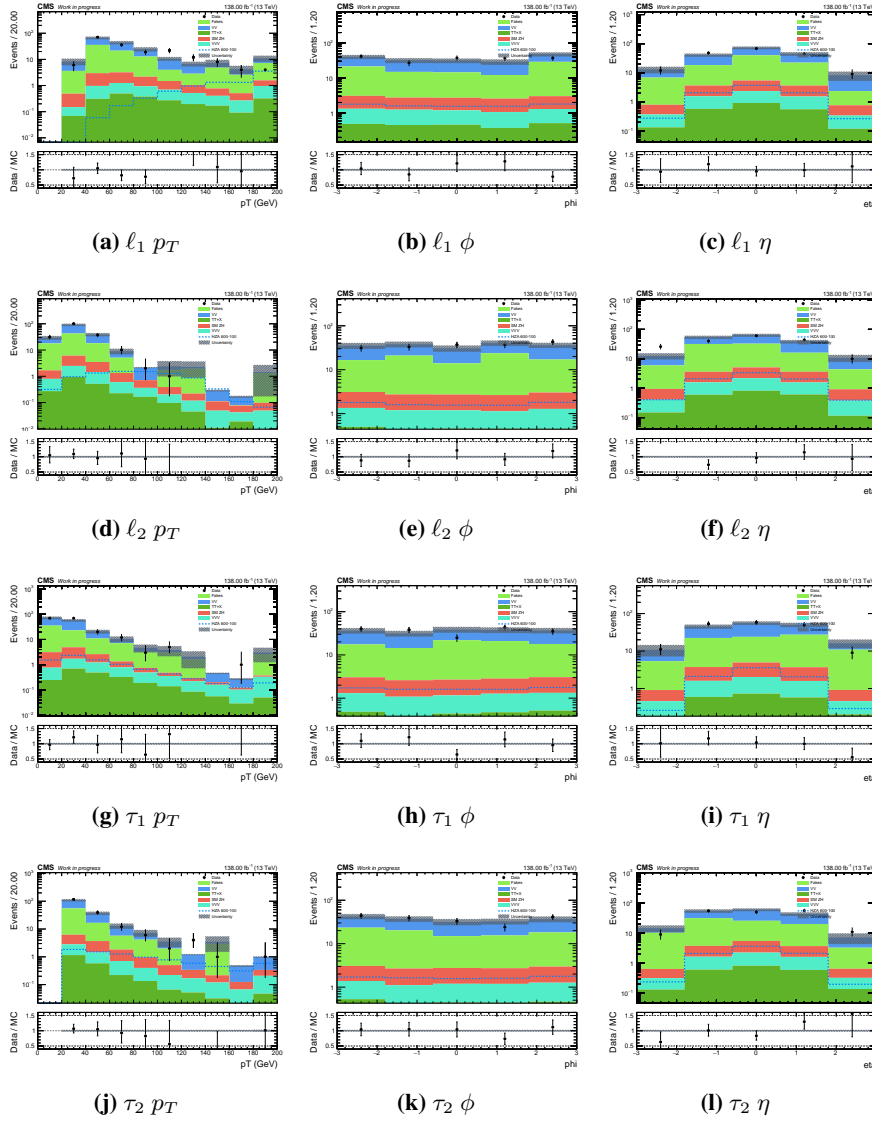
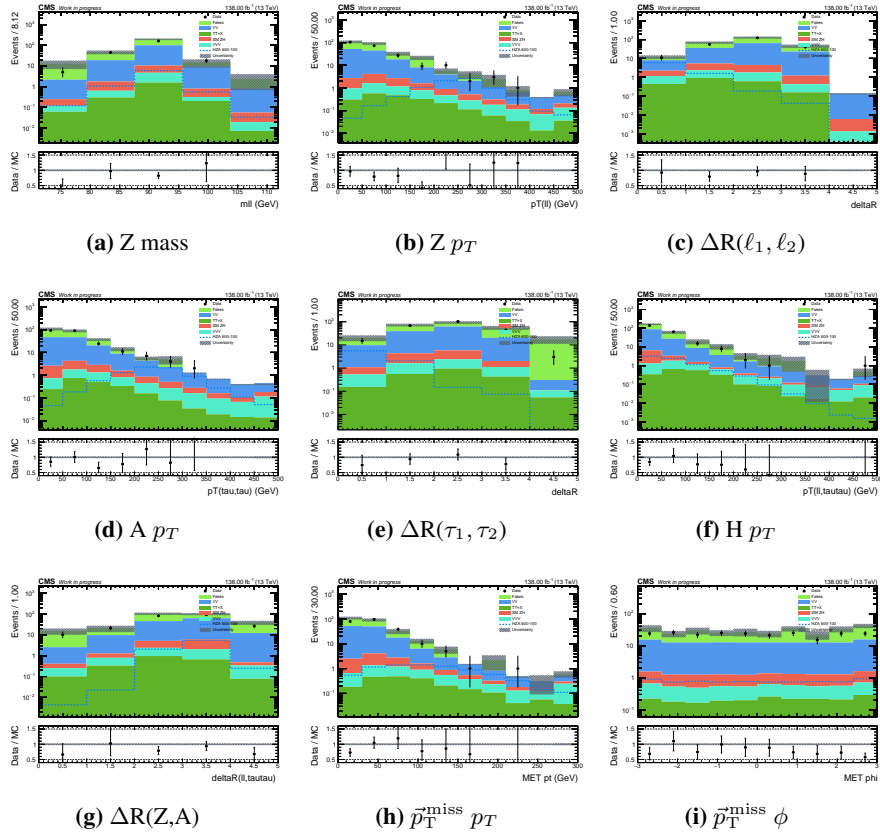
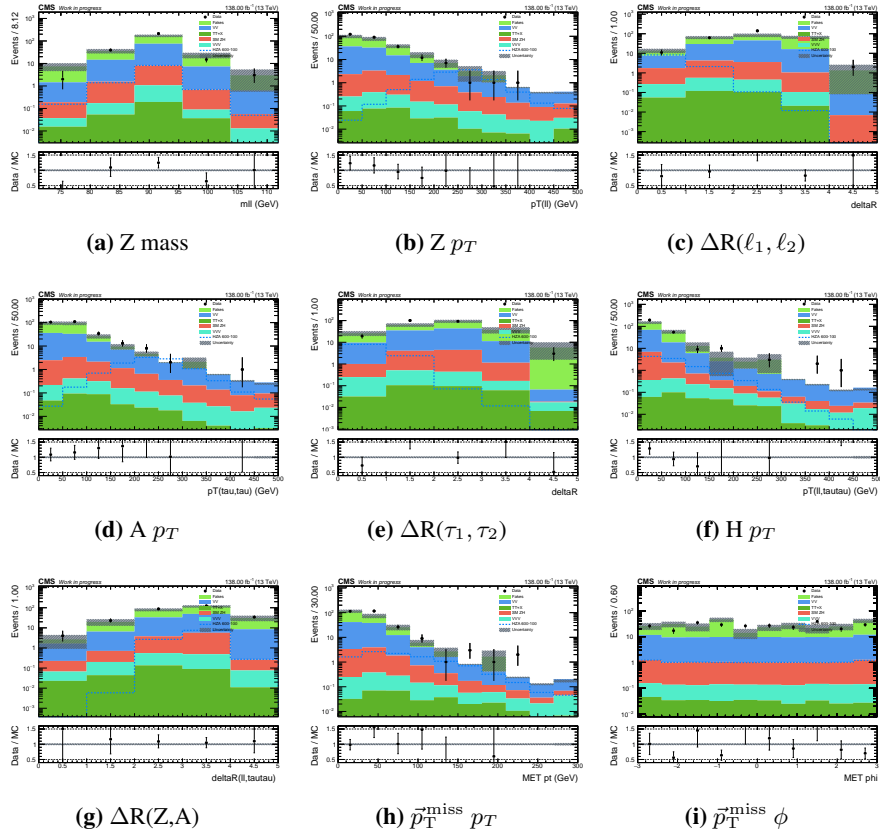


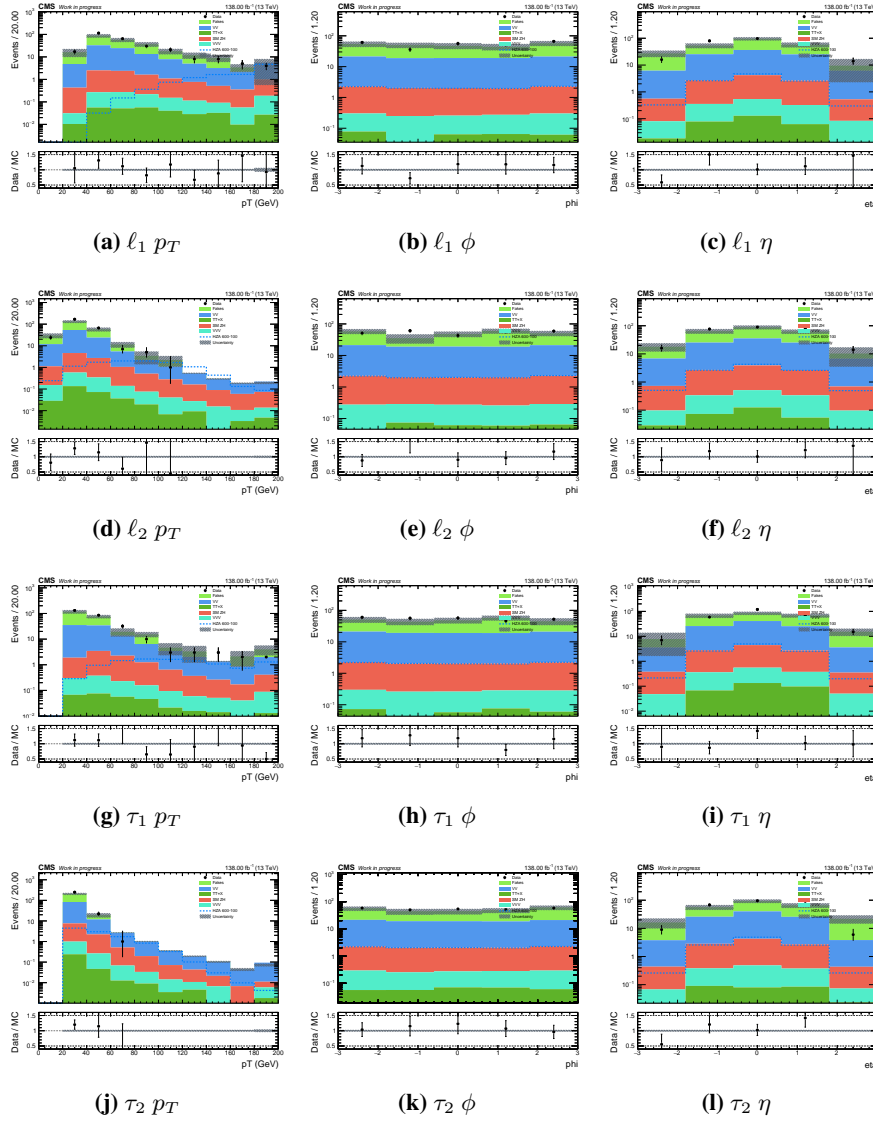
Figure 7.17: Control plots for the $Z + \mu\tau_h$ channel.

Figure 7.18: Control plots for the $Z + \mu\tau_h$ channel.


 Figure 7.19: Control plots for the $Z + e\tau_h$ channel.




 Figure 7.21: Control plots for the $Z + \tau_h \tau_h$ channel.

Figure 7.22: Control plots for the $Z + \tau_h \tau_h$ channel.

7.9 Parametric Deep Neural Network for enhanced sensitivity

In this work a parametric DNN model [288] is trained to increase the sensitivity of the search. The algorithm has been implemented using Keras [289] with TensorFlow [290] backend. One DNN is trained for each category: $Z + \mu\tau_h$, $Z + e\tau_h$ and $Z + \tau_h\tau_h$.

The variables given as input features to the network are displayed in Fig. 7.23. They are a mixture of kinematic and angular variables of the final state visible objects together with information on the \vec{p}_T^{miss} . The \vec{p}_T^{miss} variables are implicitly exploited also in the $\tau\tau$ and $\ell\ell\tau\tau$ p_T that are reconstructed using the FAST MTT algorithm [291]. This improved version of the SVFIT algorithm [292] allows for the reconstruction of not only the mass of the τ lepton pair, but of any kinematic function of the two τ leptons. More information will be given in the next section on the fitted observables (Sec. 7.10).

In order to parametrize the network in the 2D mass space, two additional input nodes are added that receive the m_A and m_H input values. In the training, m_A and m_H are fixed to the nominal values for the signals while, for the background, it is taken randomly from a uniform distribution spanning in the region of interest. All available signal samples in the form $H \rightarrow ZA$ are employed in the training. The reversed scenario with $A \rightarrow ZH$ shows the same selection efficiencies and features distributions (as visible in Figs. 7.23 and 7.24), hence it does not add more information.

The network architecture is the following:

- Input layer with 13 nodes (11 variables + 2 parametric inputs m_A and m_H)
- Three hidden layers with 132-64-64 nodes with ReLu activation function and dropout fraction of 0.2 to reduce overtraining
- Output layer with one node, with a sigmoid activation function.

During the training, the weights are optimized using the Adam algorithm to minimize the binary cross entropy loss function. The network is trained until no further improvement is observed (less than 0.1% increase in binary accuracy), for a maximum of 100 epochs. One third of the whole dataset is used for validation purpose, hence is not employed in the training step. The trends of loss and accuracy as functions of epochs are shown in Fig. 7.25 for

both the training and validation datasets, indicating no signs of overfitting in the process.

The ROC curves are shown in Fig. 7.26 and Fig. 7.27 for different mass scenarios. In these figures, the ROCs of the parametric DNN (left) are compared to the ROCs of a *naive* DNN (right) that exploits the same architecture but is trained on a mixture of all signal hypotheses together, without any parametrization on the mass. The performance of the parametric DNN are observed to be always significantly better than the *naive* DNN, proving the efficacy of the parametrization method.

In order to check the ability of the parametric DNN to interpolate in intermediate regions where it has not been trained on, we performed another check in which all the samples with $m_H=300$ GeV are removed from the training. Fig. 7.28 shows the performance of the parametric DNN trained with (left) and without (right) the 300 GeV sample: the differences in terms of area under the ROC curve (AUC) are observed to be minimal, less than 2%. Finally, for reference, some score plots are shown in Fig. 7.29 for three mass scenarios in the $H \rightarrow ZA$ and $A \rightarrow ZH$ modes, showing that the two are completely equivalent in terms of DNN response. All plots presented here refers to the $Z + \mu\tau_h$ channel, but similar conclusions hold for the other two.

7.10 Observables

In this analysis, as already mentioned in Sec. 7.9, we used the FAST MTT algorithm to reconstruct the four-momentum of the new resonance decaying to a pair of τ leptons. The algorithm is based on matrix element techniques and exploits the information on the visible products of the τ decay and the \vec{p}_T^{miss} x and y components. It typically achieves a relative resolution on the mass of 15-20% for the Higgs boson [291], while its performance worsen when the resonance mass drifts from 125 GeV. Figure 7.30 (a) shows the effect of the algorithm application on a simulated sample of $H \rightarrow ZA$ where the lighter resonance mass is 100 GeV. The algorithm shrinks and shifts the distribution towards the reference value of 100 GeV. This clearly can be translated on the

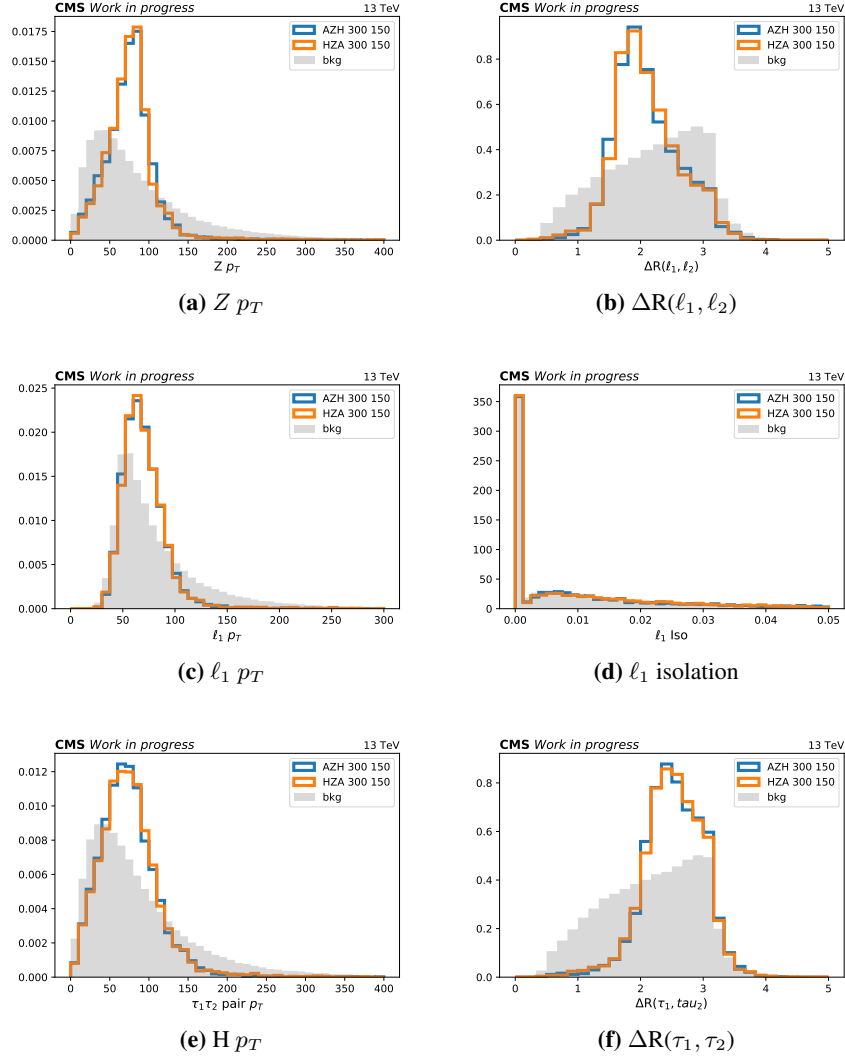


Figure 7.23: Input features for the parametric DNN training in the $Z + \mu\tau_h$ channel (1/2). All the background distributions are normalized to unit area.

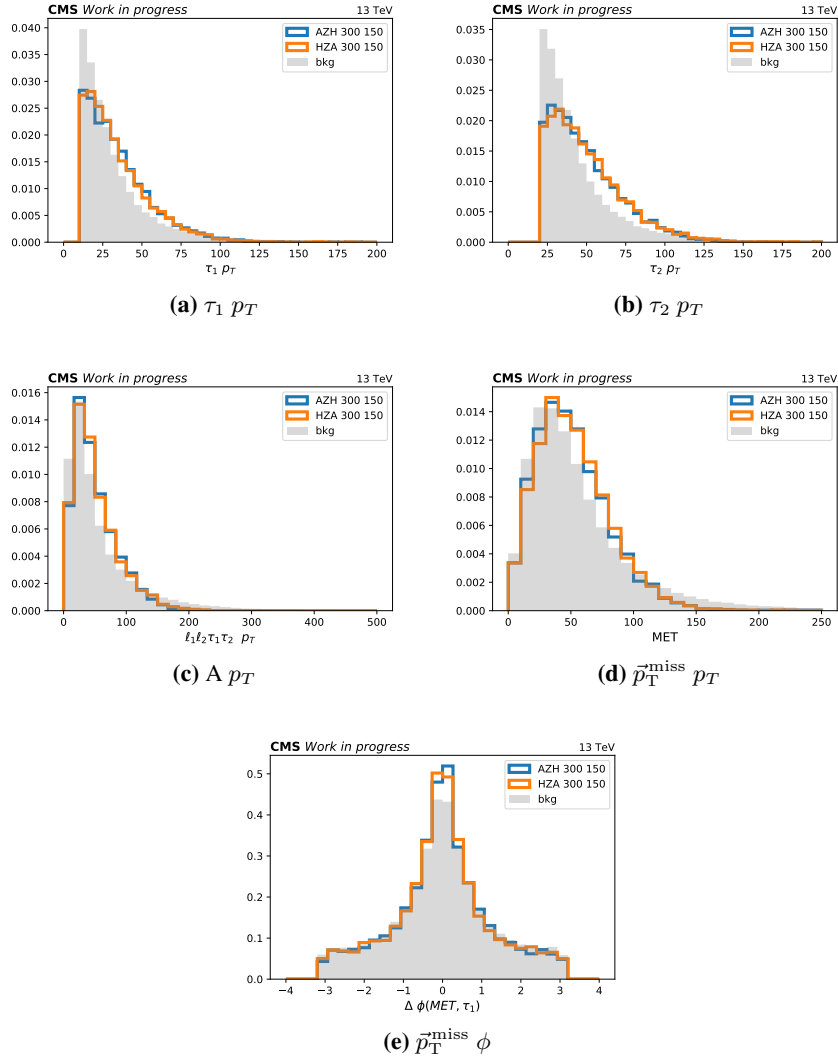


Figure 7.24: Input features for the parametric DNN training in the $Z + \mu\tau_h$ channel (2/2). All the background distributions are normalized to unit area.

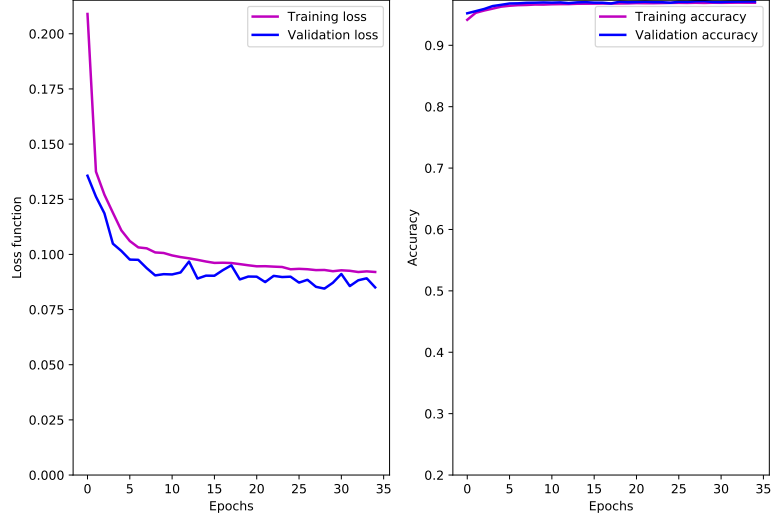


Figure 7.25: Loss and accuracy curves for training and validation dataset. There is no hint of overfitting, given that the two curves are compatible.

invariant mass of the heavier resonance and the overall effect is to distinguish more efficiently the signal from the background, moving the signal bulk away from the background one, as visible in the 2D plot in Fig. 7.30 (b).

As mentioned, the mass resolution changes with the mass of the simulated resonance and this is shown in Fig. 7.31 where the reconstructed mean and its standard deviation are reported as a function of the simulated mass, for the SVFIT algorithm estimate and the visible mass.

For this search, we tried to fit different observables and compared the results in terms of upper limits on the signal strength (see Appendix F). We concluded that the best configuration is achieved by applying a cut on the DNN score to increase purity in the signal region and then fit the 2D (m_H, m_A) distribution. This approach provides both high sensitivity and immediate physics interpretation. We decided to define elliptical binning in the 2D mass space around the reconstructed mean (m_H, m_A) of the signal in such a way that the ellipses content corresponds to 0.5σ , 1σ , 1.5σ , ..., 4σ . Then the binning is unrolled as described in Fig. 7.32, to be fitted with the CMS statistical analysis tool COMBINE [216].

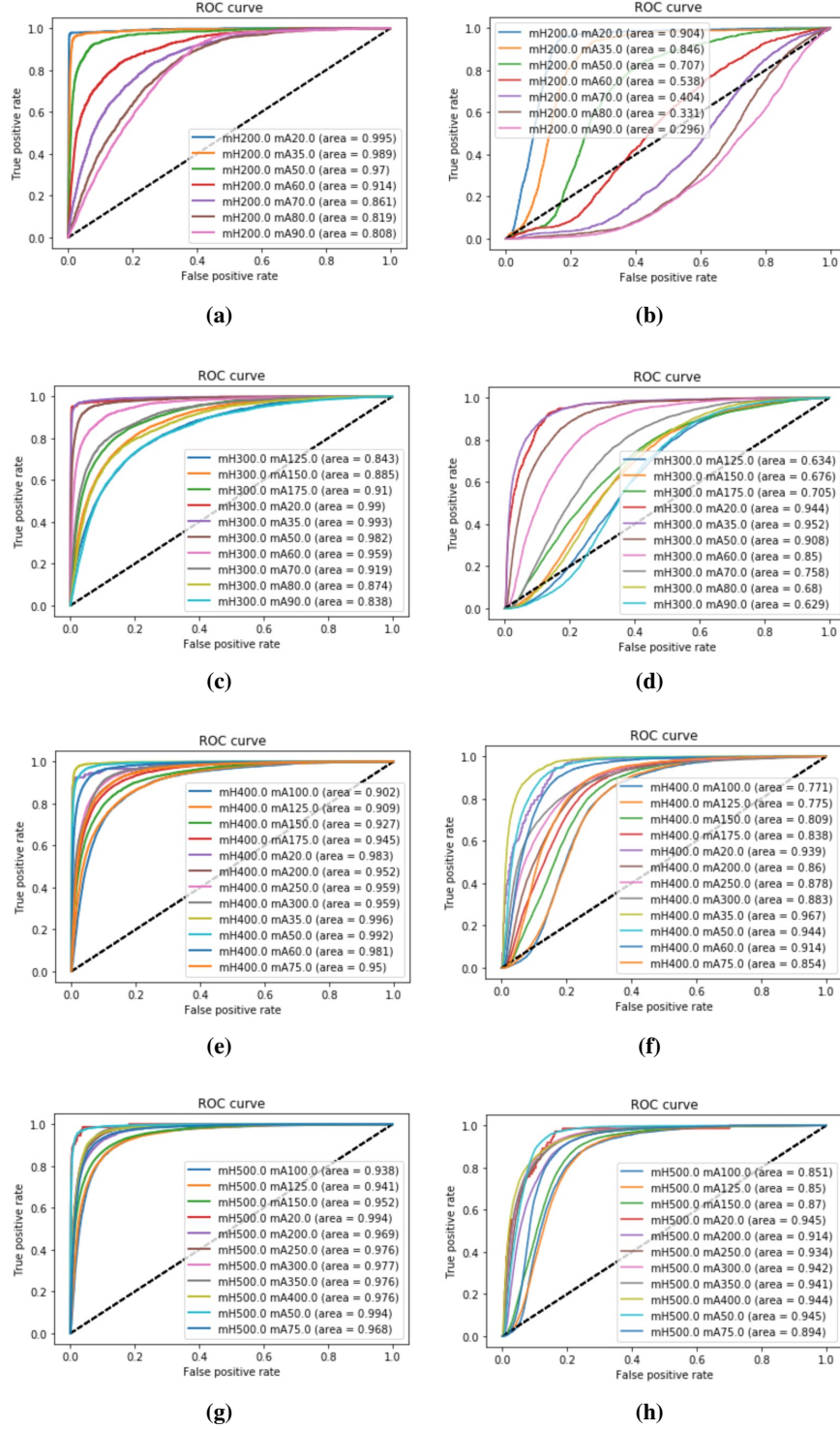


Figure 7.26: ROC curves for different mass scenarios in the case of the parametric DNN (left) or of the single standard DNN (right).

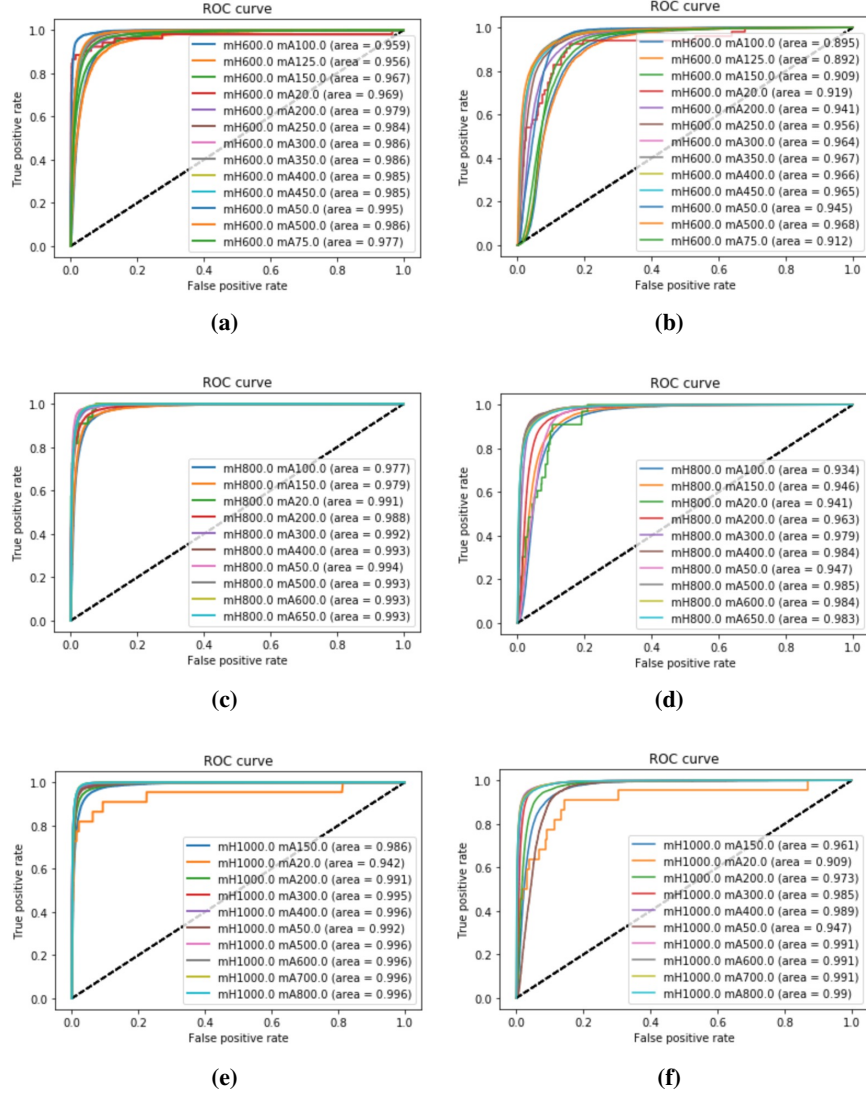


Figure 7.27: ROC curves for different mass scenarios in the case of the parametric DNN (left) or of the single standard DNN (right).

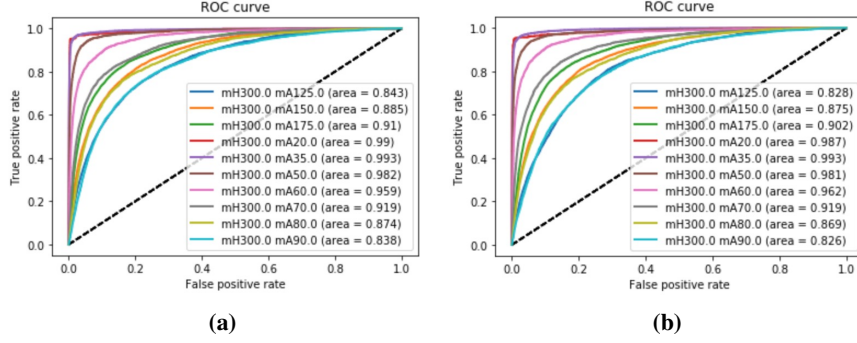


Figure 7.28: ROC curves of the parametric DNN for $m_H=300$ GeV, when the 300 GeV sample is used in the training (a) and when it is removed (b) to test the ability of the network to interpolate in intermediate regions.

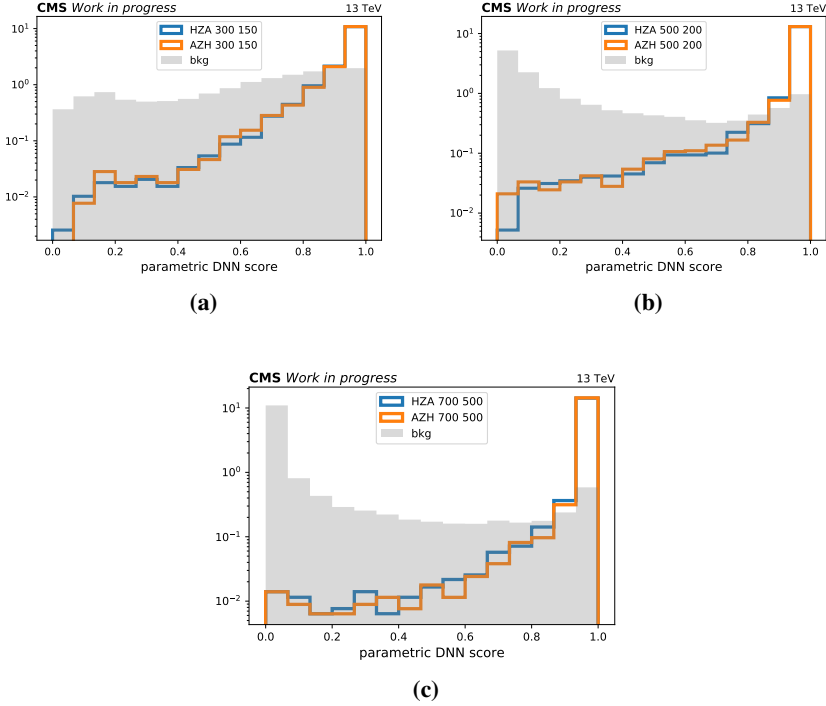
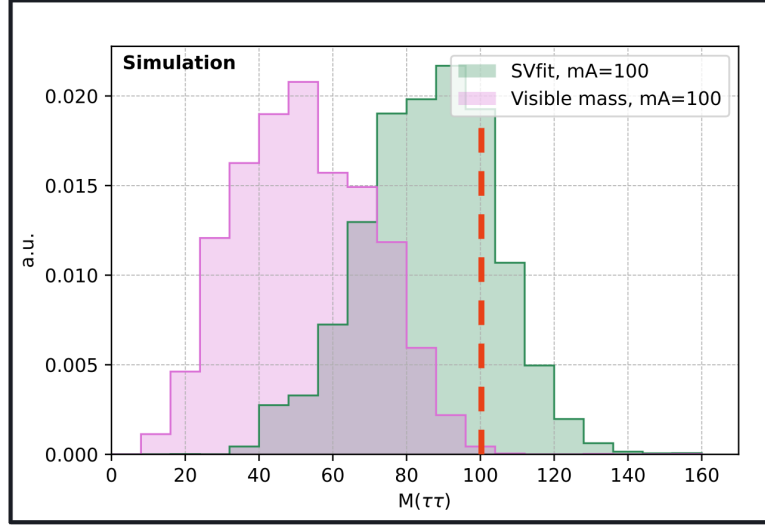
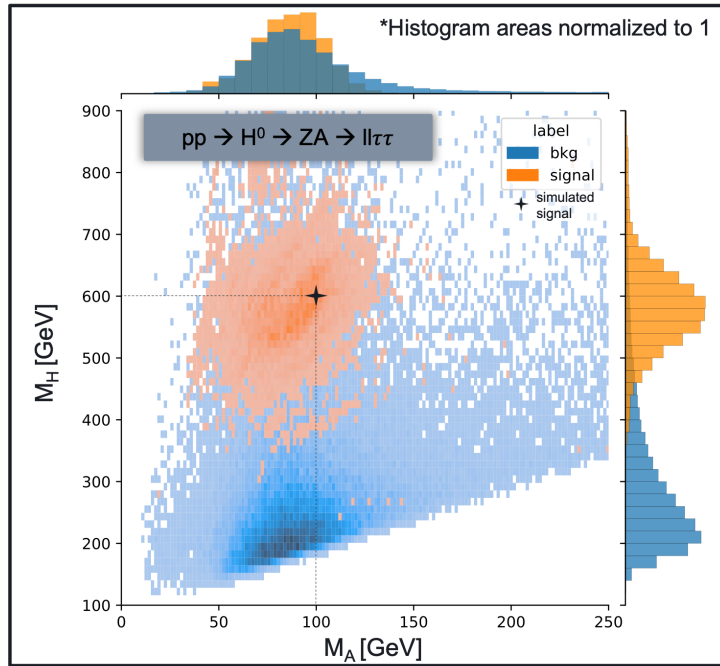


Figure 7.29: DNN score for signal and background in different mass scenarios.



(a)



(b)

Figure 7.30: (a) Invariant mass distribution of the $\tau\tau$ pair for the signal, reconstructed using only the visible decay products of the τ (pink) and applying SVFIT (green). (b) 2D (m_H, m_A) distribution for signal and background when applying SVFIT. In both plots the signal is simulated at $(m_H, m_A) = (600, 100)$ GeV.

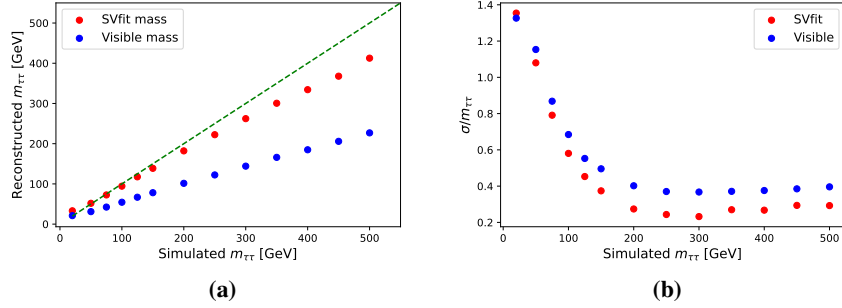


Figure 7.31: Reconstructed mean (a) and its relative standard deviation (b) as a function of the simulated tau pair mass. The value are measured for $m_H = 600$ GeV.

The final fitted distributions $m_A \times m_H$ are shown in Fig. 7.34 for $(m_H, m_A) = (600, 100)$ GeV and in Fig. 7.35 for $(m_H, m_A) = (300, 150)$ GeV, before and after the DNN cut. The value of the cut is chosen finding a compromise between $S/\sqrt{(S+B)}$ optimization and reasonable bin-by-bin statistic uncertainties. For each DNN cut value between 0.1 and 0.9 with a step size of 0.1, the naive significance $S/\sqrt{(S+B)}$ is computed while checking the bin uncertainties of the MC. The cut generating the highest significance while maintaining the MC relative statistical uncertainties in each bin lower than 20% is chosen. A minimal cut of 0.1 is imposed.

Both the DNN training and the DNN cut optimization are performed only once using the 2018 dataset and then applied also to the other eras. The signal relative efficiency of the DNN cut is shown as a function of m_H and m_A in Fig. 7.36. The efficiency is almost everywhere above 95% for all the epochs. The lower efficiencies around $m_A = 100$ GeV for $m_H < 500$ GeV are due to the tighter cuts used in that region that has the highest background population. Figure 7.33 shows the same distributions as Fig. 7.32 without (left) and with (right) DNN cut application (different cuts are applied because of different level of background contamination).

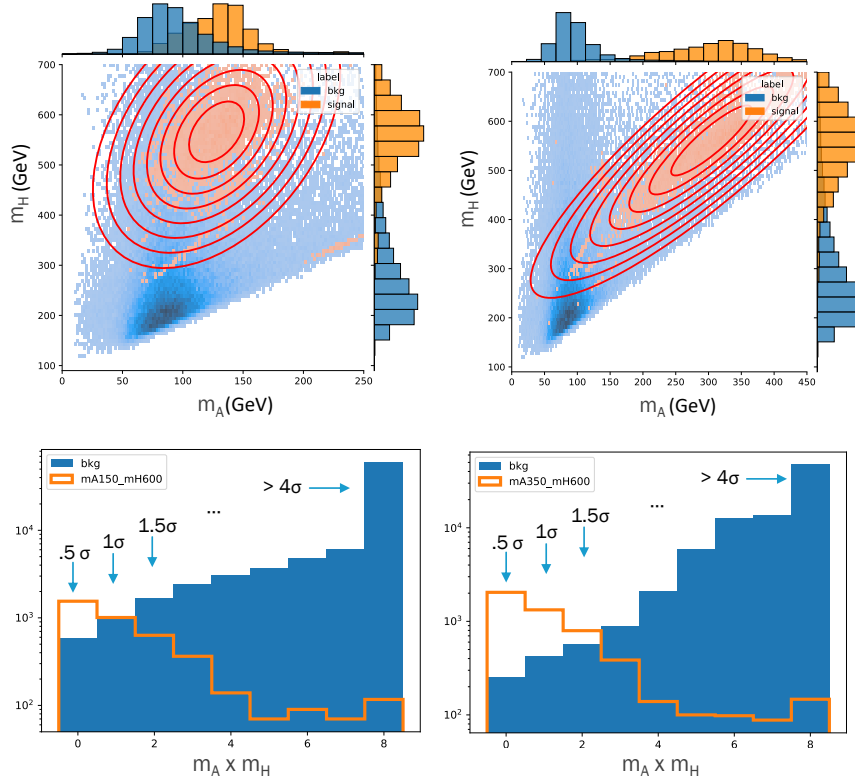


Figure 7.32: (Top row) 2D (m_H, m_A) plane with background and signal distributions for $(m_H, m_A) = (600, 150)$ GeV (left) and $(m_H, m_A) = (600, 350)$ GeV (right) mass scenarios. The calculated ellipses are drawn in red around the estimated mean of the signal distribution. (Bottom row) the elliptical binning is unrolled giving a 1D distribution in which the first bin corresponds to the content of the central ellipse, and the last one to the content outside the external ellipse.

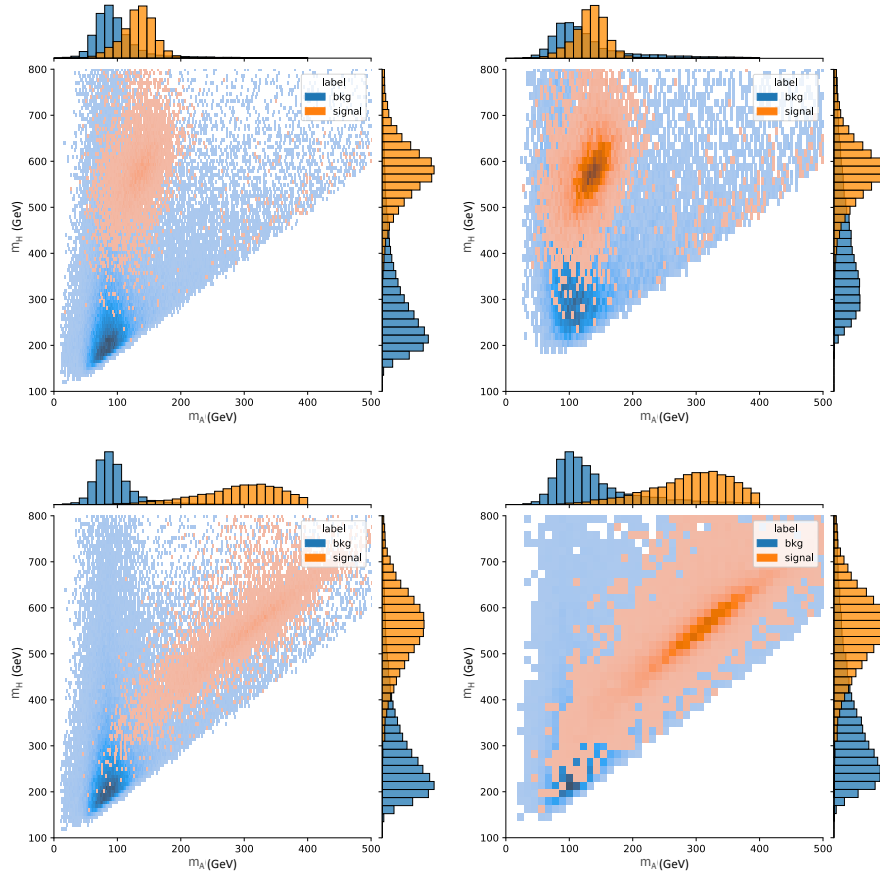


Figure 7.33: (Top row) 2D (m_H, m_A) plane with background and signal distributions for $(m_H, m_A) = (600, 150)$ GeV without (left) and with (right) DNN cut at 0.5. (Bottom row) 2D (m_H, m_A) plane with background and signal distributions for $(m_H, m_A) = (600, 350)$ GeV without (left) and with (right) DNN cut at 0.1 (minimal cut).

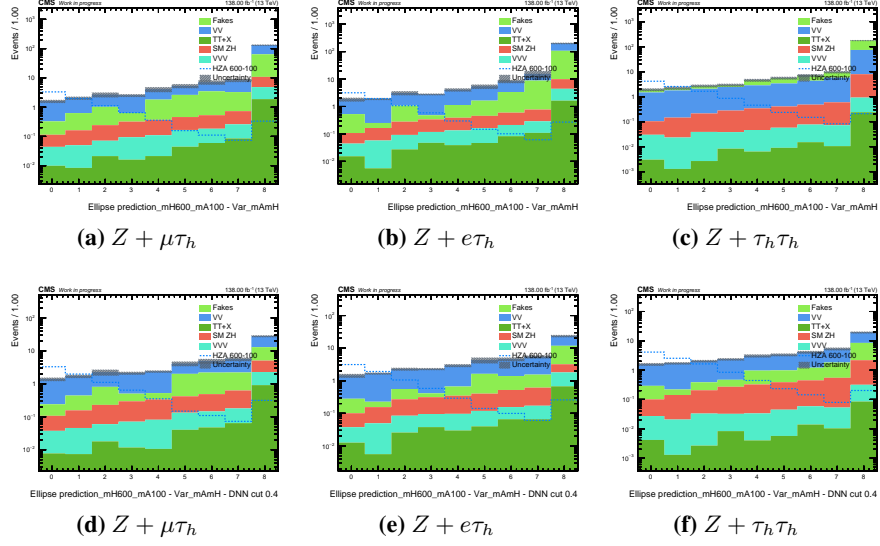


Figure 7.34: $m_A \times m_H$ distribution before (top row) and after (bottom row) the DNN cut for $(m_H, m_A) = (600, 100)$ GeV.

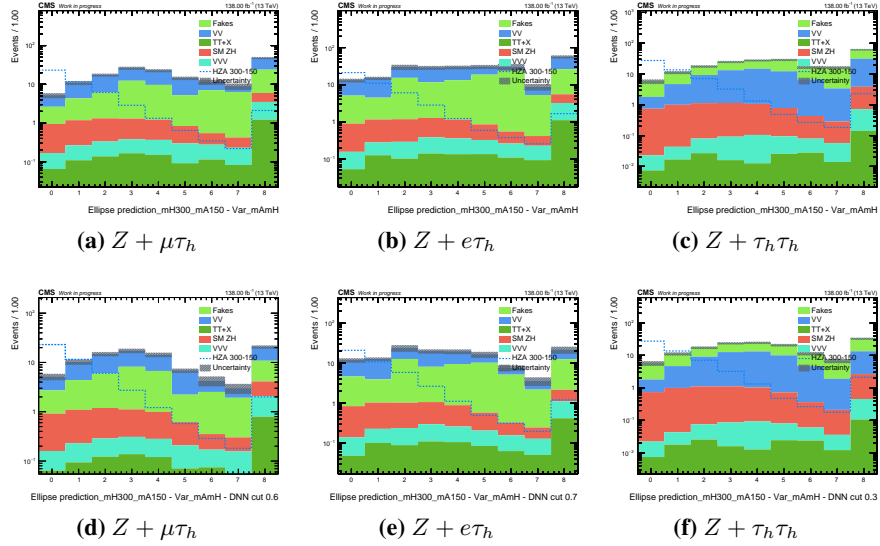


Figure 7.35: $m_A \times m_H$ distribution before (top row) and after (bottom row) the DNN cut for $(m_H, m_A) = (300, 150)$ GeV.

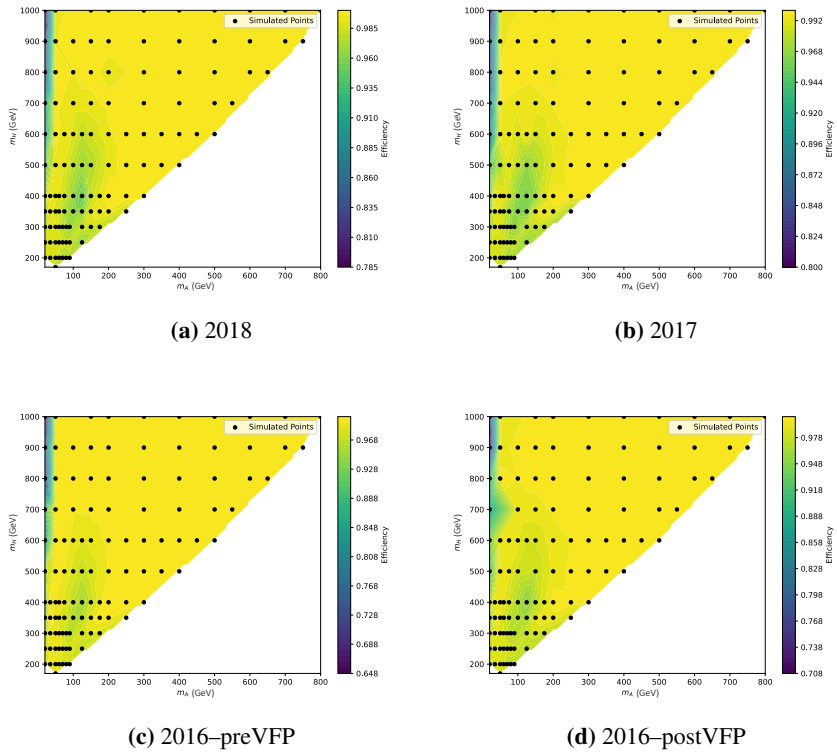


Figure 7.36: Signal efficiency of the DNN cut relative to the baseline selection as a function of m_H and m_A .

7.11 Systematic uncertainties

The instrumental uncertainties on final state objects (electron, muons, τ_h and \vec{p}_T^{miss}) are taken from POG recommendations, considering the up/down variations with respect to the nominal corrections saved in the correctionlib JSONs. These uncertainties are therefore shape uncertainties. Muon and electron uncertainties are treated as fully correlated between years, being systematically dominated. An additional lnN uncertainty of 3% is added to the $\mu\tau_h$ channel for the missing low- p_T muon isolation scale factors.

The τ_h related uncertainties for genuine τ_h candidates are treated as correlated, while the uncertainties for $e/\mu \rightarrow \tau_h$ are uncorrelated between years.

The Jet and \vec{p}_T^{miss} uncertainties are uncorrelated because of their (mostly) statistical origin.

All these uncertainties are fully correlated between the different channels.

The PU uncertainty is also a shape nuisance and is correlated between years, as recommended. The prefiring uncertainty is correlated between data taking periods 2016 and 2017.

The theoretical uncertainties related to the normalisation of the background are taken to be same as SM ZH analysis [287] with tau leptons in the final states (same final state objects, same backgrounds). In particular, the uncertainty on SM ZH includes the uncertainties on the cross section (variation of QCD scale, PDF+ α_s) and on the branching ratio. The uncertainty on the 2HDM signal is dominated by the QCD scale uncertainty. It is computed varying the renormalisation and factorisation scale from 0.5 to 2.0 times the nominal value and considering the signal yields change. The maximum shift from the nominal yield is of the order of 25% and this is assigned as lnN uncertainty.

Concerning the data driven background, the uncertainties on the estimated fake rate curves is propagated to the final templates and here they are taken as shape uncertainties for the fit. A jet-flavor-related uncertainty on the curves is introduced as explained in Appendix G. The bin-by-bin uncertainties cover for the limited number of events in the control regions used to estimate the fakes. No uncertainty is associated to the closure test, given that the predictions and observations were in good agreement within statistical uncertainties.

The uncertainty in the luminosity affects all processes estimated from simulation. The uncertainty is decomposed in several components with different correlations between the 3 years, following official recommendations [293].

Bin-by-bin uncertainties are used to take into account the limited number of events of the simulated samples (or of data for the data-driven background) in

every bin of the fitted distributions. They are implemented via the *autoMCstat* feature of *CombineHarvester* using the Barlow-Beeston approach [294].

The uncertainties are summarized in Table 7.13.

Uncertainty	Implementation	Magnitude	Correl. years
electron ID	shape	From EGammaPOG	yes
electron Reco	shape	From EGammaPOG	yes
electron Trigger	shape	From EGammaPOG	yes
muon ID (medium p_T)	shape	From MuonPOG	yes
muon ID (low p_T)	shape	From MuonPOG	yes
muon iso (medium p_T)	shape	From MuonPOG	yes
muon iso (low p_T , missing SF)	lnN	3%	yes
muon Trigger	shape	From MuonPOG	yes
τ_h ID (medium p_T)	shape	From TauPOG	yes
τ_h ID (high p_T)	shape	From TauPOG	yes
$e \rightarrow \tau_h$ FR	shape	From TauPOG	no
$\mu \rightarrow \tau_h$ FR	shape	From TauPOG	no
τ_h Energy Scale	shape	From TauPOG	yes
JER	shape	From JetMET	no
JES (total)	shape	From JetMET	no
Unclustered Energy	shape	From JetMET	no
$t\bar{t}V$ xs	lnN	4.2%	yes
VV xs	lnN	3.2%	yes
VVV xs	lnN	25%	yes
SM ZH xs	lnN	5%	yes
HZA unc. (mainly scale unc.)	lnN	25%	yes
Data driven bkg	shape	From FR curves	no
Data driven bkg (flav. unc.)	shape	From FR curves	yes
Prefiring	shape	Event-dependent	yes
PU	shape	Event-dependent	yes
Luminosity	lnN	2–3%	partial
Stat. fluctuations	autoMCstat	autoMCstat	no

Table 7.13: Sources of systematic uncertainties.

7.11.1 Impacts

The impacts for all nuisance parameters in the combined fit of all years and final states are shown in Fig. 7.37 for signal hypothesis $(m_H, m_A) = (600, 100)$ GeV and in Fig. 7.38 for $(m_H, m_A) = (300, 150)$ GeV. The theoretical uncertainty on the signal, which has the largest impact (approximately 20%), is

omitted from the plot to improve the visibility of the other contributions. The most significant instrumental uncertainties arise from τ_h identification, followed by uncertainties on the integrated luminosity. Statistical uncertainties—particularly those associated with the data-driven background estimation—also have a considerable impact, especially in the low-mass signal region where the signal is closer to the bulk of the background distribution.

Additionally, a GOF test is run in the CR where the DNN cut is failed to assess the agreement between data and simulation. It can be found in Appendix H.

7.12 Results

The results are extracted with a maximum likelihood fit of the $m_A \times m_H$ observable after the DNN cut, as shown in Figures 7.34 and 7.35.

The 95% expected upper limits on the signal strength (σ/σ_{theory}) are reported in top Fig. 7.39, demonstrating the sensitivity to exclude a big portion of the explored mass space before the top pair production threshold. The underlying model assumption is a 2HDM Type-II with $\tan\beta=1.5$ and $\cos(\beta-\alpha)=0.01$. The theoretical values for $\sigma \times \text{BR}$ are the ones reported in Tables 24, 25 and 26.

This result can be directly compared with the preliminary results from $H \rightarrow ZA \rightarrow \ell\ell b\bar{b}$ [295] which uses the same model parameters, showing similar exclusion power. The plan is to combine these two channels, together with $H/A \rightarrow ZA/H \rightarrow \ell\ell t\bar{t}$ that has the sensitivity to exclude the region after top pair production threshold.

The results are also presented in a model independent fashion in bottom Fig. 7.39 as upper limits on $\sigma \times \text{BR}$ for a generic narrow-width resonance (in this case the signal uncertainty is removed from the nuisance parameters). The model independent results can be compared with the similar analysis $A \rightarrow Zh_{SM}$ [296]. The paper quotes an upper limit on $\sigma(ggA) \times \text{BR}(A \rightarrow Zh) \times \text{BR}(h \rightarrow \tau\tau)$ between 4.5 fb and 50 fb for the $gg \rightarrow A$ process for masses between 225 GeV and 800 GeV. In this analysis for the same mass range of the heavier resonance and the lighter mass fixed at 125 GeV, the expected upper limit on $\sigma(ggH) \times \text{BR}(H \rightarrow ZA) \times \text{BR}(A \rightarrow \tau\tau)$ is between 7 fb and 60 fb.

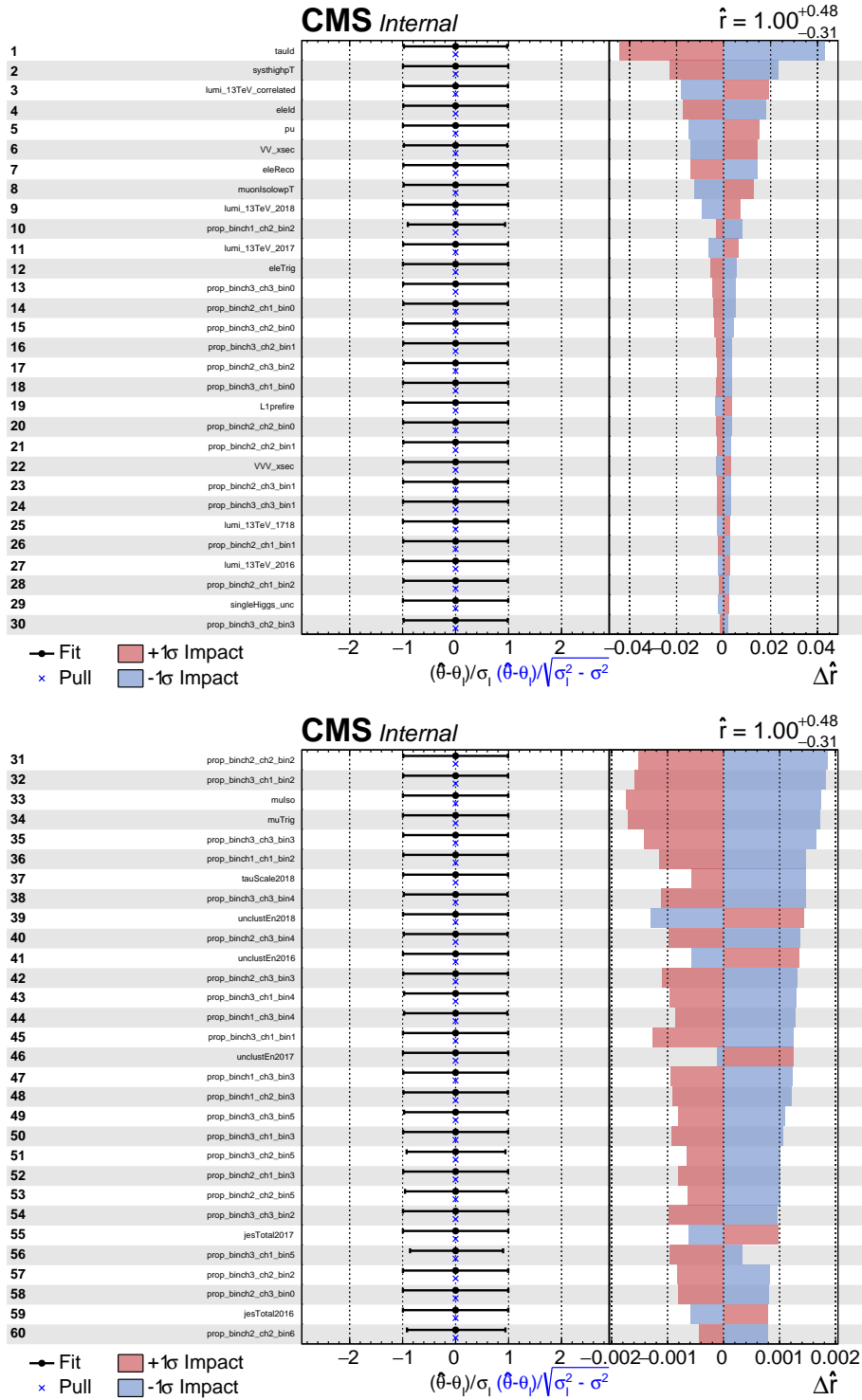


Figure 7.37: Impacts for the combination of years and final states. Signal hypothesis $(m_H, m_A) = (600, 100)$ GeV. The theory uncertainty on the signal, which is the highest ranked uncertainty ($\approx 20\%$), is omitted to better see the other contributions.

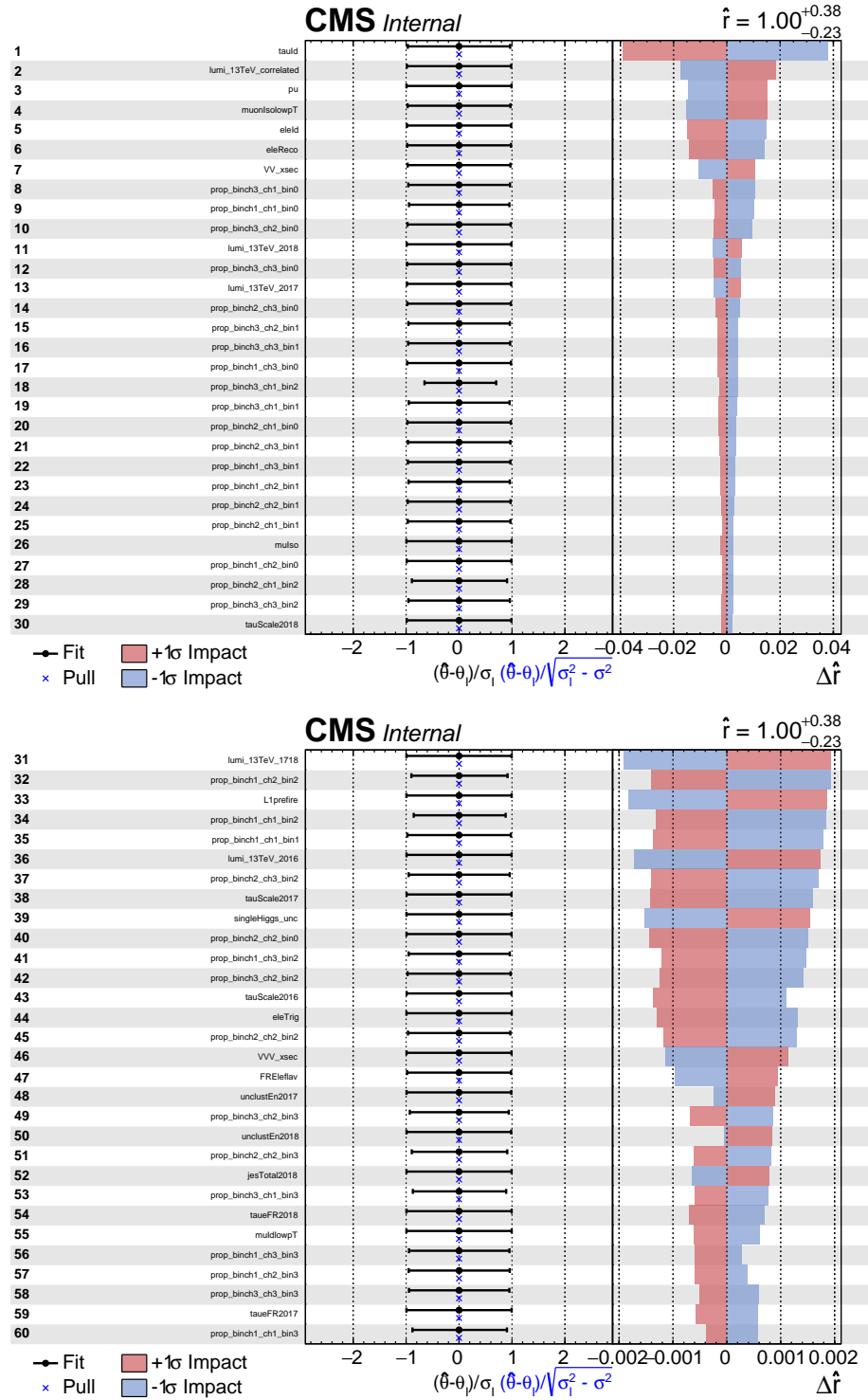
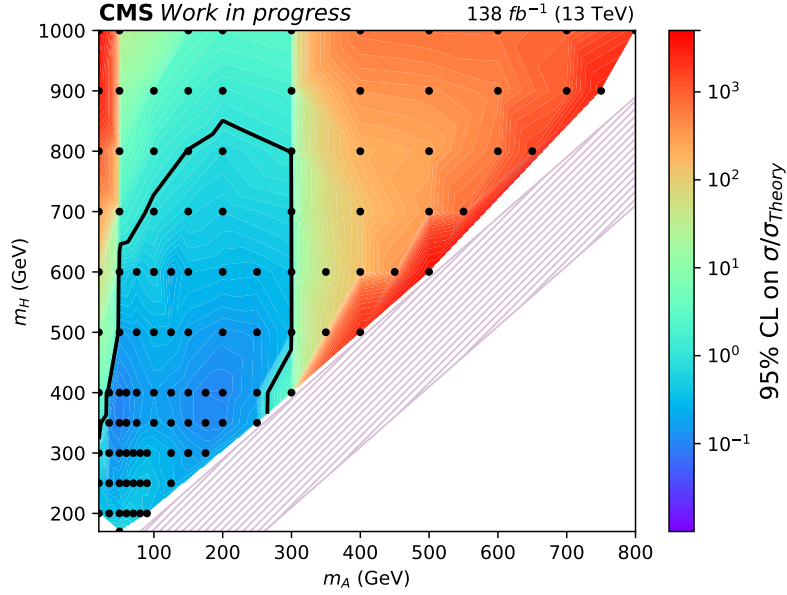
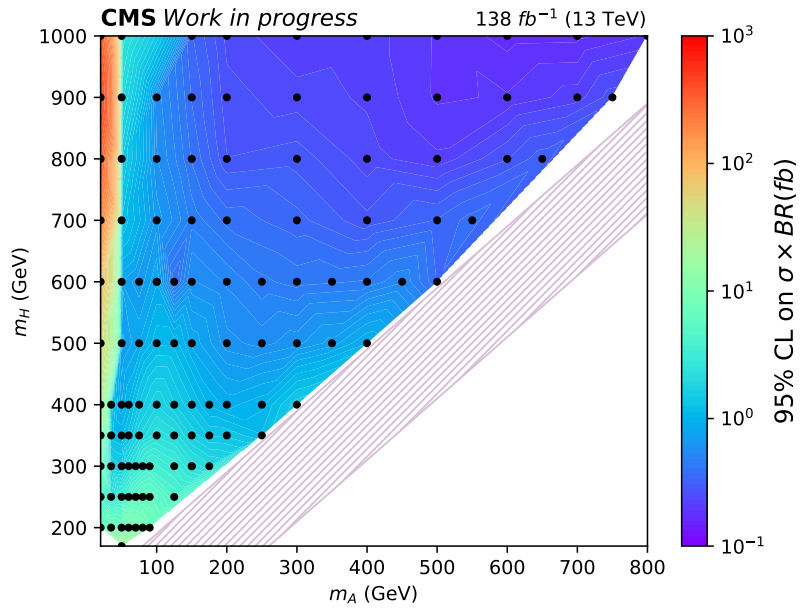


Figure 7.38: Impacts for the combination of years and final states. Signal hypothesis $(m_H, m_A) = (300, 150)$ GeV. The theory uncertainty on the signal, which is the highest ranked uncertainty ($\approx 20\%$), is omitted to better see the other contributions.



(a) 2HDM interpretation



(b) Model Independent

Figure 7.39: Upper limits on signal strength under the 2HDM interpretation (top) and upper limits on $\sigma \times BR$ for a generic narrow-width resonance (bottom) for the full Run 2 dataset.

7.13 Summary and Outlook

A search for new Higgs bosons has been conducted using proton-proton collision data at $\sqrt{s} = 13$ TeV, collected by the CMS experiment during Run 2 (2016–2018), corresponding to an integrated luminosity of 138 fb^{-1} . Events containing a Z boson and a pair of oppositely charged τ leptons were selected to study the invariant mass distributions of both the τ -lepton pair and the combined $Z + \tau\tau$ system.

Stringent limits have been set on a benchmark process predicted in a two-Higgs-doublet model: $H/A \rightarrow ZA/H \rightarrow \ell^+\ell^-\tau^+\tau^-$, where H and A denote a scalar and a pseudoscalar Higgs boson, respectively. In addition, model-independent results are provided in the form of upper limits on the production cross section times branching ratio for generic narrow-width resonances.

This analysis significantly improves upon the previous search performed with Run 1 data [255], benefiting from a substantially larger dataset, higher center-of-mass energy, and improved object reconstruction capabilities in Run 2. Moreover, a more sophisticated analysis strategy has been adopted, including the use of a parametric DNN to enhance sensitivity across all mass hypotheses.

The next steps include finalizing the CMS internal review process, presenting the observed results on data, and potentially extending the interpretation to the complementary mass hierarchy region ($m_A > m_H$). A combination with other channels is also planned in the near future.

Looking ahead, this search can be repeated using data from the ongoing Run 3, with the possibility of further investigating any hints of excess eventually observed in Run 2. Future improvements may also involve integrating machine learning techniques into the estimation of the misidentification rates, aiming to simplify the measurement and improve its precision.

HH searches at Future Hadron Colliders

In Sec.1.5.5, I discussed the role of the Higgs self-coupling within the SM framework, emphasizing how its measurement represents a crucial test of our current understanding of Nature.

It is unlikely that the current LHC run will be able to establish the Higgs boson self-interaction, unless contributions from BSM significantly enhance the HH production cross section—by at least a factor of two.

However, the upcoming high luminosity phase of the LHC (see Sec.3.4) is expected to deliver a substantially larger dataset, offering improved sensitivity to this rare process. Finally, the proposed FCC-hh (see Chapter 4) is anticipated to provide definitive insights into the subject. In both cases, the analysis of simulated events is essential to assess the potential of these future colliders and to guide the design of detectors toward the necessary performance targets.

I have contributed to projections of HH searches for both the HL-LHC and the FCC-hh, and my work is detailed in the following chapters.

8.1 Projections of non-resonant HH searches to HL-LHC

The SM search for HH production at HL-LHC has been conducted using two different approaches. The first approach, described in Sec. 8.1.1, employs DELPHES for a fast simulation of the CMS Phase-II detector and involves a full analysis of the simulated events. The second approach, presented in Sec. 8.1.2, is based on a scaling of Run 2 results, taking into account the increased integrated luminosity and incorporating assumptions on systematic uncertainties. This method does not involve any new detector simulation. De-

spite their fundamentally different methodologies, both approaches rely on the state-of-the-art knowledge from Run 2 and yield broadly consistent results.

For the fast simulation-based projections, I focused on the three leading channels contributing to sensitivity: $bb\gamma\gamma$, $bb\tau\tau$, and $bbbb$. I was responsible for every aspect of the analysis in each channel as well as their combination. This independent work is documented in Ref. [3], submitted to Snowmass 2021 [297], and later presented at ICHEP 2022 [4]. I presented this study during the Young Speaker Contest organized by the Belgian Physical Society, where I was awarded a prize and offered the opportunity to publish an article on the topic in the Belgian Journal of Physics [5].

For the projections based on Run 2 scaling, I mainly contributed to the $bbbb$ channel, in both the boosted and resolved topologies, and to the channel combination. This work was conducted within the CMS Collaboration and is included in the Run 2 HH combination paper [6].

8.1.1 Projections to HL-LHC with fast simulation

This study is based on pp collision events produced using a DELPHES fast simulation of the CMS Phase II detector as described in the Technical Design Report [143]. The assumed center of mass energy is $\sqrt{s} = 14$ TeV and the integrated luminosity corresponds to the expected total delivered by the HL-LHC, namely 3 ab^{-1} .

The analysis targets exclusively Higgs boson pair production via gluon fusion (ggHH). The dependence of the ggHH cross section on κ_λ and κ_t can be written as:

$$\sigma(\kappa_\lambda, \kappa_t) = \kappa_\lambda^2 \kappa_t^2 t + \kappa_t^4 b + \kappa_\lambda \kappa_t^3 i, \quad (8.1)$$

where $t = |T|^2$, $b = |B|^2$, and $i = |TB^* + B^*T|$, and the three contributions correspond to the triangle and box diagrams shown in Fig. 1.12, and their interference, respectively [298].

The same formula holds for every differential cross section $d\sigma/dx$ for HH production. At higher order in the QCD perturbative expansion, T and B correspond to the sum of all diagrams of the same order in κ_λ and κ_t , and the polynomial relation in Eq. 8.1 remains valid. Since the ggHH cross section can be expressed as a polynomial in κ_λ and κ_t with three independent terms, we can model the production of ggHH over a wide range of κ_λ and κ_t by evaluating the cross section at three different $(\kappa_\lambda, \kappa_t)$ values and performing a linear combination. In this case we assumed the SM value for the top Yukawa

coupling, hence $\kappa_t = 1$, and simulated three samples for different values of κ_λ , namely 1, 2.45 and 5, following the CMS Run 2 analysis strategy.

Signal events are simulated at NLO accuracy using POWHEG 2.0 [259–261], while background processes are generated with MADGRAPH5_AMC@NLO [257, 258]. Hadronization and Higgs boson decays are modeled with PYTHIA 8.2 [262], which also accounts for pileup by overlaying an average of 200 minimum-bias events.

Three final states are analyzed: $bb\gamma\gamma$, $bb\tau\tau$, and $bbbb$.

The analysis, performed within the Bamboo framework [299], consists of three major steps, similarly for all the channels: kinematic selections to identify two good Higgs boson candidates, implementation of multivariate classifiers to improve the signal-to-background ratio and extraction of results from fits to discriminating observables (potentially using multiple event categories).

In the following, the strategies adopted for the three channels are briefly outlined and the most representative plots are reported for the sake of brevity, more can be found in Ref. [3]. Results are presented in terms of the expected discovery significance and constraints on κ_λ .

$HH \rightarrow bb\gamma\gamma$

This channel is limited by a low branching ratio of only 0.26%, but it benefits from the excellent photon energy resolution and the ability to fully and unambiguously reconstruct the decay products of both Higgs bosons.

The list of simulated samples with related cross sections is shown in Table 8.1.

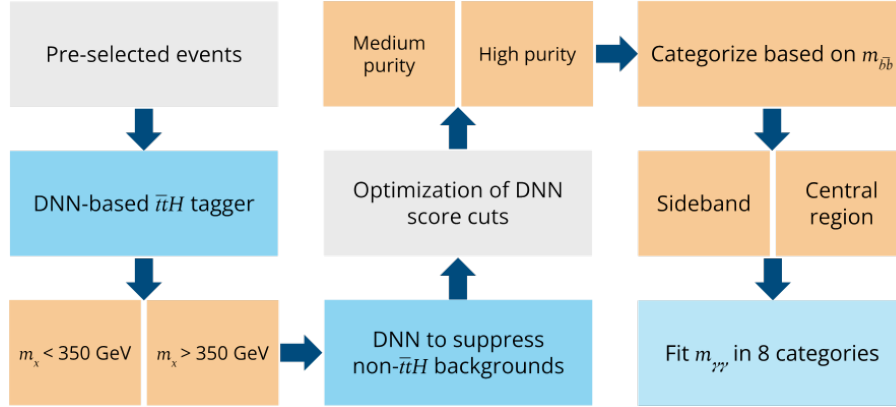
Figure 8.1 summarizes the main steps of the analysis strategy.

In this channel signal events are characterized by four exclusive objects, namely two photons and two b-jets. Several kinematic requirements (Table 8.2) are imposed on jet and photon objects to select only events with signal-like topology. In particular, the di-photon and di-jets invariant masses ($m_{\gamma\gamma}$ and m_{bb}) are required to be in a window around the 125 GeV Higgs boson nominal mass (see Fig. 8.2).

The event yields after these selections are reported in Table 8.3.

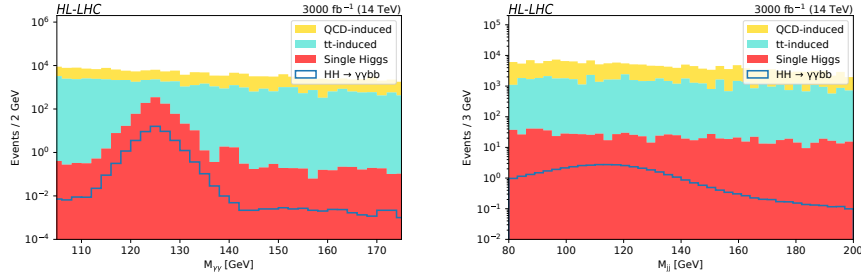
Backgrounds arise mainly from single Higgs events decaying into photons and the non-resonant QCD-induced production of two isolated, ener-

	Process	Cross section (fb)
Signal	$(gg)HH \rightarrow b\bar{b}\gamma\gamma$ ($\kappa_\lambda = 1$)	9.70×10^{-2}
	$(gg)HH \rightarrow b\bar{b}\gamma\gamma$ ($\kappa_\lambda = 2.45$)	4.09×10^{-2}
	$(gg)HH \rightarrow b\bar{b}\gamma\gamma$ ($\kappa_\lambda = 5$)	2.96×10^{-1}
Single Higgs	$(gg)H \rightarrow \gamma\gamma$	1.24×10^2
	$qqH \rightarrow \gamma\gamma$	9.71
	$VH \rightarrow \gamma\gamma$	5.67
	$ttH \rightarrow \gamma\gamma$	1.39
QCD-induced	$pp \rightarrow \gamma\gamma + jets$	9.46×10^4
	$pp \rightarrow \gamma + jets$	1.04×10^6
	$pp \rightarrow jets$	1.41×10^8
tt-induced	$pp \rightarrow t\bar{t}\gamma\gamma$	1.86×10^1
	$pp \rightarrow t\bar{t}\gamma$ had	7.92×10^2
	$pp \rightarrow t\bar{t}\gamma$ semi lep	7.71×10^2
	$pp \rightarrow t\bar{t}\gamma$ fully lep	6.23×10^2
	$pp \rightarrow t\bar{t}$ inclusive	8.64×10^5

Table 8.1: List of simulated samples for $b\bar{b}\gamma\gamma$ channel.**Figure 8.1:** Flowchart of the $b\bar{b}\gamma\gamma$ channel analysis strategy.

getic photons. DNNs are trained to suppress the different backgrounds, using Keras [289] and Tensorflow [290]. First, a DNN is trained to discriminate the signals from the single Higgs production with associated top quark pairs ($t\bar{t}H$). The contribution of the $t\bar{t}H$ background is enhanced among the single Higgs production modes since it results in a similar final state as the signal. However, its kinematic is different (more but less energetic jets and/or leptons,

Photon		Jet	
Variable	Requirement	Variable	Requirement
ID	loose	ID	tight
Iso	tight	b-tag	loose
$ \eta $	< 1.44 or in $[1.57, 2.5]$	$ \eta $	< 2.5
p_T (sub)lead	> 30 (20) GeV	p_T	> 30 GeV
$p_T/m_{\gamma\gamma}$ (sub)lead	$> 1/3$ (1/4)	m_{jj}	in $[80, 200]$ GeV
$m_{\gamma\gamma}$	in $[100, 180]$ GeV		

Table 8.2: Photon (left) and jet (right) kinematic selections.**Figure 8.2:** Di-photon (left) and di-jet (right) invariant mass distributions after kinematic selections, for signal and background processes.

Process	Yields
$(gg)HH \rightarrow b\bar{b}\gamma\gamma \kappa_\lambda = 1$	45 ± 1
$(gg)HH \rightarrow b\bar{b}\gamma\gamma \kappa_\lambda = 2.45$	18 ± 2
$(gg)HH \rightarrow b\bar{b}\gamma\gamma \kappa_\lambda = 5$	97 ± 2
$(gg)H \rightarrow \gamma\gamma$	275 ± 32
$qqH \rightarrow \gamma\gamma$	40 ± 3
$VH \rightarrow \gamma\gamma$	110 ± 3
$ttH \rightarrow \gamma\gamma$	476 ± 12
$pp \rightarrow \gamma\gamma + jets$	85997 ± 2286
$pp \rightarrow \gamma + jets$	41270 ± 2737
$pp \rightarrow jets$	0.0
$pp \rightarrow t\bar{t}\gamma\gamma$	562 ± 17
$pp \rightarrow t\bar{t}\gamma$	3939 ± 133
$pp \rightarrow t\bar{t}$	49060 ± 2020

Table 8.3: Event yields for $b\bar{b}\gamma\gamma$ channel.

closer b-jets and di-photon pairs, etc.) and this is captured by the DNN based ttH tagger, which performs extremely good (Fig. 8.3). Events with ttH score lower than a defined threshold are discarded.

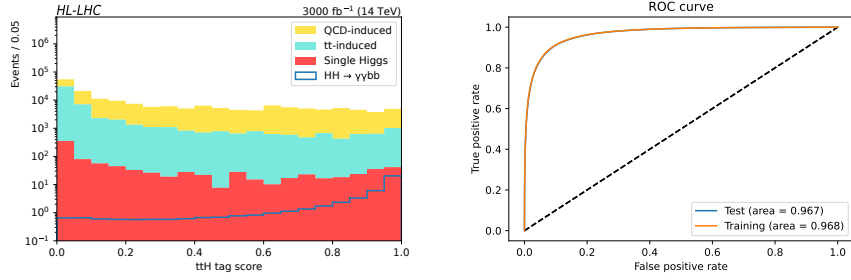


Figure 8.3: (Left) ttH tagger score for signal and stacked background. (Right) ROC curves for testing and training samples with relative AUC value.

For the next step, events are divided into two categories based on the invariant mass $m_X = m_{bb\gamma\gamma} - m_{bb} - m_{\gamma\gamma} + 250$ GeV, which reconstructs the di-Higgs mass corrected for resolution effects. As shown in Fig. 8.4, the shape of the m_X distribution is sensitive to the value of κ_λ . In the SM scenario, the lower m_X region is sparsely populated, whereas several BSM hypotheses predict a significant event yield in this region. Since current experimental constraints do not exclude such BSM scenarios, applying a strict cut on m_X could reduce sensitivity to non-SM signals. To retain sensitivity across a broad range of κ_λ values, the events are instead categorized into two regions: one with $m_X < 350$ GeV and the other with $m_X > 350$ GeV.

Two DNNs, one for each m_X region, are trained to separate the signals from the non-ttH backgrounds. Figure 8.5 shows the resulting scores for events with $m_X < 350$ GeV on the left and $m_X > 350$ GeV on the right. Events with DNN score lower than a defined threshold are discarded. The remaining ones are separated in a high and medium purity category. Cuts and category delimiters are selected through a multi-dimensional optimization procedure with the “naive” significance S/\sqrt{B} of the signal as the figure of merit.

Finally, events are further categorized into a *central* or *sideband* region based on the invariant mass m_{bb} , using a window of approximately 15 GeV around the Higgs boson mass. This categorization scheme, when combined with the previous steps, results in a total of eight event categories. Constraints

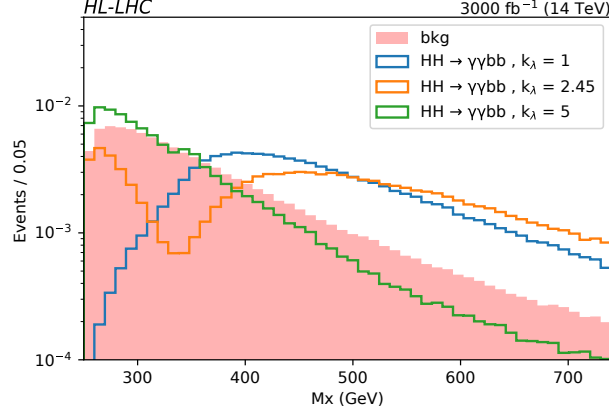


Figure 8.4: Distribution of the reconstructed m_X for different κ_λ signal hypothesis and for the background.

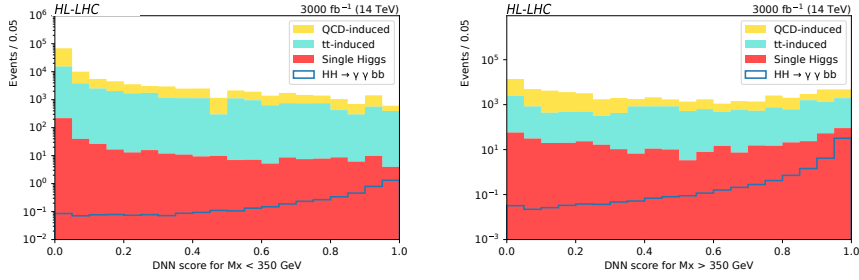


Figure 8.5: DNN score for the $m_X < 350$ GeV (left) and > 350 (right) region.

on κ_λ are extracted using a Maximum Likelihood fit of the $m_{\gamma\gamma}$ distribution performed simultaneously in the eight categories. The systematic uncertainties taken into account are reported in Table 8.4 and are drawn from Ref. [300].

$HH \rightarrow bb\tau\tau$

The list of simulated samples with related cross sections is shown in Table 8.5.

This channel is characterized by the presence of missing energy, as τ decays always involve neutrinos. With two taus in the final state, six combinations are possible: $\mu\tau_h$, $e\tau_h$, $\tau_h\tau_h$, μe , ee and $\mu\mu$. Among these six final states, only the final states that involves at least one τ_h have been considered for this analysis,

Systematic uncertainty source	Impact on yields
Luminosity	$\pm 1.0 \%$
$m_{\gamma\gamma}$ scale	$\pm 0.5 \%$
Photon energy scale	$\pm 2.0 \%$
Di-photon trigger	$\pm 2.0\%$
Photon ID efficiency	$\pm 1.0 \%$
Jet Energy Scale	$\pm 1.0\%$
B-tag efficiency	$\pm 1.0\%$
QCD scale	$+4.6\% / -6.7\%$ (ggH) $+0.4\% / -0.7\%$ (VH) $+0.5\% / -0.3\%$ (VBFH) $+6.0\% / -9.2\%$ (ttH) $+2.4\% / -3.6\%$ (tt)
PDF scale	$\pm 3.2\%$ (ggH) $\pm 1.8\%$ (VH) $\pm 2.1\%$ (VBFH) $\pm 3.5\%$ (ttH) $\pm 4.2\%$ (tt)
Signal theoretical uncertainties	$+2.1\% / -4.9\%$ (QCD scale) $\pm 3.0\%$ (PDF scale) $+4.0\% / -18.0\%$ (top mass)

Table 8.4: Systematic uncertainties for $bb\gamma\gamma$ channel.

because of the highest branching fraction. The baseline event selection ensures not only good b-jets and τ candidates but also the mutual exclusivity of the three final state categories.

Let us start considering the $H \rightarrow \tau\tau$ leg. Leptons are selected following the requirements in Table 8.6, while τ_h candidates are required to have a minimum p_T of 20 and a maximum $|\eta|$ of 2.3. Events are thus exclusively accepted into the following three categories:

- $\mu\tau_h$: exactly one primary muon and at least one τ_h with opposite charge to the selected muon. If multiple pairs pass the selection, the one with the highest isolation is selected. Exactly zero veto electrons are allowed;
- $e\tau_h$: exactly one primary electron and at least one τ_h with opposite charge to the selected electron. If multiple pairs pass the selection, the

	Process	Cross section (fb)
Signal	$(gg)HH \rightarrow b\bar{b}\tau\tau$ ($\kappa_\lambda = 1$)	2.68
	$(gg)HH \rightarrow b\bar{b}\tau\tau$ ($\kappa_\lambda = 2.45$)	1.13
	$(gg)HH \rightarrow b\bar{b}\tau\tau$ ($\kappa_\lambda = 5$)	8.18
Single Higgs	$(gg)H \rightarrow b\bar{b}$	3.18×10^4
	$(gg)H \rightarrow \tau\tau$	3.43×10^3
	$ttH \rightarrow b\bar{b}$	3.574×10^2
	$ttH \not\rightarrow b\bar{b}$	2.563×10^2
	$ZH, Z \rightarrow q\bar{q}, H \rightarrow b\bar{b}$	4.02×10^2
	$ZH, Z \rightarrow ll, H \rightarrow b\bar{b}$	1.94×10^1
	$W^+H, W \rightarrow q\bar{q}', H \rightarrow b\bar{b}$	3.62×10^2
	$W^+H, W \rightarrow ll, H \rightarrow b\bar{b}$	6.03×10^1
	$W^-H, W \rightarrow q\bar{q}', H \rightarrow b\bar{b}$	2.32×10^2
	$W^-H, W \rightarrow ll, H \rightarrow b\bar{b}$	3.87×10^1
Single Boson	$VH, H \not\rightarrow b\bar{b}$	1.46×10^3
	tW	4.506×10^4
	$\bar{t}W$	4.502×10^4
	$tZq, Z \rightarrow ll$	8.5×10^1
Double Boson	$W \rightarrow l\nu + jets$	6.052×10^7
	WW	1.31×10^5
Drell-Yan	$ZZ \rightarrow llq\bar{q}$	3.721×10^3
	$DY \rightarrow ll + jets$ HT 100 to 200	1.5×10^5
	$DY \rightarrow ll + jets$ HT 200 to 400	3.295×10^4
	$DY \rightarrow ll + jets$ HT 400 to 600	3.911×10^3
	$DY \rightarrow ll + jets$ HT 600 to 800	8.301×10^2
	$DY \rightarrow ll + jets$ HT 800 to 1200	3.852×10^2
	$DY \rightarrow ll + jets$ HT 1200 to 2500	8.874×10^1
tt	$DY \rightarrow ll + jets$ HT 2500 to Inf	1.755
	$t\bar{t}$ inclusive	8.644×10^5

Table 8.5: List of simulated samples for $b\bar{b}\tau\tau$ channel.

one with the highest isolation is selected. Exactly zero veto muons are allowed;

- $\tau_h\tau_h$: exactly zero veto muons and electrons and at least two opposite charged τ_h candidates. If multiple pairs pass the selection, the highest- p_T one is selected.

For the $H \rightarrow b\bar{b}$ leg, b-jets are selected similarly to the $bb\gamma\gamma$ channel but requiring a medium b-tag working point.

Lepton	Min p_T [GeV]	Max $ \eta $	Max iso
Primary muon	23	2.1	0.15
Primary electron	27	2.1	0.10
Veto muon/electron	10	2.4	0.30

Table 8.6: Kinematic requirements for leptons.

The event yields after these selections are reported in Table 8.7.

Process	$\mu\tau_h$	$e\tau_h$	$\tau_h\tau_h$
$HH \rightarrow b\bar{b}\tau\tau \kappa_\lambda = 1$	101 ± 3	68 ± 2	58 ± 2
$HH \rightarrow b\bar{b}\tau\tau \kappa_\lambda = 2.45$	45 ± 2	43 ± 2	61 ± 3
$HH \rightarrow b\bar{b}\tau\tau \kappa_\lambda = 5$	371 ± 19	298 ± 17	374 ± 20
$ggH, H \rightarrow b\bar{b}$	899 ± 202	90 ± 64	0.0 ± 0.0
$ggH, H \rightarrow \tau\tau$	312 ± 63	262 ± 58	125 ± 40
$ttH, H \rightarrow b\bar{b}$	6499 ± 168	3420 ± 91	365 ± 134
$ttH, H \not\rightarrow b\bar{b}$	4725 ± 122	2840 ± 74	869 ± 25
$ZH, H \rightarrow b\bar{b}$	523 ± 18	188 ± 8	103 ± 6
$WH, H \rightarrow b\bar{b}$	642 ± 27	170 ± 11	14 ± 3
$VH, H \not\rightarrow b\bar{b}$	378 ± 66	229 ± 52	97 ± 40
tW	133035 ± 3944	80708 ± 2614	4633 ± 418
$tZq, Z \rightarrow ll$	626 ± 24	409 ± 18	116 ± 8
$W \rightarrow l\nu + jets$	0.0 ± 0.0	0.0 ± 0.0	0.0 ± 0.0
WW	2374 ± 323	1145 ± 222	42 ± 42
$ZZ \rightarrow llq\bar{q}$	1347 ± 84	877 ± 64	427 ± 44
$DY \rightarrow ll + jets$	38341 ± 1553	24055 ± 1141	11822 ± 717
$t\bar{t}$	3261832 ± 82589	1952133 ± 49842	91079 ± 3156.9

Table 8.7: Event yields for $bb\tau\tau$ channel.

Top-quark pair production, Drell-Yan and single Higgs processes, with their vastly greater production cross-sections, are the backgrounds that most contaminate the signal phase space making the $HH \rightarrow bb\tau\tau$ search challenging. For this reason, also in this case DNNs were exploited to discriminate the sig-

nal from the uninteresting processes. One network per final state has been trained, and the output score is used to categorize events into a low and high purity region. Left Fig. 8.6 shows an example of DNN score for the $\tau_h\tau_h$ final state. In order to include the missing energy information, the *stransverse mass* [301–303], M_{T2} , is used in the likelihood fit, instead of the simple visible mass distribution of the τ pair, taking advantage of its higher discriminating power. An example of this variable distribution is reported in right Fig. 8.6 for the low purity category of the $e\tau_h$ channel.

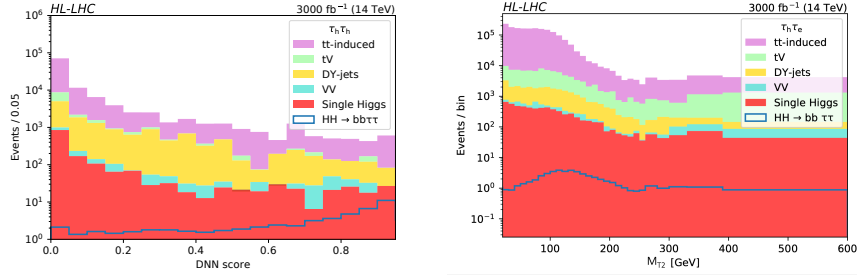


Figure 8.6: (Left) DNN score for the $\tau_h\tau_h$ final state. (Right) M_{T2} distribution in the low purity region for the $e\tau_h$ final state.

The systematic uncertainties considered for this channel are reported in Table 8.8 and are drawn from Ref. [300].

Systematic uncertainty source	Impact on yields
Luminosity	$\pm 1.0 \%$
Lepton ID efficiency	$\pm 1.0 \%$
Tau ID efficiency	$\pm 5.0\%$
Photon ID efficiency	$\pm 1.0 \%$
Jet Energy Scale	$\pm 1.0\%$
B-tag efficiency	$\pm 1.0\%$
QCD scale $t\bar{t}$ inclusive	$+2.4\% / -3.6\%$
PDF scale $t\bar{t}$ inclusive	$\pm 4.2\%$
Signal theoretical uncertainties	$+2.1\% / -4.9\%$ (QCD scale) $\pm 3.0\%$ (PDF scale) $+4.0\% / -18.0\%$ (top mass)

Table 8.8: Systematic uncertainties for $b\bar{b}\tau\tau$ channel.

$HH \rightarrow bbbb$

Despite the largest branching fraction among the HH decay channels, the $bbbb$ final state suffers from a large contamination from the multijet QCD background that makes it experimentally challenging. The list of simulated samples with related cross sections is shown in Table 8.9.

	Process	Cross section (fb)
Signal	$(gg)HH \rightarrow b\bar{b}b\bar{b} (\kappa_\lambda = 1)$	2.49×10^1
	$(gg)HH \rightarrow b\bar{b}b\bar{b} (\kappa_\lambda = 2.45)$	1.05×10^1
	$(gg)HH \rightarrow b\bar{b}b\bar{b} (\kappa_\lambda = 5)$	7.59×10^1
Single Higgs	$(gg)H \rightarrow b\bar{b}$	3.18×10^4
	$(gg)ZH, Z \rightarrow q\bar{q}, H \rightarrow b\bar{b}$	5.88×10^1
	$ZH, Z \rightarrow q\bar{q}, H \rightarrow b\bar{b}$	4.02×10^2
	$W^+H, W \rightarrow q\bar{q}', H \rightarrow b\bar{b}$	3.62×10^2
	$W^-H, W \rightarrow q\bar{q}', H \rightarrow b\bar{b}$	2.32×10^2
	$VBFH, H \rightarrow b\bar{b}$	2.49×10^3
QCD	HT 200 to 300	1.003×10^8
	HT 300 to 500	2.173×10^7
	HT 500 to 700	1.945×10^6
	HT 700 to 1000	3.806×10^5
	HT 1000 to 1500	6.881×10^4
	HT 1500 to 2000	6.053×10^3
	HT 2000 to Inf	1.087×10^3
$t\bar{t}$	$t\bar{t}$ inclusive	8.644×10^5

Table 8.9: List of simulated samples for $bbbb$ channel.

For this channel, four jets tagged as b-quark induced (medium tagger working point) are required in the final state with $p_T > 45 \text{ GeV}$ $|\eta| < 3.5$. The jets are paired in order to minimize the difference in the invariant mass of the Higgs candidates (see Fig. 8.7). The signal region is defined by considering the events that satisfy the following selection for the invariant mass of the two Higgs boson candidates H_1 and H_2 : $\sqrt{(m_{H_1} - 120 \text{ GeV})^2 + (m_{H_2} - 120 \text{ GeV})^2} < 40 \text{ GeV}$. The event yields after these selections are reported in Table 8.10.

In this case, the fitted distribution is the score of the network shown in Fig. 8.8, trained with relevant kinematic variables as the mass and transverse mo-

Process	Yields
$HH \rightarrow b\bar{b}b\bar{b} \kappa_\lambda = 1$	1376 ± 36
$HH \rightarrow b\bar{b}b\bar{b} \kappa_\lambda = 2.45$	2579 ± 79
$HH \rightarrow b\bar{b}b\bar{b} \kappa_\lambda = 5$	7438 ± 377
$ggH, H \rightarrow b\bar{b}$	1886 ± 310
$(gg)ZH, H \rightarrow b\bar{b}$	686 ± 19
$ZH, H \rightarrow b\bar{b}$	2106 ± 65
$WH, H \rightarrow b\bar{b}$	209 ± 12
$VBFH, H \rightarrow b\bar{b}$	319 ± 35
QCD	18168801 ± 773221
$t\bar{t}$	991631 ± 25819

Table 8.10: Event yields for $bbbb$ channel.

mentum of H_1 and H_2 , the separation between jets, the four-jet invariant mass, etc. The binning of the distribution is optimized to maximize the sensitivity to the SM HH signal and to ensure 5% statistical uncertainties in each bin of the distribution.

A complete list of the systematic uncertainties used for this channel and the expected impact on the event yields are reported in Table 8.11 and are drawn from Ref. [300].

Systematic uncertainty source	Impact on yields
Luminosity	$\pm 1.0 \%$
Jet Energy Scale	$\pm 1.0\%$
B-tag efficiency	$\pm 1.0\%$
QCD scale $t\bar{t}$ inclusive	$+2.4\% / -3.6\%$
PDF scale $t\bar{t}$ inclusive	$\pm 4.2\%$
Signal theoretical uncertainties	$+2.1\% / -4.9\%$ (QCD scale) $\pm 3.0\%$ (PDF scale) $+4.0\% / -18.0\%$ (top mass)

Table 8.11: Systematic uncertainties for $bbbb$ channel.

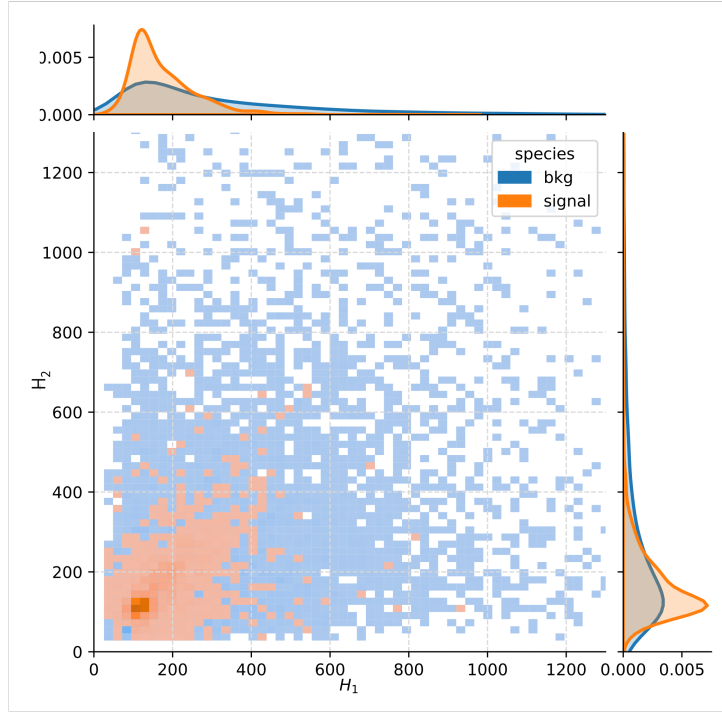


Figure 8.7: 2D distribution of H_1 mass versus H_2 mass in GeV. Correct jet pairing brings the event on the plot diagonal.

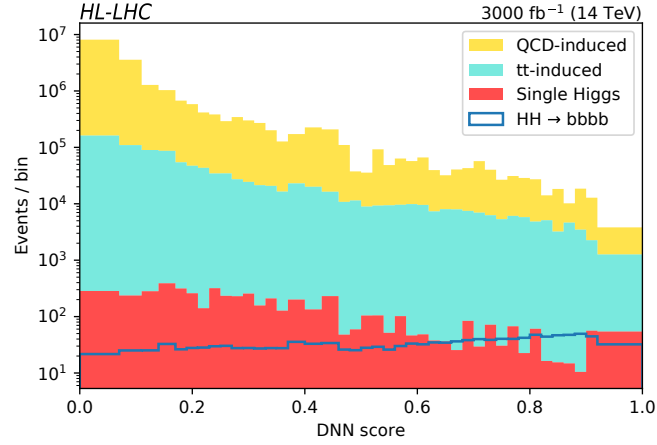


Figure 8.8: DNN score for the $bbbb$ channel.

Results

The results obtained in each of the three decay channels are combined together assuming the SM branching fractions for HH decays to the studied final states.

The analyses of the three decay channels are designed to be orthogonal thanks to the mutually exclusive object selection used for each channel. Systematic uncertainties on the theoretical assumptions or associated to the same object, such as b-tagging efficiency, are treated as correlated, while all the others are left uncorrelated. The upper limit on the signal strength for the HH combination is 0.76 corresponding to a significance of 2.80; these results are improved of about 10% with respect to the previous projections [304] (which included more channels) available at the time of this research. Results are summarized in Table 8.12.

Channel	Condition	Significance (in σ)	Upper limit on μ at 95% CL
$HH \rightarrow bb\gamma\gamma$	stat only	1.99	0.99
	stat + sys	1.94	1.09
$HH \rightarrow bb\tau\tau$	stat only	1.72	1.25
	stat + sys	1.70	1.37
$HH \rightarrow bbbb$	stat only	1.43	1.37
	stat + sys	1.06	2.00
Combination	stat + syst	2.80	0.76
	stat only	2.99	0.66

Table 8.12: Results for $bb\gamma\gamma$, $bb\tau\tau$ and $bbbb$ channels and their combination.

Assuming the presence of a HH signal with the properties predicted by the SM, prospects for the measurement of the κ_λ are given. The likelihood scans as a function of κ_λ for each channel and for the combination are shown in Fig. 8.9, where the dotted horizontal lines mark 1σ and 2σ levels. The narrowest likelihood, i.e. the highest sensitivity, is given by the $bb\gamma\gamma$ channel. For the combination, κ_λ is expected to be constrained in the range [0.47, 1.76] at 68% CL and [-0.02, 3.05] at 95% CL. The expected κ_λ confidence intervals for each channel and for the combination are summarized in Table 8.13.

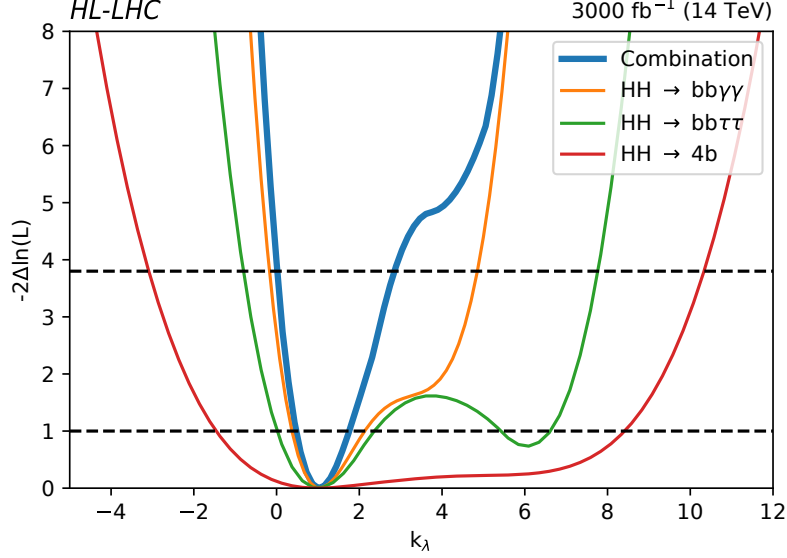


Figure 8.9: Expected likelihood scan as a function of κ_λ at HL-LHC. The curves are shown separately for the three studied decay channels and their combination.

	k_λ constraint at 68% CL	k_λ constraint at 95% CL
$HH \rightarrow bb\gamma\gamma$	[0.37, 2.13]	[-0.20, 4.9]
$HH \rightarrow bb\tau\tau$	[0.01, 2.35] & [5.41, 6.61]	[-0.84, 7.75]
$HH \rightarrow bbbb$	[-1.46, 8.41]	[-3.16, 10.41]
HH combination	[0.46, 1.73]	[-0.02, 3.05]

Table 8.13: k_λ constraint for $bb\gamma\gamma$, $bb\tau\tau$ and $bbbb$ channels and their combination.

8.1.2 Projections of Run 2 results to HL-LHC with simple scaling

The full Run 2 results presented in Ref. [6] are projected in this work to different integrated luminosity values, i.e. 300 (expected by the end of Run 3), 1000, 2000, and 3000 fb^{-1} to track the evolution during the data taking. In this study, only the $b\bar{b}\gamma\gamma$, $b\bar{b}\tau\tau$, $b\bar{b}b\bar{b}$, multilepton, and $b\bar{b}WW$ channels are included as they are the ones with the greatest sensitivity. The procedure for the statistical combination is the same as the one carried out for Run 2 [6] and the HH Inference Tool [305] is used.

The extrapolation of the Run 2 results to HL-LHC follows the same recipe used in previous projections of Higgs boson searches and measurements [304].

For the projections to a certain integrated luminosity L , the Run 2 signal and background yields, as well as the selected data events, are scaled up by a factor $k_L = L/L_{Run2}$ equal to the increase of integrated luminosity with respect to Run 2. The scaling of the data events is necessary for those analyses that rely on the data to properly model the backgrounds in the fit. The efficiency of the physics object reconstruction and identification is assumed to be the same as in Run 2. The same assumption is made regarding the experimental energy or momentum resolution of the physics objects. This is based on the premise that the upgraded CMS detector will ensure performance comparable to Run 2 despite the larger pileup and radiation damage to the detector components.

The exact level of systematic uncertainties in CMS during HL-LHC is unknown. Therefore, the projections are derived in three different scenarios of systematic uncertainties:

- *S1*: The systematic uncertainties are assumed to be at the same level of Run 2.
- *S2*: The systematic uncertainties with a statistical origin, e.g. statistical uncertainties in data/MC scale factors, are reduced by a factor $\sqrt{k_L}$, until “floor” values are reached. The “floor” values prevent uncertainties from becoming unreasonably small and are based on studies in Ref. [304]. The theoretical uncertainties in the signal and background cross sections are halved to account for the expected progress in the theory calculations throughout the next years. The uncertainties originating from the limited size of the MC samples are removed under the assumption of very large MC data sets.
- *stat. only*: No systematic uncertainties are considered in the fit.

It should be noted that the systematic uncertainties related to specific issues encountered in Run 2 have been removed from all three scenarios, including *S1*. The nominal scenario for the HL-LHC conditions is *S2*.

The treatment of the uncertainties common to multiple analysis channels is summarized in Table 8.14. The analysis-specific uncertainties are treated case by case. For example, for the $bbbb$ channel that I studied, the leading systematic is the uncertainty related to QCD estimation with data driven method. The uncertainty on the data driven background normalization is rescaled according to gain in integrated luminosity ($1/\sqrt{k_L}$). The shape uncertainty is modified

Uncertainty	Scaling with respect to Run 2
Theory uncertainties	$1/2$
Stat. uncertainties in MC simulation	Removed
b-tag efficiency stat. component	$1/\sqrt{k_L}$
b-tag efficiency (non stat. component)	Unchanged
AK4 jet scale absolute	$\max(0.3, 1/\sqrt{k_L})$
AK4 jet scale flavor	$\max(0.5, 1/\sqrt{k_L})$
AK4 jet scale relative	$\max(0.2, 1/\sqrt{k_L})$
AK4 jet scale method	$1/\sqrt{k_L}$
AK4 jet energy resolution	$\max(0.5, 1/\sqrt{k_L})$
\vec{p}_T^{miss}	$\max(0.5, 1/\sqrt{k_L})$
Luminosity	0.6
τ_h ID	Unchanged
τ_h Energy scale	Unchanged
Pileup	Unchanged
Run 2 issues	Removed

Table 8.14: Treatment of most important common systematic uncertainties in the S2 scenario.

such that the difference between the up and down variations and the nominal distribution is reduced by the same factor.

The projected upper limits on the HH signal strength in the $bbbb$ channel at different integrated luminosities are shown in the left panel of Fig. 8.10 for the resolved topology and in Fig. 8.11 for the boosted one. The upper limits reach a level close to unity for an integrated luminosity of 3000 fb^{-1} for the boosted topology that performs almost 3 times better than the resolved one. The expected improvement of the upper limits with more data is worse than the naive scaling by the square root of the integrated luminosity, given that the channel is systematically limited. Projections at 3000 fb^{-1} under different scenarios of systematic uncertainties are shown in the right panel of Fig. 8.10 and Fig. 8.11. The difference between the S1/S2 scenarios and the one assuming only the statistical uncertainties is considerable especially for the resolved category. It is interesting to notice that the stat. only upper limit for the resolved category is in very good agreement with the equivalent analysis result with fast simulation reported in the previous section in Table 8.12.

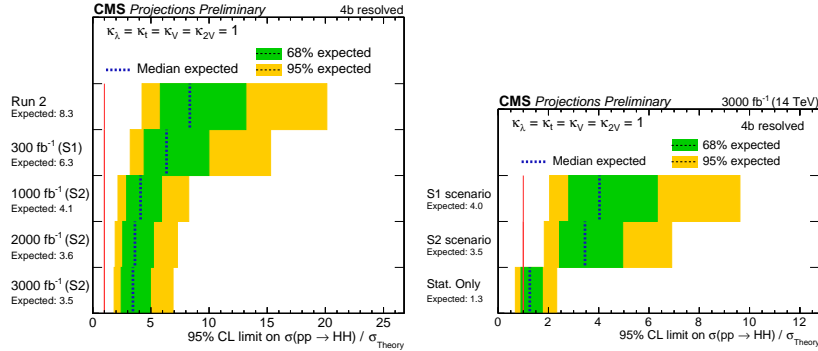


Figure 8.10: Expected upper limits on the HH signal strength from the resolved $b\bar{b}b\bar{b}$ channel at different integrated luminosities (left), and under different assumptions on the systematic uncertainties for an integrated luminosity of 3000 fb^{-1} (right).

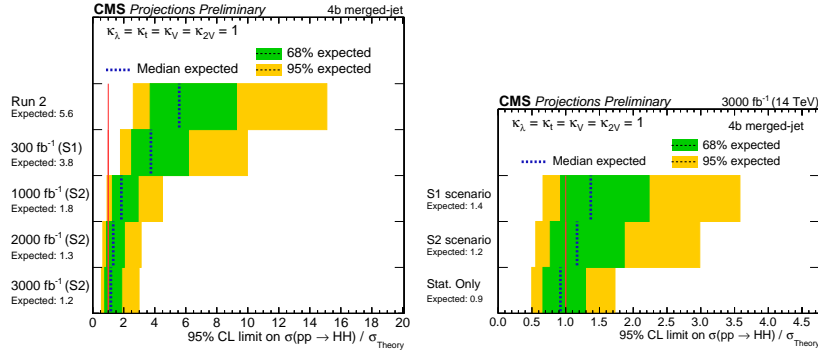


Figure 8.11: Expected upper limits on the HH signal strength from the boosted $b\bar{b}b\bar{b}$ channel at different integrated luminosities (left), and under different assumptions on the systematic uncertainties for an integrated luminosity of 3000 fb^{-1} (right).

The projected upper limits on the HH signal strength for the statistical combination of all the considered HH channels at different integrated luminosities are shown in the left panel of Fig. 8.12. Assuming SM values for HH production, we will become sensitive to excesses in HH inclusive cross section for integrated luminosities larger than 1000 fb^{-1} , when the expected upper limit drops below one. The projections at 3000 fb^{-1} under the different systematic uncertainty scenarios are shown in the right panel of Fig. 8.12.

The projected κ_λ likelihood scans are shown in Fig. 8.13. In the S2 scenario, the expected 1σ uncertainty on κ_λ is $+80\%/-60\%$ and $+60\%/-50\%$ for an integrated luminosity of 2000 and 3000 fb^{-1} , respectively.

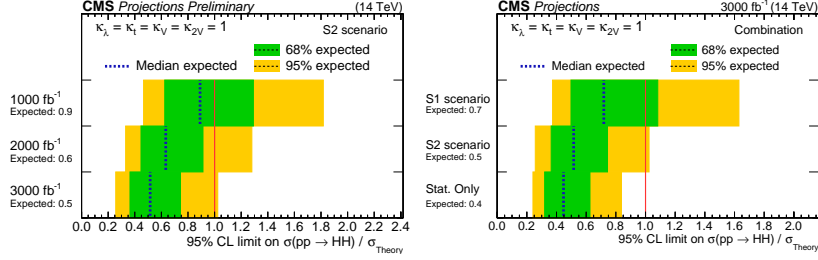


Figure 8.12: Expected upper limits on the HH signal strength from the combination of all the considered channels at different integrated luminosities (left), and under different assumptions on the systematic uncertainties for an integrated luminosity of 3000 fb^{-1} (right).

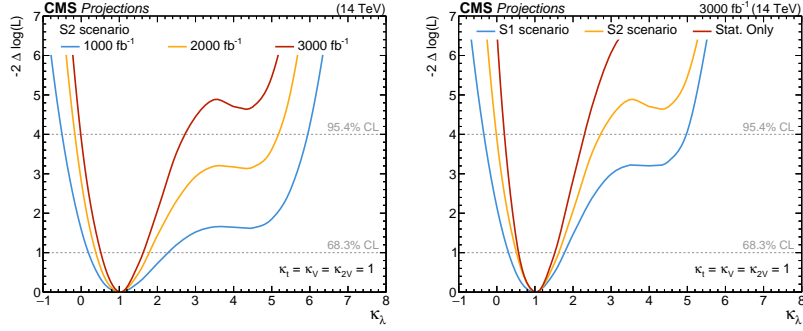


Figure 8.13: Expected κ_λ likelihood scan from the combination of all the considered channels projected at different integrated luminosities (left), and under different assumptions on the systematic uncertainties for an integrated luminosity of 3000 fb^{-1} (right).

The breakdown into channel contribution is reported in Fig. 8.14.

The expected significance for the HH signal strength assuming SM values for all parameters is summarized in Table 8.15.

CMS will observe evidence for HH production by the end of HL-LHC, with significance 3.2σ for 2000 fb^{-1} at the nominal systematic uncertainty scenario and assuming that the signal will be SM-like. Figure 8.15 on the left shows the significance that can be achieved for the SM signal as a function of the integrated luminosity. On the right, the significance is shown as a function of κ_λ . The sensitivity to the HH signal varies with κ_λ due to the effects of the interference between the box and triangle diagrams. The two diagrams have different kinematic properties, therefore, the interference varies not only the HH cross section but the HH signal acceptance rate as well. For $\kappa_\lambda < 1$ and

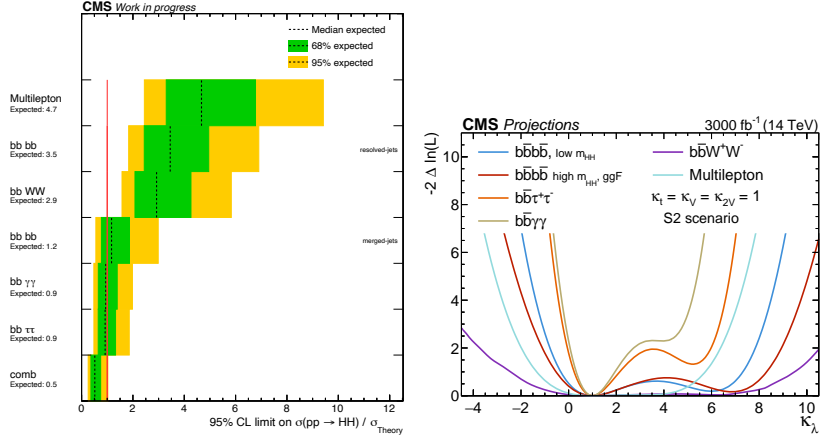


Figure 8.14: Expected upper limits on the HH signal strength (left) and κ_λ likelihood scan (right) from all the considered channels and their combination projected at 3000 fb^{-1} for the nominal scenario.

	Significance (σ) at 2000 fb^{-1}		Significance (σ) at 3000 fb^{-1}	
	S2	Stat. only	S2	Stat. only
$bb\bar{b}\bar{b}$ resolved	1.0	1.3	1.4	1.6
$bb\bar{b}\bar{b}$ merged	1.7	1.7	2.0	2.1
$bb\bar{b}\bar{b}\tau\tau$	1.7	1.9	2.1	2.3
$bb\bar{b}\bar{b}WW$	0.6	0.8	0.7	0.9
multilepton	0.4	0.6	0.4	0.7
$bb\bar{b}\bar{b}\gamma\gamma$	1.8	1.9	2.2	2.3
Combination	3.2	3.6	3.8	4.3

Table 8.15: Expected significance for the HH signal projected to 2000 or 3000 fb^{-1} under different assumptions of systematic uncertainties.

$\kappa_\lambda > 5$, we would be able to observe evidence sooner. For $1 < \kappa_\lambda < 5$ the HH signal is suppressed, and the significance will be lower than expected, with minimum significance at $\kappa_\lambda = 3.4$. The projections presented here do not take into account potential improvements in triggering [306, 307], object reconstruction and selection such as b -tagging and τ_h identification, or analysis techniques. Historically, advancements in software and analysis methods have allowed us to exceed expectations, therefore the projections shown in this work are most likely conservative.

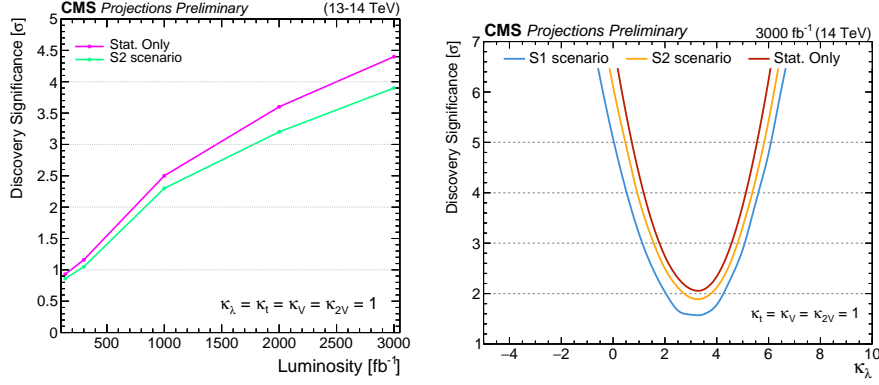


Figure 8.15: Expected signal significance as a function of integrated luminosity (left). The green curve shows the significance using the same scheme for systematic uncertainties as the nominal Run 2 result for 138 and 300 fb^{-1} . The subsequent points use the S2 scenario for systematics. The magenta curve shows the significance for statistical uncertainties only. Expected signal significance as a function of κ_λ under different assumptions on the systematic uncertainties for an integrated luminosity of 3000 fb^{-1} (right).

8.2 Projections of HH searches to FCC-hh with fast simulation

This work focuses exclusively on the HH search in the $bb\gamma\gamma$ final state, exploring both resonant and non-resonant topologies.

In the non-resonant scenario—aligned with the HL-LHC studies discussed in previous sections—the primary goal is to probe the Higgs boson self-coupling. With the anticipated dataset of 30 ab^{-1} expected to be collected during the FCC-hh operation, the self-coupling parameter could potentially be measured with percent-level precision. Previous projections for the self-coupling modifier κ_λ at 100 TeV were presented in Ref. [308], where three final states ($bb\gamma\gamma$, $bb\tau\tau$, and $bbbb$) were analyzed. These studies projected a sensitivity to κ_λ in the range of 3.4% to 7.8%, depending on detector performance and systematic uncertainties, with the $bb\gamma\gamma$ channel providing the dominant contribution.

The resonant analysis is conducted for the first time at FCC-hh within this work, and its results can be directly compared with those from analogous HL-LHC studies, such as Ref. [202]. This search is interpreted in the context of an extended Higgs sector and is used to constrain its parameters.

Both the non-resonant and resonant analyses presented here were submitted as contributions to the Update of the European Strategy for Particle Physics, and are documented in Refs. [8, 9].

8.2.1 Non-resonant analysis

In the present study, we investigate the expected precision measurement on κ_λ and on the signal strength $\mu = \sigma/\sigma_{SM}$, exploiting the most sensitive final state, $bb\gamma\gamma$, using a more sophisticated analysis strategy with respect to previous studies. The explored center-of-mass energy hypotheses are 84, 100 and 120 TeV [201], while the detector is the nominal one for FCC-hh, as described in the conceptual design report [182, 309]. The expected integrated luminosity corresponds to 30 ab^{-1} for 84 and 100 TeV, and to 12 ab^{-1} for 120 TeV. The results are also presented for different di-jet invariant mass resolution assumptions and different systematic uncertainty scenarios.

Event Generation

The studies reported here rely on simulated event samples generated by the MADGRAPH5_AMC@NLO, POWHEG 2.0 and PYTHIA 8.2 Monte Carlo programs, and processed through the fast detector simulation package DELPHES. The baseline detector concept used for the FCC-hh physics studies is described in Ref. [182, 309] and its DELPHES parameterization in Ref. [206]. The event samples have been produced with the KEY4HEP framework [310, 311]. The complete list of generated samples can be found in Ref. [312].

Di-Higgs production signal samples for the SM and BSM hypotheses with different values (1, 2.45, and 3) of κ_λ are simulated to study the expected precision. Only gluon fusion HH production is considered here. Including the $t\bar{t}HH$, VHH and $VBF\text{-}HH$ production has the potential to further improve the expected precision estimated with this study. The backgrounds considered for the study can be divided into two groups: resonant processes, where a single Higgs boson decays to photons, and non-resonant processes, where no physical Higgs bosons are produced. The main resonant background sources are the single-Higgs processes produced via gluon fusion and in associated production with top pairs. The non-resonant background consists of QCD events containing two isolated, energetic photons. The Table 8.16 reports the simulated processes with related cross-section and k-factor values.

Process	Cross-section \times BR [fb]			k-factor
	84 TeV	100 TeV	120 TeV	
<u>Signals</u>				
$ggHH$, $\kappa_\lambda = 1$	2.33	2.98	3.91	1.08
$ggHH$, $\kappa_\lambda = 2.4$	1.03	1.29	1.75	1.08
$ggHH$, $\kappa_\lambda = 3$	1.22	1.55	2.04	1.08
<u>Backgrounds</u>				
<i>Single-Higgs</i>				
ggH	1057	1334	1699	3.76
$VBFH$	153	191	239	4.3
ttH	74	102	140	1.22
VH	69	85	105	1.32
<i>Non-resonant di-photon</i>				
$\gamma\gamma jj$	14340	17970	22440	1.2

Table 8.16: Overview of signal and background samples with their cross sections at 84, 100 and 120 TeV.

Analysis Strategy

The analysis strategy consists of kinematic selections to identify the Higgs boson candidates, implementation of multivariate classifiers to improve the signal-to-background ratio, event categorization, and extraction of results from the di-photon invariant mass fit in bins of the di-jet mass.

Jets are reconstructed using the anti- k_T algorithm with a size radius of 0.4 [313]. Jets are selected to have a minimum p_T of 30 GeV, a maximum $|\eta|$ of 4 and to pass the medium b-tagging working point defined by the efficiencies reported in Table 4.8 in Sec. 4.2.3. The two highest- p_T jets are chosen to build the $H \rightarrow bb$ candidate. Photons are required to have, as well, $p_T > 30$ GeV and $|\eta| < 4$. The two highest- p_T photons are chosen to build the $H \rightarrow \gamma\gamma$ candidate. The invariant mass of the jet pair is required to be in the range [80,150] GeV, while the di-photon invariant mass in the [115,135] GeV one.

Figure 8.16 shows the di-photon and di-jet mass distributions after the baseline selection for the di-Higgs production process (both SM and BSM) and the backgrounds, at 84 TeV. The di-jet mass distribution corresponds to the nominal DELPHES one, without any mass regression. In the improved scenarios, we hypothesize a gaussian-like shape for the di-jet mass with 125 GeV mean

and resolution of 10 GeV, 5 GeV and, in the most ambitious case, of 3 GeV. In these scenarios, a cut $[100,150]$ GeV is applied on the di-jet mass.

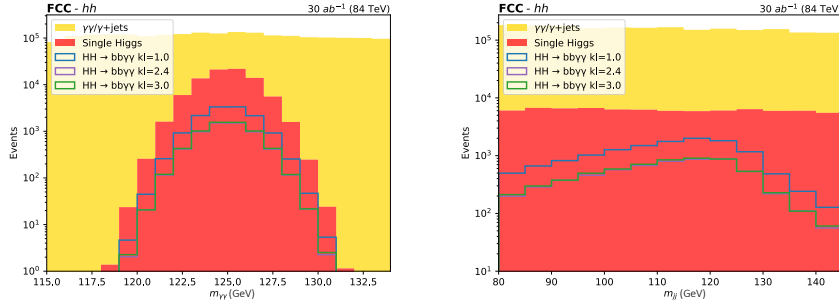


Figure 8.16: Di-photon (left) and di-jet (right) invariant mass in GeV after the baseline selection.

After the baseline selection, a DNN is trained to discriminate the signal (both SM and BSM) against the backgrounds. Several kinematic and angular variables are used in the training, exploiting the peculiar topology of the di-Higgs production with respect to the single-Higgs events and the non-resonant background. The input features are described in Ref. [8].

The DNN score is used to define three purity regions. The low-purity region is simply discarded, whereas the medium- and high-purity regions become two separate categories. The exact values of the cuts are chosen through an optimization procedure aiming to maximize the significance S/\sqrt{B} .

Tables 8.17, 8.18 and 8.19 report the yields after the baseline selection and the DNN cut (low-purity region removal) with relative efficiencies, for the investigated center-of-mass energies. For this study we assumed, very conservatively, a total non-resonant background which is twice the simulated $\gamma\gamma jj$ process, to account for QCD events where only one photon is produced (γ +jets). The background with highest pre-selection efficiency is the ttH process, which contains two real b-jets. Nonetheless, the DNN efficiently separates the ttH process from the di-Higgs production; as a result, the selected DNN cut reduces this background by $\simeq 50\%$, while having minimal impact on the signal.

Another categorization is based on the corrected di-Higgs invariant mass (visible in left Fig. 8.17), $m_X = m_{\gamma\gamma jj} - m_{\gamma\gamma} - m_{jj} + 250\text{GeV}$, and separates

Process (84 TeV, 30 ab^{-1})	Pre-Sel.	Eff.	DNN	Rel.Eff.	Tot. Eff.
$ggHH$, $\kappa_\lambda = 1$	13469	17.89%	11695	86.83%	15.53%
$ggHH$, $\kappa_\lambda = 2.4$	6068	18.31%	54276	89.44%	16.37%
$ggHH$, $\kappa_\lambda = 3$	6288	15.92%	5735	91.21%	14.52%
single-Higgs, ggH	19986	0.04%	12782	63.95%	0.03%
single-Higgs, $VBFH$	4199	0.11%	2558	60.92%	0.07%
single-Higgs, ttH	58070	3.45%	29441	50.70%	1.75%
single-Higgs, VH	3594	0.24%	3221	89.62%	0.21%
Non-res ($\gamma\gamma jj \times 2$)	2130008	0.21%	415448	66.45%	0.14%

Table 8.17: Yields table with selection efficiencies at 84 TeV, considering 30 ab^{-1} of integrated luminosity.

Process (100 TeV, 30 ab^{-1})	Pre-Sel.	Eff.	DNN	Rel.Eff.	Tot. Eff.
$ggHH$, $\kappa_\lambda = 1$	16928	17.58%	14163	83.67%	14.71%
$ggHH$, $\kappa_\lambda = 2.4$	7473	18.00%	6574	87.98%	15.84%
$ggHH$, $\kappa_\lambda = 3$	7777	15.58%	6968	89.60%	13.96%
single-Higgs, ggH	23253	0.04%	11732	50.45%	0.02%
single-Higgs, $VBFH$	5396	0.12%	2266	42.00%	0.05%
single-Higgs, ttH	76460	3.35%	38000	49.70%	1.66%
single-Higgs, VH	4361	0.24%	3748	85.94%	0.20%
Non-res ($\gamma\gamma jj \times 2$)	2703137	0.21%	1356627	50.19%	0.10%

Table 8.18: Yields table with selection efficiencies at 100 TeV, considering 30 ab^{-1} of integrated luminosity.

the region where the SM dominates ($m_X > 350$ GeV) from the one where BSM signals have higher contribution ($m_X < 350$ GeV).

The high- m_X category is the one driving the sensitivity for the SM assumption. Right Fig. 8.17 shows the DNN score with the cut chosen to define the medium- and high-purity regions in this high- m_X category, while Fig. 8.18 presents the di-photon distributions in the two purity regions for this category. The yields per category can be found in Ref. [8].

To extract the final results, a maximum likelihood fit is performed on the di-photon invariant mass distribution in few bins of the di-jet mass. The binning in di-jet mass changes with the di-jet mass resolution assumption and is chosen as

Process (120 TeV, 12 ab^{-1})	Pre-Sel.	Eff.	DNN	Rel.Eff.	Tot. Eff.
$ggHH$, $\kappa_\lambda = 1$	8679	17.19%	7064	81.39%	13.99%
$ggHH$, $\kappa_\lambda = 2.4$	4055	17.96%	3467	85.49%	15.35%
$ggHH$, $\kappa_\lambda = 3$	4075	15.47%	3547	87.06%	13.47%
single-Higgs, ggH	13385	0.05%	8010	59.84%	0.03%
single-Higgs, $VBFH$	2896	0.12%	1582	54.64%	0.07%
single-Higgs, ttH	40634	3.28%	17589	43.29%	1.42%
single-Higgs, VH	2145	0.24%	1846	86.06%	0.21%
Non-res ($\gamma\gamma jj \times 2$)	1390237	0.22%	834314	60.01%	0.13%

Table 8.19: Yields table with selection efficiencies at 120 TeV, considering 12 ab^{-1} of integrated luminosity.

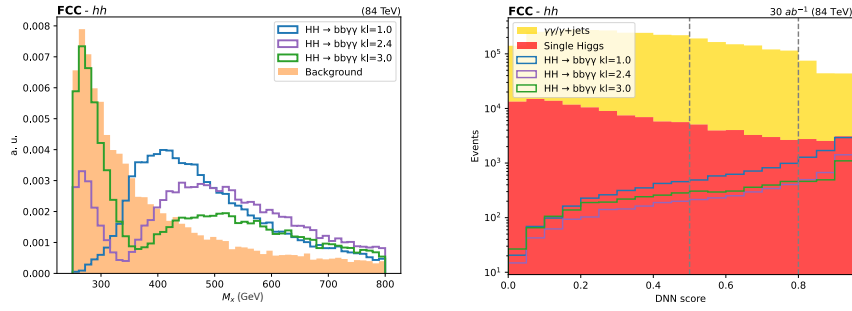


Figure 8.17: m_X distribution in GeV (left) and DNN score (right) with chosen cuts for the high- m_X category.

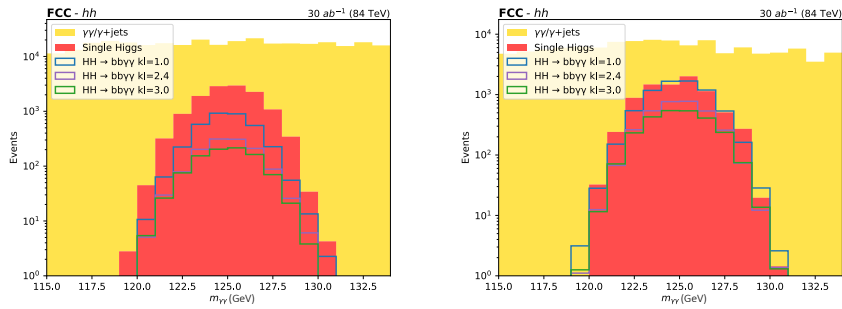


Figure 8.18: Di-photon invariant mass in GeV in the medium (left) and high (right) purity regions, in the high- m_X category.

a tradeoff between high sensitivity and reasonable number of simulated events in each bin. It is important to highlight that the sensitivity to different di-jet mass resolution hypotheses is highly dependent on this binning choice. In the future, a larger number of simulated events will enable finer binning and further improvements in the results.

Figure 8.19 shows the selected binning for the nominal DELPHES scenario and the 10 GeV resolution one, in the high-purity high- m_X category. As example, Fig. 8.20 displays the final observable in the most sensitive di-jet mass bins for the nominal scenario. In this scenario, a total of 16 regions are used to extract the final results, considering two m_X categories, two purity categories and four di-jet mass bins.

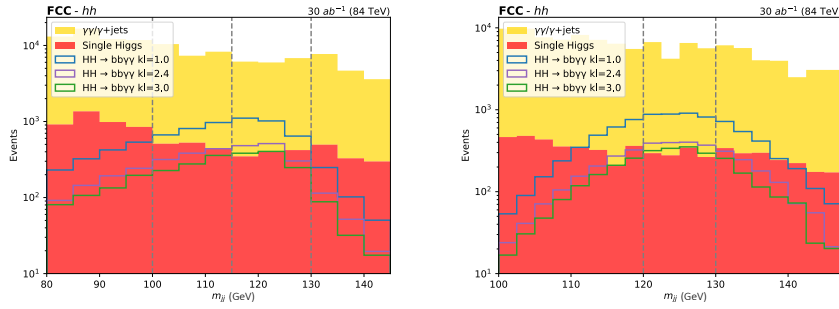


Figure 8.19: Di-jet mass distribution in GeV with chosen binning in the nominal (left) and gaussian 10 GeV scenario (right), for the high-purity, high- m_X category.

Results

The determination of the Higgs self-coupling modifier κ_λ is performed for three different benchmarks of systematic uncertainties, as listed in Table 8.20. These benchmarks have different instrumental uncertainties assumptions, while sharing the same background normalization uncertainty treatment. The non-resonant background is estimated from the sidebands of the $m_{\gamma\gamma}$, m_{bb} spectrum, hence its normalization is left free to float within 5% and is effectively constrained in the fit to 1%. For the single-Higgs background, although possibly estimated from data in the future, no dedicated control regions are defined here, therefore it is considered as derived from simulation. A normalization uncertainty of 1% is assigned to each single-Higgs process. In this study, no

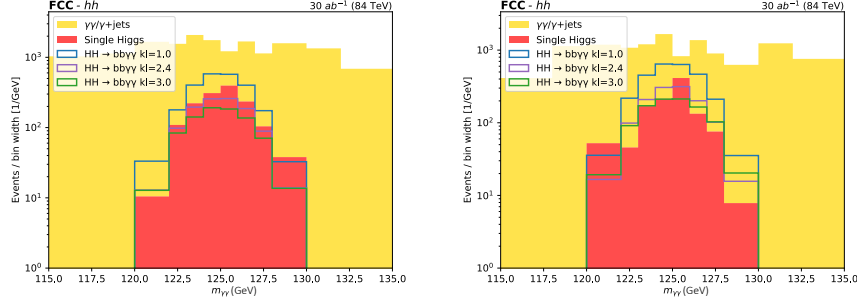


Figure 8.20: Di-photon mass distribution in GeV in the most sensitive di-jet mass bins for the nominal DELPHES scenario: $[100 - 115]$ GeV (left) and $[115 - 130]$ GeV (right). Plots refers to high-purity, high- m_X category.

hypothesis on the theoretical uncertainty of signal cross section is made, due to the difficulty of justifying a reasonable value. The systematics assumptions in scenario 3 are very conservative, and they get constrained in the fit.

Source of uncertainty	Value			Type	Applies to
	Syst. 1	Syst. 2	Syst. 3		
b-jet ID / b-jet	0.5%	1%	2%	lnN	Signal, single-Higgs
Photon ID / photon	0.5%	1%	2%	lnN	Signal, single-Higgs
Luminosity	0.5%	1%	2%	lnN	Signal, single-Higgs
single-Higgs norm.	1%	1%	1%	lnN	single-Higgs
data driven bkg	5%	5%	5%	lnU	Non-resonant bkg

Table 8.20: Overview of the systematic uncertainties scenarios.

With these systematic uncertainty benchmarks, the expected precision on κ_λ and μ is extracted from a simultaneous binned likelihood fit of the di-photon distribution in all the categories and bins described in the previous section.

The same parametrization of the di-Higgs production cross-section as a function of κ_λ as in Eq. 8.1 is exploited to extract the final results. It has the functional form of a parabola, with a minimum at $\kappa_\lambda=2.45$, which corresponds to maximum interference between the box and triangle diagram contributions. To accurately determine the shape of the parabola, a fit is performed using four different κ_λ values. Additionally, to account for the varying acceptance of the different κ_λ samples, the fit is conducted using the baseline selection yields.

All the produced results are summarized in Tables 8.21, 8.22 and 8.23 for 84, 100 and 120 TeV, respectively. The expected likelihood scans are shown in Fig. 8.21 at 84 TeV for the nominal di-jet mass resolution.

84 TeV (30 ab ⁻¹), κ_λ precision (%)	Stat. Only	Syst. 1	Syst. 2	Syst. 3
Nominal m_{jj} resolution	3.5%	4.6%	5.2%	5.4%
Gaussian m_{jj} , 10 GeV resolution	3.2%	4.3%	5.0%	5.4%
Gaussian m_{jj} , 5 GeV resolution	2.7%	3.7%	4.3%	4.6%
Gaussian m_{jj} , 3 GeV resolution	2.4%	3.2%	3.7%	3.9%
84 TeV (30 ab ⁻¹), μ precision (%)	Stat. Only	Syst. 1	Syst. 2	Syst. 3
Nominal m_{jj} resolution	2.5%	3.3%	3.7%	3.9%
Gaussian m_{jj} , 10 GeV resolution	2.3%	3.1%	3.6%	3.8%
Gaussian m_{jj} , 5 GeV resolution	1.9%	2.6%	3.0%	3.2%
Gaussian m_{jj} , 3 GeV resolution	1.7%	2.3%	2.6%	2.8%

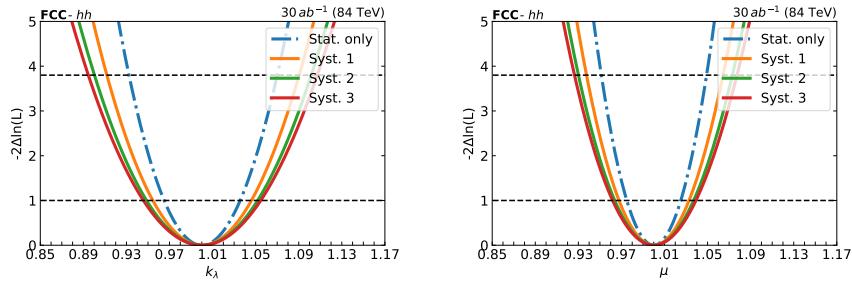
Table 8.21: Expected precision on κ_λ and $\mu = \sigma/\sigma_{SM}$ at 84 TeV.

100 TeV (30 ab ⁻¹), κ_λ precision (%)	Stat. Only	Syst. 1	Syst. 2	Syst. 3
Nominal m_{jj} resolution	2.8%	4.0%	4.6%	4.8%
Gaussian m_{jj} , 10 GeV resolution	2.4%	3.5%	4.1%	4.4%
Gaussian m_{jj} , 5 GeV resolution	2.2%	3.1%	3.6%	3.9%
Gaussian m_{jj} , 3 GeV resolution	1.9 %	2.8%	3.2%	3.4%
100 TeV (30 ab ⁻¹), μ precision (%)	Stat. Only	Syst. 1	Syst. 2	Syst. 3
Nominal m_{jj} resolution	2.0%	2.8%	3.2%	3.4%
Gaussian m_{jj} , 10 GeV resolution	1.7%	2.5%	2.9%	3.1%
Gaussian m_{jj} , 5 GeV resolution	1.5%	2.2%	2.6%	2.8%
Gaussian m_{jj} , 3 GeV resolution	1.4%	2.0%	2.3%	2.4%

Table 8.22: Expected precision on κ_λ and $\mu = \sigma/\sigma_{SM}$ at 100 TeV.

At 68% confidence level, the expected precision on κ_λ ranges from 3.2% to 5.4% at 84 TeV, from 2.8% to 4.8% at 100 TeV and from 3.2% to 6.2% at 120 TeV, depending on the di-jet mass resolution and systematic assumptions. The expected precision on μ , instead, ranges from 2.3% to 3.9% at 84 TeV,

120 TeV (12 ab^{-1}), κ_λ precision (%)	Stat. Only	Syst. 1	Syst. 2	Syst. 3
Nominal m_{jj} resolution	4.0%	4.6%	5.3%	6.2%
Gaussian m_{jj} , 10 GeV resolution	3.8%	4.4%	5.1%	6.0%
Gaussian m_{jj} , 5 GeV resolution	3.3%	3.8%	4.4%	5.1%
Gaussian m_{jj} , 3 GeV resolution	2.8%	3.2%	3.8%	4.4%
120 TeV (12 ab^{-1}), μ precision (%)	Stat. Only	Syst. 1	Syst. 2	Syst. 3
Nominal m_{jj} resolution	2.9%	3.3%	3.8%	4.4%
Gaussian m_{jj} , 10 GeV resolution	2.7%	3.1%	3.6%	4.3%
Gaussian m_{jj} , 5 GeV resolution	2.3%	2.7%	3.1%	3.6%
Gaussian m_{jj} , 3 GeV resolution	2.0%	2.3%	2.7%	3.1%

Table 8.23: Expected precision on κ_λ and $\mu = \sigma/\sigma_{SM}$ at 120 TeV.**Figure 8.21:** Expected likelihood scans as a function of κ_λ (left) and μ (right) for different systematic uncertainty scenarios.

from 2.0% to 3.4% at 100 TeV and from 2.3% to 4.4% at 120 TeV. The 100 TeV machine provides the highest sensitivity, while the 84 TeV and 120 TeV scenarios yield comparable results, as the sensitivity gain from increasing the energy to 120 TeV is offset by the expected reduction in integrated luminosity.

Figure 8.22 illustrates how the expected precision on κ_λ modifies as a function of center-of-mass energy and di-jet mass resolution. It can be inferred that, for instance, a 84 TeV machine with a 5 GeV resolution on di-jet mass would yield results competitive with those of a 100 TeV machine in the nominal scenario.

The study demonstrates the critical role of di-jet mass resolution in enhancing the κ_λ precision to the few-percent level, highlighting that its impact can be as significant as increasing the center-of-mass energy. Finally, it should

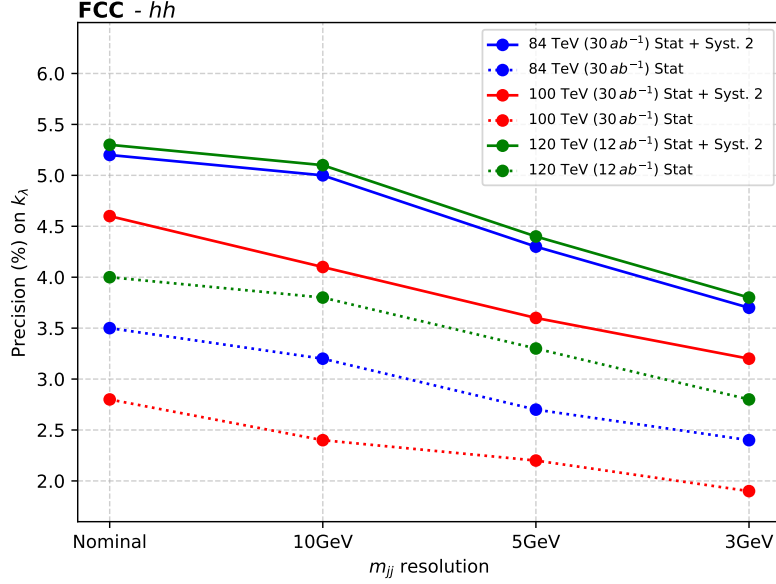


Figure 8.22: Expected precision on κ_λ in the systematic scenario 2, as a function of the m_{jj} resolution and the center of mass energy.

be noted that, although $bb\gamma\gamma$ is the leading channel, a proper combination with other di-Higgs channels, most importantly $bb\tau\tau$ and $bbbb$, is essential to achieve the best possible results, with the aim of reaching the 1% precision target. Moreover, only gluon fusion HH production was considered in this study. Including the $t\bar{t}HH$, VHH and $VBF\text{-}HH$ production, and designing specific event categories that enhance their contributions has the potential to further improve the expected precision presented here. Another potential improvement could possibly come from exploiting the impact of self-coupling information propagated to differential distributions, such as m_{hh} or via a dedicated MVA discriminator [314].

8.2.2 Resonant analysis

For the resonant interpretation of the $HH \rightarrow b\bar{b}\gamma\gamma$ analysis, we search for a heavy neutral scalar resonance, X , with mass in the range 300–1000 GeV, decaying into a pair of SM Higgs bosons. The signal is generated at LO using MADGRAPH5, considering only gluon fusion as the production mechanism and under the narrow width approximation. Simulated mass points span the

range from 300 to 1000 GeV in steps of 100 GeV. The event selection setup is identical to that used in the non-resonant analysis, including the same object reconstruction and identification criteria.

In addition to requiring both the di-jet and di-photon invariant masses to be consistent with the Higgs boson mass, we apply a selection on the four-body invariant mass $m_{bb\gamma\gamma}$ (see left Fig. 8.23), using a mass-dependent window: $[0.7 m_X, 1.3 m_X]$. In this study, only the dominant background from the $\gamma\gamma$ +jets (and γ +jets) process is considered; contributions from single Higgs production are neglected due to the focus on the high-mass region.

A single DNN is trained to distinguish all signal mass hypotheses from the non-resonant di-photon background. A threshold on the DNN score is applied to enhance the signal region purity. This step could be further optimized by training a parametric DNN to maintain uniform performance across different mass points. The resulting signal efficiencies, which include both the baseline event selection and the DNN-based selection, are shown as a function of the resonance mass in the right panel of Fig. 8.23.

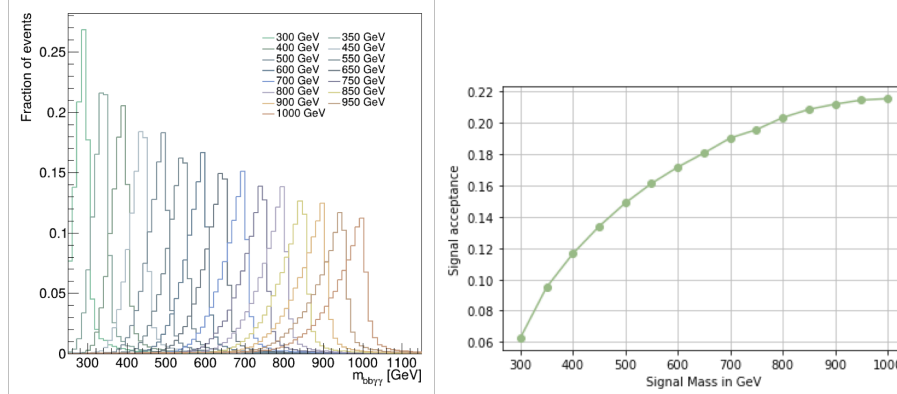


Figure 8.23: (Left) Reconstructed invariant mass of the four objects in the final state for the signal simulated with different mass values in the range 300-1000 TeV. (Right) Signal efficiency as a function of the simulated mass, including both baseline event selection and cut on the DNN score.

Model-independent 95% CL upper limits on the cross section of the process $pp \rightarrow X \rightarrow HH$ are obtained by fitting the invariant mass distribution $m_{bb\gamma\gamma}$ for the different resonance mass hypotheses. The results are presented in the left panel of Fig. 8.24, and can be directly compared to the latest HL-LHC projections shown in the right panel, taken from Ref. [202]. The expected

model-independent upper limits at FCC-hh are generally higher than those at the HL-LHC due to the significantly higher center-of-mass energy, which leads to increased background rates. However, this same energy enhancement also boosts the signal cross section (e.g. depicted by the blue and red curves in the HL-LHC plot), resulting in stronger overall sensitivity to specific models—such as the simple singlet extension of the Higgs sector discussed in Ref. [202]. This improvement is clearly illustrated in Fig. 8.25, which shows the exclusion bounds for the singlet scalar model in the parameter space of the scalar portal coupling a_2 versus the mixing angle θ , comparing FCC-hh (left) to HL-LHC (right). Notably, FCC-hh is expected to exclude the entire region of parameter space relevant for a strong first-order electroweak phase transition (SFOPT)—something that remains out of reach for the HL-LHC.

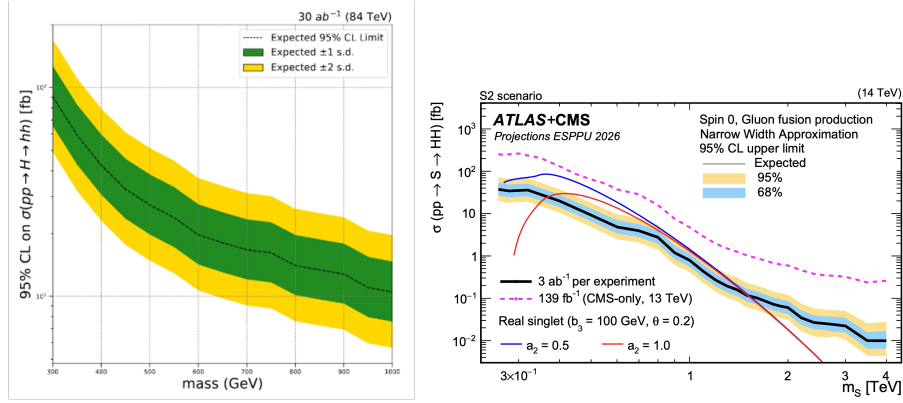


Figure 8.24: Expected 95% CL upper limits for FCC-hh (left) and HL-LHC (right) on the $\sigma(pp \rightarrow X \rightarrow HH)$ cross section as a function of the scalar mass m_X , produced via gluon fusion using the narrow width approximation. For comparison, in the HL-LHC plot, production cross section curves for the model described in Ref. [202] are shown, for two values of the scalar portal coupling a_2 .

While Fig. 8.25 highlights the exclusion potential of FCC-hh within the singlet scalar model framework, Fig. 8.26 illustrates the discovery reach. It presents the expected statistical significance (in units of σ) achievable through both the direct resonant search and precision measurement of the Higgs self-coupling. The results are shown for the subset of the parameter space consistent with a strong first-order phase transition, and for various values of the resonance mass. Under these assumptions, the FCC-hh demonstrates discov-

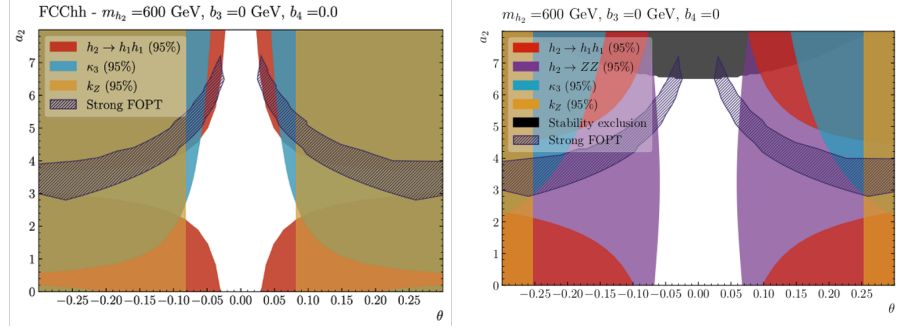


Figure 8.25: Bounds on the heavy scalar model, in the plane of the scalar portal coupling, a_2 , versus the scalar singlet mixing angle θ [315]. The dark blue hatched contours show the regions of the a_2 versus θ parameter space in the scalar singlet model where a strong first-order phase transition is possible for $m_S = 600$ GeV, $b_3 = 0$ GeV and $b_4 = 0.25$. The other contours show the 95% CL exclusion in this plane from the resonant searches into $X \rightarrow HH/ZZ$ signatures, from the H coupling to Z and from κ_λ constraints.

ery sensitivity from direct search exceeding the 5σ threshold for resonance masses up to approximately 650 GeV.

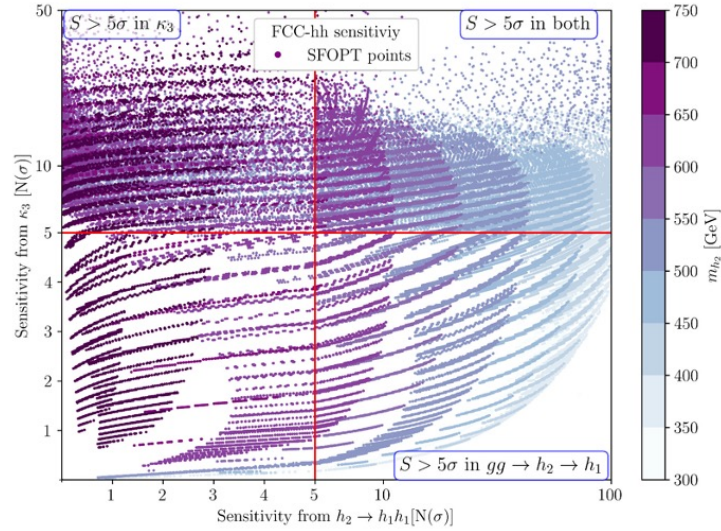


Figure 8.26: Expected sensitivity in number of σ from the direct resonant search and the precision measurement of κ_λ for the singlet model in the parameter space relevant for a SFOPT and for different resonance mass values [315].

8.3 Summary and outlook

In this chapter, I have presented the studies to which I contributed regarding Higgs boson pair production searches at future hadron colliders. The two colliders considered—HL-LHC and FCC-hh—are at very different stages in their respective timelines and approval processes.

The HL-LHC is a well-established extension of the current LHC program. Preparations for its launch have been underway for several years. As Run 3 comes to an end, the installation of upgraded detectors in CMS is entering a crucial phase. These upgrades are designed to ensure robust physics performance in the high-luminosity environment, which will involve significant increase in radiation and pileup levels.

In contrast, the FCC-hh is a much longer-term initiative and has not yet been formally approved. However, it is strongly endorsed by CERN and positioned as the natural successor to the LHC in Europe. This moment is critical for the FCC project, as a final decision is expected soon, with the European Strategy for Particle Physics Update playing a key role in the decision-making process. The projections presented in this chapter are timely contributions aimed at demonstrating the strong physics case for both colliders, particularly in the context of Higgs physics.

At the HL-LHC, the studies discussed, based on Run 2 state-of-the-art analyses, suggest that at least evidence for HH production could be achieved by the end of data taking. More recent projections [202], prepared for the European Strategy Update and incorporating Run 3 improvements (such as enhanced taggers and analysis techniques), show that a full 5σ discovery could be achieved when combining CMS and ATLAS data. This underscores the fact that earlier projections are often conservative, and ongoing advancements—particularly those driven by machine learning—continue to push the experimental reach.

This is even more true for the FCC-hh, which is envisioned to start operations only decades from now (≈ 50 years!). Despite the conservative nature of current projections, studies indicate that a measurement of the Higgs self-coupling at the percent level would be possible using only the $b\bar{b}\gamma\gamma$ final state. When this is combined with other promising channels—such as $b\bar{b}\tau^+\tau^-$, which recent projections suggest may offer comparable if not better sensitivity [316]—and additional production modes, achieving a 1% precision on the Higgs self-coupling becomes a realistic goal. This alone makes a compelling physics case for the FCC-hh, as no other proposed future collider is expected to reach this level of precision.

Additionally, the FCC-hh's unprecedented energy reach allows for direct searches for heavy new resonances that are inaccessible elsewhere. The benchmark study of a singlet model presented here highlights the significant discovery potential of the FCC-hh at the energy frontier.

Conclusion

In this thesis, I have detailed the work I carried out during my PhD years. My research focused on three main topics, for which I held primary responsibility.

As part of the Tau Group in CMS, I was in charge of the validation and calibration of the new, improved version of the DEEPTAU algorithm for the identification of hadronically decaying tau leptons. Over the years, I became increasingly involved in the group's activities, eventually taking on roles of coordination and guidance.

The expertise I developed in tau reconstruction and identification within CMS proved essential for the search for additional Higgs bosons via the process $H/A \rightarrow ZA/H \rightarrow \ell\ell\tau\tau$, using the full Run 2 CMS dataset. The expected results are presented both in a model-independent manner and in the context of a specific 2HDM. While the analysis is currently in the unblinding phase and the data is not yet disclosed, the expected limits already indicate stronger constraints on 2HDM parameters compared to previous CMS results. These improvements are primarily due to the increased integrated luminosity and the adoption of novel analysis strategies, particularly the use of DNN-based selection techniques and a refined definition and binning of the fitted observable, both of which significantly enhanced the analysis performance.

Lastly, I conducted several projection studies for di-Higgs searches at future colliders, such as the HL-LHC and the FCC-hh, to estimate their sensitivity and discovery potential. These studies demonstrate the crucial role such facilities could play in the future in deepening our understanding of the Higgs sector.

All of these topics are active areas of research, with many ongoing developments and potential future breakthroughs. For this reason, I have included an *Outlook* section at the end of each chapter, offering my personal perspective on possible next steps and improvements for each subject, to which I would be eager to contribute in the future.

Bibliography

- [1] CMS Collaboration. Identification of tau leptons using a convolutional neural network with domain adaptation in the CMS experiment. Technical report, CERN, Geneva, 2025. CMS-PAS-TAU-24-001. URL: <https://cds.cern.ch/record/2931189>.
- [2] P. Mastrapasqua. Hadronic tau lepton tagging with the CMS detector using domain adaptation to mitigate discrepancies between simulation and data. *PoS, ICHEP2024*:1039, 2025. doi:10.22323/1.476.1039.
- [3] A. Taliencio, P. Mastrapasqua and others. Higgs Self Couplings Measurements at Future proton-proton Colliders: a Snowmass White Paper. In *Snowmass 2021*, 3 2022. arXiv:2203.08042.
- [4] C. Caputo, P. Mastrapasqua and others. Higgs Self Couplings Measurements at Future proton-proton Colliders. *PoS, ICHEP2022*:1149, 2022. doi:10.22323/1.414.1149.
- [5] P. Mastrapasqua. Higgs Self-Coupling Measurements at Future Hadron Colliders: HL-LHC and FCC-hh. *Belgian Physical Society Magazine*, (1):20–27, 2024. Available online at BPS Magazine.
- [6] CMS Collaboration. Combination of searches for nonresonant Higgs boson pair production in proton-proton collisions at $\sqrt{s} = 13$ TeV. Technical report, CERN, Geneva, 2024. CMS-PAS-HIG-20-011. URL: <https://cds.cern.ch/record/2917252>.
- [7] E. Gallo, P. Mastrapasqua and others. Higgs self-coupling at the FCC-hh. In *Proceedings of the XXXI International Workshop on Deep Inelastic Scattering and Related Subjects (DIS2024)*, volume DIS2024, page 253, 2025. doi:10.22323/1.469.0253.
- [8] A. Taliencio, P. Mastrapasqua and others. Higgs self-coupling determination in the $b\bar{b}\gamma\gamma$ final state at the FCC-hh, 2025. Submit-

- ted to the 2025 Update of the European Strategy for Particle Physics. doi:10.17181/5mqfv-s _{β} xnd34.
- [9] M. Mangano, P. Mastrapasqua and others. Prospects for physics at FCC-hh, 2025. Submitted to the 2025 Update of the European Strategy for Particle Physics. doi:10.17181/bzhc2-s _{β} mem17.
- [10] ATLAS Collaboration. Observation of a new particle in the search for the Standard Model Higgs boson with the ATLAS detector at the LHC. *Physics Letters B*, 716(1):1–29, Sep 2012. doi:10.1016/j.physletb.2012.08.020.
- [11] CMS Collaboration. Observation of a new boson at a mass of 125 GeV with the CMS experiment at the LHC. *Physics Letters B*, 716(1):30–61, Sep 2012. doi:10.1016/j.physletb.2012.08.021.
- [12] S. L. Glashow. Partial Symmetries of Weak Interactions. *Nucl. Phys.*, 22:579–588, 1961. doi:10.1016/0029-s _{β} 5582(61)90469-s _{β} 2.
- [13] Steven Weinberg. A Model of Leptons. *Phys. Rev. Lett.*, 19:1264–1266, 1967. doi:10.1103/PhysRevLett.19.1264.
- [14] Abdus Salam. Weak and Electromagnetic Interactions. *Conf. Proc. C*, 680519:367–377, 1968. doi:10.1142/9789812795915_0034.
- [15] Wikipedia. Standard model. https://en.wikipedia.org/wiki/Standard_Model, 2025. Accessed: 9 September 2025.
- [16] Otto Nachtmann. *Elementary particle physics: concepts and phenomena*. Springer Science & Business Media, 2012.
- [17] LHCb Collaboration. Observation of the resonant character of the $Z(4430)^-$ state. *Phys. Rev. Lett.*, 112(22):222002, 2014. arXiv:1404.1903, doi:10.1103/PhysRevLett.112.222002.
- [18] LHCb Collaboration. Observation of $J/\psi p$ Resonances Consistent with Pentaquark States in $\Lambda_b^0 \rightarrow J/\psi K^- p$ Decays. *Phys. Rev. Lett.*, 115:072001, 2015. arXiv:1507.03414, doi:10.1103/PhysRevLett.115.072001.
- [19] Maria Elena Tejeda-Yeomans. Heavy-ion physics: freedom to do hot, dense, exciting QCD. *CERN Yellow Rep. School Proc.*, 2:137,

2021. [arXiv:2004.13812](#), [doi:10.23730/CYRSP-s _{\$\beta\$} 2021-s _{\$\beta\$} 002.137](#).
- [20] D. J. Gross and F. Wilczek. Ultraviolet behavior of non-abelian gauge theories. *Phys. Rev. Lett.*, 30, 1973. [doi:10.1103/PhysRevLett.30.1343](#).
- [21] H. David Politzer. Reliable perturbative results for strong interactions? *Phys. Rev. Lett.*, 30, 1973. [doi:10.1103/PhysRevLett.30.1346](#).
- [22] Particle Data Group Collaboration. Review of Particle Physics. *Physical Review D*, 110(3), 2024. [doi:10.1103/PhysRevD.110.030001](#).
- [23] Steven Weinberg. Mixing angle in renormalizable theories of weak and electromagnetic interactions. *Physical Review D*, 5(8):1962, 1972.
- [24] Peter W. Higgs. Broken symmetries, massless particles and gauge fields. *Phys. Lett.*, 12:132–133, 1964.
- [25] Peter W. Higgs. Broken symmetries and the masses of gauge bosons. *Physical Review Letters*, 13(16):508, 1964.
- [26] François Englert and Robert Brout. Broken symmetry and the mass of gauge vector mesons. *Physical Review Letters*, 13(9):321, 1964.
- [27] Steven D Bass, Albert De Roeck, and Marumi Kado. The Higgs boson implications and prospects for future discoveries. *Nature Reviews Physics*, 3(9):608–624, 2021.
- [28] ALEPH Collaboration, DELPHI collaboration, L3 Collaboration, OPAL Collaboration, and LEP Electroweak Working Group. Electroweak measurements in electron–positron collisions at W-boson-pair energies at LEP. *Physics reports*, 532(4):119–244, 2013.
- [29] CDF and D0 Collaboration. Combination of CDF and D0 W-boson mass measurements. *Phys. Rev. D*, 88(5):052018, 2013.
- [30] ATLAS Collaboration. Measurement of the W-boson mass in pp collisions at $\sqrt{s} = 7$ TeV with the ATLAS detector. *The European Physical Journal C*, 78(2), Feb 2018. [doi:10.1140/epjc/s10052-s _{\$\beta\$} 017-s _{\$\beta\$} 5475-s _{\$\beta\$} 4](#).

- [31] CDF Collaboration. High-precision measurement of the W boson mass with the CDF II detector. *Science*, 376(6589):170–176, 2022. arXiv:<https://www.science.org/doi/pdf/10.1126/science.abk1781>, doi:10.1126/science.abk1781.
- [32] CMS Collaboration. Measurement of the W boson mass in proton-proton collisions at $\sqrt{s} = 13$ TeV. Technical report, CERN, Geneva, 2024. CMS-PAS-SMP-23-002. URL: <https://cds.cern.ch/record/2910372>.
- [33] ATLAS Collaboration. Measurement of the CP properties of Higgs boson interactions with τ -leptons with the ATLAS detector. *The European Physical Journal C*, 83(7):563, 2023.
- [34] CMS Collaboration. Analysis of the CP structure of the Yukawa coupling between the Higgs boson and τ leptons in proton-proton collisions at $\sqrt{s} = 13$ TeV. *Journal of High Energy Physics*, 2022(6):1–67, 2022.
- [35] ATLAS Collaboration. Study of the spin and parity of the Higgs boson in diboson decays with the ATLAS detector. *The European Physical Journal C*, 76:1–14, 2016.
- [36] CMS Collaboration. Study of the Mass and Spin-Parity of the Higgs Boson Candidate via its Decays to Z Boson Pairs. *Physical Review Letters*, 110(8), February 2013. doi:10.1103/physrevlett.110.081803.
- [37] J. Wess and B. Zumino. A lagrangian model invariant under supergauge transformations. *Physics Letters B*, 49(1), 1974. doi:10.1016/0370-2693(74)90578-4.
- [38] D. B. Kaplan, H. Georgi, and S. Dimopoulos. Composite Higgs Scalars. *Phys. Lett. B*, 136, 1984. doi:10.1016/0370-2693(84)91178-X.
- [39] M. Bauer, M. Carena, and K. Gemmler. Creating the fermion mass hierarchies with multiple Higgs bosons. *Physical Review D*, 94(11), 2016. arXiv:1512.03458, doi:10.1103/physrevd.94.115030.
- [40] R. Barbieri, L. J. Hall, and V. S. Rychkov. Improved naturalness with a heavy Higgs boson: An alternative road to CERN LHC physics. *Physical Review D*, 74(1), 2006. arXiv:hep-ph/0603188, doi:10.1103/physrevd.74.015007.

- [41] D. E. Morrissey and M. J. Ramsey-Musolf. Electroweak baryogenesis. *New Journal of Physics*, 14(12), 2012. arXiv:1206.2942, doi:10.1088/1367-s β 2630/14/12/125003.
- [42] LHC Higgs Cross Section Working Group. Handbook of LHC Higgs Cross Sections: 4. Deciphering the Nature of the Higgs Sector. October 2016. arXiv:1610.07922, doi:10.23731/CYRM-s β 2017-s β 002.
- [43] CMS Collaboration. A portrait of the Higgs boson by the CMS experiment ten years after the discovery. *Nature*, 607(7917):60–68, 2022. arXiv:2207.00043, doi:10.1038/s41586-s β 022-s β 04892-s β x.
- [44] ATLAS Collaboration. Combined Measurement of the Higgs Boson Mass from the $H \rightarrow \gamma\gamma$ and $H \rightarrow ZZ^* \rightarrow 4l$ decay channels with the ATLAS detector using $\sqrt{s} = 7, 8$ and 13 TeV pp collision data. *Physical Review Letters*, 131(25), December 2023. URL: <http://dx.doi.org/10.1103/PhysRevLett.131.251802>, doi:10.1103/physrevlett.131.251802.
- [45] CMS Collaboration. Evidence for Higgs boson decay to a pair of muons. *Journal of High Energy Physics*, 2021(1), January 2021. URL: [http://dx.doi.org/10.1007/JHEP01\(2021\)148](http://dx.doi.org/10.1007/JHEP01(2021)148), doi:10.1007/jhep01(2021)148.
- [46] A detailed map of Higgs boson interactions by the ATLAS experiment ten years after the discovery. *Nature*, 607(7917):52–59, 2022. arXiv:2207.00092, doi:10.1038/s41586-s β 022-s β 04893-s β w.
- [47] Gavin P. Salam, Lian-Tao Wang, and Giulia Zanderighi. The Higgs boson turns ten. *Nature*, 607(7917):41–47, 2022. arXiv:2207.00478, doi:10.1038/s41586-s β 022-s β 04899-s β 4.
- [48] J. Alison et al. Higgs boson potential at colliders: Status and perspectives. *Reviews in Physics*, 5:100045, 2020.
- [49] C. Rovelli. Notes for a brief history of quantum gravity. In *9th Marcel Grossmann Meeting on Recent Developments in Theoretical and Experimental General Relativity, Gravitation and Relativistic Field Theories (MG 9)*, pages 742–768, 6 2000. arXiv:gr-s β qc/0006061.

- [50] L. Randall and R. Sundrum. Large mass hierarchy from a small extra dimension. *Physical Review Letters*, 83(17):3370–3373, Oct 1999. doi:10.1103/physrevlett.83.3370.
- [51] K. Freese. Review of Observational Evidence for Dark Matter in the Universe and in upcoming searches for Dark Stars. *EAS Publ. Ser.*, 36:113–126, 2009. arXiv:0812.4005, doi:10.1051/eas/0936016.
- [52] V. C. Rubin and W. K. Ford Jr. Rotation of the Andromeda Nebula from a Spectroscopic Survey of Emission Regions. *Astrophys. J.*, 159:379–403, 1970. doi:10.1086/150317.
- [53] D. Clowe, Marusa B., A. H. Gonzalez, S.W. Markevitch, M. and Randall, C. Jones, and D. Zaritsky. A direct empirical proof of the existence of dark matter. *Astrophys. J. Lett.*, 648:L109–L113, 2006. arXiv:astro-ph/0608407, doi:10.1086/508162.
- [54] Adam G. Riess et al. Observational evidence from supernovae for an accelerating universe and a cosmological constant. *Astron. J.*, 116:1009–1038, 1998. arXiv:astro-ph/9805201, doi:10.1086/300499.
- [55] Joshua Frieman, Michael Turner, and Dragan Huterer. Dark Energy and the Accelerating Universe. *Ann. Rev. Astron. Astrophys.*, 46:385–432, 2008. arXiv:0803.0982, doi:10.1146/annurev.astro.46.060407.145243.
- [56] Y. Fukuda et al. Evidence for oscillation of atmospheric neutrinos. *Phys. Rev. Lett.*, 81:1562–1567, Aug 1998. doi:10.1103/PhysRevLett.81.1562.
- [57] Q. R. Ahmad et al. Direct Evidence for Neutrino Flavor Transformation from Neutral-Current Interactions in the Sudbury Neutrino Observatory. *Phys. Rev. Lett.*, 89, Jun 2002. doi:10.1103/PhysRevLett.89.011301.
- [58] F. Capozzi et al. Global constraints on absolute neutrino masses and their ordering. *Phys. Rev. D*, 95(9):096014, 2017. arXiv:2003.08511, doi:10.1103/PhysRevD.95.096014.

- [59] S. F. King. Neutrino mass models. *Rept. Prog. Phys.*, 67:107–158, 2004. arXiv:hep-s _{β} ph/0310204, doi:10.1088/0034-s _{β} 4885/67/2/R01.
- [60] A. D. Sakharov. Violation of CP Invariance, C asymmetry, and baryon asymmetry of the universe. *Sov. Phys. Usp.*, 34(5):392–393, 1991. doi:10.1070/PU1991v034n05ABEH002497.
- [61] N. Aghanim et al. Planck 2018 results. VI. Cosmological parameters. *Astron. Astrophys.*, 641:A6, 2020. [Erratum: *Astron. Astrophys.* 652, C4 (2021)]. arXiv:1807.06209, doi:10.1051/0004-s _{β} 6361/201833910.
- [62] Michael E. Peskin. What is the Hierarchy Problem? *Nucl. Phys. B*, 1018:116971, 2025. arXiv:2505.00694, doi:10.1016/j.nuclphysb.2025.116971.
- [63] T. D. Lee. A Theory of Spontaneous T Violation. *Phys. Rev. D*, 8:1226–1239, Aug 1973. doi:10.1103/PhysRevD.8.1226.
- [64] R. D. Peccei and H. R. Quinn. CP conservation in the presence of pseudoparticles. *Phys. Rev. Lett.*, 38:1440–1443, Jun 1977. doi:10.1103/PhysRevLett.38.1440.
- [65] J. E. Kim. Light Pseudoscalars, Particle Physics and Cosmology. *Phys. Rept.*, 150:1–177, 1987. doi:10.1016/0370-s _{β} 1573(87)90017-s _{β} 2.
- [66] G.C. Branco, P.M. Ferreira, L. Lavoura, M.N. Rebelo, M. Sher, and J. P. Silva. Theory and phenomenology of two-Higgs-doublet models. *Physics Reports*, 516(1-2):1–102, Jul 2012. doi:10.1016/j.physrep.2012.02.002.
- [67] J. F. Gunion, H. E. Haber, G. L. Kane, and S. Dawson. *The Higgs Hunter’s Guide*, volume 80. 2000.
- [68] Felix Kling, Shufang Su, and Wei Su. 2HDM Neutral Scalars under the LHC. *JHEP*, 06:163, 2020. arXiv:2004.04172, doi:10.1007/JHEP06(2020)163.
- [69] ATLAS Collaboration. ATLAS searches for additional scalars and exotic Higgs boson decays with the LHC Run 2 dataset. *Phys. Rept.*,

- 1116:184–260, 2025. arXiv:2405.04914, doi:10.1016/j.physrep.2024.09.002.
- [70] CMS Collaboration. Search for MSSM Higgs bosons decaying to $\mu^+\mu^-$ in proton-proton collisions at $\sqrt{s} = 13$ TeV. Search for MSSM Higgs bosons decaying to $\mu^+\mu^-$ in proton-proton collisions at $\sqrt{s} = 13$ TeV. *Phys. Lett.*, B798:134992, 2019. arXiv:1907.03152, doi:10.1016/j.physletb.2019.134992.
- [71] CMS Collaboration. Search for direct production of GeV-scale resonances decaying to a pair of muons in proton-proton collisions at $\sqrt{s} = 13$ TeV. *JHEP*, 12:070, 2023. arXiv:2309.16003, doi:10.1007/JHEP12(2023)070.
- [72] ATLAS Collaboration. Search for scalar resonances decaying into $\mu^+\mu^-$ in events with and without b -tagged jets produced in proton-proton collisions at $\sqrt{s} = 13$ TeV with the ATLAS detector. *JHEP*, 07:117, 2019. arXiv:1901.08144, doi:10.1007/JHEP07(2019)117.
- [73] CMS Collaboration. Search for beyond the standard model Higgs bosons decaying into a $b\bar{b}$ pair in pp collisions at $\sqrt{s} = 13$ TeV. *JHEP*, 08:113, 2018. arXiv:1805.12191, doi:10.1007/JHEP08(2018)113.
- [74] CMS Collaboration. Search for bosons of an extended Higgs sector in b quark final states in proton-proton collisions at $\sqrt{s} = 13$ TeV. 2 2025. arXiv:2502.06568.
- [75] ATLAS Collaboration. Search for heavy neutral Higgs bosons produced in association with b -quarks and decaying to b -quarks at $\sqrt{s} = 13$ TeV with the ATLAS detector. 2019. arXiv:1907.02749.
- [76] CMS Collaboration. Search for additional neutral MSSM Higgs bosons in the $\tau\tau$ final state in proton-proton collisions at $\sqrt{s} = 13$ TeV. *JHEP*, 09:007, 2018. arXiv:1803.06553, doi:10.1007/JHEP09(2018)007.
- [77] CMS Collaboration. Search for a low-mass $\tau^+\tau^-$ resonance in association with a bottom quark in proton-proton collisions at $\sqrt{s} = 13$ TeV. *JHEP*, 05:210, 2019. arXiv:1903.10228, doi:10.1007/JHEP05(2019)210.

- [78] CMS Collaboration. Search for heavy neutral resonances decaying to tau lepton pairs in proton-proton collisions at $\sqrt{s} = 13$ TeV. 12 2024. arXiv:2412.04357.
- [79] CMS Collaboration. Search for new physics in high-mass diphoton events from proton-proton collisions at $\sqrt{s} = 13$ TeV. *JHEP*, 08:215, 2024. arXiv:2405.09320, doi:10.1007/JHEP08(2024)215.
- [80] ATLAS Collaboration. Search for heavy Higgs bosons decaying into two tau leptons with the ATLAS detector using pp collisions at $\sqrt{s} = 13$ TeV. 2020. arXiv:2002.12223.
- [81] CMS Collaboration. Search for a standard model-like Higgs boson in the mass range between 70 and 110 GeV in the diphoton final state in proton-proton collisions at $\sqrt{s} = 8$ and 13 TeV. *Phys. Lett.*, B793:320–347, 2019. arXiv:1811.08459, doi:10.1016/j.physletb.2019.03.064.
- [82] CMS Collaboration. Search for physics beyond the standard model in high-mass diphoton events from proton-proton collisions at $\sqrt{s} = 13$ TeV. *Phys. Rev.*, D98(9):092001, 2018. arXiv:1809.00327, doi:10.1103/PhysRevD.98.092001.
- [83] CMS Collaboration. Search for a standard model-like Higgs boson in the mass range between 70 and 110 GeV in the diphoton final state in proton-proton collisions at $\sqrt{s} = 13$ TeV. *Phys. Lett. B*, 860:139067, 2025. arXiv:2405.18149, doi:10.1016/j.physletb.2024.139067.
- [84] ATLAS Collaboration. Search for Scalar Diphoton Resonances in the Mass Range 65 – 600 GeV with the ATLAS Detector in pp Collision Data at $\sqrt{s} = 8$ TeV. *Phys. Rev. Lett.*, 113(17):171801, 2014. arXiv:1407.6583, doi:10.1103/PhysRevLett.113.171801.
- [85] ATLAS Collaboration. Search for new phenomena in high-mass diphoton final states using 37 fb^{-1} of proton–proton collisions collected at $\sqrt{s} = 13$ TeV with the ATLAS detector. *Phys. Lett.*, B775:105–125, 2017. arXiv:1707.04147, doi:10.1016/j.physletb.2017.10.039.

- [86] ATLAS Collaboration. Search for diphoton resonances in the 66 to 110 GeV mass range using pp collisions at $\sqrt{s} = 13$ TeV with the ATLAS detector. *JHEP*, 01:053, 2025. arXiv:2407.07546, doi:10.1007/JHEP01(2025)053.
- [87] CMS Collaboration. Search for heavy Higgs bosons decaying to a top quark pair in proton-proton collisions at $\sqrt{s} = 13$ TeV. 2019. arXiv:1908.01115.
- [88] CMS Collaboration. Observation of a pseudoscalar excess at the top quark pair production threshold. 3 2025. arXiv:2503.22382.
- [89] ATLAS Collaboration. Search for heavy neutral Higgs bosons decaying into a top quark pair in 140 fb¹ of proton-proton collision data at $\sqrt{s} = 13$ TeV with the ATLAS detector. *JHEP*, 08:013, 2024. arXiv:2404.18986, doi:10.1007/JHEP08(2024)013.
- [90] CMS Collaboration. Search for a new scalar resonance decaying to a pair of Z bosons in proton-proton collisions at $\sqrt{s} = 13$ TeV. *JHEP*, 06:127, 2018. [Erratum: *JHEP*03,128(2019)]. arXiv:1804.01939, doi:10.1007/JHEP06(2018)127, s_β10.1007/JHEP03(2019)128.
- [91] CMS Collaboration. Search for new heavy resonances decaying to WW, WZ, ZZ, WH, or ZH boson pairs in the all-jets final state in proton-proton collisions at $\sqrt{s} = 13$ TeV. *Phys. Lett. B*, 844:137813, 2023. arXiv:2210.00043, doi:10.1016/j.physletb.2023.137813.
- [92] ATLAS Collaboration. Search for heavy ZZ resonances in the $\ell^+\ell^-\ell^+\ell^-$ and $\ell^+\ell^-\nu\bar{\nu}$ final states using proton-proton collisions at $\sqrt{s} = 13$ TeV with the ATLAS detector. *Eur. Phys. J.*, C78(4):293, 2018. arXiv:1712.06386, doi:10.1140/epjc/s10052-s_β018-s_β5686-s_β3.
- [93] CMS Collaboration. Search for a heavy Higgs boson decaying to a pair of W bosons in proton-proton collisions at $\sqrt{s} = 13$ TeV. 2019. arXiv:1912.01594.
- [94] ATLAS Collaboration. Search for heavy resonances decaying into WW in the $e\nu\mu\nu$ final state in pp collisions at $\sqrt{s} = 13$ TeV with the AT-

- LAS detector. *Eur. Phys. J.*, C78(1):24, 2018. arXiv:1710.01123, doi:10.1140/epjc/s10052-s017-s05491-s04.
- [95] CMS Collaboration. Search for a pseudoscalar boson decaying into a Z boson and the 125 GeV Higgs boson in llbb final states. *Phys. Lett.*, B748:221–243, 2015. arXiv:1504.04710, doi:10.1016/j.physletb.2015.07.010.
- [96] CMS Collaboration. Search for a heavy pseudoscalar boson decaying to a Z and a Higgs boson at $\sqrt{s} = 13$ TeV. *Eur. Phys. J.*, C79(7):564, 2019. arXiv:1903.00941, doi:10.1140/epjc/s10052-s019-s07058-s0z.
- [97] ATLAS Collaboration. Search for a CP-odd Higgs boson decaying to Zh in pp collisions at $\sqrt{s} = 8$ TeV with the ATLAS detector. *Phys. Lett.*, B744:163–183, 2015. arXiv:1502.04478, doi:10.1016/j.physletb.2015.03.054.
- [98] ATLAS Collaboration. Search for heavy resonances decaying into a W or Z boson and a Higgs boson in final states with leptons and b-jets in 36 fb⁻¹ of $\sqrt{s} = 13$ TeV pp collisions with the ATLAS detector. *JHEP*, 03:174, 2018. [Erratum: JHEP11,051(2018)]. arXiv:1712.06518, doi:10.1007/JHEP11(2018)051, s010.1007/JHEP03(2018)174.
- [99] CMS Collaboration. Searches for a heavy scalar boson H decaying to a pair of 125 GeV Higgs bosons hh or for a heavy pseudoscalar boson A decaying to Zh, in the final states with $h \rightarrow \tau\tau$. *Phys. Lett.*, B755:217–244, 2016. arXiv:1510.01181, doi:10.1016/j.physletb.2016.01.056.
- [100] CMS Collaboration. Search for a heavy pseudoscalar Higgs boson decaying into a 125 GeV Higgs boson and a Z boson in final states with two tau and two light leptons at $\sqrt{s} = 13$ TeV. 2019. arXiv:1910.11634.
- [101] CMS Collaboration. Search for a heavy pseudoscalar Higgs boson decaying to a 125 GeV Higgs boson and a Z boson in final states with two tau and two light leptons in proton-proton collisions at $\sqrt{s} = 13$ TeV. 1 2025. arXiv:2501.14825.

- [102] CMS Collaboration. Search for Higgs boson pair production in the $bb\tau\tau$ final state in proton-proton collisions at $\sqrt{s} = 8$ TeV. *Phys. Rev.*, D96(7):072004, 2017. [arXiv:1707.00350](#), [doi:10.1103/PhysRevD.96.072004](#).
- [103] CMS Collaboration. Combination of searches for Higgs boson pair production in proton-proton collisions at $\sqrt{s} = 13$ TeV. *Phys. Rev. Lett.*, 122(12):121803, 2019. [arXiv:1811.09689](#), [doi:10.1103/PhysRevLett.122.121803](#).
- [104] ATLAS Collaboration. Searches for Higgs boson pair production in the $hh \rightarrow bb\tau\tau, \gamma\gamma WW^*, \gamma\gamma bb, bbbb$ channels with the ATLAS detector. *Phys. Rev.*, D92:092004, 2015. [arXiv:1509.04670](#), [doi:10.1103/PhysRevD.92.092004](#).
- [105] ATLAS Collaboration. Combination of searches for Higgs boson pairs in pp collisions at $\sqrt{s} = 13$ TeV with the ATLAS detector. 2019. [arXiv:1906.02025](#).
- [106] CMS Collaboration. Searches for Higgs boson production through decays of heavy resonances. *Phys. Rept.*, 1115:368–447, 2025. [arXiv:2403.16926](#), [doi:10.1016/j.physrep.2024.09.004](#).
- [107] ATLAS Collaboration. Search for the Higgs boson produced in association with a vector boson and decaying into two spin-zero particles in the $H \rightarrow aa \rightarrow 4b$ channel in pp collisions at $\sqrt{s} = 13$ TeV with the ATLAS detector. *JHEP*, 10:031, 2018. [arXiv:1806.07355](#), [doi:10.1007/JHEP10\(2018\)031](#).
- [108] CMS Collaboration. Search for the decay of the Higgs boson to a pair of light pseudoscalar bosons in the final state with four bottom quarks in proton-proton collisions at $\sqrt{s} = 13$ TeV. *JHEP*, 06:097, 2024. [arXiv:2403.10341](#), [doi:10.1007/JHEP06\(2024\)097](#).
- [109] ATLAS Collaboration. Search for decays of the Higgs boson into a pair of pseudoscalar particles decaying into $bb\tau\tau$ using pp collisions at $\sqrt{s} = 13$ TeV with the ATLAS detector. *Phys. Rev. D*, 110(5):052013, 2024. [arXiv:2407.01335](#), [doi:10.1103/PhysRevD.110.052013](#).
- [110] CMS Collaboration. Search for an exotic decay of the Higgs boson to a pair of light pseudoscalars in the final state with two b quarks and

- two τ leptons in proton-proton collisions at $\sqrt{s} = 13$ TeV. *Phys. Lett.*, B785:462, 2018. arXiv:1805.10191, doi:10.1016/j.physletb.2018.08.057.
- [111] CMS Collaboration. Search for exotic decays of the Higgs boson to a pair of pseudoscalars in the $\mu\mu b\bar{b}$ and $\tau\tau b\bar{b}$ final states. *Eur. Phys. J. C*, 84(5):493, 2024. arXiv:2402.13358, doi:10.1140/epjc/s10052-024-s024-s012727-s04.
- [112] ATLAS Collaboration. Search for Higgs boson decays into a pair of light bosons in the $b\bar{b}\mu\mu$ final state in pp collision at $\sqrt{s} = 13$ TeV with the ATLAS detector. *Phys. Lett.*, B790:1–21, 2019. arXiv:1807.00539, doi:10.1016/j.physletb.2018.10.073.
- [113] CMS Collaboration. Search for an exotic decay of the Higgs boson to a pair of light pseudoscalars in the final state with two muons and two b quarks in pp collisions at 13 TeV. *Phys. Lett.*, B795:398–423, 2019. arXiv:1812.06359, doi:10.1016/j.physletb.2019.06.021.
- [114] ATLAS Collaboration. Search for Higgs boson exotic decays into Lorentz-boosted light bosons in the four- τ final state at $\sqrt{s} = 13$ TeV with the ATLAS detector. 3 2025. arXiv:2503.05463.
- [115] CMS Collaboration. Search for light pseudoscalar boson pairs produced from decays of the 125 GeV Higgs boson in final states with two muons and two nearby tracks in pp collisions at $\sqrt{s} = 13$ TeV. 2019. arXiv:1907.07235.
- [116] ATLAS Collaboration. Search for Higgs bosons decaying to aa in the $\mu\mu\tau\tau$ final state in pp collisions at $\sqrt{s} = 8$ TeV with the ATLAS experiment. *Phys. Rev.*, D92(5):052002, 2015. arXiv:1505.01609, doi:10.1103/PhysRevD.92.052002.
- [117] CMS Collaboration. Search for an exotic decay of the Higgs boson to a pair of light pseudoscalars in the final state of two muons and two τ leptons in proton-proton collisions at $\sqrt{s} = 13$ TeV. *JHEP*, 11:018, 2018. arXiv:1805.04865, doi:10.1007/JHEP11(2018)018.
- [118] ATLAS Collaboration. Search for Higgs boson decays to beyond-the-Standard-Model light bosons in four-lepton events with the ATLAS de-

- tector at $\sqrt{s} = 13$ TeV. *JHEP*, 06:166, 2018. arXiv:1802.03388, doi:10.1007/JHEP06(2018)166.
- [119] CMS Collaboration. A search for pair production of new light bosons decaying into muons in proton-proton collisions at 13 TeV. *Phys. Lett.*, B796:131–154, 2019. arXiv:1812.00380, doi:10.1016/j.physletb.2019.07.013.
- [120] ATLAS Collaboration. Search for short- and long-lived axion-like particles in $H \rightarrow aa \rightarrow 4\gamma$ decays with the ATLAS experiment at the LHC. *Eur. Phys. J. C*, 84(7):742, 2024. arXiv:2312.03306, doi:10.1140/epjc/s10052-s0024-s012979-s00.
- [121] CMS Collaboration. Search for exotic Higgs boson decays $H \rightarrow \mathcal{A}\mathcal{A} \rightarrow 4\gamma$ with events containing two merged diphotons in proton-proton collisions at $\sqrt{s} = 13$ TeV. *Phys. Rev. Lett.*, 131:101801, 2023. arXiv:2209.06197, doi:10.1103/PhysRevLett.131.101801.
- [122] CMS Collaboration. Search for the exotic decay of the Higgs boson into two light pseudoscalars with four photons in the final state in proton-proton collisions at $\sqrt{s} = 13$ TeV. *JHEP*, 07:148, 2023. arXiv:2208.01469, doi:10.1007/JHEP07(2023)148.
- [123] ATLAS Collaboration. Search for a heavy Higgs boson decaying into a Z boson and another heavy Higgs boson in the $\ell\ell b\bar{b}$ final state in pp collisions at $\sqrt{s} = 13$ TeV with the ATLAS detector. *Phys. Lett.*, B783:392–414, 2018. arXiv:1804.01126, doi:10.1016/j.physletb.2018.07.006.
- [124] CMS Collaboration. Search for new neutral Higgs bosons through the $H \rightarrow ZA \rightarrow \ell^+\ell^-\bar{b}b$ process in pp collisions at $\sqrt{s} = 13$ TeV. 2019. arXiv:1911.03781.
- [125] CMS Collaboration. Search for neutral resonances decaying into a Z boson and a pair of b jets or τ leptons. *Phys. Lett.*, B759:369–394, 2016. arXiv:1603.02991, doi:10.1016/j.physletb.2016.05.087.
- [126] ATLAS Collaboration. Search for a CP-odd Higgs boson decaying into a heavy CP-even Higgs boson and a Z boson in the $\ell^+\ell^-\bar{t}t$ and

- $\nu\bar{\nu}b\bar{b}$ final states using 140 fb¹ of data collected with the ATLAS detector. *JHEP*, 02:197, 2024. arXiv:2311.04033, doi:10.1007/JHEP02(2024)197.
- [127] CMS Collaboration. Search for heavy neutral Higgs bosons A and H in the $t\bar{t}Z$ channel in proton-proton collisions at 13 TeV. *Phys. Lett. B*, 866:139568, 2025. arXiv:2412.00570, doi:10.1016/j.physletb.2025.139568.
- [128] S. Dimopoulos and H. Georgi. Softly Broken Supersymmetry and SU(5). *Nucl. Phys. B*, 193:150–162, 1981. doi:10.1016/0550-s_β3213(81)90522-s_β8.
- [129] E. Witten. Dynamical Breaking of Supersymmetry. *Nucl. Phys. B*, 188:513, 1981. doi:10.1016/0550-s_β3213(81)90006-s_β7.
- [130] J. R. Ellis, J.S. Hagelin, D. V. Nanopoulos, K. A. Olive, and M. Srednicki. Supersymmetric Relics from the Big Bang. *Nucl. Phys. B*, 238:453–476, 1984. doi:10.1016/0550-s_β3213(84)90461-s_β9.
- [131] R. Catena and L. Covi. SUSY dark matter(s). *The European Physical Journal C*, 74(5), May 2014. doi:10.1140/epjc/s10052-s_β013-s_β2703-s_β4.
- [132] D. Z. Freedman, P. van Nieuwenhuizen, and S. Ferrara. Progress toward a theory of supergravity. *Phys. Rev. D*, 13:3214–3218, Jun 1976. doi:10.1103/PhysRevD.13.3214.
- [133] John R. Ellis. Supersymmetry for Alp hikers. In *2001 European School of High-Energy Physics*, pages 157–203, 3 2002. arXiv:hep-s_βph/0203114.
- [134] John F. Gunion. A Simplified summary of supersymmetry. *AIP Conf. Proc.*, 397(1):41–64, 1997. arXiv:hep-s_βph/9704349, doi:10.1063/1.52979.
- [135] S.P. Martin. A supersymmetry primer. *Advanced Series on Directions in High Energy Physics*, page 1–98, Jul 1998. doi:10.1142/9789812839657_0001.

- [136] C. Csaki. The Minimal supersymmetric standard model (MSSM). *Mod. Phys. Lett. A*, 11:599, 1996. arXiv:hep-sph/9606414, doi: 10.1142/S021773239600062X.
- [137] V. Sanz and J. Setford. Composite Higgs Models after Run 2. *Adv. High Energy Phys.*, 2018:7168480, 2018. arXiv:1703.10190, doi:10.1155/2018/7168480.
- [138] O. Witzel. Review on Composite Higgs Models. arXiv:1901.08216.
- [139] Vladimir Chekhovsky et al. Model-agnostic search for dijet resonances with anomalous jet substructure in proton–proton collisions at $\sqrt{s} = 13$ TeV. *Rept. Prog. Phys.*, 88(6):067802, 2025. arXiv:2412.03747, doi:10.1088/1361-sph6633/add762.
- [140] David Eriksson, Johan Rathsmann, and Oscar Stål. 2HDMC- two-Higgs-doublet model calculator. *Computer Physics Communications*, 181(1):189–205, 2010. URL: <https://www.sciencedirect.com/science/article/pii/S0010465509003014>, doi:10.1016/j.cpc.2009.09.011.
- [141] M. Hoffmann. *The Search for a Heavy Higgs Boson in the $H \rightarrow ZZ$ Decay Channels with the ATLAS Detector at the LHC*. Theses, Université Paris-Saclay, October 2016.
- [142] CMS collaboration. CMS Luminosity measurements. URL: <https://twiki.cern.ch/twiki/bin/view/CMSPublic/LumiPublicResults>.
- [143] I. Zurbano Fernandez et al. High-Luminosity Large Hadron Collider (HL-LHC): Technical design report. 10/2020, 12 2020. doi: 10.23731/CYRM-sph2020-sph0010.
- [144] CERN and its neighbours. The High-Luminosity LHC (HL-LHC), 2025. Accessed: 10 September 2025. URL: <https://voisins.web.cern.ch/en/high-sphluminosity-sphlhc-sphhl-sphlhc>.
- [145] Elias Métral and Rogelio Tomás. Performance ramp-up in the hl-lhc era, 2025. Accessed: 10 September 2025. URL: <https://hlcb-sphnewsletter.web.cern.ch/news/>

news/wp2-s_βaccelerator-s_βphysics-s_βperformance/
performance-s_βramp-s_βhl-s_βlhc-s_βera.

- [146] Tai Sakuma. Cutaway diagrams of CMS detector, May 2019. URL: <https://cds.cern.ch/record/2665537>.
- [147] CMS Collaboration. The CMS experiment at the CERN LHC. *Journal of Instrumentation*, 3(08):S08004–S08004, aug 2008. doi:10.1088/1748-s_β0221/3/08/s08004.
- [148] UZH CMS wiki contributors. CMS coordinate system — UZH CMS wiki, 2017. [Online; accessed 3-October-2021]. URL: https://wiki.physik.uzh.ch/cms/_detail/latex:cms_coordinate_system.png?id=latex%3Aexample_spherical_coordinates.
- [149] CMS Collaboration. Precise mapping of the magnetic field in the CMS barrel yoke using cosmic rays. *Journal of Instrumentation*, 5(03):T03021–T03021, mar 2010. doi:10.1088/1748-s_β0221/5/03/t03021.
- [150] CMS Collaboration. Description and performance of track and primary-vertex reconstruction with the CMS tracker. *Journal of Instrumentation*, 9(10):P10009–P10009, oct 2014. doi:10.1088/1748-s_β0221/9/10/p10009.
- [151] CMS Collaboration. The CMS Phase-1 Pixel Detector Upgrade. *JINST*, 16:P02027. 84 p, Dec 2020. URL: <https://cds.cern.ch/record/2748381>, arXiv:2012.14304, doi:10.1088/1748-s_β0221/16/02/P02027.
- [152] CMS Collaboration. *The CMS electromagnetic calorimeter project: Technical Design Report*. Technical design report. CMS. CERN, Geneva, 1997. URL: <https://cds.cern.ch/record/349375>.
- [153] CMS Collaboration. Performance and operation of the CMS electromagnetic calorimeter. *Journal of Instrumentation*, 5(03):T03010–T03010, Mar 2010. URL: http://dx.doi.org/10.1088/1748-s_β0221/5/03/T03010, doi:10.1088/1748-s_β0221/5/03/t03010.

- [154] CMS Collaboration. *The CMS hadron calorimeter project: Technical Design Report*. Technical design report. CMS. CERN, Geneva, 1997. URL: <https://cds.cern.ch/record/357153>.
- [155] CMS Collaboration. Performance of CMS hadron calorimeter timing and synchronization using test beam, cosmic ray, and LHC beam data. *Journal of Instrumentation*, 5(03):T03013–T03013, Mar 2010. doi: 10.1088/1748-s β 0221/5/03/t03013.
- [156] A Colaleo, A Safonov, A Sharma, and M Tytgat. CMS Technical Design Report for the Muon Endcap GEM Upgrade. Technical report, 2015. CERN-LHCC-2015-012, CMS-TDR-013. URL: <https://cds.cern.ch/record/2021453>.
- [157] CMS Collaboration. Performance of CMS muon reconstruction in pp collision events at $\sqrt{s} = 7$ TeV. *Journal of Instrumentation*, 7(10):P10002–P10002, Oct 2012. URL: [http://dx.doi.org/10.1088/1748-s \$\beta\$ 0221/7/10/P10002](http://dx.doi.org/10.1088/1748-s\beta0221/7/10/P10002), doi:10.1088/1748-s β 0221/7/10/p10002.
- [158] CMS Collaboration. The CMS muon project: Technical Design Report. 1997. CERN-LHCC-97-032, CMS-TDR-3.
- [159] CMS Collaboration. Development of the CMS detector for the CERN LHC Run 3. Development of the CMS detector for the CERN LHC Run 3. *JINST*, 19(05):P05064, 2024. URL: <https://cds.cern.ch/record/2870088>, arXiv:2309.05466, doi:10.1088/1748-s β 0221/19/05/P05064.
- [160] M. Abbas et al. Benchmarking LHC background particle simulation with the CMS triple-GEM detector. *Journal of Instrumentation*, 16(12):P12026, December 2021. URL: [http://dx.doi.org/10.1088/1748-s \$\beta\$ 0221/16/12/P12026](http://dx.doi.org/10.1088/1748-s\beta0221/16/12/P12026), doi:10.1088/1748-s β 0221/16/12/p12026.
- [161] CMS Collaboration. Performance of the CMS Level-1 trigger in proton-proton collisions at $\sqrt{s} = 13$ TeV. *JINST*, 15:P10017, 2020. arXiv: 2006.10165, doi:10.1088/1748-s β 0221/15/10/P10017.
- [162] R. Frühwirth. Application of Kalman filtering to track and vertex fitting. *Nuclear Instruments and Methods in Physics Research Section*

- A: Accelerators, Spectrometers, Detectors and Associated Equipment*, 262(2):444–450, 1987. URL: <https://www.sciencedirect.com/science/article/pii/0168900287908874>, doi:10.1016/0168-s _{β} 9002(87)90887-s _{β} 4.
- [163] The CMS Collaboration. Description and performance of track and primary-vertex reconstruction with the cms tracker. *Journal of Instrumentation*, 9(10):P10009–P10009, October 2014. URL: [http://dx.doi.org/10.1088/1748-s _{\$\beta\$} 0221/9/10/P10009](http://dx.doi.org/10.1088/1748-s_{\beta}0221/9/10/P10009), doi:10.1088/1748-s _{β} 0221/9/10/p10009.
- [164] Felice Pantaleo. New Track Seeding Techniques for the CMS Experiment, 2017. URL: <http://cds.cern.ch/record/2293435>.
- [165] CMS collaboration. Particle-flow reconstruction and global event description with the CMS detector. *Journal of Instrumentation*, 12(10):P10003, oct 2017. URL: [https://dx.doi.org/10.1088/1748-s _{\$\beta\$} 0221/12/10/P10003](https://dx.doi.org/10.1088/1748-s_{\beta}0221/12/10/P10003), doi:10.1088/1748-s _{β} 0221/12/10/P10003.
- [166] Matteo Cacciari, Gavin P. Salam, and Gregory Soyez. The anti-kt jet clustering algorithm. *Journal of High Energy Physics*, 2008(04):063, apr 2008. URL: [https://dx.doi.org/10.1088/1126-s _{\$\beta\$} 6708/2008/04/063](https://dx.doi.org/10.1088/1126-s_{\beta}6708/2008/04/063), doi:10.1088/1126-s _{β} 6708/2008/04/063.
- [167] Matteo Cacciari, Gavin P. Salam, and Gregory Soyez. Fastjet user manual: (for version 3.0.2). *The European Physical Journal C*, 72(3), March 2012. URL: [http://dx.doi.org/10.1140/epjc/s10052-s _{\$\beta\$} 012-s _{\$\beta\$} 1896-s _{\$\beta\$} 2](http://dx.doi.org/10.1140/epjc/s10052-s_{\beta}012-s_{\beta}1896-s_{\beta}2), doi:10.1140/epjc/s10052-s _{β} 012-s _{β} 1896-s _{β} 2.
- [168] E. Bols, J. Kieseler, M. Verzetti, M. Stoye, and A. Stakia. Jet flavour classification using DeepJet. *Journal of Instrumentation*, 15(12):P12012, dec 2020. URL: [https://dx.doi.org/10.1088/1748-s _{\$\beta\$} 0221/15/12/P12012](https://dx.doi.org/10.1088/1748-s_{\beta}0221/15/12/P12012), doi:10.1088/1748-s _{β} 0221/15/12/P12012.
- [169] Huilin Qu and Loukas Gouskos. Jet tagging via particle clouds. *Phys. Rev. D*, 101:056019, Mar 2020. URL: <https://link>.

- aps.org/doi/10.1103/PhysRevD.101.056019, doi:10.1103/PhysRevD.101.056019.
- [170] CMS Collaboration. A unified approach for jet tagging in Run 3 at $\sqrt{s}=13.6$ TeV in CMS. 2024. CMS-DP-2024-066. URL: <https://cds.cern.ch/record/2904702>.
- [171] CMS collaboration. Performance of the DeepJet b tagging algorithm using 41.9 fb^{-1} of data from proton-proton collisions at 13TeV with Phase 1 CMS detector. *CMS-DP-2018-058*, 2018. URL: <http://cds.cern.ch/record/2646773>.
- [172] CMS Collaboration. Performance of reconstruction and identification of tau leptons in their decays to hadrons and tau neutrino in LHC Run-2. Technical Report CMS-PAS-TAU-16-002, CERN, Geneva, 2016. URL: <http://cds.cern.ch/record/2196972>.
- [173] CMS Collaboration. Performance of reconstruction and identification of τ leptons decaying to hadrons and ν_τ in pp collisions at $\sqrt{s} = 13$ TeV. *JINST*, 13(10):P10005, 2018. arXiv:1809.02816, doi:10.1088/1748-s0221/13/10/P10005.
- [174] CMS Collaboration. The Phase-2 Upgrade of the CMS Tracker. Technical report, CERN, Geneva, 2017. CERN-LHCC-2017-009, CMS-TDR-014. URL: <https://cds.cern.ch/record/2272264>, doi:10.17181/CERN.QZ28.FLHW.
- [175] CMS Collaboration. The Phase-2 Upgrade of the CMS Endcap Calorimeter. Technical report, CERN, Geneva, 2017. CERN-LHCC-2017-023, CMS-TDR-019. URL: <https://cds.cern.ch/record/2293646>, doi:10.17181/CERN.IV8M.1JY2.
- [176] CMS Collaboration. A MIP Timing Detector for the CMS Phase-2 Upgrade. Technical report, CERN, Geneva, 2019. CERN-LHCC-2019-003, CMS-TDR-020. URL: <https://cds.cern.ch/record/2667167>.
- [177] CMS Collaboration. The Phase-2 Upgrade of the CMS Barrel Calorimeters. Technical report, CERN, Geneva, 2017. CERN-LHCC-2017-011, CMS-TDR-015. URL: <https://cds.cern.ch/record/2283187>.

- [178] CMS Collaboration. The Phase-2 Upgrade of the CMS Muon Detectors. Technical report, CERN, Geneva, 2017. CERN-LHCC-2017-012, CMS-TDR-016. URL: <https://cds.cern.ch/record/2283189>, doi:10.17181/CERN.5T9S.VPMI.
- [179] European Strategy Group. 2020 update of the european strategy for particle physics, June 2020. CERN Council. URL: https://home.cern/news/news/physics/cern-s_beta_council-s_beta_adopts-s_beta_update-s_beta_european-s_beta_strategy-s_beta_particle-s_beta_physics.
- [180] FCC Collaboration. *FCC Physics Opportunities: Future Circular Collider Conceptual Design Report Volume 1*. Number CERN-2019-003 in CERN Yellow Reports: Monographs. CERN, 2019. doi:10.23731/CYRM-s_beta2019-s_beta003.
- [181] FCC Collaboration. *FCC-ee: The Lepton Collider – Future Circular Collider Conceptual Design Report Volume 2*. Number CERN-2019-004 in CERN Yellow Reports: Monographs. CERN, 2019. doi:10.23731/CYRM-s_beta2019-s_beta004.
- [182] FCC Collaboration. *FCC-hh: The Hadron Collider – Future Circular Collider Conceptual Design Report Volume 3*. Number CERN-2019-006 in CERN Yellow Reports: Monographs. CERN, 2019. doi:10.23731/CYRM-s_beta2019-s_beta006.
- [183] Peter W. Graham, Daniel E. Kaplan, and Surjeet Rajendran. Cosmological relaxation of the electroweak scale. *Phys. Rev. Lett.*, 115:221801, 2015. arXiv:1504.07551, doi:10.1103/PhysRevLett.115.221801.
- [184] J.R. Espinosa, C. Grojean, G. Panico, A. Pomarol, O. Pujolàs, and G. Servant. Cosmological Higgs-axion interplay for a naturally small electroweak scale. *Phys. Rev. Lett.*, 115:251803, 2015. arXiv:1506.09217, doi:10.1103/PhysRevLett.115.251803.
- [185] Nima Arkani-Hamed, Raffaele Tito D’Agnolo, and Hyung Do Kim. Weak scale as a trigger. *Phys. Rev. D*, 104:095014, 2021. arXiv:2012.04652, doi:10.1103/PhysRevD.104.095014.

- [186] M. Benedikt and et al. Future circular collider feasibility study report: Volume 1, physics, experiments, detectors. arXiv preprint 2505.00272, CERN, 2025. URL: <https://arxiv.org/abs/2505.00272>.
- [187] Marumi Kado. Keynote: From hl-lhc to fcc. In *FCC Week 2025*, Vienna, Austria, May 2025. Invited plenary talk. URL: https://indico.cern.ch/event/1408515/timetable/#155-s_betakeynote-s_betafrom-s_betahl-s_betahlc-s_betafo-s_betafcc.
- [188] A. Blondel and F. Zimmermann. A high luminosity e^+e^- collider in the LHC tunnel to study the Higgs boson. *arXiv preprint*, 2011. arXiv:1112.2518.
- [189] A. Blondel et al. A high luminosity e^+e^- collider to study the Higgs boson. *arXiv preprint*, 2012. arXiv:1208.0504.
- [190] P. Azzi et al. Prospective studies for LEP3 with the CMS detector. *arXiv preprint*, 2012. arXiv:1208.1662.
- [191] D. Ghosh, R. S. Gupta, and G. Perez. Is the Higgs mechanism of fermion mass generation a fact? A Yukawa-less first-two-generation model. *Physics Letters B*, 755:504–508, 2016. arXiv:1508.01501, doi:10.1016/j.physletb.2016.02.059.
- [192] A. Dery, C. Frugiuele, and Y. Nir. Large Higgs-electron Yukawa coupling in 2HDM. *Journal of High Energy Physics*, 2018(4):044, 2018. arXiv:1712.04514, doi:10.1007/JHEP04(2018)044.
- [193] W. Altmannshofer, J. Brod, and M. Schmaltz. Experimental constraints on the coupling of the Higgs boson to electrons. *Journal of High Energy Physics*, 2015(5):125, 2015. arXiv:1503.04830, doi:10.1007/JHEP05(2015)125.
- [194] D. d’Enterria, A. Poldaru, and G. Wojcik. Measuring the electron Yukawa coupling via resonant s-channel Higgs production at FCC-ee. *European Physical Journal Plus*, 137:201, 2022. arXiv:2107.02686, doi:10.1140/epjp/s13360-s_beta021-s_beta02204-s_beta2.
- [195] A. Faus-Golfe, M. A. Valdivia Garcia, and F. Zimmermann. The challenge of monochromatization. *European Physical Journal Plus*, 137:31, 2021. doi:10.1140/epjp/s13360-s_beta021-s_beta02151-s_betaY.

- [196] P. Azzurri et al. A special Higgs challenge: Measuring the mass and production cross section with ultimate precision at FCC-ee. *European Physical Journal Plus*, 137:23, 2021. [arXiv:2106.15438](#), doi: 10.1140/epjp/s13360-s β 021-s β 02202-s β 4.
- [197] P. Janot and A. Blondel. The carbon footprint of proposed e^+e^- Higgs factories, journal = European Physical Journal Plus. 137:1122, 2022. [arXiv:2208.10466](#), doi:10.1140/epjp/s13360-s β 022-s β 03319-s β w.
- [198] A. Blondel, C. Grojean, P. Janot, and G. Wilkinson. Higgs factory options for CERN: A comparative study. *arXiv preprint*, 2024. [arXiv:2412.13130](#).
- [199] Michael Benedikt et al. FCC Integrated Programme Stage 2: The FCC-hh. Technical report, CERN, Geneva, 2025. CERN-FCC-ACC-2025-0007. URL: <https://cds.cern.ch/record/2928941>, doi: 10.17181/CERN.M6OU.VG88.
- [200] G. Perez-Segurana, A. Abramov, F. Zimmermann, M. Giovannozzi, M. Benedikt, R. Bruce, T. Risselada, and W. Bartmann. A New Baseline Layout for the FCC-hh Ring. In *Proceedings of the 15th International Particle Accelerator Conference (IPAC 2024)*, JACoW, page MOPC14, 2024. URL: <https://cds.cern.ch/record/2912190>, doi: 10.18429/JACoW-s β IPAC2024-s β MOPC14.
- [201] F. Zimmermann. Scenarios for the FCC-hh. <https://doi.org/10.5281/zenodo.14934133>, 2025.
- [202] Highlights of the HL-LHC physics projections by ATLAS and CMS. 4 2025. [arXiv:2504.00672](#).
- [203] J. de Favereau, C. Delaere, P. Demin, A. Giammanco, V. Lemaitre, A. Mertens, and M. Selvaggi. DELPHES 3, A modular framework for fast simulation of a generic collider experiment. *JHEP*, 02:057, 2014. [arXiv:1307.6346](#), doi:10.1007/JHEP02(2014)057.
- [204] Delphes releases. <https://github.com/delphes/delphes/releases>. Accessed: 2025-06-18.
- [205] FCC-hh detector DELPHES card. https://github.com/delphes/delphes/blob/master/cards/FCC/scenarios/FCChh_II.tcl. Accessed: 2025-06-18.

- [206] M. Selvaggi and B. Stapf. A Delphes parameterisation of the FCC-hh detector. [https://doi.org/10.17181/71pv5-s _{\$\beta\$} tvf87](https://doi.org/10.17181/71pv5-s_{β}tvf87), 2025. Accessed: 2025-06-18.
- [207] J. de Blas et al. On the future of higgs, electroweak and diboson measurements at lepton colliders. *Journal of High Energy Physics*, 2019(12):117, 2019. arXiv:1907.04311, doi:10.1007/JHEP12(2019)117.
- [208] J. de Blas et al. Higgs boson studies at future particle colliders. *Journal of High Energy Physics*, 2020(1):139, 2020. arXiv:1905.03764, doi:10.1007/JHEP01(2020)139.
- [209] J. de Blas et al. Global SMEFT fits at future colliders; contribution to Snowmass 2021, 2022. arXiv:2206.08326.
- [210] A. Blondel, C. Grojean, P. Janot, and G. Wilkinson. Higgs factory options for cern: A comparative study, 2024. arXiv:2412.13130.
- [211] A. Freitas et al. Theoretical uncertainties for electroweak and higgs-boson precision measurements at fcc-ee, 2019. arXiv:1906.05379.
- [212] Alain Blondel, Christophe Grojean, Patrick Janot, and Guy Wilkinson. Higgs Factory options for CERN: A comparative study. 12 2024. arXiv:2412.13130.
- [213] Kyle Cranmer. Practical Statistics for the LHC, 2015. arXiv:1503.07622.
- [214] Kyle Cranmer, George Lewis, Lorenzo Moneta, Akira Shibata, and Wouter Verkerke. HistFactory: A tool for creating statistical models for use with RooFit and RooStats. Technical report, New York U., New York, 2012. URL: <https://cds.cern.ch/record/1456844>.
- [215] A L Read. Modified frequentist analysis of search results (the CL_s method). 2000. URL: <https://cds.cern.ch/record/451614>, doi:10.5170/CERN-s _{β} 2000-s _{β} 005.81.
- [216] CMS Collaboration. The CMS Statistical Analysis and Combination Tool: Combine. *Comput. Softw. Big Sci.*, 8(1):19, 2024. arXiv:2404.06614, doi:10.1007/s41781-s _{β} 024-s _{β} 00121-s _{β} 4.

- [217] Wouter Verkerke and David Kirkby. The roofit toolkit for data modeling, 2003. [arXiv:physics/0306116](https://arxiv.org/abs/physics/0306116).
- [218] Lorenzo Moneta, Kyle Cranmer, Gregory Schott, and Wouter Verkerke. The RooStats project. In *Proceedings of 13th International Workshop on Advanced Computing and Analysis Techniques in Physics Research — PoS(ACAT2010)*, volume 093, page 057, 2011. doi:10.22323/1.093.0057.
- [219] F. James and M. Roos. Minuit: A System for Function Minimization and Analysis of the Parameter Errors and Correlations. *Comput. Phys. Commun.*, 10:343–367, 1975. doi:10.1016/0010-s _{β} 4655(75)90039-s _{β} 9.
- [220] S. S. Wilks. The Large-Sample Distribution of the Likelihood Ratio for Testing Composite Hypotheses. *Annals Math. Statist.*, 9(1):60–62, 1938. doi:10.1214/aoms/1177732360.
- [221] CMS Collaboration. Searches for additional Higgs bosons and for vector leptoquarks in $\tau\tau$ final states in proton-proton collisions at $\sqrt{s} = 13$ TeV, 2022. [arXiv:2208.02717](https://arxiv.org/abs/2208.02717).
- [222] Jerzy Neyman and Egon Sharpe Pearson. On the Problem of the Most Efficient Tests of Statistical Hypotheses. *Phil. Trans. Roy. Soc. Lond. A*, 231(694-706):289–337, 1933. doi:10.1098/rsta.1933.0009.
- [223] J.K. Lindsey. *Parametric Statistical Inference*. New York: Oxford University Press, 1996.
- [224] Mathieu Vlimant. ML Overview in CMS, HEP, and beyond. https://indico.cern.ch/event/1101433/contributions/4813873/attachments/2425693/4152848/vlimant_AI4JME_April22.pdf, April 2022. Presentation at CMS JetMET Workshop, April 2022.
- [225] Facundo Bre, Juan M. Giménez, and Víctor D. Fachinotti. Prediction of wind pressure coefficients on building surfaces using artificial neural networks. *Energy and Buildings*, 158:1429–1441, 2018. URL: <https://api.semanticscholar.org/CorpusID:46947288>.
- [226] Junxi Feng, Xiaohai He, Qizhi Teng, Chao Ren, Honggang Chen, and Yang Li. Reconstruction of porous media from extremely limited infor-

- mation using conditional generative adversarial networks. *Physical Review E*, 100, 09 2019. doi:10.1103/PhysRevE.100.033308.
- [227] Diederik P Kingma and Jimmy Ba. Adam: A method for stochastic optimization. *arXiv preprint arXiv:1412.6980*, 2014.
- [228] Nitish Srivastava et al. Dropout: a simple way to prevent neural networks from overfitting. *Journal of Machine Learning Research*, 15(1):1929–1958, 2014.
- [229] MATLAB. Compare Deep Learning Models Using ROC Curves. URL: https://se.mathworks.com/help/deeplearning/ug/compare-s_beta_deep-s_beta_learning-s_beta_models-s_beta_using-s_beta_ROC-s_beta_curves.html.
- [230] MATLAB. What is Confusion Matrix and Advanced Classification Metrics? URL: https://se.mathworks.com/help/deeplearning/ug/compare-s_beta_deep-s_beta_learning-s_beta_models-s_beta_using-s_beta_ROC-s_beta_curves.html.
- [231] CMS Collaboration. Performance of reconstruction and identification of τ leptons decaying to hadrons and ν_τ in pp collisions at $\sqrt{s} = 13$ TeV. *JINST*, 13(10):P10005, 2018. arXiv:1809.02816, doi:10.1088/1748-s_beta0221/13/10/P10005.
- [232] CMS Collaboration. Identification of hadronic tau lepton decays using a deep neural network. *JINST*, 17:P07023, 2022. arXiv:2201.08458, doi:10.1088/1748-s_beta0221/17/07/p07023.
- [233] CMS Collaboration. Performance of electron reconstruction and selection with the CMS detector in proton-proton collisions at $\sqrt{s} = 8$ TeV. *JINST*, 10:P06005, 2015. arXiv:1502.02701, doi:10.1088/1748-s_beta0221/10/06/P06005.
- [234] CMS Collaboration. Performance of the CMS muon detector and muon reconstruction with proton-proton collisions at $\sqrt{s} = 13$ TeV. *JINST*, 13:P06015, 2018. arXiv:1804.04528, doi:10.1088/1748-s_beta0221/13/06/P06015.
- [235] Daniele Bertolini, Philip Harris, Matthew Low, and Nhan Tran. Pileup per particle identification. *JHEP*, 10:059, 2014. arXiv:1407.6013, doi:10.1007/jhep10(2014)059.

- [236] CMS Collaboration. Performance of reconstruction and identification of τ leptons decaying to hadrons and ν_τ in pp collisions at $\sqrt{s} = 13$ TeV. *JINST*, 13:P10005, 2018. arXiv:1809.02816, doi:10.1088/1748-s_B0221/13/10/P10005.
- [237] Sergey Ioffe and Christian Szegedy. Batch normalization: accelerating deep network training by reducing internal covariate shift. In *Proc., 32nd Int. Conf. on Machine Learning, ICML'15*, page 448. JMLR.org, 2015. arXiv:1502.03167.
- [238] Kaiming He, Xiangyu Zhang, Shaoqing Ren, and Jian Sun. Delving deep into rectifiers: Surpassing human-level performance on ImageNet classification. 2015. URL: <http://arxiv.org/abs/1502.01852>, arXiv:1502.01852.
- [239] Ian J. Goodfellow, Yoshua Bengio, and Aaron Courville. *Deep Learning*. MIT Press, Cambridge, MA, USA, 2016. <http://www.deeplearningbook.org>.
- [240] Tsung-Yi Lin, Priya Goyal, Ross Girshick, Kaiming He, and Piotr Dollár. Focal loss for dense object detection. *TPAMI*, 42:318, 2020. arXiv:1708.02002, doi:10.1109/TPAMI.2018.2858826.
- [241] Diederik P. Kingma and Jimmy Ba. Adam: A method for stochastic optimization. In *Proc., 3th Int. Conf. on Learning Representations (ICLR 2015)*, 2015. arXiv:1412.6980.
- [242] Timothy Dozat. Incorporating Nesterov momentum into ADAM. In *Proc., 4th Int. Conf. on Learning Representations (ICLR 2016)*, 2016. URL: <https://openreview.net/pdf?id=OM0jvwB8jIp57ZJjtNEZ>.
- [243] Martín Abadi et al. TensorFlow: Large-Scale Machine Learning on Heterogeneous Systems, 2015. Software available from. URL: <https://www.tensorflow.org/>.
- [244] François Chollet et al. Keras, 2015. Software available from. URL: <https://keras.io>.
- [245] Yaroslav Ganin and Victor Lempitsky. Unsupervised domain adaptation by backpropagation. 2014. arXiv:1409.7495.

- [246] CMS Collaboration. A deep neural network to search for new long-lived particles decaying to jets. *Machine Learning: Science and Technology*, page 035012, 2020. arXiv:1912.12238, doi:10.1088/2632-s β 2153/ab9023.
- [247] Lucas Russell. Identification of Hadronic Tau Lepton Decays with Domain Adaptation using Adversarial Machine Learning at CMS. Master's thesis, Imperial College London, École Polytechnique Fédérale de Lausanne, Jun 2022. URL: <https://cds.cern.ch/record/2827366>.
- [248] CMS Collaboration. Measurements of Inclusive W and Z Cross Sections in pp Collisions at $\sqrt{s} = 7$ TeV. *JHEP*, 01:080, 2011. arXiv:1012.2466, doi:10.1007/JHEP01(2011)080.
- [249] Max Baak, Stefan Gadatsch, Robert Harrington, and Wouter Verkerke. Interpolation between multi-dimensional histograms using a new non-linear moment morphing method. *Nucl. Instrum. Meth. A*, 771:39–48, 2015. arXiv:1410.7388, doi:10.1016/j.nima.2014.10.033.
- [250] Jet Energy Scale and Resolution Measurements Using Prompt Run3 Data Collected by CMS in the Last Months of 2022 at 13.6 TeV. 2023. URL: <https://cds.cern.ch/record/2865846>.
- [251] Huilin Qu and Loukas Gouskos. ParticleNet: Jet Tagging via Particle Clouds. *Phys. Rev. D*, 101(5):056019, 2020. arXiv:1902.08570, doi:10.1103/PhysRevD.101.056019.
- [252] Huilin Qu, Congqiao Li, and Sitian Qian. Particle Transformer for Jet Tagging. 2 2022. arXiv:2202.03772.
- [253] Paola Mastrapasqua. CMS Internal CADILINES: Search for a BSM (pseudo-)scalar boson in the $Z(\rightarrow LL)2\tau$. URL: [https://cms.cern.ch/iCMS/analysisadmin/cadilines?line=B2G-s \$\beta\$ 24-s \$\beta\$ 021&tp=an&id=2907&ancode=B2G-s \$\beta\$ 24-s \$\beta\$ 021](https://cms.cern.ch/iCMS/analysisadmin/cadilines?line=B2G-sβ24-sβ021&tp=an&id=2907&ancode=B2G-sβ24-sβ021).
- [254] G.C. Dorsch, S.J. Huber, K. Mimasu, and J.M. No. Echoes of the Electroweak Phase Transition: Discovering a second Higgs doublet through $A_0 \rightarrow ZH_0$. *Phys.Rev.Lett.*, 113(21):211802, 2014. arXiv:1405.5537, doi:10.1103/PhysRevLett.113.211802.

- [255] CMS Collaboration. Search for neutral resonances decaying into a z boson and a pair of b jets or leptons. *Physics Letters B*, 759, 2016. URL: <http://dx.doi.org/10.1016/j.physletb.2016.05.087>, doi:10.1016/j.physletb.2016.05.087.
- [256] Luminosity Physics Object Group (Lumi POG) – Current recommendations for luminosity estimations. (Retrieved Apr 12, 2019). URL: <https://twiki.cern.ch/twiki/bin/view/CMS/TWikiLUM#CurRec>.
- [257] Johan Alwall et al. The automated computation of tree-level and next-to-leading order differential cross sections, and their matching to parton shower simulations. *JHEP*, 2014(07):079, 2014. doi:10.1007/JHEP07(2014)079.
- [258] Rikkert Frederix et al. The automation of next-to-leading order electroweak calculations. *JHEP*, 2018(07):185, 2018. doi:10.1007/JHEP07(2018)185.
- [259] Simone Alioli, Paolo Nason, Carlo Oleari, and Emanuele Re. NLO vector-boson production matched with shower in POWHEG. *JHEP*, 2008(07):060, 2008. doi:10.1088/1126-s _{β} 6708/2008/07/060.
- [260] Paolo Nason. A new method for combining NLO QCD with shower Monte Carlo algorithms. *JHEP*, 2004(11):040, 2004. doi:10.1088/1126-s _{β} 6708/2004/11/040.
- [261] Stefano Frixione, Paolo Nason, and Carlo Oleari. Matching NLO QCD computations with parton shower simulations: the POWHEG method. *JHEP*, 2007(11):070, 2007. doi:10.1088/1126-s _{β} 6708/2007/11/070.
- [262] Torbjörn Sjöstrand et al. An introduction to PYTHIA 8.2. *Comput. Phys. Commun.*, 191:159–177, 2015. arXiv:1410.3012, doi:10.1016/j.cpc.2015.01.024.
- [263] CMS Collaboration. Extraction and validation of a new set of CMS PYTHIA8 tunes from underlying-event measurements. *CMS-GEN-17-001*, *CERN-EP-2019-007*, 03 2019. URL: <https://arxiv.org/pdf/1903.12179.pdf>, arXiv:1903.12179, doi:10.1140/epjc/s10052-s _{β} 019-s _{β} 7499-s _{β} 4.

- [264] S. Agostinelli et al. GEANT4 — a simulation toolkit. *Nucl. Instrum. Meth. A*, 506:250, 2003. doi:10.1016/S0168-s _{β} 9002(03)01368-s _{β} 8.
- [265] Celine Degrande et al. UFO - The Universal FeynRules Output. *Computer Physics Communications*, 183:1201–1214, 2012. arXiv:1108.2040, doi:10.1016/j.cpc.2012.01.022.
- [266] The general Two-Higgs-Doublet Model: UFO model 2HDMtII_NLO. <https://feynrules.irmp.ucl.ac.be/wiki/2HDM>. (Retrieved Dec 09, 2024).
- [267] Celine Degrande. Automatic evaluation of UV and R2 terms for beyond the Standard Model Lagrangians: a proof-of-principle. *Computer Physics Communications*, 197:239–262, 2015. arXiv:1406.3030, doi:10.1016/j.cpc.2015.08.015.
- [268] Richard D. Ball et al. Parton distributions for the LHC Run II. *JHEP*, 04:040, 2015. arXiv:1410.8849, doi:10.1007/JHEP04(2015)040.
- [269] Madgraph datacards for signal production. https://github.com/pmastrap/genproductions/tree/master/bin/MadGraph5_aMCatNLO/cards/production/13TeV/HToZATo2L2Tau. (Retrieved Dec 09, 2024).
- [270] HToZATo2L2Tau sample production request. [https://gitlab.cern.ch/cms-s _{\$\beta\$} b2g/b-s _{\$\beta\$} 2-s _{\$\beta\$} g-s _{\$\beta\$} m-s _{\$\beta\$} c/sample-s _{\$\beta\$} requests/-s _{\$\beta\$} /merge_requests/39](https://gitlab.cern.ch/cms-s_{β}b2g/b-s_{β}2-s_{β}g-s_{β}m-s_{β}c/sample-s_{β}requests/-s_{β}/merge_requests/39). (Retrieved Dec 09, 2024).
- [271] R. Harlander et al. SusHi: A program for the calculation of Higgs production in gluon fusion and bottom-quark annihilation in the Standard Model and the MSSM. *Comp. Phys. Commun.*, 184:1605–1617, 2013. doi:10.1016/j.cpc.2013.02.006.
- [272] A. M. Sirunyan et al. Performance of the CMS muon detector and muon reconstruction with proton-proton collisions at $\sqrt{s} = 13$ TeV. *JINST*, 13:P06015, 2018. arXiv:1804.04528, doi:10.1088/1748-s _{β} 0221/13/06/P06015.

- [273] Baseline muon selections. <https://twiki.cern.ch/twiki/bin/view/CMSPublic/SWGuideMuonId>. (Retrieved April 23, 2024).
- [274] CMS Collaboration. Performance of the CMS electromagnetic calorimeter in pp collisions at $\sqrt{s} = 13$ TeV. 3 2024. arXiv: 2403.15518.
- [275] EgammaPOG: MVA based electron identification. <https://twiki.cern.ch/twiki/bin/viewauth/CMS/MultivariateElectronIdentification>. (Retrieved April 23, 2024).
- [276] Tau ID Recommendation For Run2. <https://twiki.cern.ch/twiki/bin/viewauth/CMS/TauIDRecommendationForRun2>. (Retrieved Apr 23, 2024).
- [277] JetMET. (Retrieved April 23, 2024). URL: <https://twiki.cern.ch/twiki/bin/view/CMS/JetMET>.
- [278] MissingET Run2 Corrections. <https://twiki.cern.ch/twiki/bin/viewauth/CMS/MissingETRun2Corrections>. (Retrieved April 23, 2024).
- [279] jsonPOG-integration. https://gitlab.cern.ch/cms-s_b_nanoAOD/jsonpog-s_b_integration/-s_b/tree/master/POG?ref_type=heads. (Retrieved Apr 23, 2024).
- [280] Correctionlib. https://cms-s_b_nanoaod.github.io/correctionlib/. (Retrieved Apr 23, 2024).
- [281] Electron Scale Factors. https://twiki.cern.ch/twiki/bin/view/CMS/EgammaRunIIREcommendations#Electron_Scale_Factors. (Retrieved April 23, 2024).
- [282] Electron HLT Scale Factors. <https://twiki.cern.ch/twiki/bin/viewauth/CMS/EgHLTScaleFactorMeasurements>. (Retrieved April 23, 2024).
- [283] Muon Scale Factors. https://twiki.cern.ch/twiki/bin/viewauth/CMS/MuonPOG#User_Recommendations. (Retrieved April 23, 2024).

- [284] CMSJMECalculators. [https://cms-s \$\beta\$ analysis.docs.cern.ch/guidelines/frameworks/frameworks/](https://cms-sβanalysis.docs.cern.ch/guidelines/frameworks/frameworks/). (Retrieved April 23, 2024).
- [285] BTV Recommendations. [https://btv-s \$\beta\$ wiki.docs.cern.ch/](https://btv-sβwiki.docs.cern.ch/). (Retrieved Apr 12, 2019).
- [286] Luminosity Physics Object Group (Lumi POG). (Retrieved Apr 12, 2019). URL: <https://twiki.cern.ch/twiki/bin/viewauth/CMS/L1PrefiringWeightRecipe>.
- [287] CMS Collaboration. Measurements of higgs boson production in the decay channel with a pair of τ leptons in proton–proton collisions at $\sqrt{s} = 13\text{TeV}$. *The European Physical Journal C*, 83(7):562, 2023. doi: 10.1140/epjc/s10052-s β 023-s β 11452-s β 8.
- [288] Pierre Baldi, Kyle Cranmer, Taylor Faucett, Peter Sadowski, and Daniel Whiteson. Parameterized machine learning for high-energy physics. 01 2016. URL: <https://arxiv.org/pdf/1601.07913.pdf>, arXiv:1601.07913, doi:10.1140/epjc/s10052-s β 016-s β 4099-s β 4.
- [289] Antonio Gulli and Sujit Pal. *Deep Learning with Keras*. Packt Publishing Ltd, 2017.
- [290] Martín Abadi et al. Tensorflow: Large-scale machine learning on heterogeneous distributed systems. <https://arxiv.org/abs/1603.04467>, 2016. arXiv:1603.04467.
- [291] Lorenzo Bianchini et al. Reconstruction of the Higgs mass in events with Higgs bosons decaying into a pair of τ leptons using matrix element techniques. *Nucl. Instrum. Meth. A*, 862:54–84, 2017. arXiv: 1603.05910, doi:10.1016/j.nima.2017.05.001.
- [292] Lorenzo Bianchini et al. Reconstruction of the Higgs mass in $H \rightarrow \tau\tau$ Events by Dynamical Likelihood techniques. *Journal of Physics: Conference Series*, 513(2):022035, jun 2014. URL: [https://dx.doi.org/10.1088/1742-s \$\beta\$ 6596/513/2/022035](https://dx.doi.org/10.1088/1742-sβ6596/513/2/022035), doi:10.1088/1742-s β 6596/513/2/022035.
- [293] Luminosity Recommendations Run 2. https://twiki.cern.ch/twiki/bin/view/CMS/LumiRecommendationsRun2#Combination_and_correlations. (Retrieved Apr 12, 2019).

- [294] Roger Barlow and Claire Beeston. Fitting using finite Monte Carlo samples. *Comput. Phys. Commun.*, 77:219–228, 1993. doi:10.1016/0010-s _{β} 4655(93)90005-s _{β} W.
- [295] Khawla Jaffel. CMS Internal CADILINES: Search for neutral heavy Higgs bosons in the context of a 2HDM via $H/A \rightarrow Z(l^+l^-) \rightarrow A/H(b\bar{b})$ with full Run 2 data set . URL: [https://cms.cern.ch/iCMS/analysisadmin/cadilines?line=HIG-s _{\$\beta\$} 22-s _{\$\beta\$} 010&tp=an&id=2595&ancode=HIG-s _{\$\beta\$} 22-s _{\$\beta\$} 010](https://cms.cern.ch/iCMS/analysisadmin/cadilines?line=HIG-s_{β}22-s_{β}010&tp=an&id=2595&ancode=HIG-s_{β}22-s_{β}010).
- [296] CMS Collaboration. Search for a heavy CP-odd Higgs boson decaying into a 125 GeV Higgs boson and a Z boson in final states with two tau and two light leptons at 13 TeV. CMS Physics Analysis Summary CMS-PAS-HIG-22-004, 224. URL: [https://cms-s _{\$\beta\$} results.web.cern.ch/cms-s _{\$\beta\$} results/public-s _{\$\beta\$} results/preliminary-s _{\$\beta\$} results/HIG-s _{\$\beta\$} 22-s _{\$\beta\$} 004/index.html](https://cms-s_{β}results.web.cern.ch/cms-s_{β}results/public-s_{β}results/preliminary-s_{β}results/HIG-s_{β}22-s_{β}004/index.html).
- [297] American Physical Society / Division of Particles and Fields. *2021 US Community Study on the Future of Particle Physics (Snowmass2021)*, Seattle, WA and virtual, July 2021. Final meeting held July 2022, proceedings available via SLAC eConf C210711. URL: <https://www.slac.stanford.edu/econf/C210711/>.
- [298] Gudrun Heinrich, S. P. Jones, M. Kerner, G. Luisoni, and E. Vryonidou. Probing the trilinear Higgs boson coupling in di-Higgs production at NLO QCD including parton shower effects. *JHEP*, 2019(06):066, 2019. arXiv:1903.08137, doi:10.1007/JHEP06(2019)066.
- [299] Pieter David. Readable and efficient HEP data analysis with bamboo. In *EPJ Web Conf.*, volume 251, page 03026, 2021. doi:10.1051/epjconf/202125103026.
- [300] CMS Collaboration. Recommendations for Systematic Uncertainties for the HL-LHC and HE-LHC. <https://twiki.cern.ch/twiki/bin/viewauth/CMS/YR2018Systematics>, 2018.
- [301] C. G. Lester and D. J. Summers. Measuring masses of semiinvisibly decaying particles pair produced at hadron colliders. *Phys. Lett. B*, 463:99–103, 1999. arXiv:hep-s _{β} ph/9906349, doi:10.1016/S0370-s _{β} 2693(99)00945-s _{β} 4.

- [302] C. G. Lester. The stransverse mass, m_{T2} , in special cases. *Journal of High Energy Physics*, pages 1–17, 2011.
- [303] Tom Gillam. m_{T2} : Implementation of the stransverse mass calculator in c++ and python. <https://github.com/tpgillam/mt2>, 2016. Accessed: 2025-06-24.
- [304] M. Cepeda et al. Report from Working Group 2: Higgs Physics at the HL-LHC and HE-LHC. *CERN Yellow Rep. Monogr.*, 7:221–584, 2019. arXiv:1902.00134, doi:10.23731/CYRM-s β 2019-s β 007.221.
- [305] CMS Collaboration. CMS HH Inference Tools. [https://cms-s \$\beta\$ hh.web.cern.ch/tools/inference/index.html](https://cms-sβhh.web.cern.ch/tools/inference/index.html), 2023.
- [306] CMS Collaboration. The Phase-2 Upgrade of the CMS Data Acquisition and High Level Trigger. Technical Design Report CERN-LHCC-2021-007, CMS-TDR-022, CERN, 2021. CMS Technical Design Report. URL: <https://cds.cern.ch/record/2776282>.
- [307] CMS Collaboration. The phase-2 upgrade of the cms level-1 trigger. Technical Design Report CERN-LHCC-2020-004, CMS-TDR-021, CERN, 2020. CMS Technical Design Report. URL: <https://cds.cern.ch/record/2714892>.
- [308] Michelangelo L. Mangano, Giacomo Ortona, and Michele Selvaggi. Measuring the Higgs self-coupling via Higgs-pair production at a 100 TeV p-p collider. *EPJC*, 80(11):1030, Nov 2020. URL: [http://dx.doi.org/10.1140/epjc/s10052-s \$\beta\$ 020-s \$\beta\$ 08595-s \$\beta\$ 3](http://dx.doi.org/10.1140/epjc/s10052-sβ020-sβ08595-sβ3), doi:10.1140/epjc/s10052-s β 020-s β 08595-s β 3.
- [309] M. Aleksa et al. Conceptual design of an experiment at the FCC-hh, a future 100 TeV hadron collider. 2/2022, 2022. doi:10.23731/CYRM-s β 2022-s β 002.
- [310] Brieuc Francois and Gerardo Ganis. *The FCC software for PED studies*, December 2024. doi:10.17181/8k0c4-s β nkrr70.
- [311] Placido Fernandez Declara et al. The Key4hep turnkey software stack for future colliders. *PoS, EPS-HEP2021*:844, 2022. doi:10.22323/1.398.0844.

- [312] Birgit Stapf and Juraj Smiesko. List of fcc_v07 official FCC-hh production samples, 2025. <https://fcc-s_βphysics-s_βevents.web.cern.ch/fcc-s_βhh/delphes/fcc-s_βv07/ii> or https://fcc-s_βphysics-s_βevents.web.cern.ch/fcc-s_βhh/Delphesevents_fcc_v07/II.php.
- [313] Matteo Cacciari, Gavin P Salam, and Gregory Soyez. The anti-kt jet clustering algorithm. *Journal of High Energy Physics*, 2008(04):063–063, April 2008. URL: <http://dx.doi.org/10.1088/1126-s_β6708/2008/04/063>, doi:10.1088/1126-s_β6708/2008/04/063.
- [314] Bastien Voirin and Claude Charlot. Extracting trilinear Higgs boson self-coupling events from HH production at the FCC-hh . March 2025. doi:10.17181/6mq27-s_βncc26.
- [315] S. Tentori et al. Constraining the real scalar singlet extension of the standard model. To appear, 2025.
- [316] Degens J. Gwilliam C. Sebastiani C. Valentine S. Wood L. D’Onofrio, M. Feasibility studies for $HH \rightarrow b\bar{b}\tau\tau$ at the FCC-hh using graph-neural networks, 2025. Submitted to the 2025 Update of the European Strategy for Particle Physics. doi:10.17181/p8y5f-s_β23w42.

Appendix

A Study of (m_A, m_H) mass resolution

This section explains the strategy adopted to study the mass resolution in the (m_A, m_H) 2D plane and realise Figure 7.4 in Section 7.2.2.

Few mass scenarios were simulated and reconstructed using the SVfit algorithm for the estimate of the tau pair invariant mass. The (m_A, m_H) distribution has been fitted with a bivariate Gaussian, as shown in Left Figure 27 for the example case of $(m_A, m_H)=(400,600)$. Although the Gaussian assumption is not extremely accurate, it is easy and good enough for the sake of this exercise.

Ellipses (or probability contours) define the region of a minimum area (or volume in multivariate case) containing a given probability under the Gaussian assumption. In our case we are interested in a confidence level of 68% ($1-\sigma$). Given the 2D Gaussian fit fitted parameters, $\mu = (x_0, y_0)$ and covariance matrix Σ , is possible to evaluate the ellipse center, the height, the width and the tilt angle. While the ellipse center is simply $\mu = (x_0, y_0)$, for the other parameters few computation steps are required. The first one is to calculate the covariance matrix eigenvectors, $\mathbf{e}_1 = (e_1^x, e_1^y)$ and $\mathbf{e}_2 = (e_2^x, e_2^y)$, and eigenvalues, λ_1 and λ_2 . Then the ellipse parameters are:

$$height = 2\sqrt{\chi_2^2(0.32)\lambda_1} \quad width = 2\sqrt{\chi_2^2(0.32)\lambda_2} \quad tilt = \arctan\left(\frac{e_2^x\sqrt{\lambda_1}}{e_1^x\sqrt{\lambda_1}}\right)$$

where $\chi_2^2(\alpha)$ is the upper (100α) th percentile of the χ^2 -distribution with two degrees of freedom. An example of $1-\sigma$ is shown in Right Figure 27. In this way ellipses in Figure 28 are built. In order to extrapolate the ellipse shapes to the whole mass region of interest, the trend of the ellipses parameters is evaluated as a function of the A and H bosons mass. The x_0 coordinate is simply fitted as function of the A boson mass, while the y_0 coordinate as a function of the H mass, as reported in Figure 29. The remaining parameters are instead fitted as a function of $(m_H - m_A)/m_H$, as visible in Figure 30.

Although some fits have a high χ^2/ndf , the extrapolation succeeds in capturing the key elements of the ellipses evolution across the mass plane, i.e. the increase of the ellipse area and of the center displacement with the boson mass value and the increase of the tilt angle when approaching the diagonal.

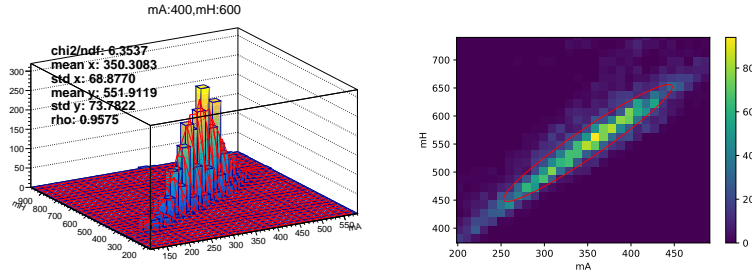


Figure 27: Example of Gaussian fit of the 2D (m_A, m_H) distribution for the simulated mass point $(m_A, m_H) = (400, 600)$ GeV (Left). The same distribution is shown together with the 1- σ ellipse, calculated from the Gaussian fit (Right).

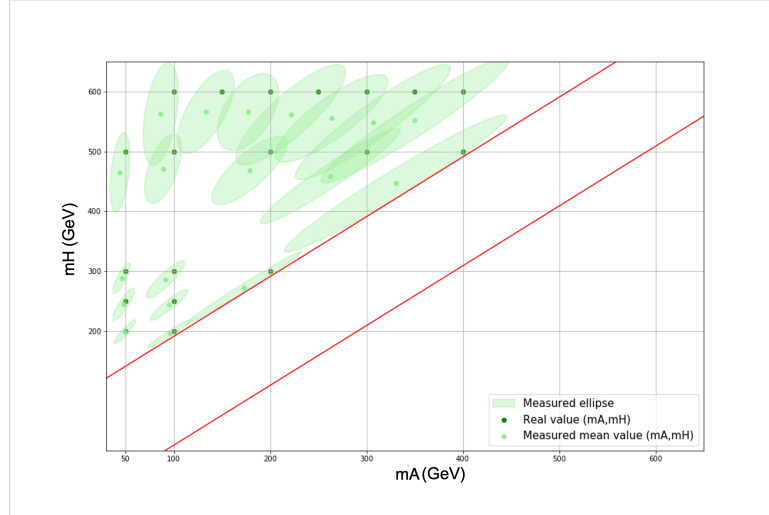


Figure 28: 1- σ ellipses calculated from the Gaussian fit for the few points simulated for this investigation.

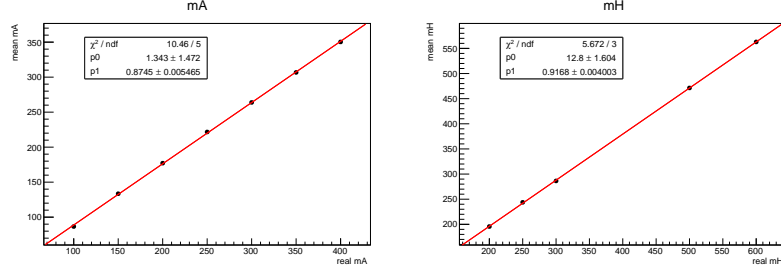


Figure 29: Linear fit of the x_0 ellipse parameter as a function of m_A (Left) and of the y_0 parameter as a function of m_H (Right).

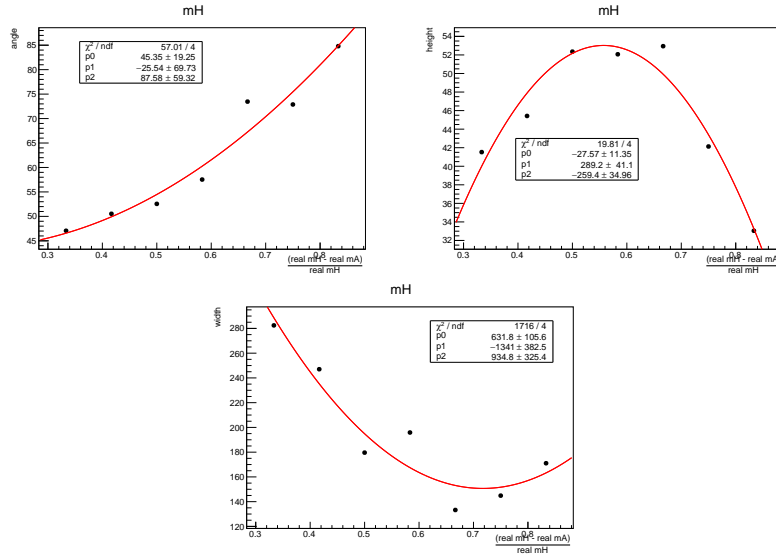


Figure 30: Second-degree polynomial fit of the ellipse angle, height and width as a function of $(m_H - m_A)/m_H$.

B Signal sample full list

Table 24: (1/3) Centrally produced HZA signals with the corresponding $\sigma \times BR$.

/HToZATo2L2Tau_170p00_50p00_1p50_ggH_TuneCP5_13TeV-amcatnlo-pythia8	0.0302 pb
/HToZATo2L2Tau_200p00_20p00_1p50_ggH_TuneCP5_13TeV-amcatnlo-pythia8	0.0192 pb
/HToZATo2L2Tau_200p00_35p00_1p50_ggH_TuneCP5_13TeV-amcatnlo-pythia8	0.0207 pb
/HToZATo2L2Tau_200p00_50p00_1p50_ggH_TuneCP5_13TeV-amcatnlo-pythia8	0.0221 pb
/HToZATo2L2Tau_200p00_60p00_1p50_ggH_TuneCP5_13TeV-amcatnlo-pythia8	0.0228 pb
/HToZATo2L2Tau_200p00_70p00_1p50_ggH_TuneCP5_13TeV-amcatnlo-pythia8	0.0233 pb
/HToZATo2L2Tau_200p00_80p00_1p50_ggH_TuneCP5_13TeV-amcatnlo-pythia8	0.0236 pb
/HToZATo2L2Tau_200p00_90p00_1p50_ggH_TuneCP5_13TeV-amcatnlo-pythia8	0.0234 pb
/HToZATo2L2Tau_250p00_125p00_1p50_ggH_TuneCP5_13TeV-amcatnlo-pythia8	0.0162 pb
/HToZATo2L2Tau_250p00_20p00_1p50_ggH_TuneCP5_13TeV-amcatnlo-pythia8	0.0125 pb
/HToZATo2L2Tau_250p00_35p00_1p50_ggH_TuneCP5_13TeV-amcatnlo-pythia8	0.0135 pb
/HToZATo2L2Tau_250p00_50p00_1p50_ggH_TuneCP5_13TeV-amcatnlo-pythia8	0.0144 pb
/HToZATo2L2Tau_250p00_60p00_1p50_ggH_TuneCP5_13TeV-amcatnlo-pythia8	0.0149 pb
/HToZATo2L2Tau_250p00_70p00_1p50_ggH_TuneCP5_13TeV-amcatnlo-pythia8	0.0153 pb
/HToZATo2L2Tau_250p00_80p00_1p50_ggH_TuneCP5_13TeV-amcatnlo-pythia8	0.0156 pb
/HToZATo2L2Tau_250p00_90p00_1p50_ggH_TuneCP5_13TeV-amcatnlo-pythia8	0.0159 pb
/HToZATo2L2Tau_300p00_125p00_1p50_ggH_TuneCP5_13TeV-amcatnlo-pythia8	0.0123 pb
/HToZATo2L2Tau_300p00_150p00_1p50_ggH_TuneCP5_13TeV-amcatnlo-pythia8	0.0124 pb
/HToZATo2L2Tau_300p00_175p00_1p50_ggH_TuneCP5_13TeV-amcatnlo-pythia8	0.0122 pb
/HToZATo2L2Tau_300p00_20p00_1p50_ggH_TuneCP5_13TeV-amcatnlo-pythia8	0.0094 pb
/HToZATo2L2Tau_300p00_35p00_1p50_ggH_TuneCP5_13TeV-amcatnlo-pythia8	0.0101 pb
/HToZATo2L2Tau_300p00_50p00_1p50_ggH_TuneCP5_13TeV-amcatnlo-pythia8	0.0108 pb
/HToZATo2L2Tau_300p00_60p00_1p50_ggH_TuneCP5_13TeV-amcatnlo-pythia8	0.0112 pb
/HToZATo2L2Tau_300p00_70p00_1p50_ggH_TuneCP5_13TeV-amcatnlo-pythia8	0.0115 pb
/HToZATo2L2Tau_300p00_80p00_1p50_ggH_TuneCP5_13TeV-amcatnlo-pythia8	0.0117 pb
/HToZATo2L2Tau_300p00_90p00_1p50_ggH_TuneCP5_13TeV-amcatnlo-pythia8	0.0119 pb
/HToZATo2L2Tau_350p00_100p00_1p50_ggH_TuneCP5_13TeV-amcatnlo-pythia8	0.0118 pb
/HToZATo2L2Tau_350p00_125p00_1p50_ggH_TuneCP5_13TeV-amcatnlo-pythia8	0.0121 pb
/HToZATo2L2Tau_350p00_150p00_1p50_ggH_TuneCP5_13TeV-amcatnlo-pythia8	0.0121 pb
/HToZATo2L2Tau_350p00_175p00_1p50_ggH_TuneCP5_13TeV-amcatnlo-pythia8	0.0120 pb
/HToZATo2L2Tau_350p00_20p00_1p50_ggH_TuneCP5_13TeV-amcatnlo-pythia8	0.0092 pb
/HToZATo2L2Tau_350p00_200p00_1p50_ggH_TuneCP5_13TeV-amcatnlo-pythia8	0.0116 pb
/HToZATo2L2Tau_350p00_250p00_1p50_ggH_TuneCP5_13TeV-amcatnlo-pythia8	0.0054 pb
/HToZATo2L2Tau_350p00_35p00_1p50_ggH_TuneCP5_13TeV-amcatnlo-pythia8	0.0099 pb
/HToZATo2L2Tau_350p00_50p00_1p50_ggH_TuneCP5_13TeV-amcatnlo-pythia8	0.0106 pb
/HToZATo2L2Tau_350p00_60p00_1p50_ggH_TuneCP5_13TeV-amcatnlo-pythia8	0.0110 pb
/HToZATo2L2Tau_350p00_75p00_1p50_ggH_TuneCP5_13TeV-amcatnlo-pythia8	0.0114 pb

Table 25: (2/3) Centrally produced HZA signals with the corresponding $\sigma \times BR$.

/HToZATo2L2Tau_400p00_100p00_1p50_ggH_TuneCP5_13TeV-amcatnlo-pythia8	0.0097 pb
/HToZATo2L2Tau_400p00_125p00_1p50_ggH_TuneCP5_13TeV-amcatnlo-pythia8	0.0097 pb
/HToZATo2L2Tau_400p00_150p00_1p50_ggH_TuneCP5_13TeV-amcatnlo-pythia8	0.0095 pb
/HToZATo2L2Tau_400p00_175p00_1p50_ggH_TuneCP5_13TeV-amcatnlo-pythia8	0.0092 pb
/HToZATo2L2Tau_400p00_200p00_1p50_ggH_TuneCP5_13TeV-amcatnlo-pythia8	0.0076 pb
/HToZATo2L2Tau_400p00_200p00_1p50_ggH_TuneCP5_13TeV-amcatnlo-pythia8	0.0085 pb
/HToZATo2L2Tau_400p00_250p00_1p50_ggH_TuneCP5_13TeV-amcatnlo-pythia8	0.0058 pb
/HToZATo2L2Tau_400p00_300p00_1p50_ggH_TuneCP5_13TeV-amcatnlo-pythia8	0.0005 pb
/HToZATo2L2Tau_400p00_350p00_1p50_ggH_TuneCP5_13TeV-amcatnlo-pythia8	0.0083 pb
/HToZATo2L2Tau_400p00_500p00_1p50_ggH_TuneCP5_13TeV-amcatnlo-pythia8	0.0088 pb
/HToZATo2L2Tau_400p00_60p00_1p50_ggH_TuneCP5_13TeV-amcatnlo-pythia8	0.0091 pb
/HToZATo2L2Tau_400p00_75p00_1p50_ggH_TuneCP5_13TeV-amcatnlo-pythia8	0.0094 pb
/HToZATo2L2Tau_500p00_100p00_1p50_ggH_TuneCP5_13TeV-amcatnlo-pythia8	0.0042 pb
/HToZATo2L2Tau_500p00_125p00_1p50_ggH_TuneCP5_13TeV-amcatnlo-pythia8	0.0043 pb
/HToZATo2L2Tau_500p00_150p00_1p50_ggH_TuneCP5_13TeV-amcatnlo-pythia8	0.0043 pb
/HToZATo2L2Tau_500p00_200p00_1p50_ggH_TuneCP5_13TeV-amcatnlo-pythia8	0.0033 pb
/HToZATo2L2Tau_500p00_200p00_1p50_ggH_TuneCP5_13TeV-amcatnlo-pythia8	0.0040 pb
/HToZATo2L2Tau_500p00_250p00_1p50_ggH_TuneCP5_13TeV-amcatnlo-pythia8	0.0034 pb
/HToZATo2L2Tau_500p00_300p00_1p50_ggH_TuneCP5_13TeV-amcatnlo-pythia8	0.0021 pb
/HToZATo2L2Tau_500p00_350p00_1p50_ggH_TuneCP5_13TeV-amcatnlo-pythia8	9.774×10^{-6} pb
/HToZATo2L2Tau_500p00_400p00_1p50_ggH_TuneCP5_13TeV-amcatnlo-pythia8	3.899×10^{-7} pb
/HToZATo2L2Tau_500p00_50p00_1p50_ggH_TuneCP5_13TeV-amcatnlo-pythia8	0.0039 pb
/HToZATo2L2Tau_500p00_75p00_1p50_ggH_TuneCP5_13TeV-amcatnlo-pythia8	0.0041 pb
/HToZATo2L2Tau_600p00_100p00_1p50_ggH_TuneCP5_13TeV-amcatnlo-pythia8	0.0018 pb
/HToZATo2L2Tau_600p00_125p00_1p50_ggH_TuneCP5_13TeV-amcatnlo-pythia8	0.0019 pb
/HToZATo2L2Tau_600p00_150p00_1p50_ggH_TuneCP5_13TeV-amcatnlo-pythia8	0.0019 pb
/HToZATo2L2Tau_600p00_200p00_1p50_ggH_TuneCP5_13TeV-amcatnlo-pythia8	0.0014 pb
/HToZATo2L2Tau_600p00_200p00_1p50_ggH_TuneCP5_13TeV-amcatnlo-pythia8	0.0018 pb
/HToZATo2L2Tau_600p00_250p00_1p50_ggH_TuneCP5_13TeV-amcatnlo-pythia8	0.0016 pb
/HToZATo2L2Tau_600p00_300p00_1p50_ggH_TuneCP5_13TeV-amcatnlo-pythia8	0.0012 pb
/HToZATo2L2Tau_600p00_350p00_1p50_ggH_TuneCP5_13TeV-amcatnlo-pythia8	8.257×10^{-6} pb
/HToZATo2L2Tau_600p00_400p00_1p50_ggH_TuneCP5_13TeV-amcatnlo-pythia8	3.518×10^{-6} pb
/HToZATo2L2Tau_600p00_450p00_1p50_ggH_TuneCP5_13TeV-amcatnlo-pythia8	1.565×10^{-6} pb
/HToZATo2L2Tau_600p00_50p00_1p50_ggH_TuneCP5_13TeV-amcatnlo-pythia8	0.0017 pb
/HToZATo2L2Tau_600p00_500p00_1p50_ggH_TuneCP5_13TeV-amcatnlo-pythia8	9.118×10^{-6} pb
/HToZATo2L2Tau_600p00_75p00_1p50_ggH_TuneCP5_13TeV-amcatnlo-pythia8	0.0018 pb

Table 26: (3/3) Centrally produced HZA signals with the corresponding $\sigma \times BR$.

/HToZATo2L2Tau_700p00_100p00_1p50_ggH_TuneCP5_13TeV-amcatnlo-pythia8	0.00083 pb
/HToZATo2L2Tau_700p00_150p00_1p50_ggH_TuneCP5_13TeV-amcatnlo-pythia8	0.00085 pb
/HToZATo2L2Tau_700p00_200p00_1p50_ggH_TuneCP5_13TeV-amcatnlo-pythia8	0.00065 pb
/HToZATo2L2Tau_700p00_200p00_1p50_ggH_TuneCP5_13TeV-amcatnlo-pythia8	0.00083 pb
/HToZATo2L2Tau_700p00_300p00_1p50_ggH_TuneCP5_13TeV-amcatnlo-pythia8	0.00058 pb
/HToZATo2L2Tau_700p00_400p00_1p50_ggH_TuneCP5_13TeV-amcatnlo-pythia8	2.2796×10^{-6} pb
/HToZATo2L2Tau_700p00_50p00_1p50_ggH_TuneCP5_13TeV-amcatnlo-pythia8	0.00075 pb
/HToZATo2L2Tau_700p00_500p00_1p50_ggH_TuneCP5_13TeV-amcatnlo-pythia8	1.1511×10^{-6} pb
/HToZATo2L2Tau_700p00_550p00_1p50_ggH_TuneCP5_13TeV-amcatnlo-pythia8	5.3147×10^{-7} pb
/HToZATo2L2Tau_800p00_100p00_1p50_ggH_TuneCP5_13TeV-amcatnlo-pythia8	0.00040 pb
/HToZATo2L2Tau_800p00_150p00_1p50_ggH_TuneCP5_13TeV-amcatnlo-pythia8	0.00041 pb
/HToZATo2L2Tau_800p00_200p00_1p50_ggH_TuneCP5_13TeV-amcatnlo-pythia8	0.00031 pb
/HToZATo2L2Tau_800p00_200p00_1p50_ggH_TuneCP5_13TeV-amcatnlo-pythia8	0.00040 pb
/HToZATo2L2Tau_800p00_300p00_1p50_ggH_TuneCP5_13TeV-amcatnlo-pythia8	0.00029 pb
/HToZATo2L2Tau_800p00_400p00_1p50_ggH_TuneCP5_13TeV-amcatnlo-pythia8	1.2237×10^{-6} pb
/HToZATo2L2Tau_800p00_50p00_1p50_ggH_TuneCP5_13TeV-amcatnlo-pythia8	0.00036 pb
/HToZATo2L2Tau_800p00_500p00_1p50_ggH_TuneCP5_13TeV-amcatnlo-pythia8	8.5131×10^{-7} pb
/HToZATo2L2Tau_800p00_600p00_1p50_ggH_TuneCP5_13TeV-amcatnlo-pythia8	4.7250×10^{-7} pb
/HToZATo2L2Tau_800p00_650p00_1p50_ggH_TuneCP5_13TeV-amcatnlo-pythia8	2.13301×10^{-7} pb
/HToZATo2L2Tau_900p00_100p00_1p50_ggH_TuneCP5_13TeV-amcatnlo-pythia8	0.00020 pb
/HToZATo2L2Tau_900p00_150p00_1p50_ggH_TuneCP5_13TeV-amcatnlo-pythia8	0.00021 pb
/HToZATo2L2Tau_900p00_200p00_1p50_ggH_TuneCP5_13TeV-amcatnlo-pythia8	0.00016 pb
/HToZATo2L2Tau_900p00_200p00_1p50_ggH_TuneCP5_13TeV-amcatnlo-pythia8	0.00020 pb
/HToZATo2L2Tau_900p00_300p00_1p50_ggH_TuneCP5_13TeV-amcatnlo-pythia8	0.00015 pb
/HToZATo2L2Tau_900p00_400p00_1p50_ggH_TuneCP5_13TeV-amcatnlo-pythia8	6.4533×10^{-7} pb
/HToZATo2L2Tau_900p00_50p00_1p50_ggH_TuneCP5_13TeV-amcatnlo-pythia8	0.00018 pb
/HToZATo2L2Tau_900p00_500p00_1p50_ggH_TuneCP5_13TeV-amcatnlo-pythia8	4.9191×10^{-7} pb
/HToZATo2L2Tau_900p00_600p00_1p50_ggH_TuneCP5_13TeV-amcatnlo-pythia8	3.8911×10^{-7} pb
/HToZATo2L2Tau_900p00_700p00_1p50_ggH_TuneCP5_13TeV-amcatnlo-pythia8	2.1485×10^{-7} pb
/HToZATo2L2Tau_900p00_750p00_1p50_ggH_TuneCP5_13TeV-amcatnlo-pythia8	9.4501×10^{-8} pb
/HToZATo2L2Tau_1000p00_150p00_1p50_ggH_TuneCP5_13TeV-amcatnlo-pythia8	0.00011 pb
/HToZATo2L2Tau_1000p00_20p00_1p50_ggH_TuneCP5_13TeV-amcatnlo-pythia8	8.1487×10^{-5} pb
/HToZATo2L2Tau_1000p00_200p00_1p50_ggH_TuneCP5_13TeV-amcatnlo-pythia8	0.00011 pb
/HToZATo2L2Tau_1000p00_300p00_1p50_ggH_TuneCP5_13TeV-amcatnlo-pythia8	7.8433×10^{-5} pb
/HToZATo2L2Tau_1000p00_400p00_1p50_ggH_TuneCP5_13TeV-amcatnlo-pythia8	3.4643×10^{-7} pb
/HToZATo2L2Tau_1000p00_50p00_1p50_ggH_TuneCP5_13TeV-amcatnlo-pythia8	9.4220×10^{-5} pb
/HToZATo2L2Tau_1000p00_500p00_1p50_ggH_TuneCP5_13TeV-amcatnlo-pythia8	2.7355×10^{-7} pb
/HToZATo2L2Tau_1000p00_600p00_1p50_ggH_TuneCP5_13TeV-amcatnlo-pythia8	2.3949×10^{-7} pb
/HToZATo2L2Tau_1000p00_700p00_1p50_ggH_TuneCP5_13TeV-amcatnlo-pythia8	1.9351×10^{-7} pb
/HToZATo2L2Tau_1000p00_800p00_1p50_ggH_TuneCP5_13TeV-amcatnlo-pythia8	1.0462×10^{-7} pb

Table 27: Centrally produced AZH signals with the corresponding $\sigma \times BR$.

/AToZHTo2L2Tau_300p00_150p00_1p50_ggH_TuneCP5_13TeV-amcatnlo-pythia8	0.04343 pb
/AToZHTo2L2Tau_500p00_200p00_1p50_ggH_TuneCP5_13TeV-amcatnlo-pythia8	0.00807 pb
/AToZHTo2L2Tau_600p00_400p00_1p50_ggH_TuneCP5_13TeV-amcatnlo-pythia8	1.8045×10^{-5} pb
/AToZHTo2L2Tau_700p00_300p00_1p50_ggH_TuneCP5_13TeV-amcatnlo-pythia8	0.00018 pb
/AToZHTo2L2Tau_700p00_500p00_1p50_ggH_TuneCP5_13TeV-amcatnlo-pythia8	2.8494×10^{-6} pb

C $Z p_T$ correction weights

$Z p_T$ correction weights applied in the analysis, measured as described in Sec. 7.4.11, for the different Run 2 eras.

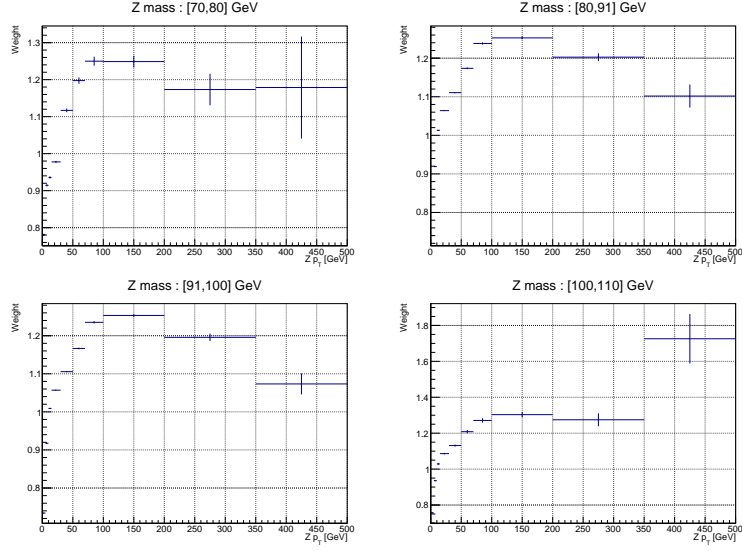


Figure 31: 2018 weights as a function of p_T , for different $m_{\ell\ell}$ regions.

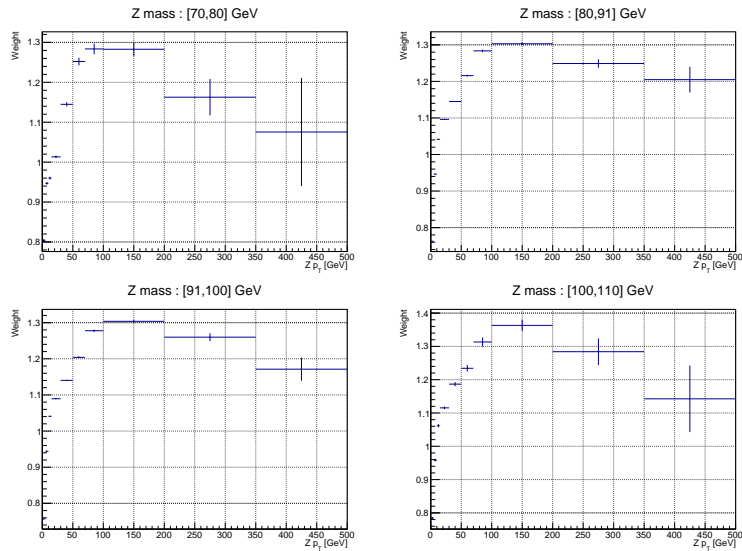


Figure 32: 2017 weights as a function of p_T , for different $m_{\ell\ell}$ regions.

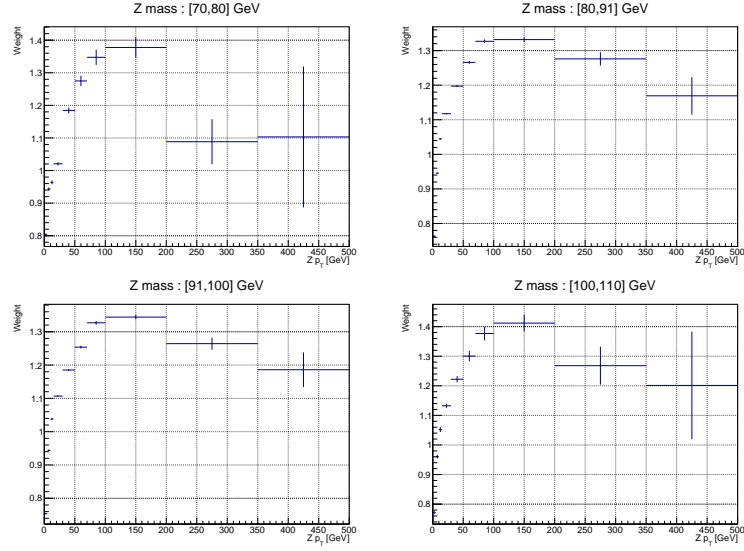


Figure 33: 2016-postVFP weights as a function of p_T , for different $m_{\ell\ell}$ regions.

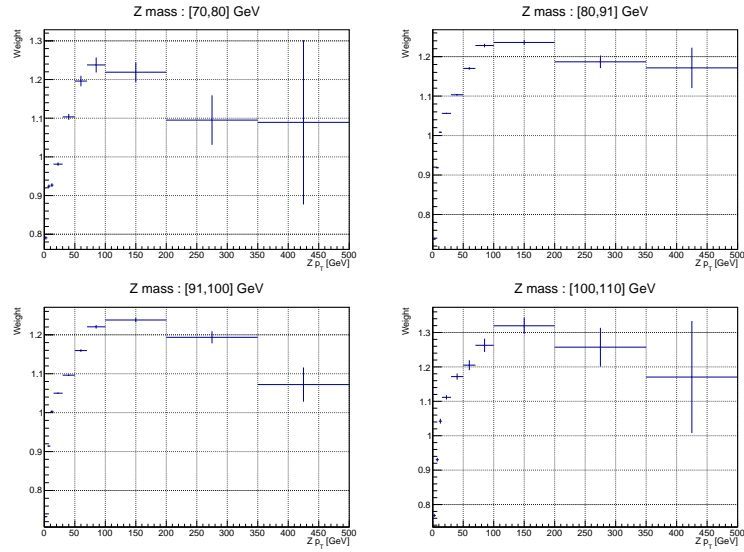


Figure 34: 2016-preVFP weights as a function of p_T , for different $m_{\ell\ell}$ regions.

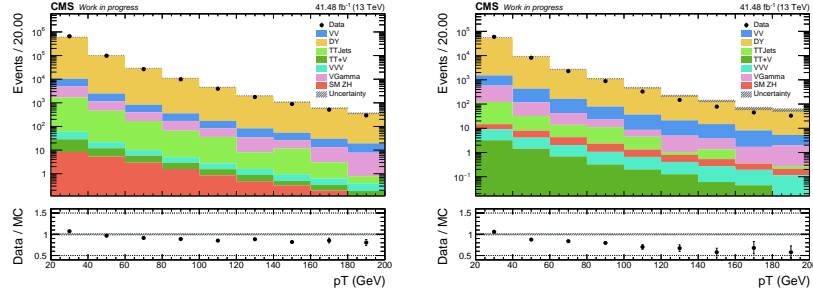
D Distributions for $Z + 1L$ CR in 2016 and 2017

Figure 35: p_T distributions in the $Z + \tau_h$ CR for the τ_h candidate passing the loose (left) and nominal (right) identification criteria. Plots refer to 2017 data taking year.

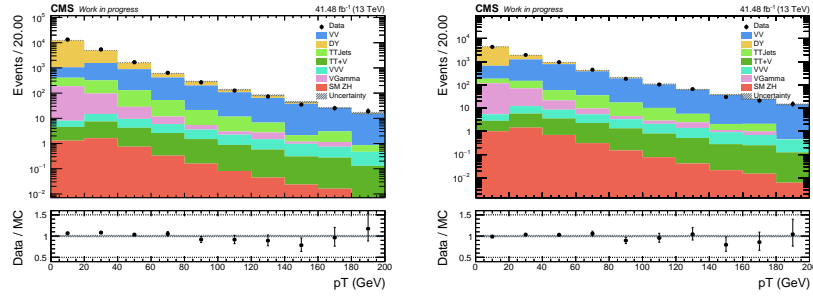


Figure 36: p_T distributions in the $Z + \mu$ CR for the muon candidate passing the loose (left) and nominal (right) identification criteria. Plots refer to 2017 data taking year.

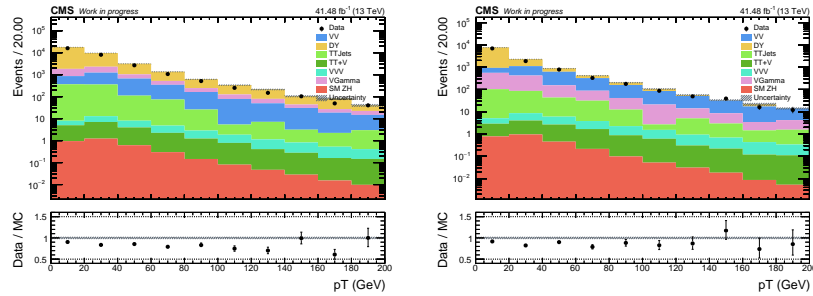


Figure 37: p_T distributions in the $Z + e$ CR for the electron candidate passing the loose (left) and nominal (right) identification criteria. Plots refer to 2017 data taking year.

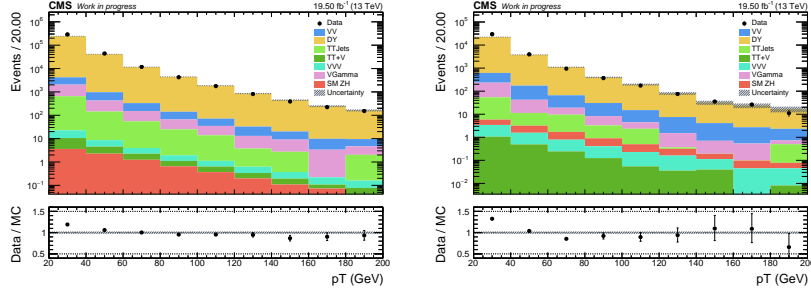


Figure 38: p_T distributions in the $Z + \tau_h$ CR for the τ_h candidate passing the loose (left) and nominal (right) identification criteria. Plots refer to 2016–preVFP data taking year.

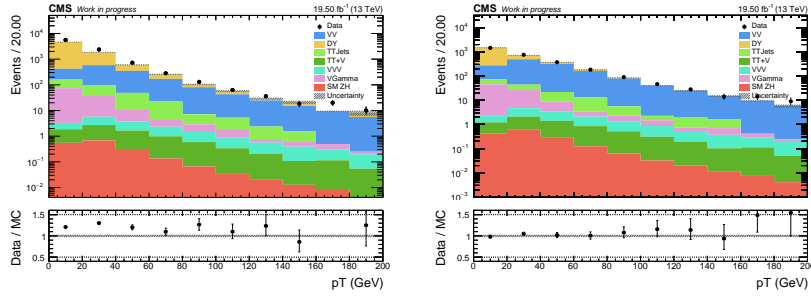


Figure 39: p_T distributions in the $Z + \mu$ CR for the muon candidate passing the loose (left) and nominal (right) identification criteria. Plots refer to 2016–preVFP data taking year.

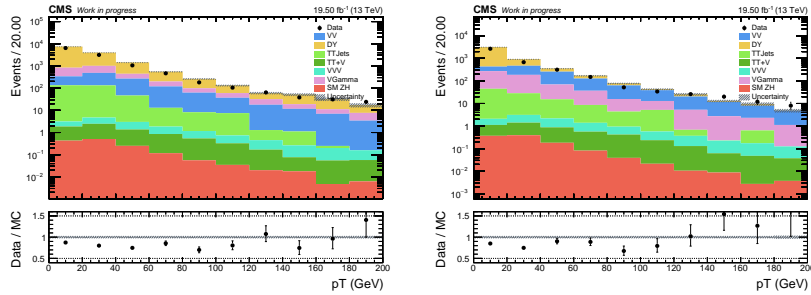


Figure 40: p_T distributions in the $Z + e$ CR for the electron candidate passing the loose (left) and nominal (right) identification criteria. Plots refer to 2016–preVFP data taking year.

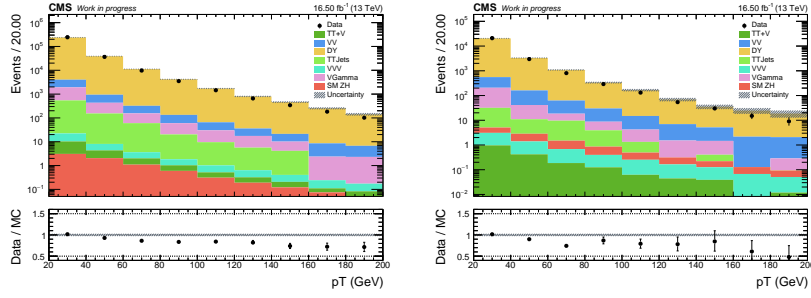


Figure 41: p_T distributions in the $Z + \tau_h$ CR for the τ_h candidate passing the loose (left) and nominal (right) identification criteria. Plots refer to 2016–postVFP data taking year.

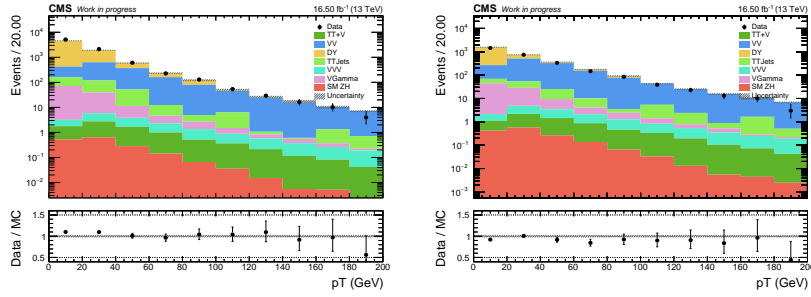


Figure 42: p_T distributions in the $Z + \mu$ CR for the muon candidate passing the loose (left) and nominal (right) identification criteria. Plots refer to 2016–postVFP data taking year.

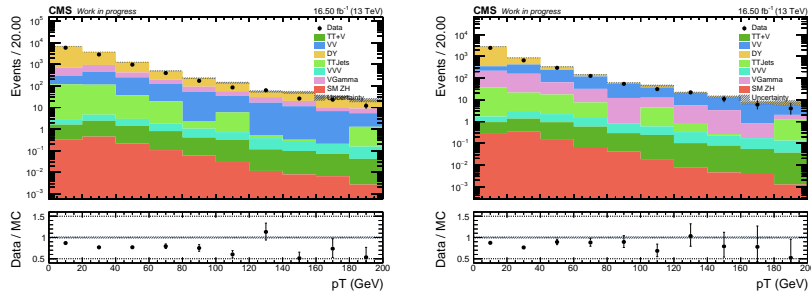


Figure 43: p_T distributions in the $Z + e$ CR for the electron candidate passing the loose (left) and nominal (right) identification criteria. Plots refer to 2016–postVFP data taking year.

E Closure Test

The results presented in this section do not exactly correspond to the final choice of the loose selection for τ_h as defined in Eq. 7.1. Initially, the Loose D_{jet} WP was used; however, during the CMS review process, further investigations revealed that adopting a looser selection—VVVLoose instead of Loose—would enhance statistical precision by increasing the number of events in the control regions. Nonetheless, the studies shown here, which are based on the initial Loose selection, are included to demonstrate the correct implementation of the method and to show that it yields consistent and reliable results.

In order to evaluate the validity of the method, we have performed a closure test using the simulated reducible background samples. The method described in Sec. 7.8.2 has been used on those simulated samples that represent exactly that kind of background topology which needs to be rejected, that is $Z/\gamma^* + \text{jets}$. In this study we also added $t\bar{t} + \text{jets}$ to increase statistics and investigate the fake rate behavior with different jet flavors.

The comparison between the results of this procedure and the true yields obtained in the signal region provides not only a reasonable measure of the validity of the method in data, but also an estimate of the systematic uncertainty associated to the data-driven method itself, in case of not full closure.

The first step is computing the fake rate curves with the MC of reducible background and compare it with the data driven curves, as it was done already in Sec. 7.8.2.

The second step is applying the Eq. 7.10 derived previously to estimate the yield in signal region from MC and compare it to the yields given by the raw MC. The results are shown for 2018 in Fig. 44 (a), (d) and (g). The results look in agreement within the statistical uncertainties.

The same method is used to extract shapes. In Fig. 44 (b), (c), (e), (f), (h) and (i) the $m(\ell\ell)$ and the $m(\tau\tau)$ variables are checked. In this binned case, there are clearly high statistical uncertainties but we can anyway conclude that there is no intrinsic error in the procedure and the closure is succeeded.

Similar results are presented for 2017 and 2016 in Fig. 45 and Figures 46, 47, respectively.

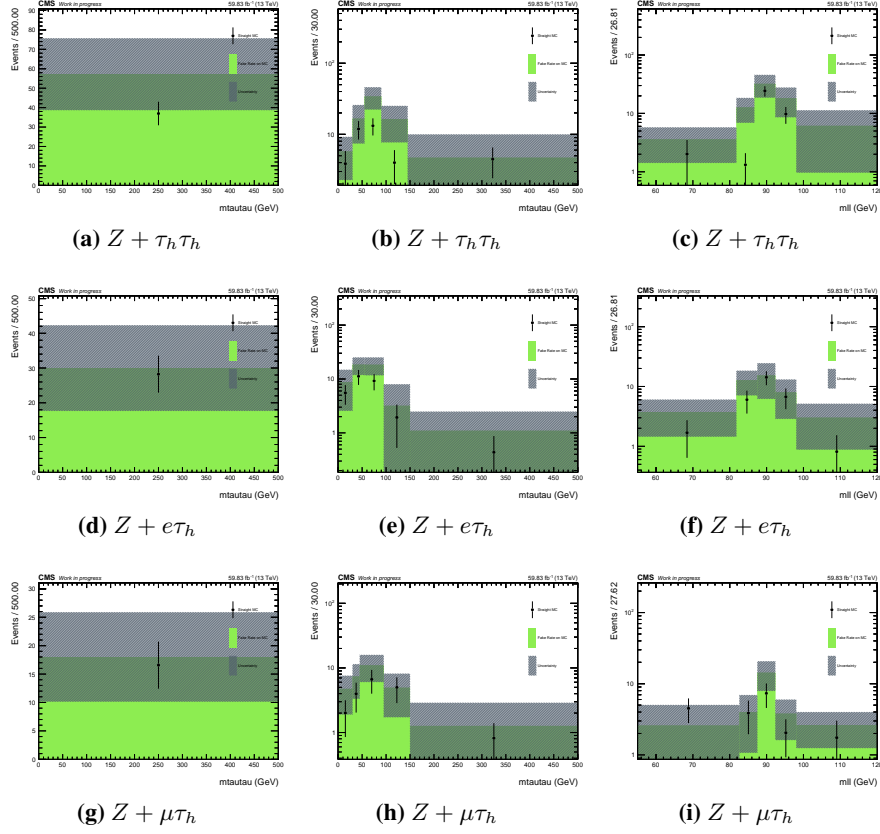


Figure 44: Yields (left column) and shapes (central and right column) in signal region obtained from straight simulation and using the fake rate method on simulation. Plots refer to 2018 data taking year.

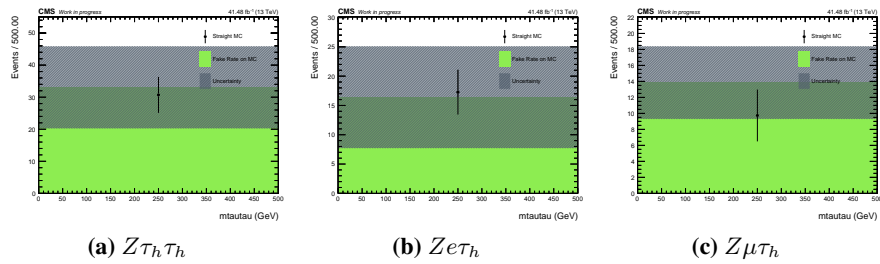


Figure 45: Yields in signal region obtained from straight simulation and using the fake rate method on simulation.

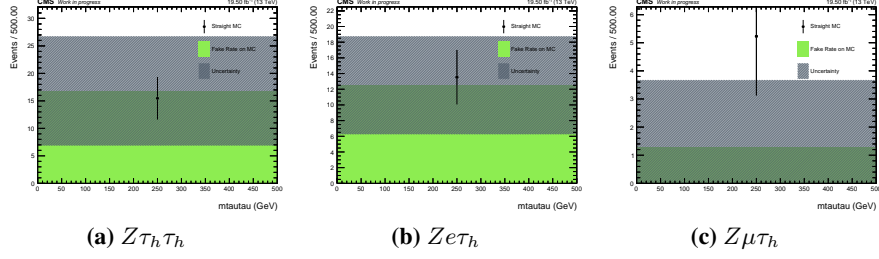


Figure 46: Yields in signal region obtained from straight simulation and using the fake rate method on simulation. Plots refer to 2016–preVFP data taking year.

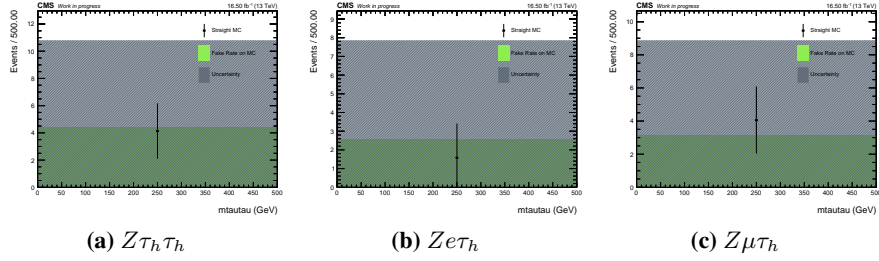


Figure 47: Yields in signal region obtained from straight simulation and using the fake rate method on simulation. Plots refer to 2016–postVFP data taking year.

F Choice of observables

The different observables have been tested to extract the final upper limits. Other than the $m_A \times m_H$ variable that is presented in the main text, we tested the $Zp_T \times \Delta M$ that combines the Zp_T and the difference in reconstructed mass between the two new resonances and proved to be optimal in a similar analysis in the $\ell\ell t\bar{t}$ channel. In addition, the DNN score was tested.

These observables are reported in Fig. 49 for example for the channel $Z + \mu\tau_h$, together with the results in terms of upper limits on signal strength for the three channels combined only in 2018 for $m_H=600$ GeV. Among the three, the $Zp_T \times \Delta M$ is the one with inferior performance, while the other two present comparable limits. Table 28 reports the limits for these observables until 400 GeV, showing better performance for the DNN for lower mass values while $m_A \times m_H$ is proven better for higher masses (also the suboptimal DNN score binning could play a role here).

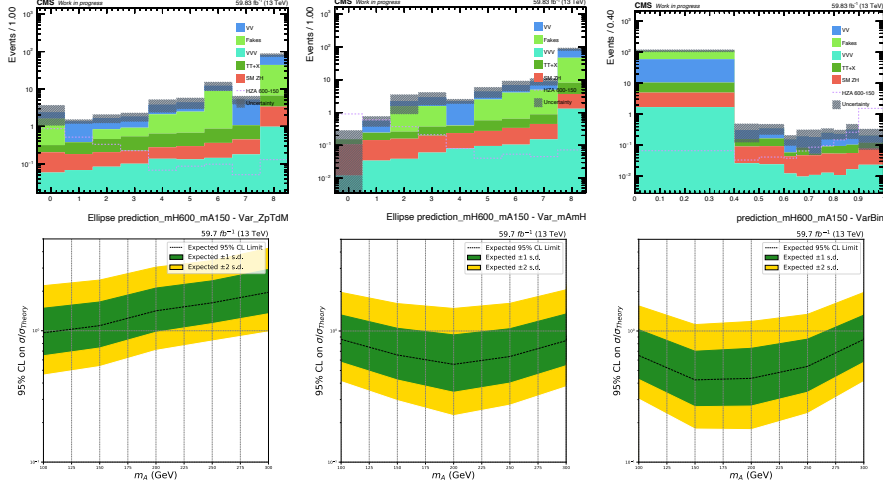


Figure 48: Observables in the $Z + \mu\tau_h$ channel (top row) and relative upper limits including all channels (bottom row) for 2018.

$m_H=600$ GeV, m_A :	$m_A \times m_H$	DNN score
100	0.863	0.650
150	0.656	0.424
200	0.557	0.435
250	0.639	0.537
300	0.844	0.863
350	101.5	143.25
400	230.0	297.5

Table 28: Expected upper limits on signal strength in 2018 for $M_H=600$ GeV for the $m_A \times m_H$ and the DNN score observables.

Finally, the power of the DNN and of the $m_A \times m_H$ observable were combined by cutting on the network score while fitting on the elliptical binned masses. Figure 49 shows how the expected upper limits change with the cut. It can be observed that a 0.2 cut leads to an improvement in the range 20-40% depending on the mass, making this final solution the best in terms of performance and interpretability of the results.

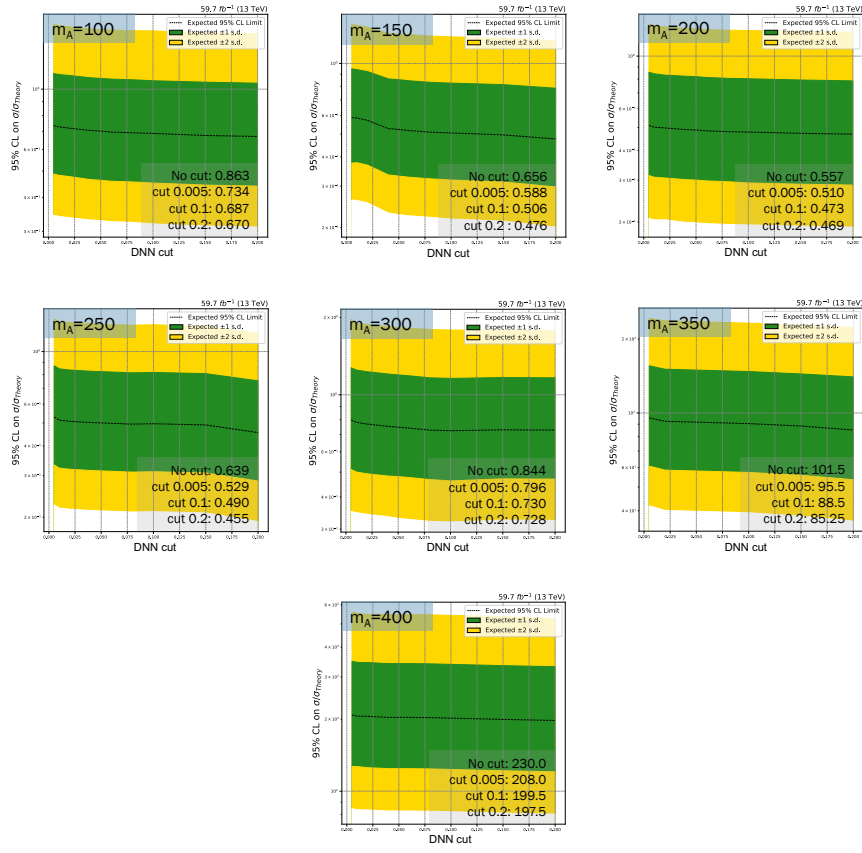


Figure 49: Upper limits for different m_A as a function of the DNN cut. Plots refer to 2018.

G Flavor-related uncertainty for the misidentification rate curves

The probability for a jet to be misidentified as a lepton can depend on the jet's flavor. To account for this dependence in the measured misidentification rate curves, a flavor-related systematic uncertainty was introduced using the following procedure. First, the flavor composition in the reference simulated samples ($Z/\gamma^* + \text{jets}$ and $t\bar{t} + \text{jets}$) is artificially modified by increasing or decreasing the fraction of heavy-flavor jets by 50% (see Figures 50, 51, and 52). The misidentification rate curves are then recomputed using these modified samples (see Figures 53, 54, and 55). The ratio between the altered and nominal curves is applied to the data-driven misidentification rate curves to define the up and down variation for this flavor-related systematic uncertainty.

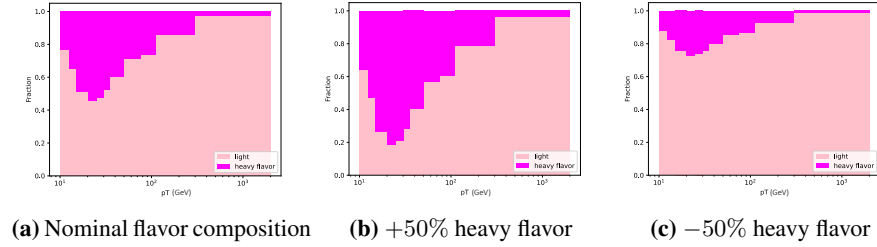


Figure 50: Flavor composition in the simulated reference samples in the $Z + e$ CR.

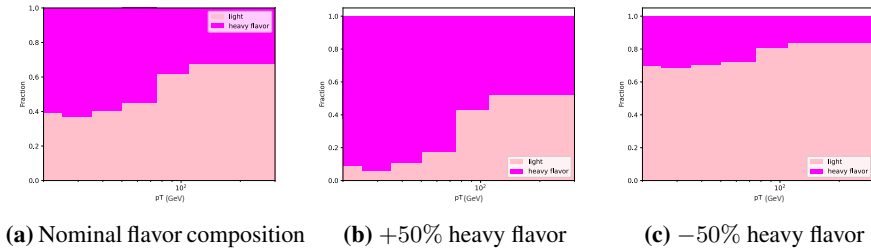


Figure 51: Flavor composition in the simulated reference samples in the $Z + \mu$ CR.

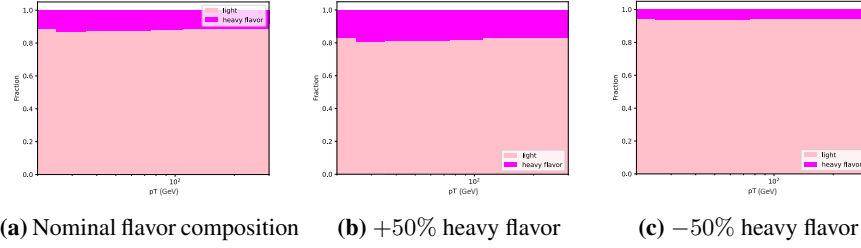


Figure 52: Flavor composition in the simulated reference samples in the $Z + \tau_h$ CR.

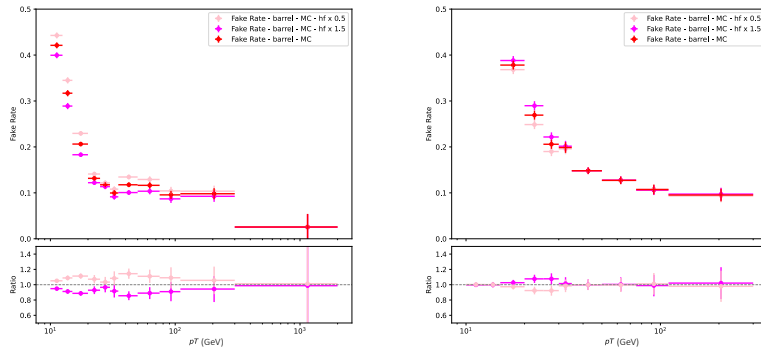


Figure 53: Misidentification rate curves for electron.

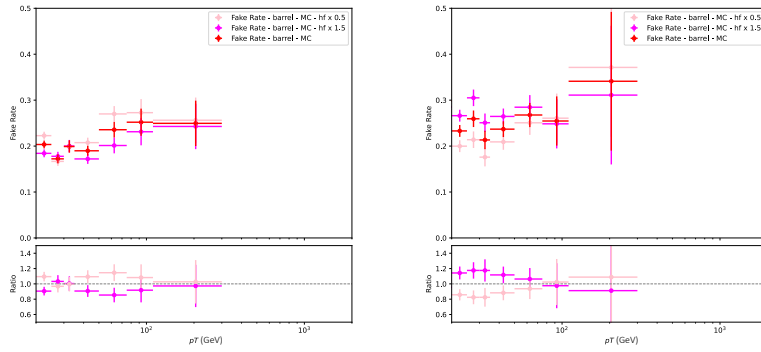


Figure 54: Misidentification rate curves for muon.

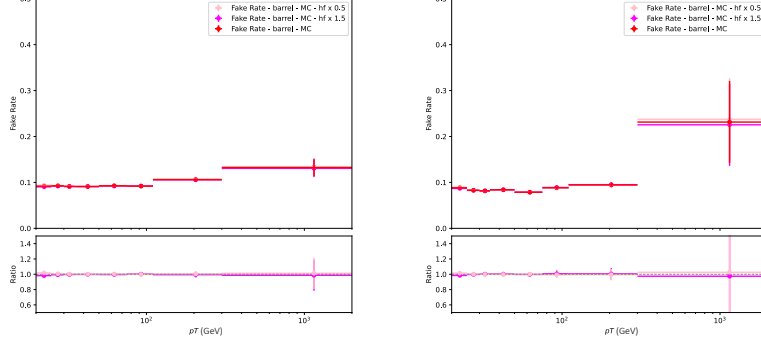


Figure 55: Misidentification rate curves for τ_h .

H Goodness of fit test

In Fig. 56 we report the $m_A \times m_H$ distribution in a control region where the DNN cut is failed, showing reasonable data/simulation agreement within the statistical uncertainties.

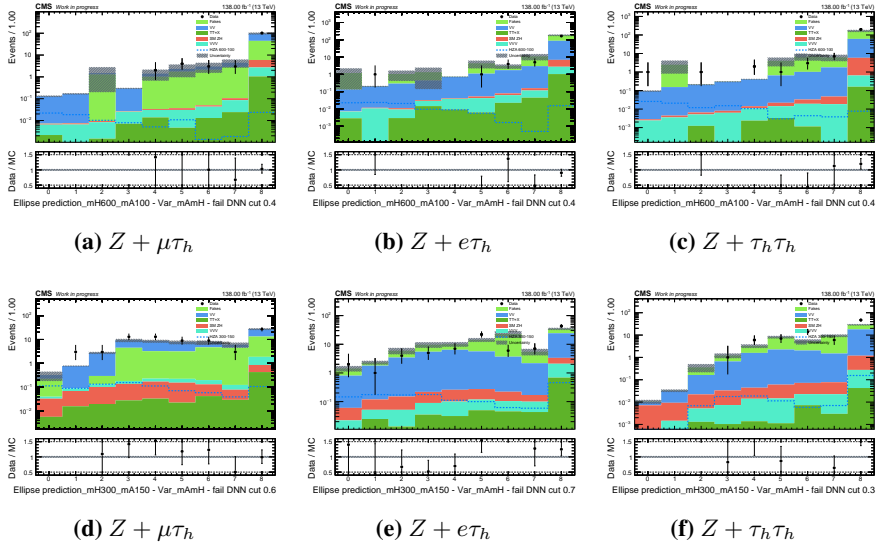


Figure 56: Control plots: $m_A \times m_H$ for events that failed the DNN cut. (Top) $(m_H, m_A) = (600, 100)$ GeV, (Bottom) $(m_H, m_A) = (300, 150)$ GeV.

A goodness of fit test was run in this control region, with real data using the saturation model. The p-values shown in Fig. 57 for $(M_H, M_A) = (600, 100)$

GeV (left) and for $(m_H, m_A) = (300, 150)$ GeV (right) are greater than 0.05 and prove that there is reasonable background modeling for these two very different mass scenarios.

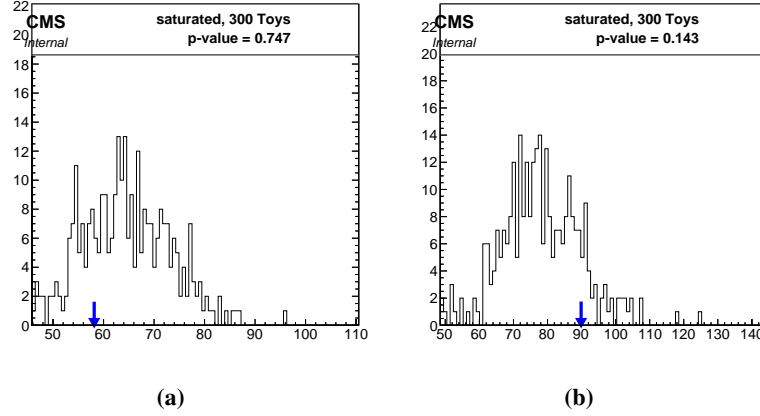


Figure 57: Goodness of fit test result for $(m_H, m_A) = (600, 100)$ GeV (left) and $(m_H, m_A) = (300, 150)$ GeV (right).